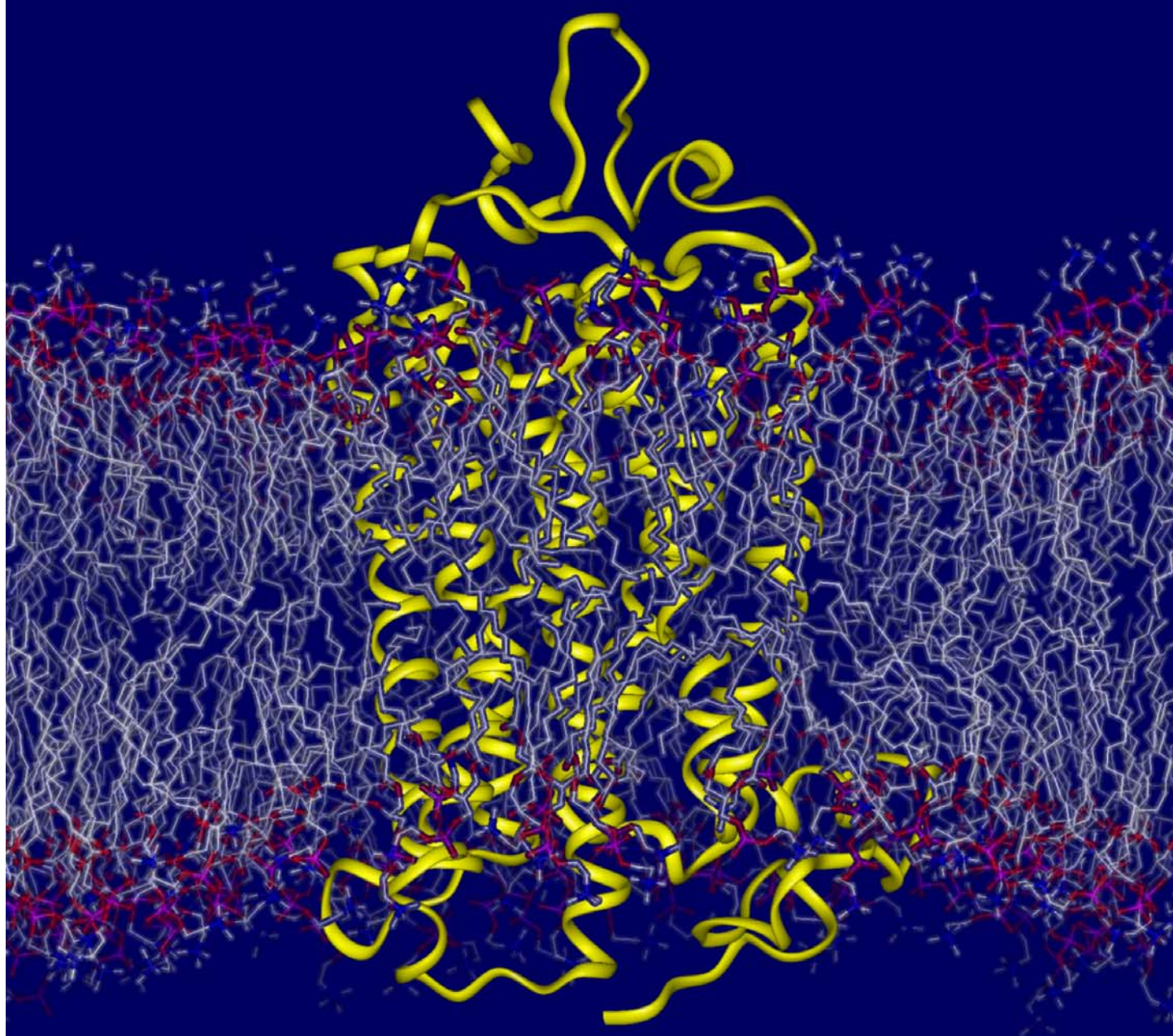


Molecular dynamics simulations of seven-transmembrane receptors

ARNAU CORDOMÍ



**PhD Thesis
Universitat Politècnica de Catalunya
Barcelona, January 2008**

ESCOLA TÈCNICA SUPERIOR D'ENGINYERIA INDUSTRIAL DE BARCELONA
UNIVERSITAT POLITÈCNICA DE CATALUNYA



Molecular dynamics simulations of seven-transmembrane receptors

PhD Thesis submitted to obtain the degree of Doctor in Science

This work has been carried out at the in the Department of Chemical Engineering under the direction of Prof. Juan Jesús Pérez.

Signature:

Prof. Juan Jesús Pérez González

Arnau Cordermí Montoya
Barcelona, January 2008

Abstract

Seven transmembrane (7-TM) G protein coupled receptors (GPCR) constitute the largest family of integral membrane proteins in eukaryotes with more than 1000 members and encoding more than 2% of the human genome. These proteins play a key role in the transmission and transduction of cellular signals responding to hormones, neurotransmitters, light and other agonists, regulating basic biological processes. Their natural abundance together with their localization in the cell membrane makes them suitable targets for therapeutic intervention. Consequently, GPCR are proteins with enormous pharmacologic interest, representing the targets of about 50% of the currently marketed drugs.

The current limitations in the experimental techniques necessary for microscopic studies of the membrane as well as membrane proteins emerged the use of computational methods and specifically molecular dynamics simulations. The lead motif of this thesis is the study of GPCR by means of this technique, with the ultimate goal of developing a methodology that can be generalized to the study of most 7-TM as well as other membrane proteins. Since the bovine rhodopsin was the only protein of the GPCR family with a known three-dimensional structure at an atomic level until very recently, most of the effort is centered in the study of this receptor as a model of GPCR.

The scope of this thesis is twofold. On the one hand it addresses the study of the simulation conditions, including the procedure as well as the sampling box to get optimal results, and on the other, the biological implications of the structural and dynamical behavior observed in the simulations. Specifically, regarding the methodological aspects of the work, the bovine rhodopsin has been studied using different treatments of long-range electrostatic interactions and sampling conditions, as well as the effect of sampling the protein embedded in different one-component lipid bilayers. The binding of ions to lipid bilayers in the absence

of the protein has also been investigated. Regarding the biological consequences of the analysis of the MD trajectories, it has been carefully addressed the binding site of retinal and its implications in the process of isomerization after photon uptake, the alteration a group of residues constituting the so-called *electrostatic lock* between helices TM3 and TM6 in rhodopsin putatively used as common activation mechanism of GPCR, and the structural effects caused by the dimerization based on a recent semi-empirical model. Finally, the specific binding of ions to bacteriorhodopsin has also been studied.

The main conclusion of this thesis is provide support to molecular dynamics as technique capable to provide structural and dynamical informational about membranes and membrane proteins, not currently accessible from experimental methods). Moreover, the use of an explicit lipidic environment is crucial for the study the membrane protein dynamics as well as for the protein-protein and lipid-protein interactions.

Acknowledgments

There are two persons that have been corner stones for the development of this thesis: Juan Jesús Pérez and Olle Edholm. I would like to thank Juanje for the supervision and support and for providing me the opportunity to work in the LEM during the last years, and to Olle not only because his pivotal contributions but also for the wonderful experience that was my stay in Stockholm. This thesis would have never been possible without them.

I would like to thank all fellow authors of the papers presented with this thesis, and particularly to Pere Garriga, Eva Ramón, Laia Bosch and Francesc Sepulcre. It has been a pleasure to collaborate with you.

I want to thank everybody that shared office in the Laboratory of Molecular Engineering in the UPC during these years for some interesting discussions, but mostly for the good atmosphere. Thanks to Dani (Evildan) Badia, Josep Cantó, Francesc Corcho, Monica Delgado, Patricia Gómez, David Jiménez, Marlet Martínez, Marta Pinto, Lourdes Roset, and very especially to Oriol Llorens, whose enthusiasm for research convinced me to start a PhD after ending my diploma thesis. Thanks also to my colleges in Albanova Physics Department in Stockholm, and to those who are or have been in our brother group in the UB-QF, Laura Delgado, Cristian Obiol, Alex Rodríguez, Oscar Villacañas and Jaime Rubio.

Finally, those who have been at my side during this time are indirect, but important contributors to this work. I want to thank them very specially for their support: my friends, my family and Carla. This thesis is also yours!

Abbreviations

BR	bacteriorhodopsin
DPPC	dipalmitoyl phosphatidylcholine
EXAFS	extended X-ray absorption fine structure
GPCR	G-protein coupled receptor
GDP	guanidine diphosphate
GTP	guanidine triphosphate
LJ	Lennard-Jones
MD	molecular dynamics
PBC	periodic boundary conditions
PC	phosphatidylcholine
PM	purple membrane
PME	particle mesh Ewald

Papers included as part of this thesis

- I. Effect of different treatments of long-range interactions and sampling conditions in molecular dynamic simulations of rhodopsin embedded in a dipalmitoyl phosphatidylcholine bilayer.**

Cordomí A, Edholm O, Perez JJ.

J Comput Chem., 2007 Apr 30;28(6):1017-30.

- II. Molecular dynamics simulations of rhodopsin in different one-component lipid bilayers.**

Cordomí A, Perez JJ.

J Phys Chem B., 2007 Jun 28;111(25):7052-63.

- III. Structural rearrangements of rhodopsin subunits in a dimer complex: a molecular dynamics simulation study.**

Cordomí A, Perez JJ.

J Mol Graph Model., 2008 Submitted.

- IV. The effect of ions on a dipalmitoyl phosphatidylcholine bilayer. A molecular dynamics simulation study.**

Cordomí A, Edholm O, Perez JJ.

J Phys Chem B., 2008 15 Jan; Epub ahead of print.

- V. Critical role of electrostatic interactions of amino acids at the cytoplasmic region of helices 3 and 6 in rhodopsin conformational properties and activation.**

Ramon E, Cordomí A, Bosch L, Zernii EY, Senin II, Manyosa J, Philippov PP, Perez JJ, Garriga P.

J Biol Chem., 2007 May 11;282(19):14272-82.

VI. Molecular dynamics simulations of rhodopsin point mutants at the cytoplasmic side of helices 3 and 6.

Cordomí A, Ramon E, Garriga P, Perez JJ.

J. Biomol. Struct. Dyn., 2008 In press.

VII. A methyl group at C7 of 11-cis-retinal allows chromophore formation but affects rhodopsin activation.

Bosch L, Cordomí A, Dominguez M, Toledo D, Morillo M, Perez JJ, Alvarez R, de Lera AR, Garriga P.

Vision Res., 2006 Dec;46(27):4472-81.

VIII. X-ray absorption and molecular dynamics study of cation binding sites in the purple membrane.

Sepulcre F, Cordomí A, Proietti MG, Perez JJ, Garcia J, Querol E, Padros E.

Proteins. 2007 May 1;67(2):360-74.

Contributions from other authors

Juan J. Perez contributed largely to the discussion of all studies as well as in the writing of the corresponding reports, mostly of Papers I, II, III, IV and VI.

Olle Edholm provided the basis for the membrane protein simulations with lipid bilayers performed in this thesis. He also largely contributed to Papers I and IV, coming with the idea of exploring the differential effect of different ions on a dipalmitoyl phosphatidylcholine bilayer.

The group of Pere Garriga, and particularly Laia Bosch, Eva Ramón and himself, wrote most of Papers IV, V and VII and performed the experiments including mutant preparation and characterization as well as the activation tests. They also contributed to the discussion and writing of Paper VI.

Francesc Sepulcre had the idea of using MD for the simulation of theoretical EXAFS spectra to be compared to the experimental ones performed by himself and his collaborators. The work is reflected in Paper VIII, where he did most of the writing.

Table of Contents

Part I. Background.....	17
Chapter 1 - Introduction.....	19
1.1 The cell membrane.....	21
1.1.1 Ions in membranes	23
1.2 Membrane proteins	25
1.3 Seven-transmembrane receptors.....	28
1.3.1 Rhodopsin.....	30
1.3.2 Activation of GPCR.....	32
1.3.2.1 Activation of Rhodopsin.....	34
1.3.3 Oligomerization of GPCR	35
1.3.4 Bacteriorhodopsin.....	37
1.3.4.1 Specific ion binding	38
1.4 Lipid-protein interactions	40
Chapter 2 - Methods.....	43
2.1 Computational Chemistry	45
2.2 MD simulations.....	46
2.2.1 MD principles.....	46
2.2.2 Force fields	47
2.2.2.1 Proteins	49
2.2.2.2 Lipids	50
2.2.2.3 The water molecule.....	50
2.2.2.4 Ions.....	52
2.2.3 Long-range interactions.....	53
2.2.4 Statistical ensemble.....	37
2.3 Simulations of membrane proteins.....	55
2.3.1 Rhodopsin simulations.....	57

Part II. Results	61
Chapter 3 - Scientific papers	63
Paper I	69
Paper II	87
Paper III	103
Paper IV	127
Paper V	143
Paper VI	157
Paper VII	175
Paper VIII	189
Chapter 4 - Conclusions	207
Bibliography	215

Part I - Background

Chapter I - Introduction

Chapter 1 - Introduction

1.1 The cell membrane

Membranes are a key element for life since they act as a physical barrier to separate the interior of a cell from the outside world. They also serve to confine its different compartments, providing the means for a cell to be out from the equilibrium with the surroundings, allowing important processes occurring in the interior. In addition to be crucial for cell integrity, cell membranes also serve as a matrix and support for many types of proteins involved in important cell functions and therefore, they are essential for cell function.

Biological membranes consist of organized assemblies of lipids and proteins. The current knowledge of how they are structured is still scarce due to the difficulties associated to the experimental techniques required to investigate their properties. The modern view of biological membranes is basically based on the fluid mosaic model proposed in the seventies (Singer 1972), in which lipids are arranged in bilayers, where proteins are embedded, and subject to a lateral freely diffusion. At that time, however, the involvement of lipids in membrane function was overemphasized, partly because membrane proteins were not readily accessible and their function was poorly understood. With the growing knowledge of membrane proteins, the accepted vision has become more protein centered and the crucial role of lipids diluted. It is not until more recently that, with a better understanding of lipid-protein interactions, the role of lipids in protein function is again having an increasing attention (White 1999; Lee 2003; Lee 2004; Vigh 2005). The current vision of membranes is more as a mosaic than a fluid: lipids organize a matrix where proteins are distributed in regions of biased composition with varying protein environment (Engelman 2005).

Membranes consist of a complex mixture of lipids, where different proteins both, integral and peripheral are embedded. Protein content varies greatly among

the different kinds of membranes, ranging typically between 15 to 75%, depending on the functions that they must carry out (Guidotti 1972). Furthermore, lipid composition changes from one membrane to another due to the enormous structural diversity found, that can be associated with the differential roles and properties of each membrane or region. The most widely found lipids consist of a structure of a fatty acid linked by an ester bond to an alcohol such as glycerol or cholesterol, or through amide bonds to a sphingoid base or to other amines. Most lipids have a highly polar head group and two hydrocarbon tails. In a typical membrane, approximately half of the lipids are phospholipids, mainly phosphatidyl -cholines (PC), -ethanolamines (PE) and -serines (PS). Other major components following in importance are sphingolipids, glycolipids and cholesterol (Tanford 1973). Interestingly, since the two sides of the membrane bilayer must deal with different surroundings, the two leaflets of a membrane typically exhibit an asymmetric composition. The lateral distribution of lipids is also non-homogeneous in regard to lipid components, providing regions with different levels of molecular order that are known as rafts. These seem to be important for the function of membrane proteins (Simons 1997). Finally, the presence of specific components such as cholesterol has been found to trigger domain formation in lipid bilayer membranes (Bachar 2004).

Since PC is the most abundant type of lipid in animal cells, bilayers constituted by these lipids are among the most widely studied model membrane systems. PC consist of a glycerol backbone bound to two fatty acid chains named sn-1 and -2 and a phosphate group attached to choline. A 2D plot of four different PC lipid structures is shown pictorially in Figure 1 of Paper II. Lipid membranes made of a single lipid species display a discrete phase transition from a stiff gel phase to the biologically relevant fluid liquid-crystalline phase (L_{α}) at a defined phase transition temperature. The phase transition is known to be due to bond rotations of the hydrocarbon chains which weaken the van der Waals attractions, resulting in a lack of lateral structure both in the chains and in the head-groups.

As an example, a DPPC lipid bilayer in the L_{α} -phase, taken from a molecular dynamics (MD) simulation, is depicted in Figure 1.1.

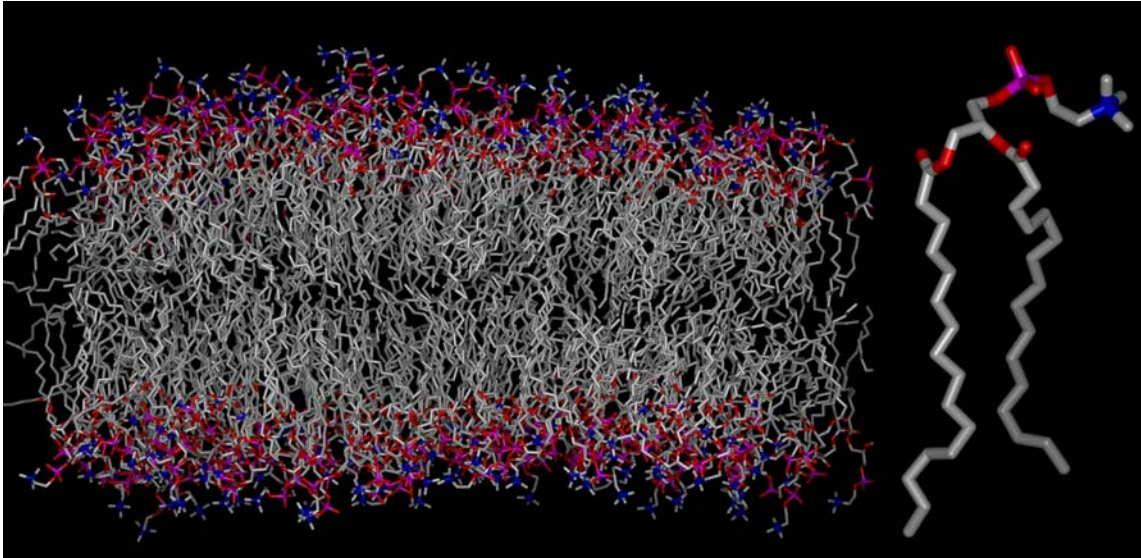


Fig 1.1 – Structure of a DPPC lipid bilayer in the L_{α} -phase taken from a MD simulation from Paper II (left) and a close up of a specific DPPC lipid (right). The atoms are colored by atom type; hydrogen atoms are not present.

1.1.1 Ions in membranes

All higher life forms require a subtle and complex electrolyte balance between the intracellular and extracellular milieu. At physiological conditions membranes are in contact with an aqueous solvent that contains ions such as sodium, potassium, calcium, magnesium, chloride, phosphate, and hydrogen carbonate. The maintenance of precise osmotic gradients of electrolytes is important because they affect and regulate the hydration of the body, blood pH and are critical for nerve and muscle function.

Experimental work performed in the last few decades shows that ions play an essential role in the structure, dynamics and stability of membranes, but also in the binding and insertion of proteins, membrane fusion and transport across them (Parsegian 1975; Brown 1977; Lis, Parsegian 1981; Lis, Lis 1981; Akutsu

1981; Loosleyman 1982; Altenbach 1984; Herbette 1984; Tatulian 1987; Cunningham 1988; Roux 1990; Clarke 1999). Therefore, a study of the interactions between lipids and ions is a matter of substantial interest (Berkowitz 2006). The specific binding of ions to model lipid bilayers has been studied in a variety of systems including, both negatively charged and zwitterionic lipids. For charged lipids, the obvious role of ions is to act as a counter charge (Elmore 2006; Zhao 2007). However, several studies have confirmed that ions interact in an analogous way in zwitterionic lipid bilayers (Pandit 2003b; Böckmann 2003; Böckmann 2004; Sachs 2004; Gurtovenko 2005).

Despite early experimental evidence that some ions may alter the structural properties of lipid bilayers (Watts 1981; Hauser 1984), the difficulties associated with precise experimental determinations still leave open questions. A recent study of ion binding to a phosphatidylcholine (PC) bilayer concluded that some ions affect the gel to liquid crystalline phase transition (Binder 2002). Similarly, MD simulations of lipid bilayers with ionic solutions show the effect of ions in reducing the area per lipid in the case of negatively charged lipids (Pandit 2002; Mukhopadhyay 2004; Pedersen 2006; Zhao 2007) as well as for zwitterionic ones (Pandit 2003b; Böckmann 2003; Böckmann 2004). Moreover, heat capacity measurements suggest that sodium ions reduce the area per lipid in zwitterionic PC bilayers (Böckmann 2003). Similarly, a recent study on the nano-mechanics of lipid bilayers revealed different effects attributable to such increase (Garcia-Manyes 2005). In contrast, in a recent X-ray diffraction study the authors found that potassium ions do not alter the structure of PC bilayers (Petrache 2006), exhibiting an apparent differential behavior to the previous results. Paper IV describes the results of a MD study of DPPC lipid bilayers with different cations.

1.2 Membrane proteins

Membrane proteins are attached to or associated with either the cell membrane or an organelle. They are often classified into two groups: integral and peripheral, based on the strength of their association with the membrane. Specifically, the former are permanently attached to the membrane, whereas the latter are only temporarily attached either to the lipid bilayer or to integral proteins. Integral proteins are divided into transmembrane (TM) and monotopic proteins. While the former span along the entire membrane, the latter are permanently attached to the membrane from only one side. Membrane function is mediated in a large extent by integral membrane proteins, which are often organized as assemblies of polypeptide segments interacting with the lipid bilayer and serving as channels, receptors and energy transducers. Accordingly, they constitute biological machines involved in essential biological process like ion and molecular transport across the membrane, cell communication and signaling. Therefore, their study is a field of enormous interest.

An analysis of the human genome indicates that about a quarter of the cellular proteins are found embedded in membranes, where they perform critical biological functions (Boyd 1998). Despite their importance, most of their structural and functional properties still need to be unraveled. The lack of knowledge regarding both membranes and membrane proteins arises from technical issues associated to the work with these systems. Moreover, the difficulties in isolating purifying and crystallizing membrane proteins resulted in a extremely low number of available crystal structures of membrane proteins when compared to that of globular proteins (White 1999; Berman 2000; White 2004).

Membrane proteins exhibit special structural features not found in globular proteins due to the high proportion of hydrophobic amino acids, particularly in the regions embedded in the membrane. Specifically, they exhibit only two structural motifs: β -stranded barrels or α -helical segments that span the membranes,

analogous to the examples shown in Figure 1.2. β -barrels have only been found in outer membranes of Gram-negative bacteria, cell wall of Gram-positive bacteria, outer membranes of mitochondria and chloroplasts. On the contrary, α -helices are present in all types of biological membranes (including outer membranes) and therefore, they are the predominant motif present in membrane proteins (White 1999). The structures that can be formed using only this motif include, however, many different kinds of TM proteins such as transporters, channels and enzymes, which have been collected in specialized databases (Jayasinghe 2001; Raman 2006).

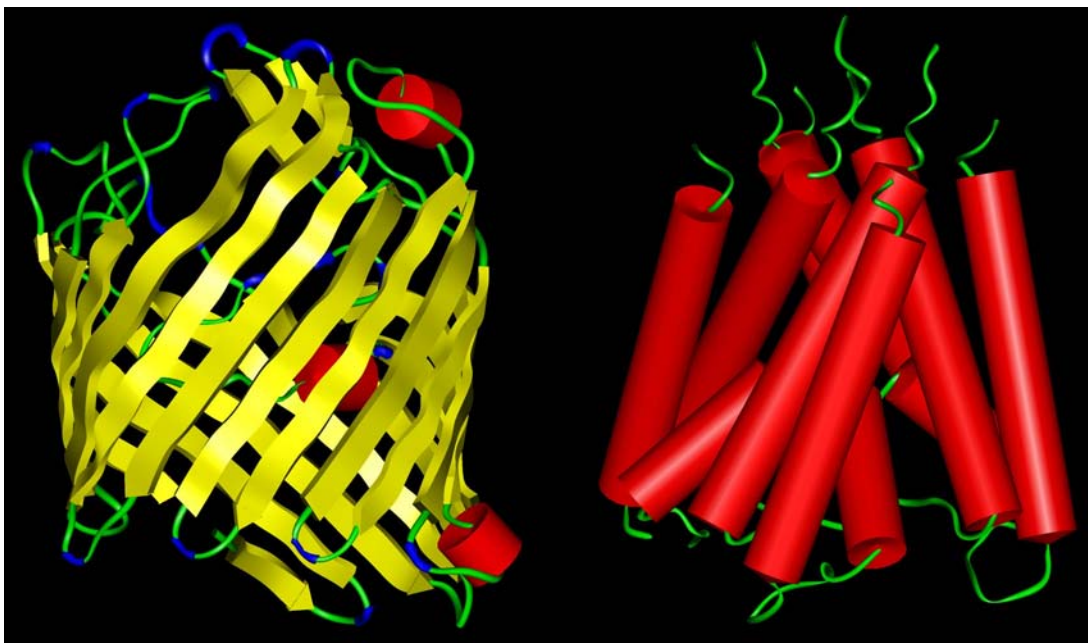


Figure 1.2 – Typical structures of spanning TM proteins: a β -stranded barrel (left side; PDB:2OMF) and an α -helical ion channel (right side; PDB:1BL8). Red cylinders represent α -helices, yellow arrows β -strands and blue and green lines β -turns and random coils, respectively.

The polypeptide of a α -helix is arranged in a right-handed helical structure, 0.54 nm wide. Moreover, each amino acid corresponds to a turn of 100° in the helix -3.6 residues per turn- and a translation of 0.15 nm along the helical axis. Most importantly, the N-H group of an amino acid (i) forms a hydrogen bond with

the C=O group of the amino acid four residues earlier. Repeated $i+4 \rightarrow i$ hydrogen bonding define an α -helix, whereas consecutive $i+3 \rightarrow i$ and $i+5 \rightarrow i$ interactions form alternative 3_{10} - and π -helices, respectively. Although these are relatively rare, 3_{10} helix is often found at the ends of α -helices. A helix has an overall dipole moment caused by the aggregate effect of all the individual dipoles of the carbonyl groups of the peptide bond pointing along the helix axis.

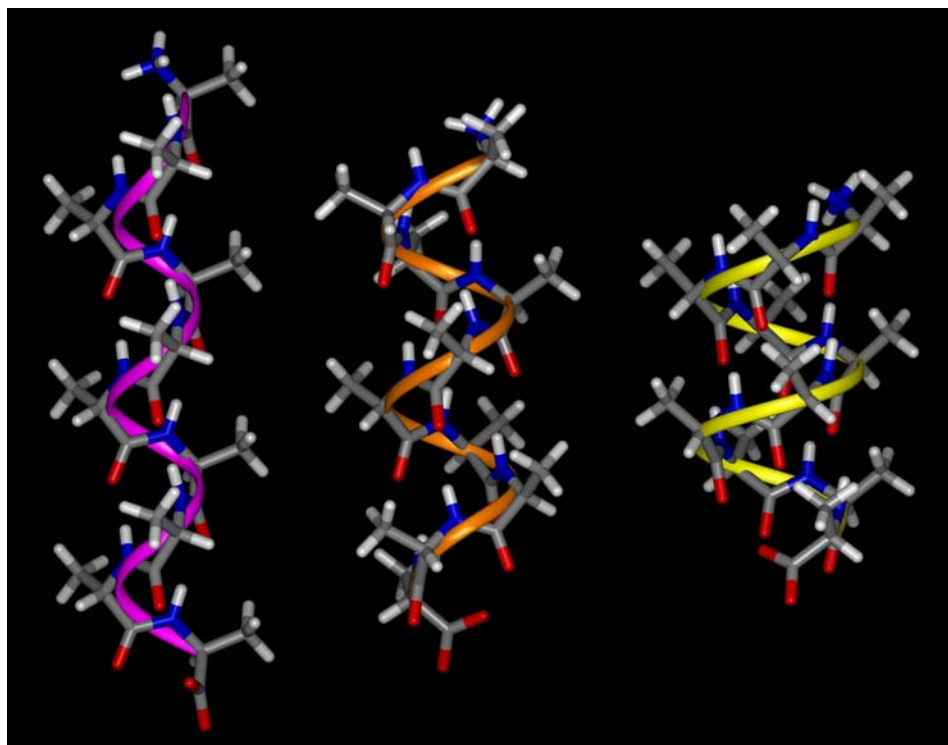


Figure 1.3 – Lateral views of an Ala decapeptide forming 3_{10} (left, purple), α (center, orange) and π (right, yellow) helices. Atoms are colored by type.

Different amino-acid sequences have different propensities to form α -helical structures. Specifically, methionine, alanine, leucine, glutamic acid and lysine exhibit high helix-forming propensities, whereas other residues such as proline and glycine play a role as helix disrupters. Proline tends to break or kink helices because it cannot donate an amide hydrogen bond, its side chain interferes sterically and its ring structure restricts its backbone. At the other extreme, glycine tends also to disrupt helices because its high conformational flexibility, making entropically expensive adopting the relatively constrained α -helical structure.

Finally, residues with polar side chains can also induce helix distortions due to their side chains interfering within the backbone-backbone interactions. Regarding the packing of helices in a bundle, the main stabilizing force between α -helical segments are van der Waals forces and more specifically, London dispersion.

1.3 Seven-transmembrane receptors

7-TM receptors constitute the largest, most ubiquitous and versatile family of membrane receptors. In eukaryotes, these proteins are coupled to G proteins and therefore, they are also called G-protein coupled receptors (GPCR). The family comprises more than 1000 members that encode more than a 2% of the human genome, which makes it by far the largest family of integral TM proteins (Palczewski 2006). These receptors play a key role in transmission of transduction cell signals responding to hormones and neurotransmitters, regulating basic physiological processes, being of great pharmacological interest (Ellis 2004). Their natural abundance together with their localization in the cell membrane make them suitable targets for therapeutic intervention, accounting for more than 50% of the currently marketed drugs (Archer 2003). The ligands that bind and activate them include light-sensitive compounds, odors, pheromones, hormones, and neurotransmitters, which vary in size from small molecules to peptides and large proteins.

Despite their important biological function, there is scarce structural information about them, pointing to the necessity to get a better understanding of their structure-function relationships (Stenkamp, Teller 2002; Filipek, Stenkamp 2003; Filipek, Teller 2003; Yeagle and Albert 2006). Thus, although it is well established that GPCR are arranged in seven helix bundles, differential features, both sequential and structural among the several existing subfamilies have been described (Attwood 1994; Sakmar 2002). As stated in the preceding section, the

lack of structural information at present is basically due to the difficulties associated with the crystallization of membrane proteins.

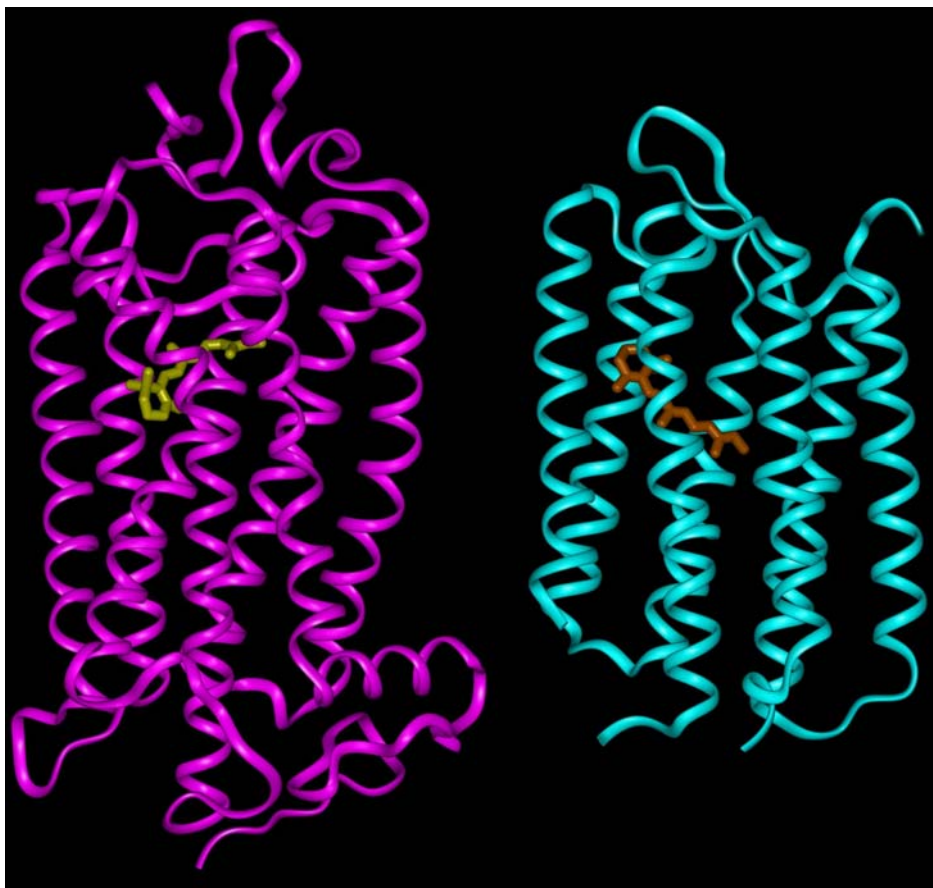


Figure 1.4 – Crystal structures of rhodopsin (left; PDB:1U19) and bacteriorhodopsin (right; PDB:1CW3) in their dark states. The ribbons represent each protein structure and 11-*cis* and all-*trans* retinal is shown in yellow and orange, respectively.

Early structural models for GPCR were constructed based on the weak analogy to another 7-TM protein, bacteriorhodopsin (BR), shown in Figure 1.4 (see section 1.3.4), for which a structure had been determined by both electron (Henderson, Baldwin 1990) and X ray-based crystallography (Henderson and Schertler 1990; Pebay-Peyroula 1997; Luecke 1998; Takeda 1998; Luecke 1999). The structure of the bovine Rho was solved (Palczewski 2000) later, constituting the first crystal structure of a GPCR and clearly showing that while

the TM helices were conserved, both structures differed significantly from each other (Figure 1.4). Other Rho crystal structures were reported afterwards (Palczewski 2000; Teller 2001; Okada 2002; Li 2004; Okada 2004). Finally, by the time of editing this thesis two crystal structures of another GPCR receptor, the human β_2 adrenergic, became available at atomic resolution (Rasmussen 2007; Rosenbaum 2007; Cherezov 2007), representing a large step forward into the structural characterization of such receptors.

Various general numbering systems have been implemented with the aim of facilitating the comparison between equivalent amino acids in different GPCR. The most widely used nowadays is the adopted by Ballesteros and Weinstein (Ballesteros 1995). According to this scheme, the most conserved residue in each TM helix is defined as X.50, where X is the helix number, and other residues in the same helix are numbered according to their relative position.

1.3.1 Rhodopsin

Rhodopsin (Rho) is a key photoreceptor protein involved in the signaling process that eventually converts a photon into visual response in vertebrates. Specifically, bovine Rho consists of a polypeptide chain of 348 amino acids known as opsin, folded into the seven TM α -helical bundle characteristic of GPCR, interconnected by hydrophilic extramembranous loops. Its binding site contains the chromophore 11-*cis*-retinal covalently bound to K296 in TM7 via a protonated Schiff base linkage, having E113 in TM3 as its counter-ion. The molecule acts as an inverse agonist until photoactivation of the receptor by light absorption induces the isomerization of the 11-*cis*-retinal to its all-*trans* configuration. This event initiates a conformational change in the receptor, triggering a cascade of biochemical reactions known as visual phototransduction, which is the main molecular mechanism of the visual process. The bovine Rho was the only GPCR whose 3D structure was available at atomic resolution until very recently (Palczewski 2000;

Teller 2001; Okada 2002; Li 2004; Okada 2004), therefore it is considered the prototype of GPCR and has been largely studied. Thus, besides being a template for modeling studies of other GPCR (Stenkamp, Filipek 2002; Oliveira 2004), Rho provides a useful model to carry out detailed studies addressed to assess different structural features of GPCR, as well as to get a deeper understanding of how its dynamical behavior is related to its biological function.

The chromophore retinal is a derivative of the alcohol *all-trans*-retinol, commonly known as Vitamin A, which is originated ultimately from a group of molecules known as carotenes, present in vegetables -including carrots-. The structure of retinal, displayed in Figure 1 of Paper VII, is characterized by having a β -ionone ring and a polyene chain. It will be later described that BR contains also a bound retinal, though in its *all-trans* form in the inactive state. The study of retinal conformations and the characterization of the retinal pocket are of outstanding interest in order to understand the first events of the protein activation process. The conformer of retinal in the dark-state is well characterized after the crystal structures became available: 6-*s-cis*,11-*cis*,12-*s-trans*,15-16-*anti*. These structures show that the chromophore adapts to the binding pocket by generating distortions in the polyene chain through a twist that affects the absorption maxima of the visual pigments and the movements of the chromophore after the initial photoisomerization. The conformation of retinal in the different active intermediates is still uncertain because its pocket has been shown to tolerate both 6-*s-cis* and 6-*s-trans* conformers, convertible with a 180° rotation of the C6-C7 dihedral angle (Sugihara 2002; Lau 2007). This dihedral is suspected to be crucial for the protein activation because it determines the relative orientation of the β -ionone ring with the polyene chain (Nakanishi 2000). Moreover, there is an ongoing debate regarding a possible flip of the ionone ring occurring as part of the transition between some intermediates (Albeck 1989; Ishiguro 2000; Jang 2001; Fishkin 2004). However, there are observations compatible with intermediates that retain the chromophore in its original form in Rho until the

active state (Spooner 2002; Spooner 2003; Spooner 2004). The use of retinal analogs has been shown to be invaluable for the study of the chromophore conformational changes through the visual cycle -in particular when combined with opsin mutations- because they can block or alter a critical conformation (Nakanishi 1995; Jang 2001; Fujimoto 2001; Fujimoto 2002; Alvarez 2003; Fishkin 2004; Vogel 2005).

1.3.2 Activation of GPCR

The activation of GPCR is commonly described in terms of a ternary complex involving the hormone (in general: ligand), the receptor and the G protein (Samama 1993; Weiss 1996a; Weiss 1996b; Weiss 1996c). Moreover, it is assumed that a receptor molecule exists in a conformational equilibrium between active and inactive biophysical states (Rubenstein 1998). In these conditions, the binding of full or partial agonists, as well as the specific interaction with the G protein may shift the equilibrium toward the active receptor states. GPCR ligands are classified according to its influence on this equilibrium: agonists stabilize the active state, inverse agonists stabilize the inactive, and antagonists do not affect the equilibrium.

Signal transduction by the receptor through the membrane is not completely understood. The G protein consist of a heterotrimer of subunits called α , β and γ . Once the ligand is recognized, the signal progresses from the extracellular side to the intracellular domain of the receptor through the TM bundle, by shifting the receptor conformation and thus mechanically binding and activating the G protein, forming the ternary complex. This favors the exchange of GDP to GTP in the α subunit that favors the division of the heterotrimeric G protein in two parts: α unit on the one hand, and $\beta\gamma$ on the other. At this stage both fragments can modulate a variety of systems leading to a cellular response such as the regulation of the enzyme adenylate cyclase (see Paper V). After that,

the α subunit hydrolyzes GTP to GDP, ending up with the G protein returning in its inactive state.

A set of intermolecular interactions involving a group of highly conserved amino acids throughout the members of the GPCR superfamily and located at the cytoplasmic sides of helices TM3 and TM6, have been suggested to form part of a general activation mechanism for all members of the family. These interactions -often referred to as to *the electrostatic lock*- were proposed to constrain receptors in their inactive conformation by restraining the motion of certain domains (Scheer 1996; Ballesteros 1998; Ballesteros 2001). Moreover, the spontaneous release of such interactions acts as a molecular switch that, in some cases, can lead to active forms of the receptor that is able to bind the G protein with high affinity, favoring its activation.

In the late 1990s, evidence began accumulating that some GPCR were able to signal without G proteins. Moreover, some proteins exhibit a significant basal signaling in the absence of agonist: constitutive activity, which is caused by small populations of the receptor being in the active state. In this regard, the mutation of a single amino acid can be sufficient to increase this constitutive activity (Samama 1993; Scheer 1996). Studies of the β_2 -adrenergic receptor show that constitutive activated mutants of this receptor exhibit a larger degree of conformational flexibility, attributed to the disruption of stabilizing conformational constraints (Gether 1997).

The study of the activation mechanism starting from the molecular switch between TM3 and TM6 has been the focus of several works with Rho (Franke 1990; Cohen 1993; Min 1993; Arnis 1994; Sheikh 1996; Farrens 1996; Kim 1997) or other GPCR (Rosenthal 1993; Scheer 1996; Ballesteros 1998; Rasmussen 1999; Ballesteros 2001; Greasley 2002; Huang 2002). Specifically, site-directed mutagenesis studies provided experimental evidence about the relevance of a set

of interactions around R135(3.50) involved in a possible common activation mechanism of most GPCR. Different studies have addressed the effect of mutating either R135(3.50) (Min 1993; Rosenthal 1993; Scheer 1996; Ballesteros 1998), E134(3.49) (Scheer 1996; Ballesteros 1998; Rasmussen 1999), E247(6.30) (Ballesteros 2001; Huang 2002) or T251(6.34) (Greasley 2002) in different GPCR. Particularly, protonation of E134(3.49) or the mutation of either E134(3.49), E247(6.30) or T251(6.34) to residues lacking their charged/polar groups have been shown to increase either the constitutive activity of the receptor in the absence of ligand or its dark activity in its presence (Cohen 1993; Ballesteros 2001; Li 2001; Huang 2002; Periole 2004). These studies have great significance in clarifying several aspects of GPCR function. However the molecular interpretation of these functional effects is sometimes difficult and may be based in wrong hypothesis. The available crystal structures of Rho in its dark-state (Palczewski 2000; Teller 2001; Okada 2002; Li 2004; Okada 2004) show clearly that residues E134(3.49), R135(3.50), E247(6.30) and T251(6.34) are involved in a network of hydrogen bond interactions, being R135(3.50) simultaneously hydrogen-bonded to E134(3.49), E247(6.30) and T251(6.34). These interactions are believed to stabilize Rho and other GPCR in its inactive form, in such a way that mutations changing the chemical profile of the residues tend to weaken the hydrogen bond network, facilitating the transition to a partially activated state and enhancing the activity of the receptor. The combination of site-directed mutagenesis and MD simulations such as the one presented in Papers V and VI has demonstrated to be a useful approach to explore the molecular mechanisms underlying GPCR activation (Scheer 1996; Ballesteros 2001; Kristiansen 2004; Urizar 2005).

1.3.2.1 Activation of Rhodopsin

The gap regarding the structure of the activated form of Rho is beginning to be reduced with the release –additionally to the dark-state crystal structures– of the

first X-ray and electron crystallographic structures of some intermediates (Nakamichi 2006a; Nakamichi 2006b; Salom 2006). At present, it is well established that activation is triggered by the absorption of a photon followed by the isomerization from 11-*cis* to 11-*trans* retinal, a process that leads to bathoRho, the first intermediate, in 200 fs. After that, the local conformational change in the chromophore and subsequent thermal relaxation leads to several spectroscopically identified early states including a blue-shifted intermediate, lumiRho and metaRho₁, which finally brings to the agonist-bound state termed metaRho₁₁ (where the Schiff base has been deprotonated). Finally, the process ends up with large-scale conformational changes in the protein which involve helix motions. At this stage, the interaction of the extramembranous cytoplasmic loops with transducin (G_t), a member of the G-protein superfamily, activates the enzymatic cascade leading to visual transduction. Moreover, the hydrolysis of cGMP to GMP, inactivates MetaRho₁₁ by phosphorylation with Rho kinase, closing cation-specific channels in the rod outer segment of visual cells and building up an electric potential that leads to the generation of a neural signal providing the sensation of vision (Stryer 1991; Sakmar 1991; McBee 2001; Rando 2001).

1.3.3 Oligomerization of GPCR

In line with the classical view of a freely diffusing particle in a fluid membrane model (Singer 1972), early biophysical experiments described Rho as a drifting monomer (Cone 1972; Liebman 1974). However, in recent years there has been increasing evidence suggesting that GPCR may exist and function as homo- and hetero-dimers/oligomers as is discussed in recent reports (Salahpour 2000; Gomes 2001; Angers 2002; George 2002; Gazi 2002; Terrillon 2004; Park 2004; Bulenger 2005; Fotiadis 2006; Milligan 2006; Milligan 2007). Indeed, the crystal structures of rhodopsin (Palczewski 2000; Teller 2001; Okada 2002; Li 2004; Okada 2004) were solved as a dimer, although in a non-physiological orientation (Filipek, Stenkamp 2003). The most direct demonstration about the propensity of

GPCR to form dimers is the recent atomic force microscopy study of native disk membranes from rod outer segments, which provided large paracrystalline arrays of subunits under native conditions (Fotiadis 2003; Liang 2003). By fitting the crystal structure of rhodopsin to the atomic force microscopy map, the authors developed an atomistic semi-empirical model of a rhodopsin oligomer in groups of two subunits interacting through their TM4 and TM5 helices, shown in Figure 1.5. These and other domains involved in the dimerization reported for a variety of GPCR have recently been reviewed (Milligan 2007). Nevertheless, with the recent finding that each rhodopsin molecule binds its own signaling protein (Hanson 2007), it is yet unclear whether the oligomerization is required for proper function and signaling or not (Lee, O'Dowd 2003; Fotiadis 2004; Milligan 2004; Filizola 2005; Kota 2006; Jastrzebska 2006; Fotiadis 2006; Modzelewska 2006; Hanson 2007).

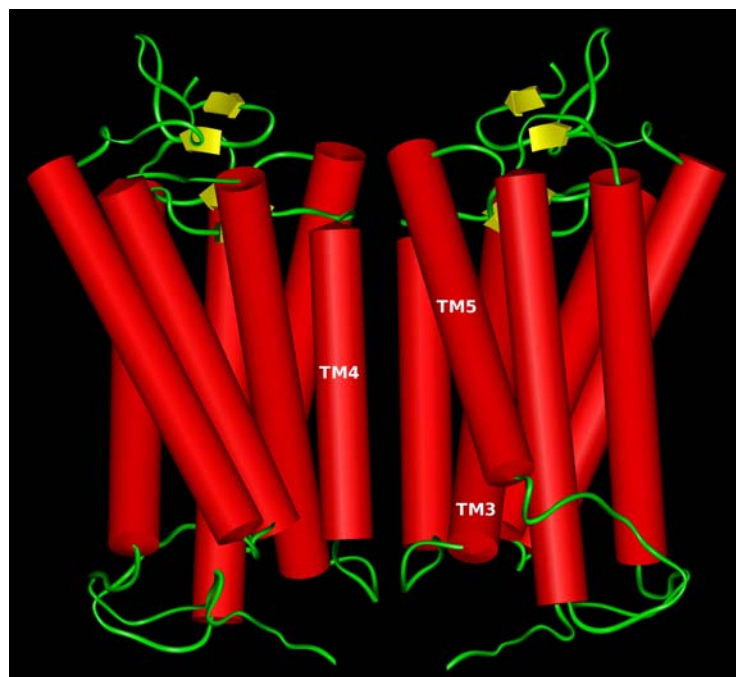


Figure 1.5 - Model structure of a rhodopsin dimer (PDB:1NM3) derived from the crystal structure of the rhodopsin monomer (PDB:1HZX) and the results from atomic force microscopy. Red cylinders account for α -helices, yellow arrows for β -strands and green lines for random coils. The labels indicate that the TM4 helix of each subunit interacts with TM3 and TM5 segments of the complementary one.

Additionally to the homodimers, it is generally accepted that GPCR can also form heterodimers and possibly more complex oligomeric structures. However, although heterodimerization seems to be essential for the function of some receptors, it is presently unproven that true heterodimers exist since the present biochemical and physical techniques lack the resolution to distinguish between distinct homodimers assembled. It is also unclear what the functional significance of oligomerization might be, although it is thought that the phenomenon may contribute to the pharmacological heterogeneity of GPCR in a manner not previously anticipated.

Considering the success of MD studies in obtaining information about structural and dynamical features of Rho monomers not accessible from experimental data (Saam 2002; Crozier 2003; Huber 2004; Pitman 2005; Schlegel 2005; Grossfield 2006), it is reasonable to expect that MD can be useful as well for the study of the conformational arrangement of the dimer and the adaptation between subunits. Accordingly, the first simulations of Rho dimers and oligomers embedded in membrane models are starting to be reported (Filipek 2004; Filizola 2006). Paper III reports the results of a MD simulation of a Rho dimer embedded in a DPPC lipid bilayer.

1.3.4 Bacteriorhodopsin

Bacteriorhodopsin (BR) is the only membrane protein of the purple membrane (PM) of the archeas (*Halobacterium salinarum*). Its function is to act as a light-driven proton pump through the generation of a proton gradient across the cell membrane, which is subsequently converted to chemical energy (Lanyi 2001; Hirai 2003). PM is isolated as 0.5 μm diameter sheets where 75% of the weight corresponds to BR and the remaining 25% to phospho- and sulpho- lipids (Dracheva 1996). They usually consist of two-dimensional crystalline patches

constituted by hexagonal lattices that can occupy up to nearly 50% of the archaeal cell surface area. The repeating elements of the hexagonal patches are three identical protein chains, each rotated by 120 degrees relative to the others (Krebs 2000). Analogously to Rho, BR exhibits a retinal chromophore covalently linked to K216 via a protonated Schiff base, which provides the characteristic color to the PM. When BR absorbs a photon, the protein undergoes a photochemical cycle by which retinal isomerizes from the *all-trans* to a *13-cis* configuration. This cascade of events induces protein conformational changes that result in the translocation of a proton from the intra- to the extra-cellular side, followed by a subsequent return of both, the retinal molecule and the protein, to their initial states.

Together with Rho, BR belongs to the seven-TM receptor family of proteins (Ovchinnikov Yu 1982), although the former is coupled to G-proteins whereas the latter is not. In the first use of electron crystallography to obtain an atomic-level protein structure, BR was resolved before the structure of any GPCR was known (Henderson and Schertler 1990; Henderson, Baldwin 1990), and therefore, it was subsequently used as a template to build homology models of GPCR (Oliveira 2004). However, although the tertiary structure of BR resembles that of vertebrate Rho, they exhibit specific and differenced structural features (Figure 1.4) originated from their diverse functions and the lack of homology between their amino acid sequences (Luecke 1999; Palczewski 2000). Many molecules have homology to BR, including the light-driven chloride pump halorhodopsin (for whom the crystal structure is also known), and some directly light-activated channels like channelrhodopsin.

1.3.4.1. Specific ion binding

It is known from a variety of experiments that the PM binds ions in a proportion of 4 moles of Ca^{2+} and 1 mole of Mg^{2+} per mole of BR (Kimura 1984; Chang 1985). Although some reports support the hypothesis that cation interaction occurs via

non-specific binding sites (Szundi 1987; Szundi 1988b; Szundi 1988a; Szundi 1989; Varo 1999), a vast majority of studies suggest the existence of specific sites, although its location is still uncertain at present. Specifically, ^{13}C nuclear magnetic resonance techniques showed the existence of a cation binding site located on the loop between helices F and G (Tuzi 1999). Moreover, a high-affinity site located near the retinal pocket has been described by several authors (Jonas 1991; Zhang 1992; Stuart 1995; Sepulcre 1996; Tan 1996; Zhang 1997; Pardo 1998; Sepulcre 2004). The purple form can be regenerated by adding a wide variety of mono-, di- or trivalent cations (Kimura 1984; Chang 1986; Ariki 1986; Dunach 1987). Furthermore, the removal of the endogenous natural lipids is associated with a decrease of the number of cations (Griffiths 1996), leading to a deionized form of the membrane that exhibits a shift in the absorption maximum and affecting the proton pumping activity (Kimura 1984; Chang 1985; Dunach 1987).

Due to its high relative mass and electronic properties, Mn^{2+} is a useful experimental probe to analyze the structural role of bound cations as well as their localization in BR, assuming a similar binding behavior to Ca^{2+} . In this direction, Mn^{2+} regenerated BR has been studied using electron spin resonance (Dunach 1987), Fourier transform infrared spectroscopy (Heyes 2002), magnetic susceptibility (Pardo 1998) and extended x-ray absorption fine structure (EXAFS) measurements (Sepulcre 1996). Furthermore, the existence of a Mn^{2+} -specific binding site on the extracellular part of the membrane has been recently established, with residues E194 and E204 directly involved in cation binding (Eliash 2001; Sanz 2001). Overall, it is known that the deionized membrane exhibits a high-affinity site, three sites of medium and one site of low affinity (Dunach 1987). Paper VIII describes a study aimed at identifying candidate binding sites combining computational chemistry methods and the EXAFS technique.

1.4 Lipid-protein interactions

The role of membranes has been neglected by biochemists until recently, when the growing experimental evidence stressing the importance of the membrane on protein function attracted the interest of the scientific community (White 1999; Lee 2003; Lee 2004; Vigh 2005). Most membrane proteins have one or more hydrophobic segments in an α -helical configuration that span the membrane (see section 1.2). Therefore, proteins can interact with the surrounding membrane lipids via a wide range of interactions including hydrophobic and electrostatic, hydrogen bond and dipolar interactions (with the lipid/water interfacial region). The strong influence of the membrane on protein function can be understood in the context of the present view of the membrane as an heterogeneous landscape with regions of biased composition with varying protein environment (Engelman 2005). Specifically, intrinsic membrane proteins must have co-evolved with the lipid component of the membrane to achieve optimal function, within the constraints imposed by the role of lipids in the general physiology of the cell and by the requirements of the biosynthetic machinery for translation and insertion of proteins into membranes. Despite the necessity to understand the protein-lipid interplay in detail, the rules describing the relationship between the lipid and protein components of the membrane are still being defined (Mouritsen 1984; Venturoli 2005). The study of model TM peptides (Mishra 1994; Weiss 2003; Killian 2003; Ganchev 2004; Goodyear 2005; Nymeyer 2005; Leontiadou 2006; Yeagle, Bennett 2006; Kandasamy 2006; Yandek 2007) and proteins (Harroun 1999b; Harroun 1999a) are of pivotal importance in this regard.

The hydrophobic matching between the protein and the membrane has been identified as one of the most critical aspects of this interaction (Dumas 1999; Weiss 2003; Jensen 2004). Hydrophobic mismatch is defined as the difference between the hydrophobic length of the TM segments of a protein and that within the two leaflets of the surrounding lipid bilayer. Since the cost of exposing hydrophobic groups to water is high, the hydrophobic width of the

protein TM helices needs to be similar to the hydrophobic thickness of the bilayer around the helices. This means that if the protein width is not equal to the bulk thickness of the lipid bilayer, the later will be distorted around the protein to give a thicker or thinner bilayer (Mouritsen 1984; Saiz 2004; Venturoli 2005; Bond 2006). However, it is known that the thickness of a lipid bilayer in the liquid crystalline phase fluctuates as a consequence of the molecular motion of the lipids including undulatory and peristaltic motions (Wiener 1992; Tieleman 1997; Lindahl 2000). Further, biological membranes contain a wide variety of lipid species with different fatty acyl chains (see section 1.1) so that lateral diffusion of lipid molecules within the plane of the membrane will result in fluctuating local thicknesses for the membrane (Mitra 2004; Venturoli 2005).

Regarding the specific electrostatic or hydrogen bond interactions between protein side chains and lipid head-groups, two main types of residues have been described to be important: amphipathic aromatic (Trp, Tyr and His) and basic residues (Arg and Lys) (Mishra 1994; Strandberg 2003). The use of MD simulations provided the atomistic detail necessary for the study of such interactions, revealing that residues belonging to the preceding groups have their hydrophobic regions interacting with the lipid acyl chains and their polar ones interacting with lipid head-groups (Tieleman 1998; Grossfield 2002; Deol 2004; Bond 2006). Paper II deals with the hydrophobic matching between different one-component lipid bilayers and rhodopsin as well as with specific hydrophobic and polar interactions.

Chapter 2 - Methods

Chapter 2 – Methodology

2.1 Computational Chemistry

The work reported in this thesis has been performed using computational chemistry methods, i.e.: a diverse set of techniques maturing in parallel with computer advances that apply theoretical methodologies to the study of a variety of problems. Computational chemistry studies can be performed mainly at two levels of approximation, using either quantum mechanics or molecular mechanics methods. The first constitute the most detailed approximation possible, although its use requires solving the Schrödinger equation, which is computationally prohibitive for large systems. On the contrary, being much simpler, molecular mechanics methods make the computation of large systems affordable, although still with a remarkable computational effort. Specifically, classical methods neglect the electronic motion and compute the energy only as a function of nuclear coordinates. Therefore, although it is not possible to study neither excited states, nor reactivity or complex electronic structures, it is useful for the study of many problems of biochemical/biophysical interest. In the case of the systems presented here, the number of explicit particles (atoms or heavy atoms) is typically between 60,000 and 120,000.

Since each paper presented with this thesis contains its own specific methods section, only some brief general ideas and references are provided in the present chapter. The following paragraphs concern a short description of MD simulations, the main technique used for this thesis. A more detailed description of this and other computational chemistry methods can be found in many text books, for example in (Leach 2001; Cramer 2002; Schlick 2002; Rapaport 2004).

2.2 MD simulations

Molecular dynamics (MD) has provided many insights concerning the internal motions of macromolecules since the first protein was studied over 25 years ago. A nice historical review has been recently published by one of the pioneers of the methodology (Karplus 2003). The power of MD lies in its capability to investigate biological motions that are often not accessible to experiments. Nowadays, the synergy between theory and experiments is necessary to progress in the understanding of different biological aspects. With the continuing advances in the methodology and the speed of computers, MD studies are progressively pushed to larger systems, greater conformational changes and longer scale times. The current situation points towards a promising role of MD in the years to come for the study of biochemical problems. There are many MD simulation packages available for the study of biomolecules. All the simulations presented here have been performed using the suite of program GROMACS (Berendsen 1995; Lindahl 2001), except the work reported in Paper VII, which was performed using the AMBER package (Case 2005).

2.2.1 MD principles

Using MD it is possible to simulate the time-evolution of a molecular system, which is represented classically considering a set of particles defined by their positions and momenta. The main principles are described in excellent texts on computational chemistry quoted in the preceding section, as well as in books specially devoted to MD (Haile 1992; Frenkel 1996).

Starting from a coordinate set -taken for example from a crystal structure- and assigning velocities to each atom -typically from a Boltzmann distribution at a given temperature-, successive coordinates and velocities are obtained by integrating the Newton's equation for the motion in each coordinate direction. In one dimension, the equation can be written as:

$$\frac{d^2 x_i}{dt^2} = \frac{F_{x_i}}{m_i}$$

where m_i and x_i are the mass and position of each atom, respectively and F_{x_i} is the derivative of the potential according to a force field equation that is described in the next section. The result is a trajectory that shows how atomic positions and velocities evolve with time according to the influence of the remaining atoms in the system. Due to the large number of particles interacting with each other, the integration is performed numerically most commonly using the leap-frog algorithm (Van Gunsteren 1990). The integration step is limited to the fastest motion in the system. Therefore, for atomistic simulations the step size is usually 1 fs, or 2 fs if restraining bond lengths, generally done using SHAKE (Van Gunsteren 1977) and LINCS (Hess 1997) algorithms.

2.2.2 Force fields

The calculation of the interaction energy within a classical description of a molecular system requires a force field. A force field is built up from two distinct components, a set of equations used to generate the potential energies (and their derivatives, the forces) and the parameters used in these equations. Nowadays, there are four main force fields in common use for simulating biological macromolecules: AMBER (Pearlman 1995), CHARMM (Brooks 1983; MacKerell 1998; Mackerell 2004), GROMOS (Van Gunsteren 1987) and OPLS (Jorgensen 1996).

The intramolecular potential energy is typically represented by harmonic oscillators for bond stretching and angle bending, a Fourier series for each torsional angle, and Coulomb and Lennard–Jones (LJ) accounting for the interactions between atoms separated by three or more bonds. The latter two terms -referred together as non-bonded terms- are evaluated between all atom pairs in the system to yield the intermolecular energy. Such force fields compute

the energy as a sum of terms representing bond elongation, angle and dihedral deformation, and non-bonded interactions with the following general form:

$$E = \sum_{bonds} V^{str} + \sum_{angles} V^{bend} + \sum_{torsions} V^{tors} + \sum_{LJ} V^{LJ} + \sum_{Coulomb} V^{Coul}$$

where the three first summations correspond the bonded terms (that include atoms connected up to three consecutive bonds) and the last two refer to the non-bonded ones. All summations can be easily calculated from the coordinates of the system at a given time. For each pair of bonded atoms (i and j), the stretching term is computed as:

$$V_{ij}^{str}(r_{ij}) = k_{ij}^r (r_{ij} - r_{ij}^o)^2$$

where k_{ij}^r is the stretching force constant and r_{ij} and r_{ij}^o are the distance between atoms and its equilibrium bond length, respectively. For every group of three bonded atoms (i, j and k), the angle term is described as:

$$V_{ijk}^{bend}(\theta_{ijk}) = k_{ijk}^\theta (\theta_{ijk} - \theta_{ijk}^o)^2$$

where k_{ijk}^θ is the bending force constant, θ_{ijk} and θ_{ijk}^o are the angle between atoms and its equilibrium value, respectively. For every group of four bonded atoms (i, j, k, l), the dihedral term is often represented as a cosine expansion:

$$V_{ijkl}^{tors}(\phi_{ijkl}) = k_{ijkl}^\phi [1 + \cos(n\phi_{ijkl} - \phi_{ijkl}^o)]$$

where k_{ijkl}^ϕ is a dihedral constant affecting the barrier height, n is number of minima in a 360° rotation, and ϕ_{ijkl} and ϕ_{ijkl}^o are the dihedral angle and the equilibrium value according the biochemical convention (*trans* $\phi=180^\circ$, *cis* $\phi=0^\circ$ and *gauche* $\phi=60^\circ/300^\circ$), respectively. The first non-bonded term is often represented by a 6-12 LJ potential, a simple mathematical model (Lennard-Jones 1931) that accounts for two distinct forces (an attractive and a repulsive) that neutral atoms and molecules are subject to:

$$V_{ij}^{LJ}(r_{ij}) = \left[\left(\frac{A_{ij}}{r_{ij}} \right)^{12} - \left(\frac{B_{ij}}{r_{ij}} \right)^6 \right]$$

where A_{ij} and B_{ij} are parameters that depend from on each pair of atoms. The first term accounts for the attractive forces at long range (van der Waals or dispersion) and the other for the repulsive forces at short range, resulting from the overlap between electron orbitals. Finally, the last term in the force field equation is a Coulombic potential describing the electrostatic interactions:

$$V_{ij}^{Coul}(r_{ij}) = \frac{q_i q_j}{4\pi\epsilon_o r_{ij}}$$

where q_i and q_j are the charges of atoms i and j , r_{ij} the relative distance between them and ϵ the vacuum permittivity.

The constants and parameters of the preceding equations need to be fed from biophysical experiments and/or quantum mechanics calculations which differ from one force field to another. The specific force fields parameters of the different components present in the systems studied –proteins, lipids, water molecules and ions are discussed in the following sections. Except in Paper VIII, where the AMBER force field have been used, the simulations presented with this thesis have been performed using a microscopic description that combines the *all-atom* OPLS force field (Jorgensen 1996) for the protein, water molecules and ions with the Berger force field for the lipids (Berger 1997).

2.2.2.1 Proteins

The parameters for the amino acids are well adjusted in the majority of force fields designed to compute biological macro-molecules. Therefore, once one has selected a force field (AMBER, CHARMM, GROMOS, OPLS...) to perform the simulation there are not many critical choices to be done except for non-standard residues, such as the retinal bound lysine in Rho and BR or the palmitoylated cysteines used in the present Rho studies.

2.2.2.2 Lipids

For the simulation of lipid bilayers there are two largely used force fields: one that is part of the official CHARMM distribution (MacKerell 1998) and the other introduced by (Berger 1997), developed with parameters taken from OPLS and GROMOS for its use in the GROMACS package (Allen 1987; Berendsen 1995; Lindahl 2001). There is no experimental information indicating that one force field is substantially better than the other. Although both force fields are microscopic, CHARMM includes explicitly all lipid atoms in the system, whereas the one developed by Berger, does not account explicitly for the non-polar hydrogen atoms and CH₂ and CH₃ groups are treated as a single particle. This approximation is often referred as a *united-atom* force field.

Another approach (not explored in this thesis) is the use of the so-called coarse-grained models to perform mesoscopic simulations by grouping a bunch of atoms together (Venturoli 2005; Bond 2006; Sperotto 2006; Shih 2006; Muller 2006; Marrink 2007). This allows to use a longer integration step –up to 40 fs– (Periole 2007). Although with a lesser detailed description, they allow longer simulation time scales as well as the possibility to deal with larger systems than with the atomistic approximation at a much less computational effort. In this regard, the recently developed MARTINI force field for mesoscopic simulations is very promising (Marrink 2005; Periole 2007). The lipid force field developed by Berger can be considered as a small coarse-grain model and accordingly, it permits using a time-step of 4 fs.

2.2.2.3 The water molecule

Many water models are available in the literature for an accurate representation of the liquid water, reviewed in references (Wallqvist 1999; Guillot 2002; Jorgensen 2005). The most common ones are often distributed together with the force fields described above. These models have been parametrized to

reproduce physical and thermodynamical properties such as the density, enthalpy of vaporization, radial distribution functions, energies of hydration or dipole moment. They can be classified by the number of points used to define the model (atoms plus dummy sites), whether the structure is rigid or flexible, and whether the model includes polarization effects or not. The simplest -and most popular- models for MD are TIP3P (Jorgensen 1983) and SPC (Berendsen 1987) series, which have three interaction sites, corresponding to the three atoms of the water molecule with rigid geometry. Each atom has a point charge assigned and the oxygen atom also gets Lennard-Jones parameters. The more complex 4-site or 5-site models such as TIP4P and TIP5P, respectively, place the negative charge on either a dummy atom placed near the oxygen along the bisector of the HOH angle or on two dummy atoms representing the lone pairs of the oxygen atom. These models improve the electrostatic distribution around the water molecule, though to a larger computational cost because of the larger number of electrostatic interactions to compute. Because TIP3P has been shown to provide a good compromise between quality and computational cost it has been chosen as the water model for all simulations that are part of this thesis.

If one needs to explore longer time scales, the use of coarse graining models cited the preceding section can be desired (Venturoli 2005; Izvekov 2005; Marrink 2007). It can also be interesting to treat solvent molecules at different levels of detail depending on their relative distance to the protein, that is, an adaptive MD simulation (Praprotnik, Matysiak 2007; Praprotnik, Delle Site 2007). However these methods are still not generally implemented in the common MD programs.

2.2.2.4 Ions

Ion parameters for MD simulations are typically obtained by adjusting the LJ parameters to reproduce ionic hydration free energy and the radial density

distributions. This strategy was first used for the determination of parameters for alkali (Åqvist 1990) and alkaline earth (Åqvist 1994) ions, but extended lately to other metals (Babu 2006). Such sets of parameters describe a free ion without explicit consideration of its coordination capabilities although they can accurately reproduce the geometries of the first coordination shell. However, it is known that uncertainties of microscopic parameters, reflecting an incomplete experimental knowledge of the structural properties of ionic aqueous solutions at finite molality, translate into large differences in the computed radial distribution functions (Patra and Karttunen 2004).

2.2.3 Long-range interactions

The computation of the pair-wise non-bonded interactions is the most time-consuming part of a MD simulation as the evaluation of the forces scales quadratically with the number of atoms in the system. Accordingly, several approximations have been used the last 20 years in order to reduce the computational effort needed (Loncharich 1989). One of the simplest approximations is to use of a cutoff that defines the maximum distance between pairs of atoms before computing their energy of interaction, under the assumption that the force between atoms can be neglected when they are largely separated. Typical cutoffs used are about 1-2 nm.

Since the LJ forces are short-range in nature, their contribution seems to be properly modeled with such cutoffs, although more accurate strategies have recently been reported (Lague 2004; Klauda 2007). However, dealing with the Coulombic term, the use of a cutoff is much more critical for the reliability of the simulations (Gilson 1995; Cheatham 1995). Accordingly, the treatment of long-range interactions has been an active field of research in the last years and is still a topic of considerable interest (Heinz 2005; Baumketner 2005). The most common alternative to truncation is to use the Ewald summation procedure (Allen

1987) or the computationally more effective Particle Mesh Ewald or PME (Darden 1993), where the long-ranged electrostatic interactions are calculated with fast Fourier transforms. These methods provide an exact solution for the electrostatic interactions for an infinite periodic system. The easiest way of simulating a periodic system is to treat it enclosed in a box and consider replicated boxes (to infinity) by rigid translation in all the three Cartesian directions, completely filling the space. This approximation is called periodic boundary conditions or PBC.

The treatment used for electrostatics is an important issue for systems with abundance of charged groups such as nucleic acids (Cheatham 1995; Louise-May 1996; Beck 2005), ions (Auffinger 1995) or lipids (Venable 2000; Tobias 2001; Pandit 2002; Patra 2003; Anézo 2003; Patra, Karttunen 2004), but also for neutral systems like liquid water (Feller 1996; Hess 2002). In regard to lipid bilayers, the studies addressed the effects of using a cutoff on the bilayer structure, showing that the area per lipid is very sensitive to force field parameters, as well as to the way electrostatics are treated. Furthermore, the use of a cutoff together with some criteria to group atoms into neutral charge groups, may increase lipid order, resulting in thicker bilayers with smaller areas per lipid (Wohlert 2004). However, the situation is less clear for systems consisting of peptides or proteins and requires further analysis (Loncharich 1989; Schreiber 1992b; Schreiber 1992a; Monticelli 2004; Beck 2005; Baumketner 2005; Monticelli 2006). In Paper I we compared the performance of a plain cutoff with the PME method in a system containing a lipid bilayer with an embedded membrane protein.

2.2.4 Statistical ensemble

In order to relate the microscopic features of individual atoms and molecules to the macroscopic or bulk thermodynamic properties of materials one needs to use statistical mechanics methods. In this context, an ensemble formalizes the notion

that, repeating an experiment again and again, a physicist may expect to observe a range of different outcomes under the same macroscopic conditions, but unable to control the microscopic details. Different macroscopic environmental constraints lead to different types of ensembles, with particular statistical characteristics. The most important ensembles used in MD simulations of biological systems are described below and impose several restrictions. The microcanonical ensemble (NVE) requires keeping the total energy of the system constant (i.e. a system thermally isolated). In contrast, in the canonical ensemble (NVT) a system shares its energy with a large heat reservoir or heat bath (Berendsen 1984; Nose 1984), allowing the system to exchange energy assuming that the heat capacity of the reservoir is so large as to maintain a fixed temperature for the coupled system. In both cases (NVE and NVT) the initials N and V account for a constant number of atoms and volume (i.e. a fixed box shape). The NPT ensemble is analogous to the NVT one, but imposes a barostat in the same spirit as the temperature coupling that maintains a fixed pressure instead of considering a constant volume (Parrinello 1981; Nose 1983; Berendsen 1984).

Other largely used ensembles in the context of lipid bilayer simulations are NP_zAT and $NP_z\gamma T$, which can be considered as a modification of the NVT ensemble where the pressure is only allowed to change in one direction (z), by imposing either a fixed area (A) or a constant surface tension (γ). There is little difference between simulations performed at fixed pressure in two (NP_zAT or $NP_z\gamma T$) or in all three (NPT) directions (Tieleman 1996). However, the choice of the surface tension in $NP_z\gamma T$ seems to have important effects on the area per lipid (Sankararamakrishnan 2004; Zhu 2005). In the case of the NVT ensemble, it has the disadvantage of requiring a previous accurate estimation of the area and volume per lipid to be able to choose the correct box dimensions. Indeed, this is tricky for pure lipid bilayers, but even more difficult for those with embedded

proteins. In Paper I we compared the performance of NPT and NVT in a system containing a lipid bilayer with an embedded membrane protein.

2.3 Simulations of membrane proteins

Despite the importance of obtaining structures from x-ray crystals, a major drawback of this technique is that it does not permit to study membrane proteins in their natural environment. Thus, the development of other techniques that can provide structural information under more native conditions is of great interest. An emerging group of such methods are computer simulations of membrane proteins (Ash 2004; Fanelli 2005), and more specifically the use of MD with the proteins embedded on different model lipid bilayers (Tieleman 1998; Tieleman 2006). These approaches can provide useful information about the structural features of a protein and about its dynamical behavior that are not available from other experimental methods. Analogously to the difficulties associated to the experiments with membranes and membrane proteins, the necessity to mimic the hydrophobic environment provided by the membrane has been a major obstacle for the simulation of such proteins. One of the most important issues is the relevance of including explicitly the lipidic environment in the systems. Until recently, MD simulations of membrane proteins were carried out either using implicit models (Roux 1994; Strahs 1997; Roux 2000; Im 2002; Im, Lee 2003; Im, Feig 2003) or hydrophobic solvents that mimicked the membrane environment instead (Åqvist 2000; Govaerts 2001; Rohrig 2002; Deupi 2004). These approximations have the advantage of being computationally cheaper than the simulations that include a more detailed description of the membrane. However, implicit models describe poorly the hydrophobic/hydrophilic boundary and cannot account for specific protein-lipid interactions (see section 1.4), which is a field of growing interest (Engelman 2005).

The increasing power of computers in the last years provided the opportunity to consider explicitly the lipid bilayer in the simulations. In this context, atomistic MD simulations of lipid bilayers represent a detailed microscopic picture of interactions and processes in biological membranes. However, the complexity of real membranes, containing many different proteins, lipids and other molecules, are still not presently affordable at this level of detail. For this reason, the study of model one-component pure hydrated lipid bilayers has been the focus of attention of a large amount of work published in the last years (van der Ploeg 1982; Tieleman 1996; Tieleman 1997; Berger 1997; Smondyrev 1999; Lindahl 2000; Feller 2000; Feller 2002; Saiz 2002; Anézo 2003). These studies, together with the effort in the characterization of lipid bilayers (Nagle 2000), have been pivotal in order to extend the simulations to more complex membranes such as phospholipid mixtures (Pandit 2003a; Gurtovenko 2004; Leekumjorn 2006) and/or the inclusion of other compounds such as cholesterol (Hofsäß 2003; Pitman 2004; Pitman 2005) or ions (Pandit 2002; Pandit 2003b; Böckmann 2003; Böckmann 2004; Mukhopadhyay 2004; Sachs 2004; Gurtovenko 2005). Furthermore, the study of model peptides (Tieleman, Sansom 1999; Tieleman, Berendsen 1999; Petrache 2000; Kandasamy 2006) provided the necessary background for the simulations of membrane proteins.

BR was the first integral membrane protein to be simulated embedded in a lipid bilayer (Edholm 1995). However it was not until much later that the technique was more widely used. An updated review on the state of the art regarding common simulation setups and conditions for MD of lipid membranes with embedded or attached proteins can be found in two recent works (Ash 2004; Sperotto 2006). The conclusion of these studies is that the explicit inclusion of lipids is crucial for describing protein dynamics and to provide realistic simulations ranging over several tens or hundreds of nanoseconds and even reaching the microsecond (Martinez-Mayorga 2006). From these and other reports it is clear that modeling GPCR or other membrane proteins in its lipidic environment

requires a careful selection of the system and computational protocol to avoid possible artifacts in the simulations. Accordingly, thorough analyses need to be carried out in order to assess the effect of the different approximations assumed in the simulations, as well as to understand their relevance to ensure that MD simulations are realistic. Regarding the system choice, the selection of the protein environment -including lipid composition and ion concentrations- the system size and several structural features of the protein -such as the protonation state-, can be crucial to obtain accurate results. On the other hand the choice of some simulation conditions and approximations seems to have also an effect on the quality of the results. With the aim of clarifying some of these points, Paper I shows a systematic study of some simulation choices and Papers II and IV regard aspects of the system composition.

2.3.1 Rhodopsin simulations

A large number of MD studies of Rho addressing diverse objectives have been published in the last years, providing the basis for the simulations presented here. The simulations reported in the literature were performed with the protein embedded in either saturated (Schlegel 2005), monounsaturated (Saam 2002; Grossfield 2002; Crozier 2003; Huber 2004; Lemaitre 2005) or polyunsaturated model bilayers (Feller 2003; Pitman 2004; Pitman 2005; Grossfield 2006). It is known that GPCR are embedded in membranes rich in polyunsaturated lipids containing chains of docosahexanoic acid, a fatty acid with 22 carbon atoms and 6 double bonds evenly distributed over the length of an acyl chain. More specifically, it represents 50% of the fatty acid content in the retinal rod outer segment disk membrane that hosts Rho. MD studies have shown that polyunsaturated lipids have unique features that are reflected in the properties of the lipid matrix which, in turn, can affect protein function at the molecular level (Feller 2003; Carrillo-Tripp 2005; Grossfield 2006). The results of these studies suggest the existence of specific sites on Rho surface accommodating

polyunsaturated lipids. Furthermore, the presence of tightly packed lipids has also been reported to weaken the inter-helical packing (Feller 2003; Pitman 2005; Grossfield 2006).

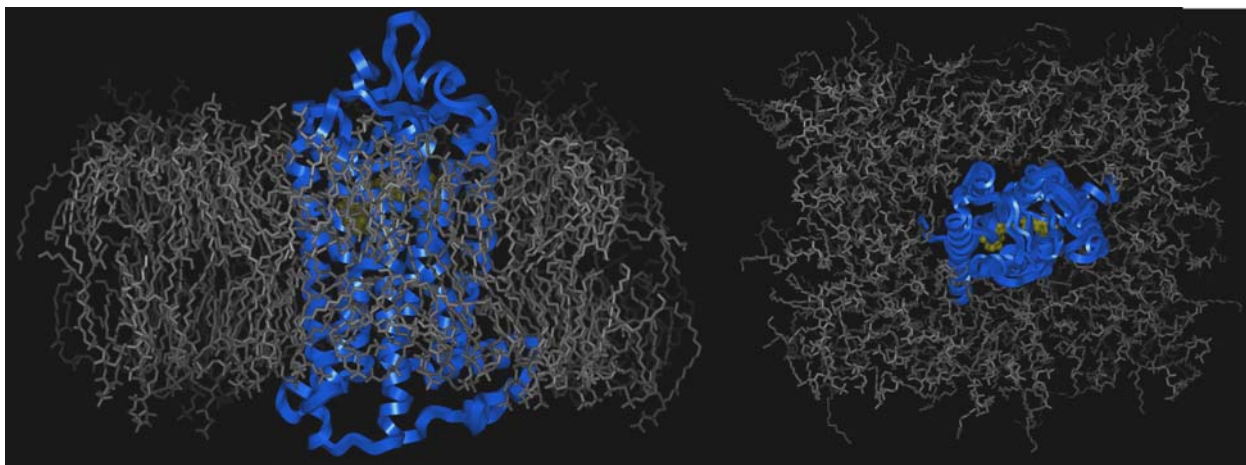


Figure 2.1 – Rhodopsin embedded in a DPPC lipid bilayer from a MD trajectory; side view (left) top view (right). The protein ribbon is shown in blue, lipids in grey and retinal in gold.

The effect of different lipid types on the structure and function of the protein is not yet clear. Moreover, as stated in the preceding section, the complexity of real membranes, containing many different proteins, lipids and other molecules, are still not presently affordable at atomistic level of detail because of the lack of knowledge regarding the specific effects and interactions of the different species present. Additionally, the use of more complex membranes, including phospholipid mixtures or cholesterol require much longer simulations because they need to diffuse to their preferred locations. Accordingly, the majority of the simulations are still performed using bi-, mono-unsaturated or saturated one-component lipid bilayers because they are better characterized biophysically and therefore the force field parameters are more accurate than for the polyunsaturated. A cartoon of a system consisting in a rhodopsin protein embedded in a DPPC bilayer is shown in Figure 2.1.

Part II - Results

Chapter 3 – Scientific papers

Chapter 3 - Scientific papers

Overview

The objective of the present thesis has been the study of seven-transmembrane receptors by means of MD simulations, with the ultimately goal of developing a robust methodology that can be generalized to the study of most GPCR as well as other membrane proteins embedded in a realistic environment. With this purpose in mind, most of the effort regarding the work presented is based in the study of bovine Rho –as the prototype of GPCR– embedded in one-component lipid bilayers. The systems studied are explained in detail in the specific methods section in each article. Half of the work presented is basically methodologically oriented while the other half makes use of the techniques studied in order to address specific biochemical questions. Table I displays a summary of the components presents in such systems.

There are many key issues when performing MD simulations of membrane proteins that need to be properly understood in order to get reliable results. Some of them are related to methodological concerns such as different choices for treatments of long-range interactions (section 2.2.3) and for the choice of the statistical ensemble (section 2.2.4). This is the focus of the work reported in **Paper I**. Some other are oriented to the system choice and more specifically, to the use of a proper solvent for the membrane protein. In this context, the use of an explicit membrane mimic is a critical point since otherwise one has to add restrictions to the protein accounting for the lack of hydrophobic contacts which would destabilize the protein structure (see **Paper VIII**). The effect of the specific lipid interactions to the protein structure is not yet fully understood. This motivated the study of Rho embedded in different model one-component lipid bilayers, presented in **Paper II**. Since in physiological conditions membranes are in contact with a solvent that contains ions, another issue of similar nature, is the effect of

the inclusion of several mono- bi- and tri-valent ions in the water/lipid-polar phase. This is reported in **Paper IV**, which outlines the specific behavior of potassium ions in agreement with some experiments.

paper	I	II	III	IV	V	VI	VII	VIII
protein	<i>Rho</i>	<i>Rho</i>	<i>Rho</i> (<i>dimer</i>)	-	<i>Rho</i>	<i>Rho</i>	<i>Rho</i>	<i>BR</i>
lipids	<i>DPPC</i>	<i>DPPC</i> <i>POPC</i> <i>DMPC</i> <i>PLPC</i>	<i>DPPC</i>	<i>DPPC</i>	<i>DPPC</i>	<i>DPPC</i>	<i>DPPC</i>	-
ions	Na^+ Cl^-	Na^+ Cl^-	Na^+ Cl^-	M^+ Cl^-	Na^+ Cl^-	Na^+ Cl^-	Na^+ Cl^-	Mn^{2+} Ca^{2+}

Table I – Components present in the systems reported in the papers included in this thesis. Those components shown in *italics* are a main part of the discussion in a specific report. M^+ accounts for Li^+ , Na^+ , K^+ , Ca^{2+} , Mg^{2+} , Sr^{2+} , Ba^{2+} and Ac^{3+} , respectively.

Regarding the work oriented to specific biochemical problems, we addressed the study of structural features related to the stability and activation mechanisms of Rho, as a model of GPCR, and BR. Additionally to the previously described methodological issues, **Paper II** reported a study of the hydrophobic matching and the specific lipid-protein interactions. Another topic of great interest nowadays is the possible existence of Rho in oligomeric states. In **Paper III** we reported a study of a Rho dimer based on a recently published semi-empirical model. The critical role of a group of amino acids at the cytoplasmic side of TM helices 3 and 6 regarding conformational properties and activation of GPCR (section 1.3.2) has been the focus of **Papers V and VI**. In the case of Rho, another important issue regarding the activation process is how the isomerization of the retinal chromophore occurs (section 1.3.2.1). Furthermore, with the use of a modified retinal, **Paper VII** provided some insight into this regard. Finally, the stabilizations of many membrane proteins (including Rho and BR) by cations are

a topic of some discussion. In **Paper VIII** we reported a study of the cation binding sites in BR (section 1.3.4).

Effect of different treatments of long-range interactions and sampling conditions in molecular dynamic simulations of rhodopsin embedded in a dipalmitoyl phosphatidylcholine bilayer

Cordomí A, Edholm O, Perez JJ

J Comput Chem., 2007 Apr 30;28(6):1017-30

Effect of Different Treatments of Long-Range Interactions and Sampling Conditions in Molecular Dynamic Simulations of Rhodopsin Embedded in a Dipalmitoyl Phosphatidylcholine Bilayer

ARNAU CORDOMÍ,¹ OLLE EDHOLM,² JUAN J. PEREZ¹

¹Dept d'Enginyeria Química, Technical University of Catalonia (UPC), Av. Diagonal 647, 08028 Barcelona, Spain

²Theoretical Biological Physics, Royal Institute of Technology (KTH), SE-10691 Stockholm, Sweden

Received 12 July 2006; Accepted 9 October 2006

DOI 10.1002/jcc.20579

Published online 31 January 2007 in Wiley InterScience (www.interscience.wiley.com).

Abstract: The present study analyzes the effect of the simulation conditions on the results of molecular dynamics simulations of G-protein coupled receptors (GPCRs) performed with an explicit lipid bilayer. Accordingly, the present work reports the analysis of different simulations of bovine rhodopsin embedded in a dipalmitoyl phosphatidylcholine (DPPC) lipid bilayer using two different sampling conditions and two different approaches for the treatment of long-range electrostatic interactions. Specifically, sampling was carried out either by using the statistical ensembles NVT or NPT (constant number of atoms, a pressure of 1 atm in all directions and fixed temperature), and the electrostatic interactions were treated either by using a twin-cutoff, or the particle mesh Ewald summation method (PME). The results of the present study suggest that the use of the NPT ensemble in combination with the PME method provide more realistic simulations. The use of NPT during the equilibration avoids the need of an *a priori* estimation of the box dimensions, giving the correct area per lipid. However, once the system is equilibrated, the simulations are irrespective of the sampling conditions used. The use of an electrostatic cutoff induces artifacts on both lipid thickness and the ion distribution, but has no direct effect on the protein and water molecules.

© 2007 Wiley Periodicals, Inc. J Comput Chem 28: 1017–1030, 2007

Key words: molecular dynamics; lipid bilayer; simulation setup; membrane protein; rhodopsin; electrostatics; ensembles

Introduction

G-Protein coupled receptors (GPCRs) are the largest family of membrane proteins and mediate a major part of transduction signals responding to a diverse range of molecules, including ions, peptides, lipids, biogenic amines, and even photons. These proteins play a key role in cell signal transmission and in the regulation of basic physiological processes, being proteins of enormous pharmacological interest.¹ Their natural abundance, together with their key physiological role, make them suitable targets for therapeutic intervention, accounting for more than 50% of the currently marketed drugs.²

Despite their important biological function, scarce structural information necessary to get a better understanding of the structure–function relationships of GPCRs, is currently available. The present lack of information is basically due to the difficulties associated with the crystallization of membrane proteins. Thus,

although it is well established that GPCRs are arranged in seven helix bundles, differential features, both sequential and structural among the several existing subfamilies have been described.³ Bovine rhodopsin is the only GPCR whose 3D structure is currently available at atomic resolution.^{4–8} This makes this protein to be a suitable template for modeling studies of other GPCRs. Rhodopsin is involved in the visual signal transduction cascade in vertebrates. It contains the chromophore molecule 11-*cis* retinal covalently linked to Lys296 via a Schiff base. Photon uptake induces the isomerization of the 11-*cis* retinal to the all-*trans* configuration, starting a cascade of protein conformational changes that leads to vision. Accordingly, in addition to its

Correspondence to: A. Cordoní; e-mail: arnau.cordomi@upc.edu

Contract/grant sponsor: The Spanish Ministry of Science and Technology; contract/grant number: SAF2005-08148-C04-01

intrinsic enormous interest, rhodopsin is a useful model to study different structural features of this family of proteins and to provide insights on how its dynamic behavior is related to its biological function. Molecular dynamics (MD) is a suitable methodology to carry out this kind of studies, since it provides detailed information about the structural features of the system as well as about its dynamical behavior.⁹ However, for the simulations to be meaningful, the models and protocols used in the actual calculations need to be continuously tested and contrasted to guarantee the production of reliable simulations.

In the case of membrane proteins, an important issue to be assessed is the relevance of including explicitly the lipidic environment in the simulations. Early MD simulations of membrane proteins were carried out either using implicit models^{10–14} or hydrophobic solvents that mimicked the membrane environment instead.^{15–17} These approximations have the advantage of reducing the computational cost considerably compared to simulations that include more detailed descriptions of the membrane. However, implicit models cannot account for specific protein–lipid interactions and furthermore, they describe poorly the hydrophobic/hydrophilic boundary. The increasing power of computers in the last years has provided the opportunity to consider the lipid bilayer explicitly in the simulations. Specifically, in the case of rhodopsin, different studies using a wide range of lipid bilayers and addressing diverse objectives have been published in the last years.^{18–26} The results of these studies suggest that the explicit inclusion of lipids is crucial to describing protein dynamics and to provide realistic simulations ranging over several tens or even hundreds of nanoseconds.

Modeling GPCRs in its lipidic environment requires a careful selection of a computational protocol to avoid possible artifacts in the simulations. Accordingly, thorough analyses need to be carried out to assess the effect of the different approximations assumed in the simulations, as well as to understand their relevance to ensure that MD simulations are realistic. A recent study has focused on the influence of several structural features like the protonation state of some residues or the use of different membrane-mimicking environments on the structure of bovine rhodopsin.²⁵ The present study focuses on the effects of different simulation setups. Specifically, the goal of the present work is to compare the performance of different approximations for handling the electrostatic interactions and the use of different sampling conditions. Similar studies have already been performed for pure hydrated lipid bilayers.²⁷

The treatment of long range interactions has been an active field of research during the last 20 years,²⁸ and it is still a topic of considerable interest (see refs. 29 and 30 and references therein). It is well established that the approximations used to treat the electrostatic interactions are critical to obtain reliable simulations.^{31,32} Indeed, this is not only important for systems with abundance of charged groups such as nucleic acids,^{32–34} ions,³⁵ or lipids,^{36–41} but also for systems like water.^{42,43} In regard to lipid bilayers, several studies have addressed the effects of truncation on the bilayer structure.^{36–41} These studies show that the area per lipid is very sensitive to force field parameters, as well as to the way electrostatics are treated. Indeed, it has been shown that the use of a cutoff together with some criteria to group atoms into neutral charge groups may increase lipid order,

resulting in thicker bilayers with smaller areas per lipid.⁴⁴ However, the situation is less clear for systems consisting of peptides or proteins and requires further analysis.^{28,30,34,45–48}

In regard to the ensemble used in the simulations, for pure hydrated lipid bilayers it has been shown that there is little difference between simulations performed at fixed pressure (NPT; constant number of atoms, a pressure of 1 atm in all directions, and fixed temperature) or in one (NP_zAT) coordinate direction, at constant surface tension (NP_zγT), or at fixed periodic box dimensions (NVT; constant number of atoms, volume, fixed box shape, and temperature).²⁷ However, the choice of nonzero surface tension has important effects on the area per lipid.^{49,50} The NVT ensemble requires, however, that one knows the area and volume per lipid accurately to be able to choose the correct box dimensions. Indeed, this is even more difficult for lipid bilayers with embedded membrane proteins.

In the present study, simulations were performed either with the canonical/NVT or the NPT ensemble. The long-range electrostatic interactions were computed either using a cutoff or the particle mesh Ewald summation method (PME).⁵¹ For this purpose, simulations were performed on a system consisting of one molecule of bovine rhodopsin soaked in a box containing a dipalmitoyl phosphatidylcholine (DPPC) lipid bilayer, water molecules, and ions under different simulation conditions. Five different simulations were carried out combining two statistical ensembles and two different approximations for the treatment of long-range electrostatics.

Methods

The Rhodopsin Structure

Rhodopsin atomic coordinates were retrieved from the Protein Data Bank⁵² (entry 1GZM).⁷ In contrast to other previously published crystal structures,^{4–6} this structure contains the coordinates of all the amino acids of the intradiscal and cytosolic loops. In addition, coordinates of the atoms of some missing C-terminal residues were taken from a different source⁶ and adapted by superposition of the α -carbon skeleton of both protein structures. The starting model of the protein also incorporated two palmitoyl chains located on the cytoplasmic end, which are covalently linked to two consecutive cysteine residues, believed to be important as membrane anchoring points to the membrane. All the amino acids were modeled in the protonation state they exhibit as free amino acids in water at pH 7, with the exception of Asp83 and Glu122 that were considered as protonated and neutral respectively, according to experimental evidence.⁵³ This is reasonable, since both residues are located in the protein hydrophobic core and there are no possible counter charges in their neighborhood. Similarly, His196 was considered charged based on pK_a calculations using the DaPDS program.⁵⁴ Taking into account these considerations and with the C-terminus of the protein negatively charged, the protein exhibits a total of 19 positive and 21 negative charges yielding a net charge of -2 . This is compensated in the box by adjusting the balance between sodium and chloride ions to give an electro-neutral system, as described in detail later.

Protein Embedding

The simulation box consisted of a mixture of DPPC lipids and water molecules generated and equilibrated according to the procedure described previously.⁵⁵ The box had an initial size of $10.3 \times 8.0 \times 10.2 \text{ nm}^3$ (XYZ), organized in such a way that the bilayer plane was oriented on the XY plane. Before protein insertion, the box contained 256 lipids (corresponding to an area per lipid of 0.64 nm^2) and circa 17,000 water molecules. The protein was placed in the center of the box, and the overlapping molecules were removed. Specifically, all water molecules with oxygen atoms closer than 0.40 nm to a nonhydrogen atom of the protein, as well as all lipid molecules with at least one atom closer than 0.25 nm to a nonhydrogen atom of the protein were removed. This resulted in a final system containing 197 lipids and circa 16,000 water molecules. Removal of these atoms introduced small voids between the protein and water or lipid molecules that disappeared during the first part of the MD simulation, in which a progressive adjustment of the lipid bilayer and water molecules to the protein takes place. Next, 114 randomly selected water molecules were replaced by 58 sodium and 56 chloride ions, providing a neutral system with a concentration approximately 0.2 M on sodium chloride. This concentration is fairly similar to that found in biological organisms, although they exhibit different intra- and extra-cellular ion concentrations. In addition to the water added, consistent with the water molecules present in the crystal structures of rhodopsin (entries 1GMZ and 1LH9),^{6,7} 23 crystallographic water molecules were included in the starting structure.

Molecular Dynamic Simulations

All computer simulations were performed using a parallel version of the GROMACS 3.2 package.^{56,57} The system was subjected to periodic boundary conditions in the three coordinate directions. The temperature was kept constant at 323 K (well above the gel/liquid crystalline phase transition temperature of 314 K) using separate thermostats for the protein, water, ions, and lipid molecules.⁵⁸ The time constant for the thermostats was set to 0.1 ps except for water, for which a smaller value of 0.01 ps was used. The pressure in the three coordinate directions was kept at 0.1 MPa by independent Berendsen barostats⁵⁸ using a time constant of 1.0 ps. Although other methods have the advantage of giving an ensemble with correct fluctuations,^{59,60} the simpler methods for pressure and temperature control were used here to guarantee faster convergence. The equations of motion were integrated using the leapfrog algorithm with a time step of 2 fs. All bonds within the protein and lipid molecules were kept frozen using the LINCS algorithm.⁶¹ The bonds and the angle of water molecules were fixed using the analytical SETTLE method. Lennard-Jones interactions were computed using a cutoff of 1.0 nm. The electrostatic interactions were treated either using a cutoff or the PME technique.⁵¹ In the former case, electrostatic forces were computed every time step for atom pairs up to a distance of 1 nm, and every time step, and every 10 time steps for atoms pairs in the interval 1–1.8 nm, with a simultaneous update of the list of close neighbors.

The all-atom OPLS force field,⁶² currently implemented in GROMACS, was used for all molecules of the system except for the DPPC molecules, which were modeled using the force field parameters described in ref. 63. Nonbonded pair interactions were computed as combinations of single atomic parameters to account for protein–lipid interactions. These parameters reproduce the experimental area per lipid of pure DPPC in the liquid crystalline phase.^{44,63,64} Water molecules were modeled using the TIP3P model.⁶⁵ Fractional charges of retinal atoms were taken from quantum chemical calculations⁶⁶ and have already been used in other MD simulations of rhodopsin.¹⁸ Fractional atomic charges for palmitoylated cysteines were derived from electrostatic potential calculations at HF/6-31G* level.

Simulation Procedure

Once the protein was inserted in the bilayer, the system was energy minimized. Subsequently, the system was subjected to a 0.5 ns MD simulation at a temperature of 323 K to allow for the removal of voids present between the protein and the lipids or water. These simulations were performed allowing the three periodic box dimensions to change size until a pressure of 0.1 MPa was reached in each coordinate direction. The atomic coordinates of the protein were restrained to their crystallographic positions. Two different simulation boxes were generated after this process using two different treatments of the long range electrostatic interactions: box no. 1 generated using the PME method and box no. 2, generated using a cutoff. Starting from either simulation box no. 1 or 2, five different 16-ns-MD simulations under different conditions were performed and analyzed (Table 1). Two simulations were performed at constant pressure and temperature, with the electrostatics treated using either the PME method (simulation no. 1) or a cutoff (simulation no. 2). The first 6 ns of these simulations were considered as equilibration period and were not included in the analysis. The starting boxes for these two simulations were those generated during the molecular reorganization process using the corresponding treatment for the electrostatic interactions (i.e., box no. 1 and 2, respectively). The remaining simulations (simulation nos. 3–5) were performed at fixed box dimensions. Specifically, in simulation no. 3 the electrostatic interactions were treated using the PME method, whereas in simulation nos. 4 and 5 a cutoff was used. Starting boxes for simulations nos. 3 and 4 were taken from simulation nos. 1 and 2, respectively after 0.5 ns run (box no. 1+ and box no. 2+). Simulation no. 5 was performed using a cutoff, starting from a box no. 1+. Furthermore, to compare the physical properties of the lipids, we additionally performed four simulations of pure hydrated DPPC bilayers as reference. These simulations were performed without ions using the PME method (simulation no. 6) or a cutoff (simulation no. 7) for the electrostatics and with a 0.2 M concentration in sodium chloride using either PME (simulation no. 8) or a cutoff (simulation no. 9). The systems consisted of 256 lipid molecules with a hydration of 67 waters per lipid and were run for 10 ns at similar conditions to those performed with the protein embedded. For all simulations, coordinates were collected every 10 ps and stored for further analysis.

Table 1. Summary of the Simulations Performed in the Present Work.

Simulation	Production run			Bilayer rearrangement around the protein						P–P thickness (nm)	Hydr. thickness (nm)	Area/lipid (nm ²)
	Ensemble	Electrostatics	Time (ns)	Box	Ensemble	Electrostatics	Time (ns)	Rhod.	NaCl			
1	NPT	PME	16	1	NPT	PME	0.5	+	+	4.07 ± 0.03	2.97 ± 0.03	0.59 ^c
2	NPT	cutoff	16	2	NPT	cutoff	0.5	+	+	4.31 ± 0.04	3.22 ± 0.04	0.54 ^c
3	NVT	PME	16	1+	NPT	PME	1 ^a	+	+	3.75 ± 0.02 ^b	2.66 ± 0.02	0.66 ^c
4	NVT	cutoff	16	2+	NPT	cutoff	1 ^a	+	+	3.90 ± 0.02 ^b	2.84 ± 0.02	0.62 ^c
5	NVT	cutoff	16	1+	NPT	PME	1 ^a	+	+	3.68 ± 0.02 ^b	2.62 ± 0.02	0.67 ^c
6	NPT	PME	10					–	–	3.93 ± 0.03	2.82 ± 0.03	0.625 ± 0.011
7	NPT	cutoff	10					–	–	4.17 ± 0.02	3.04 ± 0.02	0.576 ± 0.003
8	NPT	PME	10					–	+	4.06 ± 0.02	2.96 ± 0.02	0.590 ± 0.003
9	NPT	cutoff	10					–	+	4.45 ± 0.04	3.35 ± 0.04	0.513 ± 0.017

Rhod specifies when the system contains rhodopsin. NaCl refers to the presence or not of ions. P–P thickness refers to the phosphate–phosphate bilayer thickness and hydrophobic refers to the tail–tail bilayer thickness.

^aThe last 0.5 ns of equilibration correspond to the first 0.5 ns of simulation nos. 1 or 2.

^bThickness restrained due to the use of fixed size box.

^cEstimated values by linear regression of simulation nos. 6–9.

Results and Discussion

Table 1 summarizes details of the different simulations reported in the present work, including the ensemble used to sample the system (NPT or NVT), as well as the treatment of long-range electrostatic interactions (PME or cutoff). The average bilayer thickness and the computed area per lipid, key parameters in membrane biology,⁶⁷ are also included in the table. The analysis of the results is focused on the structural aspects of the protein and on its interactions with the lipid bilayer, aimed at providing new insights into the problem of the hydrophobic matching between the lipids and the protein. For the sake of clarity, the results are discussed successively for each of the components of the system, i.e. protein, lipid molecules, ions, and water molecules. This includes an analysis of the deviation from the starting protein structure as well as its fluctuations around the equilibrated average coordinates, the stability of the helices, the lipid bilayer thickness, ion distribution, and the behavior of water molecules inside and around the protein.

The Bilayer Thickness

Lipid order is often described either by the average area per lipid or by the bilayer thickness. The computation of the former in simulations of bilayers with embedded proteins requires the calculation of the cross-sectional area of the protein, which changes along the bilayer normal, since the protein does not have a fixed regular shape and therefore is rather difficult to compute. In contrast, the computation of the bilayer thickness is straightforward in these systems, and since the volume per lipid is essentially fixed, the average thickness of a pure bilayer can easily be calculated. A fully hydrated DPPC bilayer in the liquid crystalline phase has an area per lipid of 0.64 ± 0.02 nm² and a volume per lipid of 1.232 nm³, the latter being a measure that can be obtained more accurately.⁶⁸ However, since the water/lipid boundary is not sharp, the bilayer thickness can be defined

and measured in different ways.⁶⁸ In the present work, we chose to measure it as the distance between the average planes of the two monolayers, defined either by the positions of the phosphorus atoms or by the carbons adjacent to the ester carbonyls. These thicknesses will be denoted as phosphate-to-phosphate (P–P) and hydrophobic, respectively. In the liquid crystalline phase for DPPC with an area of 0.64 nm² per lipid, the P–P thickness is 3.9 nm, whereas in the ordered gel phase with the area of 0.48 nm² the P–P thickness is 5.1 nm. The average P–P and hydrophobic thickness obtained in the different simulations reported in the present work is listed in Table 1. In all the simulations, the difference between the P–P and the hydrophobic thickness is roughly 1 nm, in good agreement with the experimentally determined values (see D_B and D_C in ref. 68). The area per lipid can be computed from the relation: $A = 1.75/T$, where A is the area per lipid in nm² and T is the hydrophobic thickness in nm, based on the linear correlation obtained from the analysis of simulation nos. 6–9. It is important to note that the intrinsic definition of the hydrophobic thickness allows a direct comparison with the hydrophobic width of the protein and therefore is a useful measure for studying the hydrophobic matching.

To be used as a reference, to analyze the effects of protein embedding, simulations of pure hydrated DPPC lipid bilayers without ions (simulation nos. 6–7) and with a 0.2 M concentration in sodium chloride (nos. 8–9) were also performed. Bilayer thicknesses obtained in these simulations are summarized in Table 1. It can be seen that bilayer thickness as well as the area per lipid obtained in the NPT simulations differ from those obtained in pure hydrated bilayers without salt. For pure bilayers, this represents a decrease of the area per lipid from 0.625 to 0.590 nm² using the PME method, and from 0.576 to 0.513 nm² using a cutoff. With the same sampling conditions, in the simulations of rhodopsin, the average hydrophobic bilayer thickness obtained using the PME method (simulation no. 1) and a cutoff (simulation no. 2) are 2.97 and 3.22 nm, corresponding to areas per lipid of 0.59 and 0.54 nm², respectively. These

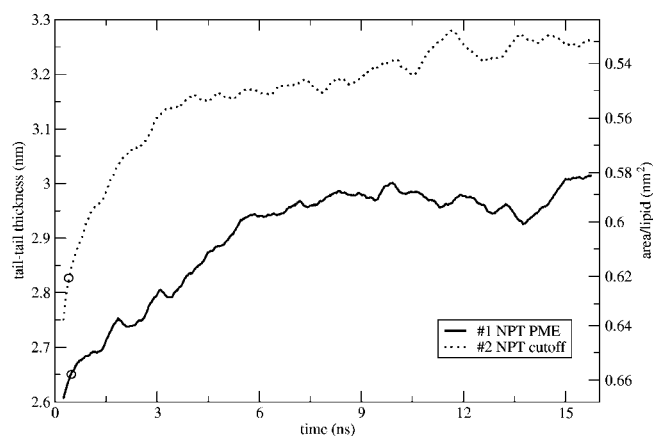


Figure 1. Time-evolution of the hydrophobic bilayer thickness for the simulations performed in the NPT ensemble, depending on the electrostatics used. The lines displayed are running averages over 0.5 ns. The area per lipid is shown for a better comparison with biophysical studies of pure lipid bilayers (see text). The circles in the plots indicate the starting points for simulations nos. 3–5 (see methods).

results agree well with previous simulations of pure DPPC bilayers with sodium chloride^{69,70} and exhibit the same behavior found for pure DPPC bilayers, regarding the effect of different treatments of long-range electrostatics.^{39,44} Accordingly, the bilayer thickness is sensitive to the treatment electrostatic interactions, with a trend to exhibit larger values when a cutoff is used, both in pure lipid bilayers as well as in bilayers with a protein embedded.

The time-evolution of the average bilayer thickness provides interesting information about the events governing the interactions between the different components of the system. Figure 1 shows pictorially the time-evolution of the hydrophobic bilayer thickness along the NPT-simulations (nos. 1 and 2). In both cases, the bilayer thickness reaches a steady value after about 6 ns, reason why only the last 10 ns of the MD trajectories were used in the analysis. In these simulations, the lipid bilayer expands compared to the pre-equilibrated pure bilayer in response to both ion concentration^{69,70} as well as to the perturbation caused by the protein.^{21,71,72} Different biophysical studies suggest that the presence of electrolytes may alter the structure and dynamics of the dipolar phosphatidylcholine (PC) head groups.^{73–79} Moreover, recent MD simulations suggest that sodium ions bind tightly to the lipid head groups inducing changes in the head-group tilt, which increase the thickness of zwitterionic lipid bilayers when the area of the simulation box is not fixed.^{69,70,80,81} This observation is compatible with recent studies regarding the effect of sodium chloride on the mechanical properties of lipid bilayer films.⁸² In contrast, recent experiments for bilayers with potassium chloride and bromide indicate a negligible effect on the area and thickness for ion concentrations of the order of 1 M.⁸³

Regarding the electrostatics, present results demonstrate that a cutoff always increases the bilayer thickness compared to simulations using the PME method, in agreement with earlier results.^{36,39–41,44} Whereas for pure hydrated lipid bilayers, the effect was 8% regarding the hydrophobic thickness (simulation

nos. 6–7), for bilayers with 0.2 M sodium chloride (simulation nos. 8–9) the effect raised to 13% due to the reinforcing effects of electrolytes. The effect was again 8% for bilayers with protein and ions (simulation nos. 1–2). In contrast, in the simulations carried out using the NVT ensemble (simulation nos. 3–5), the thickness and the area per lipid are constrained as a consequence of the fixed box size. Therefore, the simulations using the NVT ensemble can be considered to have been performed under an applied stress, resulting in an artificial negative surface tension, since the bilayer tends to expand adjusting to 0.1 MPa pressure in all directions.

Since lipids are more flexible than proteins,⁶⁷ the hydrophobic matching tends to be more important in the lipids adapting to the protein surface than *vice versa*.^{84–86} This has been analyzed in the present simulations in terms of the bilayer thickness as a function of the distance from the protein (Fig. 2). Since the thickness at long distances from the protein is comparable to that of a pure bilayer, the alteration observed in the average value in the proximity of the protein can be understood as a local ordering of the lipids, induced by the hydrophobic surface matching and/or by the fairly flat protein surface. The results displayed in Figure 2 indicate that the bilayer thickness is clearly modulated by the protein in its vicinity. The surface gain due to the hydrophobic matching between the protein and the lipids can lead to important variations in the thickness close to the protein, ranging between 7%–20% when compared to the values measured far from the protein. However, due the fact that the increase of the surface involves a cost due to the necessary bilayer deformation, there must be a limit on these differences, and therefore the average thickness restricts its value close to the protein. Thus, the results obtained in the simulations using the NPT ensemble, which do not impose any restraint on bilayer thickness, should be those which provide the most realistic results. However, this is not true for the simulation performed using a cutoff (simulation no. 2), where lipids do not adapt to the hydrophobic width of the protein. This indicates that the arti-

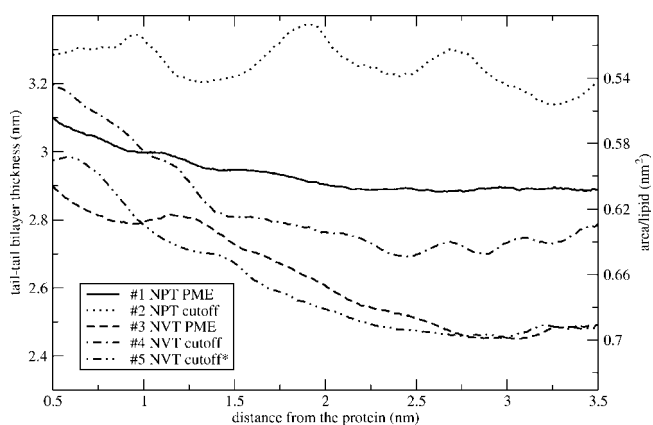


Figure 2. Variation of the hydrophobic bilayer thickness from the protein surface. Values are running averages over 0.2 nm. The area per lipid is shown for a better comparison with biophysical studies of pure lipid bilayers (see text). *The preceding process involving the bilayer rearrangement around the protein was performed using the PME method (Table 1 for simulation details).

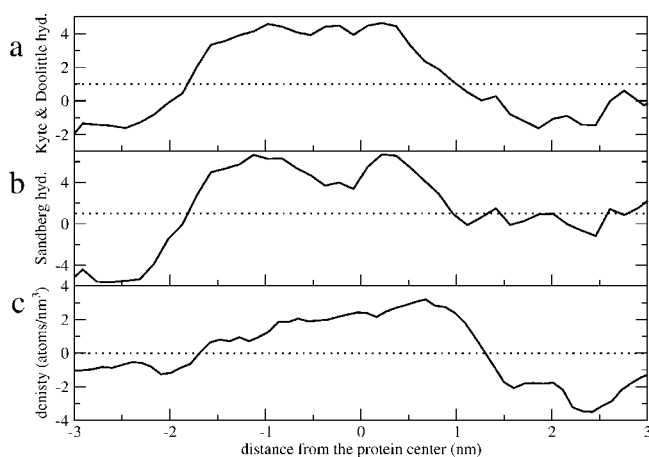


Figure 3. Measures of the hydrophobicity of the protein profile along the direction normal to the bilayer computed using different scales. (a) Kyte and Doolittle coefficients;⁷⁷ (b) free amino acid energies of solvation extracted from a dipolar approximation;⁴⁴ (c) difference of number densities computed for hydrophobic and non-hydrophobic residues. The dotted lines represent the average value in each scale for the whole protein. The negative and positive portions on the X axis represent the intradiscal and cytoplasmatic sides of the membrane, respectively.

ficial increase on the average bilayer thickness due to the use of a cutoff extends to the lipid distribution according to the distance from the protein.

The values of hydrophobic thickness close to the protein range between 2.9 and 3.3 nm. These values are similar to the hydrophobic width of the protein for which an independent estimate can be obtained considering different approximations. For its computation, the crystallographic protein structure was divided into slices along the Z axis, normal to the bilayer plane. For each slice, a sum of the different hydrophobicity contributions was calculated and normalized by the number of residues per slice. For the sake of comparison, three different procedures were used: two different hydrophobic scales, the Kyte and Doolittle scale⁸⁷ and a scale based on fundamental physics⁸⁸ that reproduces free energies of solvation of the amino acids; and a procedure based on the difference between number densities of hydrophobic and nonhydrophobic residues. For comparison purposes, the numbers of the hydrophobicity scales were rescaled, so that the average value for the protein was 1. The numbers obtained are shown in Figure 3. Inspection of the figure indicates that it is ambiguous to extract a value for the hydrophobic width of the protein, since the transition between hydrophobic and hydrophilic regions is continuous. However, they permit the determination of a lower limit for the protein hydrophobic width that is in reasonable agreement with the hydrophobic bilayer thickness of lipids in the vicinity of the protein. The three different approximations used yield 2.80, 2.76, and 2.88 nm, respectively. These values are slightly smaller than the hydrophobic width of the bilayer, suggesting that the fairly flat protein surface has a direct ordering influence on the neighboring lipids.

The use of the PME method stabilizes the liquid crystalline phase and makes the bilayer thickness less sensitive to the perturbing

influence of salt and protein. When the process of molecular reorganization after protein insertion is performed using the PME method for the electrostatics, the lipid distribution exhibits a similar profile in all the simulations, even when using a cutoff in the production run, suggesting that truncation is not suitable for this process. This is in agreement with recent results of lateral mobility of lipids with different handling of electrostatics.⁴¹ Accordingly, the bilayer thickness obtained in simulation no. 1 of about 3.1 nm should be taken as reference. In this case, the average bilayer thickness is similar to that of the corresponding system without protein (simulation no. 8), and only a minor reorganization of lipids is necessary after protein insertion, involving a change of the hydrophobic thickness of about 8%. For the simulations performed using the PME method and the NVT ensemble (simulation no. 3), the thickness in the proximity of the protein is 2.9 nm, slightly smaller than that computed using the NPT ensemble (simulation no. 1), due to the fact that in simulation no. 3 the area per lipid was larger. Similarly, in the simulations performed using a cutoff (simulation nos. 2, 4–5), values of the thickness in the proximity of the protein exhibit variations due to the different average thickness of each system. However, when starting the NVT simulations with a large enough area per lipid (simulation no. 5), the thickness close to the protein exhibits a value of 3.0, just between the values obtained in the two simulations using the PME method (simulation nos. 1 and 3).

In summary, present results show that 0.2 M sodium chloride increases the bilayer thickness by 8%–13%. In regard to the effect caused by the protein, experimental evidence suggests that membrane proteins have an important effect on the bilayer thickness.⁸⁵ Present simulations demonstrate that they only induce local effects on the bilayer thickness. The increase induced ranges between 8%–20%, depending on the difference between the average bilayer thickness and the protein width. On the other hand, comparison of simulation nos. 1 and 8 demonstrate that at long distances from the protein the average bilayer thickness is essentially similar to the value of the pure systems. Accordingly, the effect on the average area per lipid depends on the concentration of proteins. Present results correspond to a model, where the fraction of membrane area occupied by the protein is around a 20%. Real systems may exhibit different concentrations, e.g., in the outer segment of rod cells about 50% of the membrane area is occupied by proteins, mostly rhodopsin. Finally, present simulations show that the lipid bilayer exhibits an area per lipid in between the crystalline and the gel phases in the neighborhood of the protein, due to both the effect of the protein and the presence of the ions.

Protein Structure

Structure evolution along the MD process was analyzed by computing its root mean square deviation (rmsd) from the crystal structure, both as a whole and per residue. In addition, the fluctuations of the secondary structural elements of the protein, as well as the deviations of each transmembrane segment from the ideal helical structure were studied along the trajectory. It should be borne in mind however that, since the different components of the system are not fully independent, it is difficult to identify

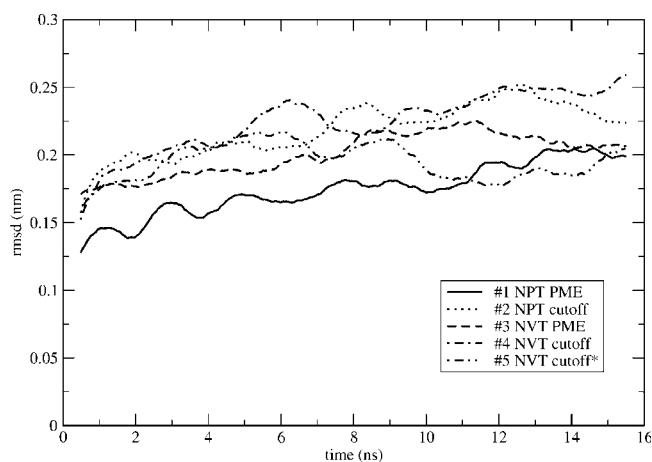


Figure 4. Average rms deviation of the protein $C\alpha$ atom positions for the different setups studied averaged over 1 ns. The C-terminal segments have been omitted. *The preceding process involving the bilayer rearrangement around the protein was performed using the PME method (Table 1 for simulation details).

direct effects of the simulation conditions on the protein structure from indirect effects induced by the rest of the components of the system and in particular by the lipid bilayer. Specifically, artifacts on lipid thickness observed in the simulations due to the use of a cutoff to treat long-range electrostatic interactions may have effects on both the structure and the dynamics of the protein.

The overall deviation of the protein structure from the initial crystal structure was analyzed by computing the rmsd of the alpha carbons ($C\alpha$) and it is depicted pictorially in Figure 4. In the computation of the rmsd, the C-terminal segment beyond the palmitoylated cysteines was excluded since it is involved in large fluctuations that may require longer simulation times for a proper statistical sampling. Anyway, the short helix at the C-terminus is located on the bilayer surface making this segment more sensitive to the bilayer thickness than to possible effects caused by the simulation setup. Inspection of Figure 4 shows that the rmsd observed in simulation nos. 1, 3, and 5 achieve an asymptotic value around 0.2 nm, whereas simulations nos. 2 and 4 exhibit larger deviations, achieving asymptotic values around 0.25 nm. In any case, these deviations are small and typical in MD simulations of proteins of the size of rhodopsin. Deviations from the initial structure may arise from inaccuracies of the force fields and also to the different environment felt by the protein. However, differences may also be attributable to the characteristics of the initial structure (simulation box) used in the different simulations, since the differences are mainly observed in the loops and in the C-terminus and are mostly been generated during the short period of molecular reorganization after protein insertion.

Comparisons reported in the literature of MD simulations of soluble proteins or peptide^{28,30,34,45–48} performed either using the PME method or a cutoff showed, in general, smaller rms deviations of the protein/peptide when the PME method is used. However, in regard to membrane proteins, a recent 4 ns MD simulation of alamethicin channel forming peptides embedded in

a lipid bilayer showed smaller rmsd in the protein using a cutoff than using the PME method.⁸⁹ The time-evolution of the protein rmsd, displayed in Figure 4 shows that though the rmsd exhibits a slower increase when using the PME method, the values reached after 16 ns are close to those observed in the simulations using a cutoff. This results together with those of previous studies mentioned before suggest that the bilayer may act as a boundary, dumping the truncation effects observed on soluble proteins.

At the residue level, the most important deviations from the crystal structure are found in the most mobile parts of the protein, i.e. loops, terminal regions, and helix ends. In contrast, the trans-membrane segments remain stable in all the simulations. Figure 5a shows the rmsd per residue for all the simulations reported in the present work. Three major peaks, located in the cytoplasmic loops C2, C3, and on the C-terminus can be clearly distinguished. Interestingly, in simulation no. 2 the thicker bilayer seems to be responsible of the higher rmsd values beyond residue 320 on the C-terminus. Additional minor peaks can also be observed corresponding to the remaining loops C1, E1, E2, and E3 and to the N-terminus. The flexibility of the different parts of the protein can be characterized by the root mean square fluctuations of the $C\alpha$ atoms (rmsf) around the average structures computed over the last 10 ns. In all the simulations, the resulting plots are similar irrespective of the treatment of the long range electrostatics, and exhibit maxima in the same regions where residues exhibit higher rmsd values (Fig. 5b). These results are similar to those found in the earlier studies of bacteriorhodopsin,⁹⁰ showing that the mobility of the protein was asymmetric with respect to the mid-plane of the membrane, and this was reflected on the lipid fluctuations. Thus, the largest fluctuations are found in the cytoplasmic segments of the protein, specifically in loops C2 and C3, as well as in the C-terminus as also found in recent MD studies of rhodopsin.²⁰ These common structural features may be related to conformational changes associated with protein activation, which should favor interactions with other proteins in the cytoplasmic side of the protein. The fact that the magnitude of the rmsf profiles is not the same for the different simulations cannot be attributed to the setup used. This may be due to local interactions between segments of the protein (e.g., the cytoplasmic loops C2, C3, and the C-terminus) and also between the protein and the lipid environment, which difficult the sampling. This later will be strongly dependent on the average bilayer thickness as well as the thickness distribution profile. There are, however no significant differences in the rmsf between the constant volume and constant pressure simulations. The rmsf values are in good qualitative agreement with crystallographic B-factors from the available structures which have been plotted in Figure 5c for all known crystal structures^{4–8} for the $C\alpha$ atoms. The experimental crystallographic B-factors are related to the root mean square fluctuations as:

$$B = \frac{8\pi^2}{3} (\text{rmsf})^2$$

This expression allows a direct comparison between the experiments and the simulations showing that, despite the good agreement in terms of the location of the maxima, the B-factors cal-

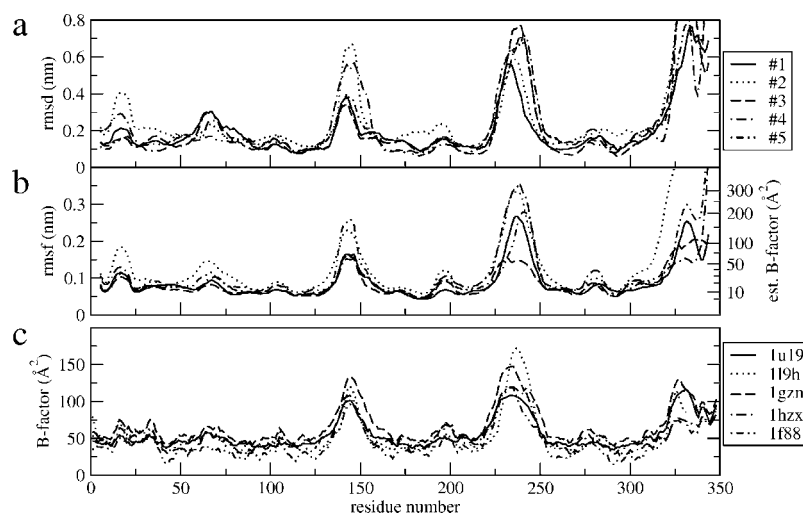


Figure 5. (a) Running averages over 10 residues of protein-carbons root mean square deviations for the different simulations (rmsd); (b) same as (a) for the fluctuations (rmsf). The estimated crystallographic B-factors are also shown for the sake of comparison. (c) Experimental B-factors of all available crystal structures.

culated for the membrane-spanning helices are in general lower than that experimentally determined. Regarding the peaks located on the C2 and C3 loops and on the C-terminus, they exhibit larger or smaller values than the crystallographic ones depending on the simulation. These differences may come from packing effects,²¹ due to the lipid environment or by a deficient sampling in the extra-membrane regions, as stated in a recent study regarding the conformational sampling of membrane proteins performed using a similar time-scale.⁹¹

Important differences in the C α positions in the C3 loop and in the cytoplasmic ends of helices 5 and 6 can be observed when superposing the available crystal structures. These differences are reflected on the B-factors of the C3 loop that are smaller for structures 1F88, 1HZ1, 1L9H, and 1U19 than for the structure 1GZM. In regard to the C2 loop, differences can be rationalized in terms of the packing effects that may hinder the motion of the loop. Similarly to what is observed in the crystal structure 1GZM, in almost all the cases, the simulations yield higher B-factors for the C3 loop than for the C2. A noteworthy difference between the simulations and the crystal structures is the much larger mobility of the C-terminal region observed in the former. This may be due to an artificial order in the crystalline environment. The rmsd and rmsf plots along the protein sequence show great similarity. In fact, there is a nice linear correlation between the rmsd and the rmsf (data not shown). The correlation is stronger for points with low rmsd and rmsf (below 0.20 and 0.30 nm, respectively) resulting in ratios rmsf/rmsd between 0.3 and 0.6.

The protein C α trace rmsd values are small in all the setups, being the largest deviations and fluctuations observed outside the transmembrane segments, which exhibit small structural changes during the simulation. The abundance of localized net charges on specific regions of the sequence has been shown to be responsible of the major artifacts due to the use of a cutoff.³⁵ Charged residues in rhodopsin (as in other GPCRs) are mostly located in terminal segments and loops (Table 2). These regions

are intrinsically the most mobile parts and also more sensitive to the membrane thickness because of their location close to the membrane surface. This makes difficult to discriminate the possible effects of using a cutoff from other effects, such as sampling or the bilayer thickness. In any case, the results indicate that the concentration of net charge in rhodopsin is small enough so that the known artifacts for the use of a cutoff cannot be detected. Moreover, it can well be that the lipid bilayer plays a role in stabilizing the protein structure.

As it has been shown above, the rmsd of the C α atoms of transmembrane segments are significantly smaller than those corresponding to the loops and terminal segments. The helix bundle of bovine rhodopsin is widely used as a template to model other GPCRs, to be used further for ligand docking studies. It is therefore crucial to show that present simulation techniques can keep the helices stable in a long simulation. Otherwise, it could not be expected to reproduce the structural features of the protein with enough accuracy to be used for that purpose. Therefore, an analysis of helix stability was undertaken using the last 10 ns of each trajectory. This was performed in three ways: (1) A search for deviations from ideal helicity; (2) An identification of secondary motifs using the implementation of the Dictionary of Protein Secondary Structure (DSSP)⁹² in GRO-MACS; (3) The analysis of the hydrogen bonding between backbone atoms within the transmembrane segments.

The deviation from an ideal helix has been computed through the average helical radius (data not shown), which can be understood as a two-dimensional rmsd. The majority of the transmembrane helices exhibit values close to that of an ideal α -helix, about 0.23 nm. No significant differences between the different simulations are observed. Helices 6, 7, and 2, in decreasing order of importance, are the only ones that exhibit significant deviations from this value. A sequence examination pointed out that the abundance of charged residues at the cytoplasmic end of helix 6 and the existence of helix disrupting amino acids in

Table 2. Residues Involved in the Different Domains of the Bovine Rhodopsin Structure (Taken From ref. 7).

Segment		Sequence	no. res	Net charge	+q	-q	
C-term	1	MNGTEGPNFYVPFSNKTGVVRSPEAPQYYLAE	33	33	-1	2	3
H1	34	PWQFSMLAAYMFLILMLGFPINFLTLVTVQ	64	31	0	0	0
C1	65	HKKLRT	70	6	+3	3	0
H2	71	PLNYILLNLAVADLFMVFGGFTTTLTSLH	100	30	0	0	0
E1	101	GYFVF	105	5	0	0	0
H3	106	GPTGCNLEGGFATLGGIEALWLSLVLAIERVVVVC	140	35	-1	1	2
C2	141	KPMSNFRFG	149	9	+2	2	0
H4	150	ENHAIMGVAFWVMALACAAPPLV	173	24	-1	0	1
E2	174	GWSRYIEPGMQCSCGIDYYPHEETN	199	26	-2	2	4
H5	200	NEFVVIYMFVVHFIPLIVIFFCYGQLVFTV	230	31	-1	0	1
C3	231	KEAAAQQQES	240	10	-1	1	2
H6	241	ATTQKAEKEVTRMVHIMVIAFLICWLPYAGVAFYIF	276	36	+1	3	2
E3	277	THQGSDFGP	285	9	-1	0	1
H7	286	IFMTIPAFFAKTSAVYNPVIYIMM	309	24	+1	1	0
C4	310	N	310	1	0	0	0
sH8	311	KQFRNCMVTTL	321	11	+2	2	0
N-term	322	CCGKNPLGDDEASTTVSKTETSQVAPA	348	28	-3	2	5

For the sake of comparison, residues involved in α -helix, according to the Dictionary of Protein Secondary Structure (DSSP),⁸⁰ are shown in bold. Charged residues in the simulations have been underlined. The number of residues and the total, negative, and positive charge per segment are shown in the last four columns.

helices 2 and 7 are responsible for these deviations. In the analysis of the secondary structure using the program DSSP, no significant changes in the number of structuring residues forming α -, 3^{10} -, and π -helices, turns, and coils were observed compared to the crystal structure. This shows that the helices are properly preserved through the simulations irrespective of the setup used. There might, however, be alterations in the helices that are too subtle to be observed at this level but still may have significant importance. Therefore, the intrahelical backbone hydrogen bonding has been analyzed along the trajectories (Table 3). For every residue i the existence of possible intrahelical backbone hydrogen bonds with residues at positions $i + 3$, $i + 4$, and $i + 5$ has been considered. Accordingly, the predominant hydrogen bond type (if existent) has been assigned to each resi-

due. Note that multiple consecutive turns with $(i, i + 3)$; $(i, i + 4)$; and $(i, i + 5)$ interactions give 3^{10} -, α -, and π -helices, respectively. Helix limits have been defined as in the crystal structure⁷ and the total number of hydrogen bonds has been computed as the sum of $(i, i+n)$ contributions for $n = 3-5$. This shows a slight decrease in the number of turns irrespective of the setup used in the simulations compared to the starting⁷ as well as other crystallographic structures.^{6,8} This may be the effect of an optimization of protein-lipid interactions. A significant decrease took place at the helix ends before the production run started, pointing clearly towards the new lipidic environment as responsible for the alteration of this structural feature. Our results suggest that the number of $(i, i+n)$ interactions between backbone residues in the helices of the crystal structures may be

Table 3. Number of Intra-Helical Backbone Hydrogen Bonds Between Residues i and $i + n$ in the Crystal Structures, and Calculated Along the Trajectories.

	1GZM ⁷	1U19 ⁸	1L9H ⁶	NPT, PME (1)	NPT, cutoff (2)	NVT, PME (3)	NVT, cutoff (4)	NVT, cutoff ^a (5)
TM								
$i, i + n$	201	197	190	188	187	184	171	182
$i, i + 4$	167	152	146	137	131	132	127	133
$i, i + 3$	29	41	41	48	54	49	41	46
$i, i + 5$	5	4	3	3	2	3	3	3
Non-TM								
$i, i + n$	14	16	19	15	13	21	13	15
$i, i + 4$	0	0	6	3	2	5	3	5
$i, i + 3$	14	16	13	12	11	15	10	10
$i, i + 5$	0	0	0	0	0	1	0	0

Hydrogen bonds are displayed for both the transmembrane segments (top) and for the non-TM regions. Definitions of the transmembrane segments have been taken from crystal structure 1GZM.⁷

^aThe preceding process involving the bilayer rearrangement around the protein was performed using the PME method (see Table 1 for simulation details).

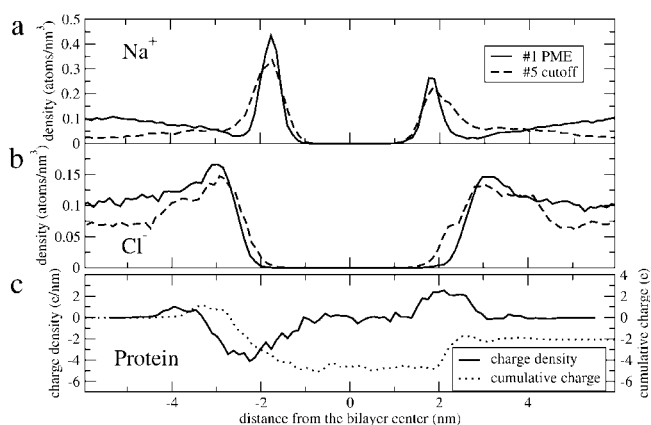


Figure 6. (a) Density distributions of simulation nos. 1 and 5 for the sodium ion along a direction perpendicular to the membrane plane. (b) same as (a) for chloride ions. The density profiles of the remaining simulations exhibit similar results to those performed with equal treatment of electrostatics (Table 1). The densities on simulation no. 5 have been rescaled according to the box size of simulation no. 1 but maintaining the area for easy comparison. The asymmetry of the ion distributions can be understood in terms of the protein charge distribution and the corresponding cumulative charge (shown in Fig. 6c).

overestimated due to crystallographic contacts and the lack of dynamic effects. Dynamic effects on the secondary structure involve local formation and rupture of hydrogen bonds between backbone atoms in the helices (mainly at the ends), which cannot be seen in a crystal structure. Thus, for a better comparison one should average every residue to its predominant ($i, i + n$) interaction through the simulation. This leads to an increase of about 1%–2% in the total number of hydrogen bonds and indicates that dynamics is important for the secondary structure. Additionally, another part of the observed decrease seems to be due to a shortening in the helix length, particularly in the cytoplasmic ends of helices 5 and 6 when comparing the simulations with 1GZM.⁷ However, these helix exhibit various lengths when comparing the different crystal structures of rhodopsin.^{6–8}

An interesting observation is that the fractions of different backbone ($i, i + n$) hydrogen bonds differ between simulations and crystal structures (Table 3). Thus, in all simulations a considerable conversion of ($i, i + 4$) interactions to ($i, i + 3$) can be observed, while the amount of ($i, i + 5$) remains always residual and unaltered. The total amount of ($i, i + 3$) interactions is about 10% higher in the simulations than in the starting crystal structure.⁷ This suggests that though the α -helix structure is preserved, there is a trend to form ($i, i + 3$) turns, characteristic of a 3^{10} -helices. If the analysis is carried out considering the predominant average type of backbone atom interactions, the average amount of residues forming ($i, i + 3$) interactions decreases about 4%. This shows that there is a dynamic equilibrium between ($i, i + 4$) and ($i, i + 3$) interactions within the helices. An explanation for this observation can be found in equilibrium studies between α - and 3^{10} -helices, which show that the α -helix is energetically stabilized while 3^{10} -helices are entropically favored. Thus, less polar environments may be associated

with a marginally increased stability of the 3^{10} helix.^{93,94} The larger hydrophobicity of the lipid bilayer compared to the crystallographic environment may be responsible for these alterations. However, one should not discard possible effects of the temperature used or force field parameters (see methods). Regarding this issue, recent studies suggest that current force-field parameters have problems to reproduce the relative stability of different helix types.^{95–97} Interestingly, ($i, i + 3$) interactions seem to provide an intermediate state between the ideal α -helices, formed only by ($i, i + 4$) interactions, and the unfolded state. This mechanism appears both at the helix ends and in the center of the transmembrane segments, near helix disrupting residues.

The possible effects of the sampling conditions and the handling of electrostatics on the rigid-body elements in the protein have also been examined. Specifically, the time-evolution of protein and helix tilts relative to the bilayer normal and the most significant helix kinks has been examined (data not shown). The results show similar tilt and kink angles in all the simulations suggesting that, neither the handling of electrostatics nor the ensemble used have influence on these movements, at least with the time-scale of the current simulations. Only values from simulation no. 4 exhibit subtle deviations from those of the remaining simulations that can be due to an unrealistic lipid environment created by the use of a cutoff during the process of bilayer rearrangement around the protein, which can only be restored by changing to NPT on the production run (simulation no. 2). Specifically, a recent study showed that a truncation at 1.8 nm as used here gives lateral diffusion rates for lipids significantly smaller than those obtained with PME.⁴¹ Accordingly, this suggests that the truncation is not the method of choice for the process of bilayer rearrangement around the protein, in perfect agreement with our results.

Present results do not provide clear evidence that the different ways to treat long-range electrostatic interactions affect the protein structure. If existent, the effects should be of the same order of magnitude as other details like the thickness of lipids around the protein or particular loop conformations derived from specific protein–lipid interactions in every simulation.

The Ion Distributions

It is important to take into account that ions in MD simulations of biological systems are not only used to balance the total charge of a system, but also have significant influence on the properties of several system components such as lipids or proteins due to the screening effects, as recently discussed in different reports.^{83,98,99} It has been shown in the preceding sections that ions have effects on the average bilayer thickness. Moreover, a study of the effect of truncating long-range electrostatics in an aqueous solution containing 1 M NaCl showed an artifact in the radial distribution function of both ions at the cutoff distance.³⁵

The ion distribution along a direction perpendicular to the bilayer normal has been analyzed for all the systems containing rhodopsin reported in the present work. The results clearly show that the distribution of ions is different depending on the treatment of long range electrostatics. In contrast, simulations using different statistical ensembles provide roughly the same results. Representative distributions for simulations performed with PME (no. 1) and with an electrostatic cutoff (no. 5) are shown in Fig-

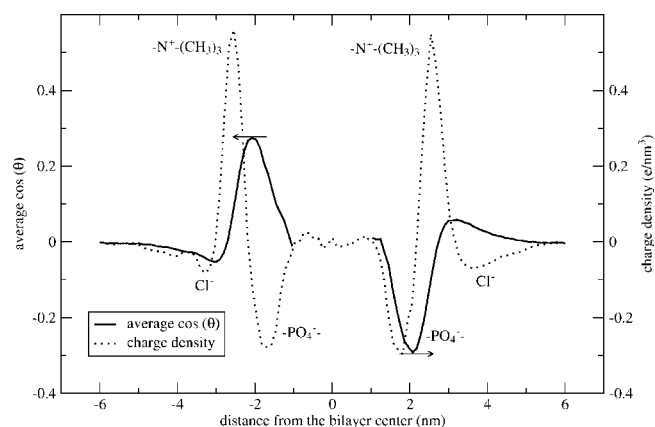


Figure 7. Polarization of water molecules in simulation no. 1, as displayed by the average dipole orientation (continuous line). Similar results are obtained for the remaining simulations independently of the setup used. The dashed line shows the charge density of all the molecules of the system except water (ions, lipids, and protein). Arrows represent the water dipole induced by lipid head-groups.

ure 6a with the coordinates of the second simulation rescaled to compensate for the obvious difference in membrane thickness. Similar profiles have also been reported in previous studies of pure lipid bilayers,^{69,70} apart from the asymmetry in the distributions found in present work, which is clearly due to the protein. The present ion distributions exhibit higher positive ion densities on the intradiscal than on the cytoplasmic side, whereas negative ion densities are similar on both sides. The asymmetry in the sodium distribution can be rationalized from the charge density in rhodopsin (Fig. 6b). According to the protonation state listed in Table 2, rhodopsin has 38 charged residues exposed to solvent and accessible to the ions: 13 on the cytoplasmic and 25 in the intradiscal side. The protein has a net charge of +3 on the cytoplasmic side and -5 in the intradiscal side, which produces a strong electrostatic field that is compensated by the asymmetric sodium ion distribution. The reason that the differences are located more in the sodium than in the chloride distributions is because sodium ions are found closer to the protein than the latter and, therefore, play a more active role in balancing the protein charge distribution. The difference in area under the two sodium peaks at the intradiscal and the cytoplasmic sides gives a net charge of 2–7 charges depending on the simulation (data not shown). This result is reasonable considering the net charge difference between the cytoplasmic and the intradiscal halves. The position of the peaks differs slightly from simulation to simulation, consistent with the different average thickness found in the simulations (data not shown). The protein charge distribution tends to compensate the net dipole generated by the lipid bilayer and therefore modulates the ion distribution. This might be related to the lower average thickness observed in the simulations performed with a cutoff (no. 2) than without protein (no. 9).

Present simulations show differences in the ionic distribution along the normal axis of the bilayer depending upon the treatment of long range electrostatic interactions. In the PME simulations, both sodium and chloride ions reach a constant concentration at long distances from the membrane, giving a neutral sys-

tem out there. On the contrary, in the simulations using a cutoff, the sodium ion concentration decreases with the distance from the membrane while the chloride ions reach a constant concentration. This results in a non-neutral system far off from the membrane. This is clearly an artifact due to the use of a cutoff which overestimates the electrostatic interactions between sodium ions and the bilayer. Concerning chloride distributions, all the simulations exhibit a similar asymptotic value in contrast to what has been observed on the distributions of sodium ions. However, the density decreases more slowly when moving in the direction opposite to the bilayer center when using the PME method (simulation nos. 1 and 3), than when using a cutoff (simulation nos. 2, 4, and 5). Overall, on the one hand, the use of a cutoff itself has effects on the density distribution of ions due to an overestimation of the interaction between the ions and the bilayer. Additionally, there are indirect effects produced by the bilayer thickness that are enhanced when a cutoff is used.

The Water Molecules

The interfacial water of a liquid crystalline DPPC bilayer has recently been studied.¹⁰⁰ In this and other studies of pure full hydrated lipid bilayers, it has been shown that there is an ordering effect on water molecules caused by the interaction with the lipid head-group dipoles.^{39,101} The ordering of water can be measured by the average cosine of the angle between the water dipole and the bilayer normal. A maximum value of 1 is achieved when the dipole is aligned with the Z-axis. On the contrary, at long distances, the water dipoles are randomly oriented and this parameter is approximately zero. The variation in the cosine angle in regard to the distance to the center of the bilayer is shown in Figure 7. As can be seen, the highest polarization is roughly 30% of the maximum value and occurs in a small region close to the lipid head groups (about 2 nm of the bilayer center), in agreement with the results reported for pure hydrated DPPC bilayers containing ions.³⁹ In addition, the distributions also exhibit a shoulder at 3 nm, the highest value of the chloride ion distribution. The difference between simulations in the position of the maximum water polarization is in agreement with the different average bilayer thickness (data not shown). The polarization of water molecules can be easily rationalized from the charge distribution of the remaining components in the system, i.e.: ions, lipids and the protein (see the dashed line on Fig. 7).

The role of protein internal water molecules has been analyzed for the different simulations. The starting model had 23 crystallographic waters, as described in the methods section. However, some of them were solvent exposed and exchanged with other solvent molecules during the simulation. We chose to define an internal water molecule as the one that stays closer than 1 nm to a protein atom during more than 75% of the simulation time. Then, an average of 15 internal water molecules was found in the different simulations. Thirteen of the initial crystallographic water molecules remained stable during the production in all simulations. The positions of these water molecules are in good agreement with the predictions made using GRID^{102,103} interaction maps. Figure 8 depicts pictorially a GRID contour map at 8 kcal/mol above the absolute minimum. It can be seen that all hydrophilic internal sites of the protein

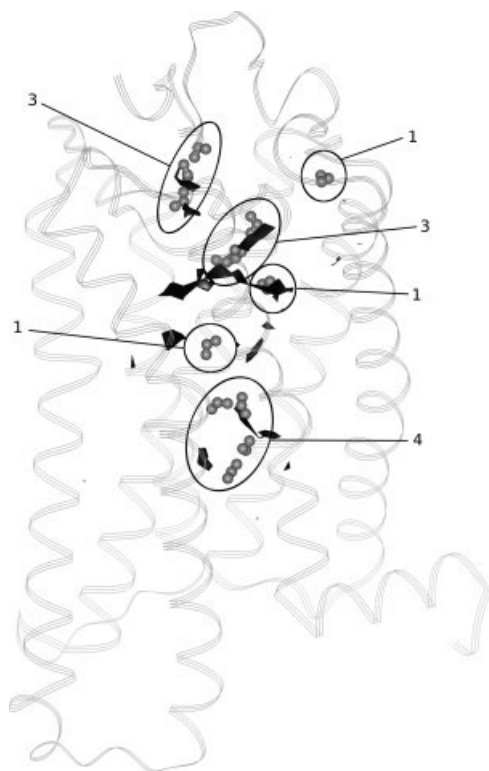


Figure 8. Crystallographic water molecules (colored by atom type) remaining as internal through the different MD trajectories. The backbone of rhodopsin (line ribbon lines) has been taken from the X-ray structure 1GZM.⁷ The number of water molecules in each pocket is shown explicitly. The regions predicted to exhibit high affinity for water molecules based on GRID calculations are shown in black.

are filled with water molecules in all simulations. In addition to the 13 crystallographic water sites, present results show that protein and lipid molecules induce ordering on other water molecules, although their mobility is higher, and they exhibit shorter interaction time-scales with the protein and lipids than the previous ones. Thus, considering the number of water molecules that remain close to the protein during 50 and 25% of the trajectory, the average numbers grow to 28 and more than 1400 waters, respectively. The different methodologies show no significant differences in the number and position of internal water molecules, which suggests that long range electrostatics is of small importance for this.

Conclusions

The present study reports a comparative analysis of a set of five 16-ns-MD simulations of rhodopsin embedded in a DPPC lipid bilayer, using different simulation protocols. Additionally, four simulations of the membrane with and without ions have been performed and taken as reference, for a better understanding of the effect caused by the protein and ions on the structural properties of the bilayer. The simulations have been carried out considering two different approximations for the treatment of long-range electrostatics: on the one hand, the use of a cutoff and on the

other, the PME method, in combination with two different sampling ensembles: the canonical (NVT) and the constant pressure (NPT). Recent studies of membrane proteins aimed at understanding the effect of different treatments of long-range electrostatics interactions,⁸⁹ the use of different statistical ensembles,⁴⁹ or their combined effects⁵⁰ are available. Here, these issues are studied together on the bovine rhodopsin. However, we are confident that the results can be extrapolated to the simulations of other GPCRs and (to a less extent) to other families of membrane proteins.

One of the most important outcomes of the study is that any of the approaches tested here is suitable for simulating bovine rhodopsin embedded in a DPPC bilayer with a physiological concentration of sodium chloride in the limited nanosecond time-scale examined. This is supported by the observation that the protein structure does not change significantly from the starting crystal structure in any of the simulations and furthermore, lipid bilayer properties behave in accordance with the available data of pure bilayers. Moreover, the explicit consideration of the membrane avoids problems associated to the stability of the starting protein structure. However, although the use of a one-component lipid bilayer appears to be a good approximation of a membrane, the use more realistic membrane models in the MD simulations of membrane proteins with the inclusion of other lipid molecules may be necessary for studying their specific effects on protein function.^{104–106}

A more detailed analysis of the results reported in the present work suggests that the approach chosen both to treat long range interactions together with the sample ensemble used affects the quality of the results obtained. Accordingly, the use of a cutoff to treat electrostatic interactions affects the description of different components of the system. Specifically, the use of a cutoff has effects on the lipid bilayer thickness, similarly to what has already been reported for pure bilayers, as well as on the distribution of ions. However, it reduces by a factor of 2 the computer time required, irrespective of the statistical ensemble used. In contrast, no significant deviations have been found on the protein structure, at least within the time-range of current simulations. The reason for this behavior can be explained by the small number of charged residues in rhodopsin and furthermore, due to their distribution, basically located on short length loops, that exhibit a restricted conformational profile. On the other hand, the explicit lipid bilayer can be considered a physical constraint of the α -helix structure on the transmembrane segments.

The statistical ensemble used in the simulations has influence on the bilayer thickness, but not in other components of the system. Specifically, the use of the NVT ensemble strongly restrains the lipid bilayer thickness since the area per lipid is constrained. The present study shows that for both, membrane equilibration and during the segment of the simulation involving the bilayer rearrangement around the protein, an adjustable cell geometry provided by the use of the NPT ensemble with independent barostats in all directions is necessary. In contrast, sampling within the NVT ensemble requires guessing the dimensions of a suitable periodic cell that gives the proper area per lipid. This may be doable for pure bilayers, but is quite tricky for bilayers that contain more components such as a protein or electrolytes. The effect on the protein when running simulations at a constant volume with the wrong box dimensions is usually

small. Interestingly, once the bilayer rearrangement around the protein using the NPT ensemble has been performed, the ensembles used afterwards provide no differences for systems of the size treated in the present study. However, since the use of the canonical ensemble (NVT) restrains the bilayer thickness, this ensemble is useful to avoid undesired artifacts due to the effects of the cutoff on lipids. We conclude that the combined choice of statistical ensembles and the type of long-range electrostatics have important effects, at least on lipid order.

An interesting result of the current study is that a proper description of the lipid–protein matching is crucial for the stability of the protein. The simulations performed with the NPT ensemble allow significant changes on lipid order, the average bilayer thickness being about 8% larger when using a cutoff compared to the corresponding simulations performed using the PME method. The use of a cutoff also has significant effects in the distributions of ions around the membrane. Accordingly, the combination of the NPT ensemble together with the PME method to treat the electrostatic interactions appears to be the more realistic selection. However, present results suggest that in spite of the artifacts that may be observed on the bilayer structure, the use of a cutoff can be a good compromise to study membrane proteins due to its lower computational cost and parallel efficiency. This choice is supported by the small differences found in the description of the protein structure and more specifically on its transmembrane segments, which are often the regions with higher biological interest. In the simulations performed within the NVT ensemble, the lipid bilayer is not able to reorganize once the box size is defined, and therefore lipid properties remain stable. Thus for studies focused on membrane protein properties, the combination of the NVT ensemble and a cutoff for the electrostatic interactions can be of special interest to avoid the artificial increase of the lipid thickness due to the use of a cutoff.

In summary, special care must be taken when selecting the statistical ensemble and the type of treatment for long-range electrostatics. The use of NPT is necessary for the bilayer equilibration and for the process involving the bilayer rearrangement around the protein. The use of the PME method provides a better description of lipids and ions but with a higher computational cost. Considering the sampling limitations of simulations with the time-scale of the present ones,⁹¹ it is important that these issues are continuously revised as longer time-scales become computationally accessible.

Acknowledgments

AC acknowledges a doctoral fellowship from the Universitat Politècnica de Catalunya. We are grateful to Barcelona Supercomputer Center for a generous allocation of computer time granted to the project “Molecular dynamics simulations of G-protein coupled receptors”.

References

- Ellis, C. *Nat Rev Drug Discov* 2004, 3, 575, 577.
- Archer, E.; Maigret, B.; Escrieut, C.; Pradayrol, L.; Fourmy, D. *Trends Pharmacol Sci* 2003, 24, 36.
- Attwood, T. K.; Findlay, J. B. *Protein Eng* 1994, 7, 195.
- Palczewski, K.; Kumasaka, T.; Hori, T.; Behnke, C. A.; Motoshima, H.; Fox, B. A.; Le Trong, I.; Teller, D. C.; Okada, T.; Stenkamp, R. E.; Yamamoto, M.; Miyano, M. *Science* 2000, 289, 739.
- Teller, D. C.; Okada, T.; Behnke, C. A.; Palczewski, K.; Stenkamp, R. E. *Biochemistry* 2001, 40, 7761.
- Okada, T.; Fujiyoshi, Y.; Silow, M.; Navarro, J.; Landau, E. M.; Shichida, Y. *Proc Natl Acad Sci USA* 2002, 99, 5982.
- Li, J.; Edwards, P. C.; Burghammer, M.; Villa, C.; Schertler, G. F. X. *J Mol Biol* 2004, 343, 1409.
- Okada, T.; Sugihara, M.; Bondar, A. N.; Elstner, M.; Entel, P.; Buss, V. *J Mol Biol* 2004, 342, 571.
- Ash, W. L.; Zlomislic, M. R.; Oloo, E. O.; Tieleman, D. P. *Biochim Biophys Acta Biomembr* 2004, 1666, 158.
- Strahs, D.; Weinstein, H. *Protein Eng* 1997, 10, 1019.
- Roux, B.; Berneche, S.; Im, W. *Biochemistry* 2000, 39, 13295.
- Im, W.; Roux, B. *J Mol Biol* 2002, 322, 851.
- Im, W.; Feig, M.; Brooks, C. L., III. *Biophys J* 2003, 85, 2900.
- Im, W.; Lee, M. S.; Brooks, C. L., III. *J Comput Chem* 2003, 24, 1691.
- Åqvist, J.; Luzhkov, V. *Nature* 2000, 404, 881.
- Govaerts, C.; Lefort, A.; Costagliola, S.; Wodak, S. J.; Ballesteros, J. A.; Van Sande, J.; Pardo, L.; Vassart, G. *J Biol Chem* 2001, 276, 22991.
- Rohrig, U. F.; Guidoni, L.; Rothlisberger, U. *Biochemistry* 2002, 41, 10799.
- Saam, J.; Tajkhorshid, E.; Hayashi, S.; Schulten, K. *Biophys J* 2002, 83, 3097.
- Grossfield, A.; Woolf, T. B. *Langmuir* 2002, 18, 198.
- Crozier, P. S.; Stevens, M. J.; Forrest, L. R.; Woolf, T. B. *J Mol Biol* 2003, 333, 493.
- Huber, T.; Botelho, A. V.; Beyer, K.; Brown, M. F. *Biophys J* 2004, 86, 2078.
- Feller, S. E.; Gawrisch, K.; Woolf, T. B. *J Am Chem Soc* 2003, 125, 4434.
- Pitman, M. C.; Suits, F.; Mackerell, A. D., Jr.; Feller, S. E. *Biochemistry* 2004, 43, 15318.
- Pitman, M. C.; Grossfield, A.; Suits, F.; Feller, S. E. *J Am Chem Soc* 2005, 127, 4576.
- Schlegel, B.; Sippl, W.; Holtje, H. D. *J Mol Model (Online)* 2005, 12, 49.
- Grossfield, A.; Feller, S. E.; Pitman, M. C. *Proc Natl Acad Sci USA* 2006, 103, 4888.
- Tieleman, D. P.; Berendsen, H. J. C. *J Chem Phys* 1996, 105, 4871.
- Loncharich, R. J.; Brooks, B. R. *Proteins* 1989, 6, 32.
- Heinz, T. N.; Hunenberger, P. H. *J Chem Phys* 2005, 123, 34107.
- Baumketner, A.; Shea, J. E. *J Phys Chem B* 2005, 109, 21322.
- Gilson, M. K. *Curr Opin Struct Biol* 1995, 5, 216.
- Cheatham, T. E.; Miller, J. L.; Fox, T.; Darden, T. A.; Kollman, P. A. *J Am Chem Soc* 1995, 117, 4193.
- Louise-May, S.; Auffinger, P.; Westhof, E. *Curr Opin Struct Biol* 1996, 6, 289.
- Beck, D. A.; Armen, R. S.; Daggett, V. *Biochemistry* 2005, 44, 609.
- Auffinger, P.; Beveridge, D. L. *Chem Phys Lett* 1995, 234, 413.
- Venable, R. M.; Brooks, B. R.; Pastor, R. W. *J Chem Phys* 2000, 112, 4822.
- Tobias, D. J. *Curr Opin Struct Biol* 2001, 11, 253.
- Pandit, S. A.; Berkowitz, M. L. *Biophys J* 2002, 82, 1818.
- Patra, M.; Karttunen, M.; Hyvönen, M. T.; Falck, E.; Lindqvist, P.; Vattulainen, I. *Biophys J* 2003, 84, 3636.
- Anézo, C.; de Vries, A. H.; Holtje, H. D.; Tieleman, D. P.; Marrink, S. J. *J Phys Chem B* 2003, 107, 9424.

41. Patra, M.; Karttunen, M.; Hyvonen, M. T.; Falck, E.; Vattulainen, I. *J Phys Chem B* 2004, 108, 4485.
42. Feller, S. E.; Pastor, R. W.; Rojnuckarin, A.; Bogusz, S.; Brooks, B. R. *J Phys Chem* 1996, 100, 17011.
43. Hess, B. *J Chem Phys* 2002, 116, 209.
44. Wohler, J.; Edholm, O. *Biophys J* 2004, 87, 2433.
45. Schreiber, H.; Steinhauser, O. *Biochemistry* 1992, 31, 5856.
46. Schreiber, H.; Steinhauser, O. *J Mol Biol* 1992, 228, 909.
47. Monticelli, L.; Colombo, G. *Theor Chem Acc* 2004, 112, 145.
48. Monticelli, L.; Simoes, C.; Belvisi, L.; Colombo, G. *J Phys: Condens Matter* 2006, 18, S329.
49. Zhu, Q.; Vaughn, M. W. *J Phys Chem B* 2005, 109, 19474.
50. Sankaramakrishnan, R.; Weinstein, H. *J Phys Chem B* 2004, 108, 11802.
51. Darden, T.; York, D.; Pedersen, L. *J Chem Phys* 1993, 98, 10089.
52. Berman, H. M.; Westbrook, J.; Feng, Z.; Gilliland, G.; Bhat, T. N.; Weissig, H.; Shindyalov, I. N.; Bourne, P. E. *Nucleic Acids Res* 2000, 28, 235.
53. Fahmy, K.; Jager, F.; Beck, M.; Zvyaga, T. A.; Sakmar, T. P.; Siebert, F. *Proc Natl Acad Sci USA* 1993, 90, 10206.
54. Sandberg, L.; Edholm, O. *Proteins* 1999, 36, 474.
55. Lindahl, E.; Edholm, O. *Biophys J* 2000, 79, 426.
56. Berendsen, H. J. C.; van der Spoel, D.; Vandrunen, R. *Comput Phys Commun* 1995, 91(1–3), 43.
57. Lindahl, E.; Hess, B.; van der Spoel, D. *J Mol Model (Online)* 2001, 7, 306.
58. Berendsen, H. J. C.; Postma, J. P. M.; DiNola, A.; Haak, J. R. *J Chem Phys* 1984, 81, 3684.
59. Nose, S. *Mol Phys* 1984, 52, 255.
60. Hoover, W. G. *Phys Rev A* 1985, 31, 1695.
61. Miyamoto, S.; Kollman, P. A. *J Comput Chem* 1992, 13, 952.
62. Jorgensen, W. L.; Maxwell, D. S.; TiradoRives, J. *J Am Chem Soc* 1996, 118, 11225.
63. Berger, O.; Edholm, O.; Jähnig, F. *Biophys J* 1997, 72, 2002.
64. Hofsäß, C.; Lindahl, E.; Edholm, O. *Biophys J* 2003, 84, 2192.
65. Jorgensen, W. L.; Chandrasekhar, J.; Madura, J. D.; Impey, R. W.; Klein, M. L. *J Chem Phys* 1983, 79, 926.
66. Hayashi, S.; Tajkhorshid, E.; Schulten, K. *Biophys J* 2002, 83, 1281.
67. Engelman, D. M. *Nature* 2005, 438, 578.
68. Nagle, J. F.; Tristram-Nagle, S. *Biochim Biophys Acta Rev Bioembr* 2000, 1469, 159.
69. Pandit, S. A.; Bostick, D.; Berkowitz, M. L. *Biophys J* 2003, 84, 3743.
70. Böckmann, R. A.; Hac, A.; Heimbürg, T.; Grubmüller, H. *Biophys J* 2003, 85, 1647.
71. Harroun, T. A.; Heller, W. T.; Weiss, T. M.; Yang, L.; Huang, H. W. *Biophys J* 1999, 76, 3176.
72. Harroun, T. A.; Heller, W. T.; Weiss, T. M.; Yang, L.; Huang, H. W. *Biophys J* 1999, 76, 937.
73. Parsegian, V. A. *Ann NY Acad Sci* 1975, 264, 161.
74. Brown, M. F.; Seelig, J. *Nature* 1977, 269, 721.
75. Looselymillman, M. E.; Rand, R. P.; Parsegian, V. A. *Biophys J* 1982, 40, 221.
76. Tatulian, S. A. *Eur J Biochem* 1987, 170, 413.
77. Cunningham, B. A.; Gelerinter, E.; Lis, L. J. *J Chem Phys Lipids* 1988, 46, 205.
78. Roux, M.; Bloom, M. *Biochemistry* 1990, 29, 7077.
79. Clarke, R. J.; Lupfert, C. *Biophys J* 1999, 76, 2614.
80. Sachs, J. N.; Nanda, H.; Petrace, H. I.; Woolf, T. B. *Biophys J* 2004, 86, 3772.
81. Mukhopadhyay, P.; Monticelli, L.; Tieleman, D. P. *Biophys J* 2004, 86, 1601.
82. Garcia-Manyes, S.; Oncins, G.; Sanz, F. *Biophys J* 2005, 89, 1812.
83. Petrace, H. I.; Tristram-Nagle, S.; Harries, D.; Kucerka, N.; Nagle, J. F.; Parsegian, V. A. *J Lipid Res* 2006, 47, 302.
84. Weiss, T. M.; van der Wel, P. C.; Killian, J. A.; Koeppe, R. E., II; Huang, H. W. *Biophys J* 2003, 84, 379.
85. Mitra, K.; Ubarretxena-Belandia, I.; Taguchi, T.; Warren, G.; Engelman, D. M. *Proc Natl Acad Sci USA* 2004, 101, 4083.
86. Jensen, M. O.; Mouritsen, O. G. *Biochim Biophys Acta* 2004, 1666, 205.
87. Kyte, J.; Doolittle, R. F. *J Mol Biol* 1982, 157, 105.
88. Sandberg, L.; Edholm, O. *J Phys Chem B* 2001, 105, 273.
89. Tieleman, D. P.; Hess, B.; Sansom, M. S. P. *Biophys J* 2002, 83, 2393.
90. Edholm, O.; Berger, O.; Jähnig, F. *J Mol Biol* 1995, 250, 94.
91. Faraldo-Gomez, J. D.; Forrest, L. R.; Baaden, M.; Bond, P. J.; Domene, C.; Patargias, G.; Cuthbertson, J.; Sansom, M. S. *Proteins* 2004, 57, 783.
92. Kabsch, W.; Sander, C. *Biopolymers* 1983, 22, 2577.
93. Smythe, M. L.; Huston, S. E.; Marshall, G. R. *J Am Chem Soc* 1995, 117, 5445.
94. Kinoshita, M.; Okamoto, Y.; Hirata, F. *J Am Chem Soc* 2000, 122, 2773.
95. Feig, M.; MacKerell, A. D.; Brooks, C. L. *J Phys Chem B* 2003, 107, 2831.
96. Sorin, E. J.; Pande, V. S. *Biophys J* 2005, 88, 2472.
97. Sorin, E. J.; Pande, V. S. *J Comput Chem* 2005, 26, 682.
98. McLaughlin, S. *Annu Rev Biophys Chem* 1989, 18, 113.
99. Cevc, G. *Biochim Biophys Acta* 1990, 1031, 311.
100. Åman, K.; Lindahl, E.; Edholm, O.; Håkansson, P.; Westlund, P. O. *Biophys J* 2003, 84, 102.
101. Saiz, L.; Klein, M. L. *J Chem Phys* 2002, 116, 3052.
102. GRID Version 21.0, 2003, Molecular Discovery Ltd, Oxford.
103. Goodford, P. J. *J Med Chem* 1985, 28, 849.
104. Litman, B. J.; Mitchell, D. C. *Lipids* 1996, 31 (Suppl), S193.
105. Burger, K.; Gimpl, G.; Fahrenholz, F. *Cell Mol Life Sci* 2000, 57, 1577.
106. Polozova, A.; Litman, B. J. *Biophys J* 2000, 79, 2632.

**Molecular dynamics simulations of rhodopsin in different
one-component lipid bilayers**

Cordomí A, Perez JJ

J Phys Chem B., 2007 Jun 28;111(25):7052-63

Molecular Dynamics Simulations of Rhodopsin in Different One-Component Lipid Bilayers

Arnau Cordermi* and Juan J. Perez

Dept d'Enginyeria Química, Technical University of Catalonia (UPC), Diagonal 647, 08028 Barcelona, Spain

Received: January 30, 2007; In Final Form: April 4, 2007

Four 20 ns molecular dynamic simulations of rhodopsin embedded in different one-component lipid bilayers have been carried out to ascertain the importance of membrane lipids on the protein structure. Specifically, dimyristoyl phosphatidylcholine (DMPC), dipalmitoyl phosphatidylcholine (DPPC), palmitoyl oleoyl phosphatidylcholine (POPC), and palmitoyl linoleyl phosphatidylcholine (PLPC) lipid bilayers have been considered for the present work. The results reported here provide information on the hydrophobic matching between the protein and the bilayer and about the differential effects of the protein on the thickness of the different membranes. Furthermore, a careful analysis of the individual protein–lipid interactions permits the identification of residues that exhibit permanent interactions with atoms of the lipid environment that may putatively act as hooks of the protein to the membrane. The analysis of the trajectories also provides information about the effect of the bilayer on the protein structure, including secondary structural elements, salt bridges, and rigid-body motions.

Introduction

The importance of the lipidic membrane in protein function is a topic that has only recently been the focus of attention of the scientific community.¹ The present view of the membrane is based on the fluid mosaic model of Singer–Nicholson² where proteins are distributed in regions of biased composition with varying protein environment. In this heterogeneous landscape, lipids are thought to play a strong influence on protein function, and consequently, it is important to understand the protein–lipid interplay in detail.³ Specifically, the hydrophobic matching between the protein and the membrane has been identified as one of the most critical aspects of this interaction.⁴

Hydrophobic mismatch is defined as the difference between the hydrophobic length of the transmembrane segments of a protein and the hydrophobic width of the surrounding lipid bilayer. Because of the present difficulties associated with experiments involving membranes or membrane proteins, molecular dynamics (MD) simulations represent an excellent tool to provide some insight into the understanding of lipid–protein interactions. In this sense, the study of model transmembrane peptides^{5–10} has provided the necessary background for studying proteins. Of special interest is the recent study where the length of a peptide and the lipid hydrophobic thickness have been studied systematically.⁵

Despite the high number of MD simulations on model peptides reported in the literature, simulations involving membrane proteins are still scarce. Within this group of proteins, G-protein coupled receptors (GPCRs) represent the largest family, being encoded by more than 2% of the human genome, and therefore are of substantial scientific interest. GPCRs mediate a major part of transduction signals responding to a diverse range of molecules, including ions, peptides, lipids, biogenic amines, and photons. These proteins play a key role in cell signal transmission and in the regulation of basic physiological processes. Their key physiological function

together with their natural abundance makes them suitable targets for therapeutic intervention, accounting for more than 50% of the currently marketed drugs¹¹ and, therefore, are proteins of enormous pharmacological interest.¹² Despite their important biological function, scarce structural information, necessary to get a better understanding of the structure–function relationships of GPCRs, is currently available because basically of the difficulties associated with the crystallization of membrane proteins.¹³ Bovine rhodopsin, a protein involved in the visual signal transduction cascade in vertebrates, is the only GPCR whose 3D structure is currently available at atomic resolution.^{14–18} This makes this protein to be a suitable template for modeling studies of other GPCRs. Recently, different groups have reported simulations of rhodopsin in monounsaturated^{19–22} and polyunsaturated model bilayers.^{23–25} The results of these studies suggest the existence of specific sites on the rhodopsin surface to accommodate polyunsaturated lipids, and furthermore, the weakening of the interhelical packing with the presence of tightly packed lipids has also been reported.^{23–25} However, the effect of different lipid bilayers on the structure and function of the protein is not yet clear.

The aim of the present study is to provide some insight into the understanding of the main features of protein–lipid interactions using rhodopsin as a model of GPCRs. For this purpose, a set of molecular dynamics (MD) simulations of rhodopsin embedded in different lipid environments were performed. Specifically, four 10 ns simulations of rhodopsin embedded in one-component lipid bilayers including dimyristoyl phosphatidylcholine (DMPC), dipalmitoyl phosphatidylcholine (DPPC), palmitoyl oleoyl phosphatidylcholine (POPC), and palmitoyl linoleyl phosphatidylcholine (PLPC) were considered for the present work. Figure 1 depicts pictorially the structures of the different lipids selected for the present study. These lipids were selected for being the best characterized experimentally nowadays and because some inferences can be done in regard to the presence of saturated and unsaturated acyl chains and also the effect of different chain lengths. Despite that these lipids are not the major components of the native membranes where

* To whom correspondence should be addressed. Phone: +34 934010810. Fax: +34 934017150. E-mail: arnau.cordermi@upc.edu.

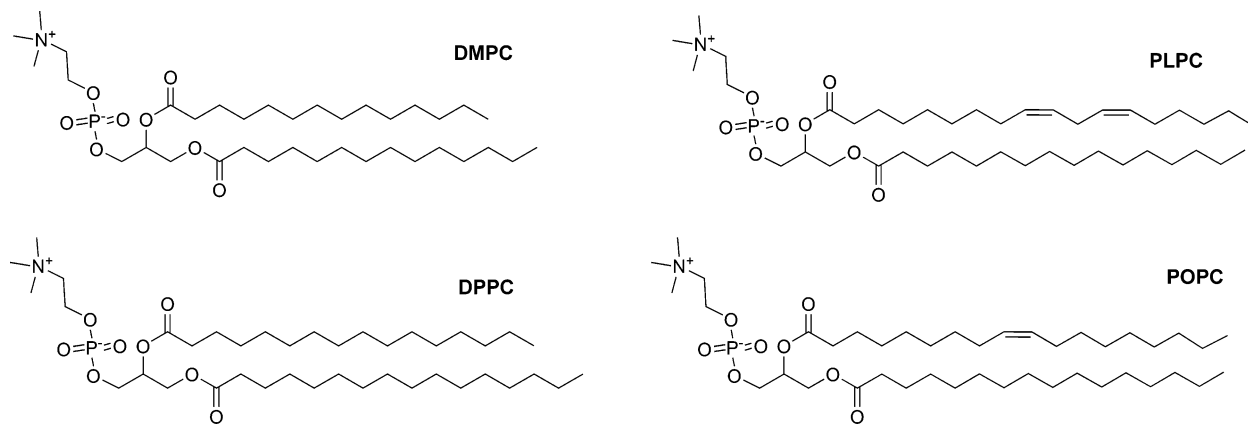


Figure 1. Chemical structures of the different phosphatidylcholine (PC) lipids used in the present work.

rhodopsin is normally found, their choice has special interest since they are some of the most studied lipids and also because force field parameters for them have been widely tested.

Methods

The Rhodopsin Structure. Rhodopsin atomic coordinates were retrieved from the Protein Data Bank²⁶ (entry 1GZM¹⁷). In contrast to other published crystal structures,^{14–16} this one includes the coordinates of all the amino acids of the intradiscal and cytosolic loops. The atomic coordinates of some missing C-terminal residues were taken from a different source¹⁶ and were adapted by superposition of the α -carbon skeleton of both protein structures. Accordingly, the starting model of the protein contained all N- and C-terminal amino acids, including the N-terminal acetyl group and two palmitoyl chains at the cytoplasmic end that are covalently linked to two consecutive cysteine residues, believed to be important as membrane anchoring points of the protein to the membrane. All amino acids were modeled in the protonation state they would have as free amino acids in water at pH 7 with the exception of D83 and E122, which were treated as protonated and neutral according to experimental evidence.²⁷ Moreover, H196 was considered charged, as supported by pK_a calculations using the program DaPDS.²⁸ In these conditions, the protein exhibits a total of 19 positive and 21 negative charges yielding a net charge of -2 . This net charge is later compensated in the simulation box by adjusting the balance between sodium and chloride ions to give an electroneutral system, as described in detail later. In addition, 23 crystallographic water molecules, consistent with those found in the crystal structures 1GMZ and 1LH9 of the Protein Data Bank,^{16,17} were included in the starting structure.

Box Preparation and Protein Embedding. Four boxes consisting of a lipidic bilayer of 256 molecules of DMPC, DPPC, POPC, or PLPC, respectively, were arranged. For convenience, each system was organized in such a way that the bilayer plane was oriented on the XY plane. Introduction of additional water molecules on the systems permits the generation of thick water layers on each side of the bilayer, providing enough space for allocating the hydrophilic parts of the protein. This procedure led to the generation of four boxes of dimensions approximately $8.5 \times 8.5 \times 10$ nm (XYZ). Next, sodium chloride was added to the systems to reach a salt concentration of 0.2 M. For this purpose, a different number of water molecules depending on the system were replaced by Na^+ and Cl^- ions one at a time at those positions where the electrostatic potential was more favorable, using the GENION program of GROMACS V3.2.^{29,30} The procedure was followed until the desired conc-

centration was reached. Next, each system was equilibrated for 20 ns according to the procedure described elsewhere.³¹ Finally, rhodopsin was placed in the center of the different boxes and the overlapping molecules were removed, following the procedure described previously.³² Specifically, all water molecules with oxygen atoms closer than 0.40 nm to a non-hydrogen atom of the protein, as well as all lipid molecules with at least one atom closer than 0.25 nm to a non-hydrogen atom of the protein, were removed. This resulted in four final systems containing 197 lipids and ca. 16 000 water molecules.

Molecular Dynamics Simulations. All computer simulations were performed using a parallel version of the GROMACS 3.2 package.^{29,30} Each of the systems was subjected to periodic boundary conditions in the three-coordinate directions. The temperature was kept constant at 323 K for the DPPC system (well above the gel/liquid crystalline phase-transition temperature of 314 K) and at 300 K for the remaining systems using separate thermostats for the protein, water, ions, and lipid molecules.³³ The time constant for the thermostats was set to 0.1 ps except for water, for which a smaller value of 0.01 ps was used. The pressure in the three-coordinate directions was kept at 0.1 MPa by independent Berendsen barostats³³ using a time constant of 1.0 ps. The equations of motion were integrated with the leapfrog algorithm using a time step of 2 fs for the simulations with protein and 4 fs for the rest. All bonds in the protein and lipid molecules were kept frozen using the LINCS algorithm.³⁴ The bonds and the angles of water molecules were fixed using the analytical SETTLE method. Lennard-Jones (LJ) interactions were computed using a cutoff of 1.0 nm. The electrostatic interactions were treated using the particle mesh Ewald (PME) technique.³⁵

The all-atom OPLS force field³⁶ currently implemented in GROMACS was used for all molecules of the system except for the lipids. In this case, the force field used is based on a parametrization made for DPPC lipids reported in ref 37, which has been shown to reproduce the experimental areas per lipid of pure DPPC in the liquid-crystalline phase.^{37–40} For PLPC lipids, the torsion parameters involving the bis-diene moiety were taken from ref 41. Files containing the force field parameters were downloaded from <http://moose.bio.ucalgary.ca/>. To account for protein–lipid interactions, nonbonded pair interactions were computed as combinations of single atomic LJ parameters. Water molecules were modeled using the TIP3P model.⁴² Fractional charges of retinal atoms were taken from quantum chemical calculations⁴³ and have already been used in other MD simulations of rhodopsin.²¹ Fractional atomic

TABLE 1: Hydrophobic Bilayer Thickness for the Systems Studied in the Present Work: Pure Bilayers without Salt (Top), with 0.2 M NaCl (Middle), or with 0.2 M NaCl and Rhodopsin (Bottom)^a

pure	hydrophobic thickness (nm)		area per lipid (nm ²)	
DMPC	2.53	±0.02	0.605	±0.005
DPPC	2.82	±0.02	0.634	±0.006
POPC	2.98	±0.02	0.609	±0.004
PLPC	2.82	±0.02	0.647	±0.004
NaCl 0.2 M	hydrophobic thickness (nm)		area per lipid (nm ²)	
DMPC	2.63	±0.03	0.564	±0.004
DPPC	2.94	±0.03	0.588	±0.006
POPC	3.07	±0.03	0.585	±0.005
PLPC	2.92	±0.03	0.621	±0.005
rhodopsin	hydrophobic thickness (nm)		P–P thickness (nm)	
DMPC	2.65	±0.03	3.75	±0.03
DPPC	2.92	±0.03	4.03	±0.03
POPC	3.02	±0.03	4.12	±0.03
PLPC	2.94	±0.03	4.04	±0.03

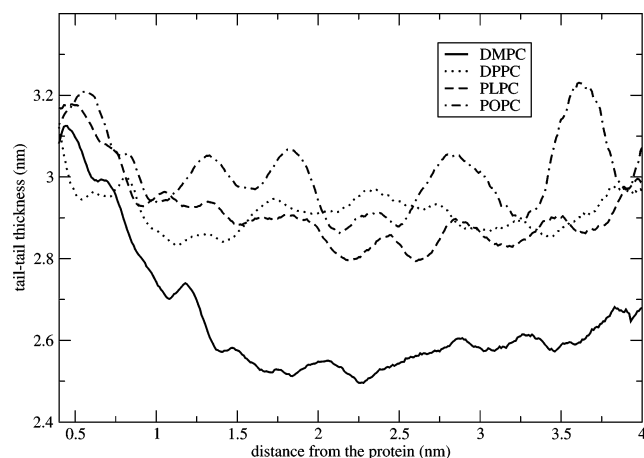
^a For the systems without protein, the areas per lipid are also shown, and for those containing rhodopsin, the phosphate–phosphate (P–P) thickness is displayed instead.

charges for palmitoylated cysteines were derived from electrostatic potential calculations performed at the HF/6-31G* level.

Once the protein was inserted in each lipidic bilayer, the system was energy minimized. Subsequently, each system was subjected to a 0.5 ns MD simulation to allow for the removal of voids present between the protein and the lipids or water. These simulations were performed allowing the three periodic box dimensions to change size according to a pressure of 0.1 MPa in each coordinate direction. The atomic coordinates of the protein were restrained to their crystallographic positions. Next, the restraints were released and the four MD trajectories containing rhodopsin were computed up to 20 ns each. As a reference, eight additional simulations were performed without protein and either with or without ions lasting 20 ns each. For all simulations, coordinates were collected every 10 ps and were stored for further analysis. In all cases, the first 10 ns were considered as equilibration period, and therefore they are not included in the analysis.

Results and Discussion

Effect of the Protein on Lipid Order. The order in a lipid bilayer can be characterized by NMR order parameters, the fraction of trans bonds, from the area per lipid, or through the bilayer thickness. The area per lipid can be directly computed from the total area in systems with no protein embedded. In contrast, this is not straightforward on a system containing a protein because of the bumpy surface exhibited.³² Therefore, bilayer thickness is preferred as a measure of order for systems containing proteins, measured either from the distance between the two planes formed by the phosphate groups or from the hydrophobic width, that is, the segment of the bilayer corresponding to the acyl chains. In the present work, the hydrophobic width is used since it allows, in the systems with rhodopsin, a direct comparison with the hydrophobic thickness of the protein. Steady values of the bilayer thickness averaged over the last 10 ns for the different simulations are listed in Table 1. The area per lipid for the systems without protein is also given to be used as reference. Average areas of the pure hydrated systems compare well with reported experimental values and with earlier MD simulations of DPPC,^{37,38,40,44} DMPC,^{38,45} PLPC,⁴¹ and POPC,^{46,47} considering the limitations of the lipid parameters

**Figure 2.** Variation of the bilayer thickness along a radial distance to the protein.

available.⁴⁸ Furthermore, although comparison with experimental results is not necessarily simple because of the different temperatures used to perform the measurements, the values reported in the present work are within error margins associated to the experimental techniques.³⁸

In regard to the effect produced by ions, cations are known to bind to the lipid headgroups promoting lipid order. However, the process of binding requires large simulation times.⁴⁹ To use an efficient procedure, we explored the performance of two alternative methods for including ions into the bilayer. Accordingly, we compared a method where ions are placed using a potential-based function versus a random placing. Results suggest that the former procedure provides steady values of the bilayer thickness much faster, being the one used in the present calculations, as explained in Methods. Specifically, the time required for the binding of sodium ions to the lipid headgroups in the present simulations was about 10 ns. Inspection of Table 1 points out that the addition of sodium chloride provides thicker bilayers and, consequently, lower areas per lipid, in agreement with previous results for both pure bilayers^{49–51} and bilayers with proteins embedded on them.³² The decrease in the area per lipid because of the binding of cations to the bilayer is about 7% for DPPC and DMPC and about 4% for POPC and PLPC. These results point out a direct effect of the fatty acid composition on the binding of ions to the lipid headgroups. The decrease is larger in the saturated phospholipids because of a tighter lipid–lipid packing.^{52–54}

In regard to the rhodopsin simulations, the results listed in Table 1 indicate that the effect of the protein on the average bilayer thickness is small or negligible for a protein/lipid ratio of about 1/200 as in the systems studied. Similar results were recently obtained in simulations of rhodopsin embedded on a DPPC bilayer under different sampling conditions and handling of the electrostatics.³² However, in spite of the small average effects produced by the protein on the bilayer thickness, lipids do accommodate to the protein surface in an energetically favorable process known as hydrophobic matching, producing local effects on the bilayer in the neighborhood of the protein. This can be observed from the plot of the bilayer thickness as a function of the distance from the protein, averaged on all the lateral directions, as shown in Figure 2. The differential profile exhibited by each lipid bilayer depends on the difference between the equilibrium lipid bilayer thickness and the hydrophobic thickness of the protein. The four systems studied exhibit a similar thickness of 3.1 nm in the neighborhood of the protein, in good agreement with a previous estimate of 3.0 nm for the

TABLE 2: Average Lennard-Jones (LJ), Coulomb, and Total Interaction Energies between Lipids and the Protein in kJ/mol

	LJ	Coulomb	total
DMPC	-3342	-1145	-4487
DPPC	-3423	-1250	-4673
POPC	-3501	-1136	-4637
PLPC	-3653	-1664	-5317

hydrophobic protein width.³² Interestingly, this value is close to the hydrophobic thickness of bilayers with a 0.2 M concentration of NaCl (see Table 1) except for DMPC, for which the thickness is significantly smaller than the hydrophobic width of rhodopsin. Therefore, the radial distributions of the bilayer thickness exhibit small variations for DPPC, PLPC, and POPC bilayers, whereas the DMPC system exhibits larger fluctuations basically affecting lipids within a 1.5 nm radius from the protein surface. Furthermore, the profiles displayed in Figure 2 suggest that the thicker region close to the protein is compensated with an increase of the thickness far from the protein, being even lower than the average value without rhodopsin.

Lipid-Protein Interactions. The evolution of both the Coulomb and the Lennard-Jones (LJ) contributions to the lipid-protein interaction energy was investigated along the MD trajectories. In all systems studied, both terms reach a steady value after about 10 ns of simulation. Table 2 lists the values of both contributions for the different systems studied, suggesting a strong interaction between the lipids and the protein in all cases, the magnitude of the LJ contribution being about double the electrostatic one.

LJ interactions account basically for the dispersion contribution to the interaction energy and can be used to evaluate the contact surface, hydrophobic matching, between the protein and the bilayer. The analysis of Table 2 points out that average LJ interaction energies are not the same for the different phospholipids, following the order PLPC > POPC > DPPC > DMPC. Comparison of the LJ interactions for the different systems suggests that their magnitude correlates with the number of carbons on the acyl chain and with the presence of double bonds, which is associated with a better matching of the acyl chains to the protein. More specifically, the smaller LJ contribution exhibited by DMPC in comparison to DPPC (both phospholipids with saturated acyl chains) can be explained as because of the shorter acyl chains of the former, suggesting that they should have to adopt an extended conformation in the vicinity of the protein to account for the differences between their hydrophobic widths and, consequently, impairing an optimal hydrophobic matching. On the other hand, the results of POPC and PLPC suggest that although both have the same number of carbons, the two unsaturations of PLPC provide additional adaptability to the protein when compared to the single one in POPC. These results agree well with the trend observed of an increased bilayer fluidity with a growing number of double bonds of the lipid acyl chains.⁵³

Specific hydrophobic lipid-protein interactions have been analyzed along the different trajectories within a radius of 0.4 nm between any hydrophobic heavy atom of rhodopsin and the lipid molecules. Following this approach, about 100–115 residues were identified to exhibit contacts with lipids in at least half of the snapshots analyzed for all systems studied in the present work (Table 3A). This number represents almost one-third of the total number of protein residues, indicating a potential role of lipids in modulating protein structure and function. Obviously, the major part of the interactions observed (90–97% depending on the system) occurs at the lipid tails.

TABLE 3: Summary of Lipid-Protein Hydrophobic Interactions in Each Lipid Bilayer System. (A) Number of Residues Exhibiting Hydrophobic Contacts with the Protein. (B) Number of Residues Grouped per Residue Type**(A) Number of Residues Exhibiting Hydrophobic Contacts with the Protein**

	DMPC	DPPC	PLPC	POPC
total residues	102	102	114	110
head	10	10	6	10
tail	92	92	108	100

(B) Number of Residues Grouped Per Residue Type

	DMPC	DPPC	PLPC	POPC	total	%
Ala	6	6	5	4	29	18
Arg	2	2	1	0	7	18
Asn	1	0	0	3	15	7
Asp	0	1	0	1	5	10
Cys	0	1	1	1	10	8
Gln	0	1	1	0	12	4
Glu	0	0	2	2	17	6
Gly	0	0	0	0	23	0
His	2	2	2	3	6	38
Ile	16	16	17	17	22	75
Leu	15	16	17	16	28	57
Lys	1	0	1	0	11	5
Met	7	6	8	8	16	45
Phe	19	19	20	19	31	62
Pro	4	4	6	5	20	24
Ser	1	0	2	1	15	7
Thr	3	2	3	2	27	9
Trp	3	4	4	4	5	75
Tyr	9	9	8	9	18	49
Val	13	13	16	15	31	46
total	102	102	114	110	348	31

This is the case of the residues located on the transmembrane (TM) regions. The remaining interactions involve the lipid-head methyl groups with helix ends or with the loops, which are rich in aromatic residues. Regarding the type of amino acids involved (Table 3B), phenylalanine, leucine, isoleucine, and valine—an aromatic and the most hydrophobic/aliphatic residues—exhibit the largest number of contacts. A second group of amino acids following in importance includes tyrosine and aliphatic residues with shorter side chains like methionine and alanine.

In regard to lipid-protein electrostatic interactions, differences in the energies are observed within the systems studied, despite sharing the same lipid headgroup (see Table 2). This suggests that there is a connection between the hydrophobic matching and the optimization of the electrostatic interactions. Specifically, all systems exhibit average values of about -1200 kJ/mol except PLPC that yields an interaction energy close to -1700 kJ/mol. To understand the source of the Coulomb interactions between the protein and the phospholipids, a careful study of the hydrogen bonds created and broken along the MD trajectory was carried out. Accordingly, two different cutoffs of 0.25 and 0.40 nm were considered to identify direct and water-mediated hydrogen bonds, respectively, involving protein side chain donors and lipid oxygens acting as acceptors. Figure 3 displays residues identified to be involved in more than 5% of the trajectory in direct hydrogen bonds with the lipid molecules or more than 10% of the trajectory in water-mediated hydrogen bonds. The results indicate that the total number of long-time protein-lipid hydrogen bonds depends on the bilayer and ranges from 12 to 21 for the direct and between 21 and 29 when adding the direct plus water mediated ones. Interestingly, an analysis of the figure shows that there are a few residues that are found in all the systems studied and that can be considered as anchoring points of the protein to the lipid bilayer,

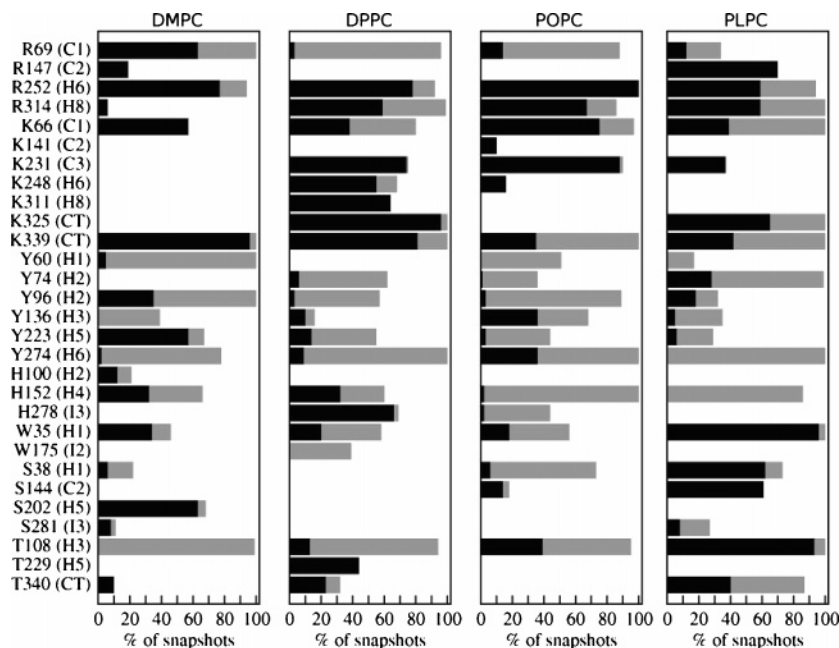


Figure 3. Residues involved in lipid–protein interactions. Only interactions present at least in 10% of the snapshots using a cutoff of 0.40 nm are considered. The location within the protein motifs is indicated in brackets. For each residue, the total bar lengths indicate the percentage of snapshots where the interaction exists. The black and the gray portions of each bar represent the preferences of residues for the phosphate or the carbonyl oxygens, respectively.

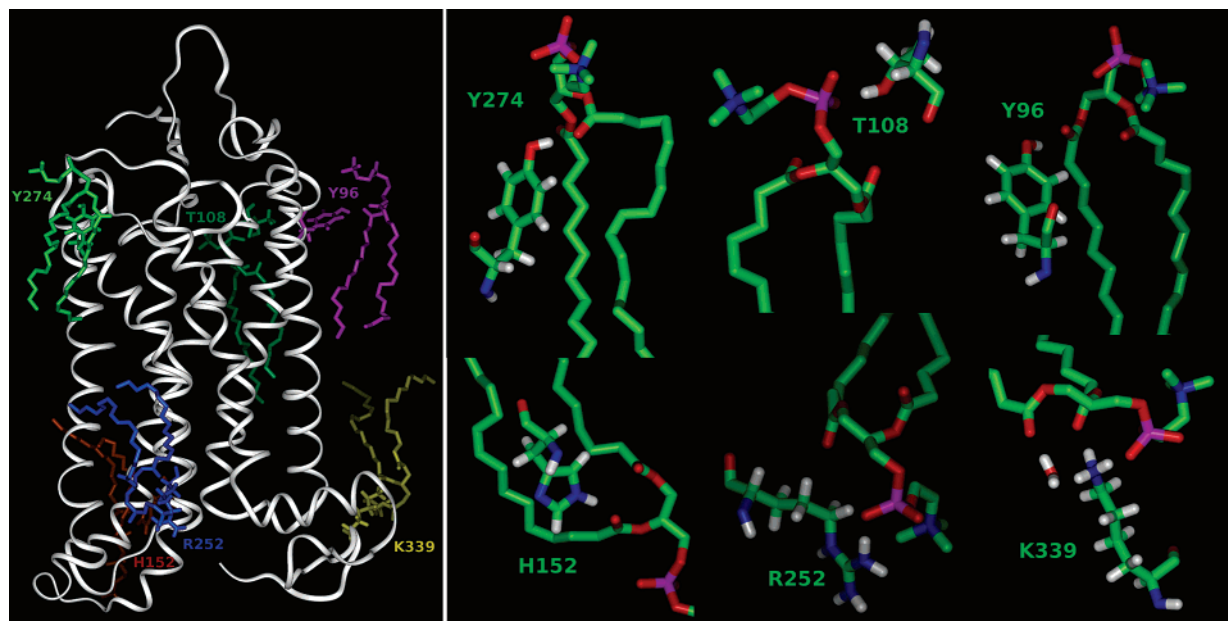


Figure 4. Typical protein–lipid electrostatic interactions involving residues found in common in the four systems to interact with lipids in more than half of each trajectory. The left panel displays the side chain/lipid complexes extracted from representative snapshots of the four simulations superposed to the average protein C α trace corresponding to the DMPC system. The right one displays a closer view of these interactions, with atoms colored by atom type. The structures displayed for Y274, Y96, and H152 show examples of interactions with the lipid carbonyl oxygens; those of T108 and R252 show interactions with the lipid phosphate oxygens; finally, K339 shows an example of simultaneous interactions with both the lipid carbonyl and phosphate oxygens, including an interaction mediated by a water molecule.

although there is a majority that are only involved in specific systems. According to Figure 3, residues R252, K339, Y96, Y274, H152, and T108 are found in common in the four simulations to be involved in hydrogen bonds with lipid molecules in more than half of each trajectory. A model displaying the location of these residues together with representative interactions with the lipid molecules is shown in Figure 4, where lipid coordinates have been taken from selected snapshots of the four simulations. Additionally, residues K66, R69, Y136, Y223, and W35 participate also in hydrogen bonds

with lipid molecules in all systems, though to a lower extent. K339, identified to be present in more than 90% of the four trajectories analyzed, has already been reported to be particularly relevant in both experimental reports⁵⁵ and in MD simulations.¹⁹ Most of these critical hydrogen bond interactions (see Figure 3) involve contacts between lipid oxygens and either basic amino acids, lysine and arginine, or polar aromatic ones—tyrosine, histidine, and tryptophan. The short-chain amino acids having hydroxyl groups, serine and threonine, and residues interacting through the backbone nitrogen follow in importance. Examples

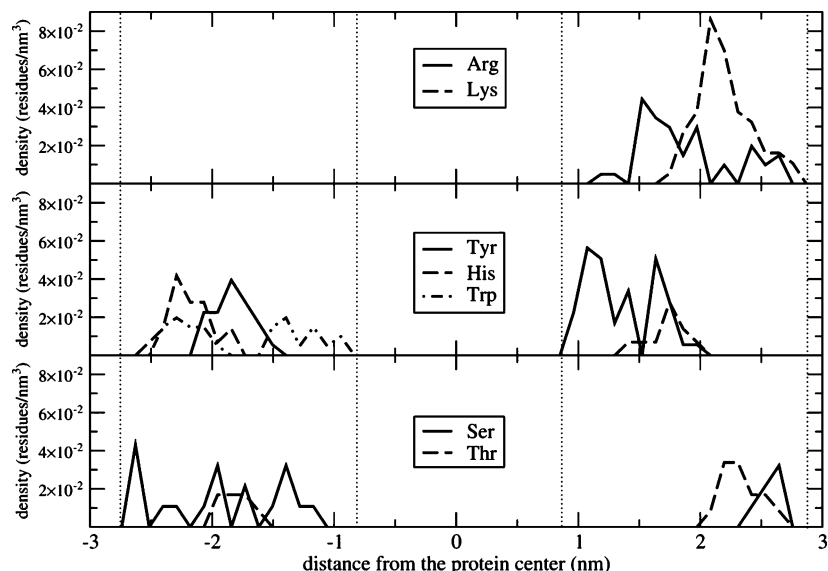


Figure 5. Partial number densities of the residues interacting with lipid oxygens normalized to the number of atoms per residue.

of these interactions between the polar protein side chains and the lipid oxygens can be found in Figure 4.

The preference of each residue for phosphate or alkyl carbonyl oxygens was analyzed. The results were compared with those obtained in both recent MD simulations and experiments on model peptides and proteins.^{56–60} The present results show that basic amino acids exhibit a clear preference for phosphate oxygens, in agreement with those results. Polar aromatic residues exhibit also specific preferences: tyrosine exhibits a preference to interact with alkyl carbonyl oxygens, in agreement with other recent reports,^{61,62} whereas histidine and tryptophan can be seen to interact indistinctly with both types of oxygens. These differences seem to arise from the location of the hydrogen bond donor, out of the ring in the former. Serine and threonine residues, as well as those residues interacting with the lipids through the backbone nitrogen, do not show a preference for any lipid oxygen type. This is reasonable because of their short side chains, which force them to form hydrogen bonds with the closest lipid oxygens available, independently of their nature. The fact that none of the hydrogen bond interactions through backbone nitrogens are found in common among the different systems suggests that they are formed just to reinforce other existing neighboring hydrogen bonds.

The preference observed by the different amino acids to interact with either the phosphate or carbonyl lipid oxygens suggests that they may not be randomly distributed in the rhodopsin structure. Indeed, Figure 5 depicts pictorially the distribution per amino acid of the different residues shown in Figure 3 along the direction perpendicular to the bilayer normal. As can be seen, the amino acids are grouped around two areas at both sides of the protein located about 2 nm from the protein core, covering a region of approximately 2 nm each. Interestingly, the distribution of these amino acids at both sides of rhodopsin is asymmetric. Thus, arginine and lysine residues are only found on the cytoplasmic side, like most of the tyrosine residues. However, the former are located in the most external segment according to their preference to interact with the phosphate oxygens, whereas the latter are never located at the most external part of the density profiles, according to their preferences for the carbonyl oxygens. Moreover, whereas the majority of arginine and lysine residues interacting with lipids in rhodopsin are located on loops, all tyrosine residues are found in the TM helices, even

in quite internal positions such as in the case of Y223. The amphiphilic character of the tyrosine residues together with the long distance between the α -carbon and the hydroxyl group (typically 0.65 nm) is responsible of this behavior. Regarding the tryptophan, histidine, serine, and threonine side chains involved in specific interactions with the lipids, their number is too small to extract general conclusions to be extrapolated to other GPCRs, although the corresponding analysis is performed in detail below. All histidine residues are found closer to the two ends of the protein than tyrosine, probably because of the lower distance between the α -carbon and the ring nitrogen atoms (about 0.45 nm). Despite that tryptophan residues are often present at the TM ends in membrane proteins, only two of them exhibit protein–lipid interactions in rhodopsin, and both are located in the intradiscal side, exhibiting similar relative positions as those found for histidine or tyrosine. Finally, regarding nonaromatic residues with hydroxyl groups, the only serine and the two threonine residues present in the cytoplasmic side are located in the most external part of the density profile. In contrast, in the intradiscal side, the only threonine residue found is located in the central part of the diagram, whereas the three serine amino acids are widely distributed over the whole area.

These results suggest that the distribution of the amino acids involved in interactions with the lipid oxygens is indeed optimized according to each residue type, indicating that rhodopsin sequence, and probably that of other membrane proteins, may have evolved to make use of these preferred locations. These results also show that the majority of the hydrogen bonds identified between rhodopsin and the lipid oxygens lies in the cytoplasmic side. Moreover, considering that the activation of GPCRs involves the cytoplasmic loops bound to the G-proteins, the present results suggest that the existence of specific lipid–protein hydrogen bonds can be important to modulate loop conformations and, in turn, for the signal transduction process.

For all systems studied, most of the aromatic residues—tyrosine, histidine, and tryptophan—involved in hydrophobic interactions participate also in hydrogen bonds with the lipid oxygens. This finding agrees with recent results regarding the importance of this type of residues as anchoring hooks to the lipid bilayer.^{58,60} Previous studies of membrane proteins proposed that lysine and arginine residues may “snorkel” to the

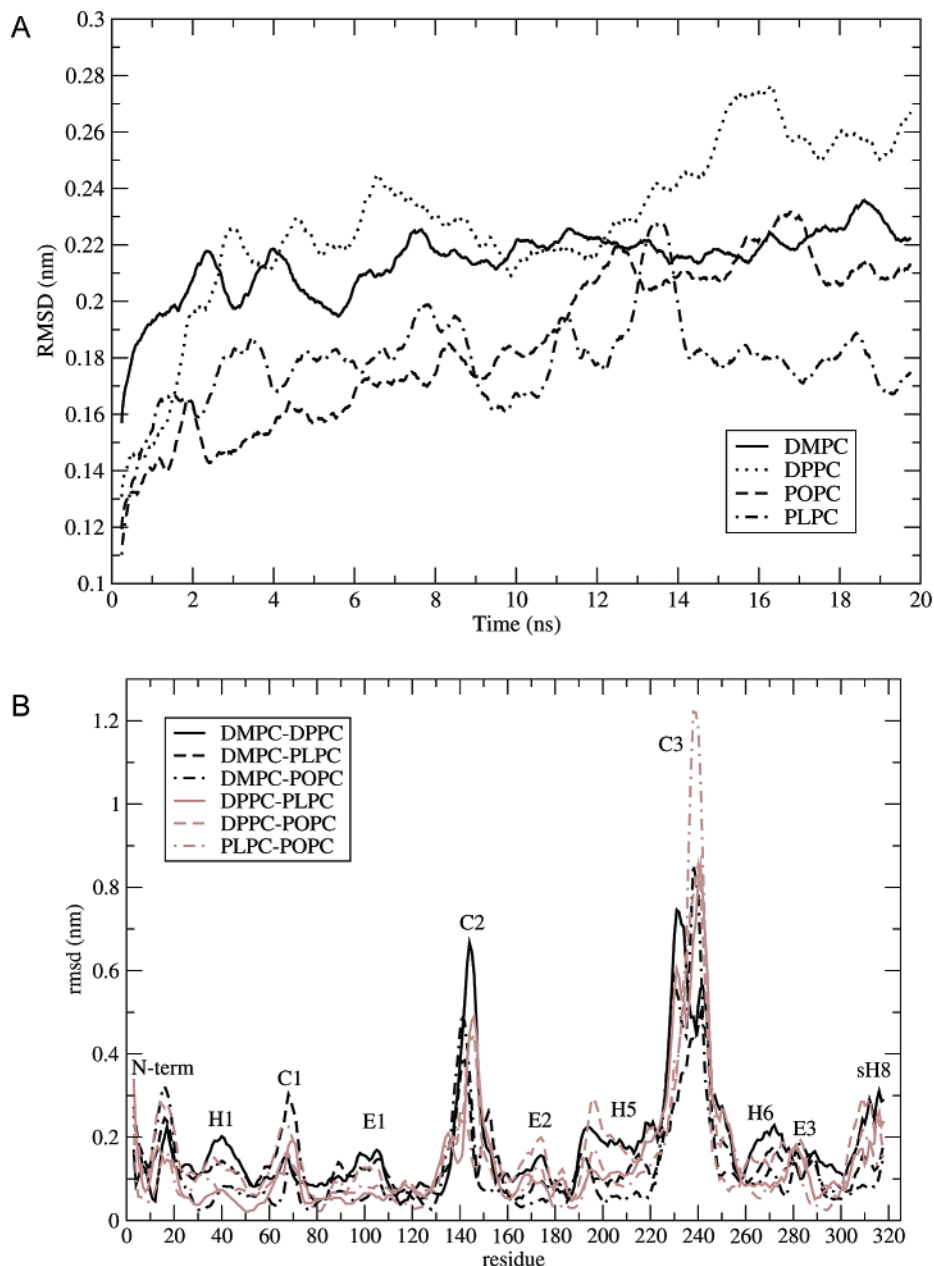


Figure 6. (A) Evolution of the root-mean-square deviations (rmsd) of the α -carbon atom subset from the starting structure excluding the C-terminal segment (see text). Lines are drawn using a running average over 0.5 ns. (B) Rmsd per residue between average structures obtained from the last 5 ns of each simulation.

lipid headgroups through charge–charge interactions with lipid head oxygens and hydrophobic interactions between their side chains and the lipid acyl chains. However, the number of hydrophobic interactions involving these residues in our study is small, suggesting a specific distribution of these residues in the direction of the bilayer normal either for rhodopsin or for GPCRs in general.

Protein Structure. Time evolution of the protein structure was monitored through the root-mean-square deviation (rmsd) from the starting structure measured on the $C\alpha$ skeleton. Because of the flexibility of the C-terminus, and since it is sensitive to the bilayer thickness close to the protein,³² the segment up to the palmitoylated cysteines was excluded from the calculations. The results are depicted pictorially in Figure 5 for the different systems studied. The different rmsd values range between 0.16 and 0.28 nm and can be considered as small taking into account the uncertainties of the X-ray structure used as starting point and the length of the simulations. However,

the fact that the rmsd values differ from one system to another suggests that lipids stabilize the starting structure in different manners or that each lipid type can modulate the protein structure in a different way.

Inspection of Figure 6A indicates that the rmsd decreases inversely to the number of insaturations with the lipid molecules. This agrees with the observation that the number of double bonds of the acyl chains increases the fluidity of the bilayer and helps in maintaining the crystal structure.⁵³ The largest rmsd values are found for the DPPC system, followed by the other unsaturated system, the DMPC one. In the latter case, the lower rmsd may be due to the requirement to keep an extended conformation to maximize the hydrophobic matching, which in turn reduces the flexibility of the hydrophobic chains around the protein. These results suggest that the complementarity between the bilayer thickness and the protein hydrophobic width, together with the intrinsic conformational profile of the lipid chains, affects protein structure.

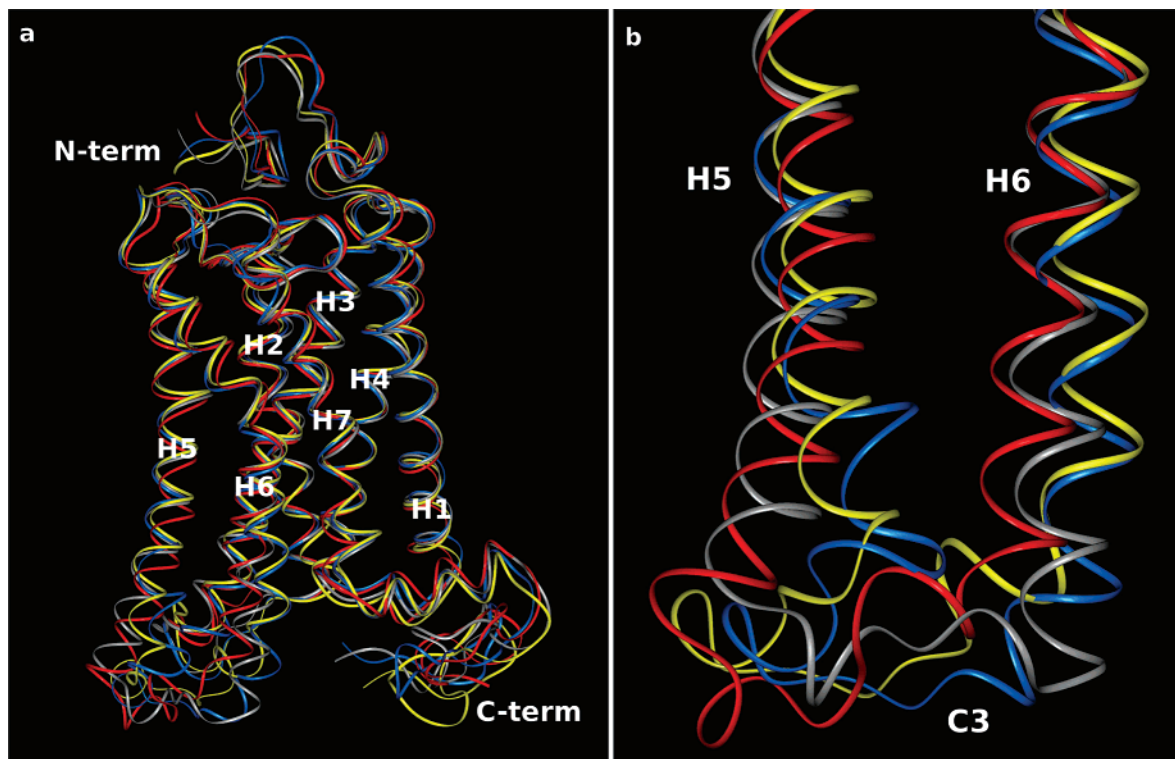


Figure 7. Trace superposition of the average protein structures computed from the last 10 ns of each simulation: (a) the α -carbons of the whole protein and (b) only the cytoplasmic ends of helices 5 and 6. The structures computed from each system are shown in different colors: DMPC (blue), DPPC (red), POPC (brown), and PLPC (yellow).

To assess the regions of the protein with a larger deviation from the initial structure, averages structures from the last 5 ns of each simulation have been produced. A trace superposition of these structures is shown in Figure 7a. Inspection of the figure reveals that the largest deviations, though small, are located in the cytoplasmic half of the protein, mainly in regions out of the TM segments, but also in the cytoplasmic halves of helices 5 and 6 (Figure 7b). On the contrary, the intradiscal side does not change much except in the N-terminus, where minor differences are observed. For a better characterization, the rmsd per residue has been computed and the results are displayed pictorially in Figure 6B. Inspection of this plot clearly highlights that the deviations are small in all cases except for the solvent exposed parts, that is, loops and terminal segments, but mainly on the second and third cytoplasmic loops. In the latter case, the deviations extend to the cytoplasmic halves of helices 5 and 6 in agreement with Figure 7b. However, despite being known that rhodopsin loops are not properly sampled in simulations of the length of the present one,^{63,64} the results suggest the active role of the lipid molecules in the modulation of these loops, which are involved in the interaction with G-proteins. The remaining segments of the protein exhibit rmsd values around 0.1 nm.

Transmembrane Helix Lengths and Secondary Structure.

The effects of the membrane structure on the secondary structure of rhodopsin were analyzed using the procedure described elsewhere.³² MD simulations allow the consideration of dynamic effects present in the secondary structure that cannot be observed in the crystals. Specifically, the evolution of the intrahelical hydrogen bonds among residues located on the TM helices was monitored, and the predominant interaction for each pair of residues was identified (Table 4). This analysis provides consensus boundaries for the TM helices, which is of great importance taking into account the existing discrepancies among the available crystallographic structures of rhodopsin. Specif-

ically, the largest ones are located on the cytoplasmic segments of helices 5 and 6 possibly because of crystal packing artifacts. As shown in Table 5, the consensus TM segments obtained are as follows: H1: 34–65; H2: 72–101; H3: 107–140; H4: 149–169; H5: 201–233; H6: 244–279; H7: 288–309; and sH8: 309–320, where H1–H7 are helices 1–7 and sH8 is the short helix 8 perpendicular to the bundle. Interestingly, the most significant discrepancies with the crystal structures are located on the cytoplasmic side of helices 4–7.

The results, shown in Table 4, highlight the existence discontinuities in the TM helices associated in most cases to the localization of helix kinks reported for the crystal structure.¹⁷ The kinks are known to improve the packing of the TM helices but also to play an important role during the activation process. Some of these kinks are proline-induced, with most of the prolines being conserved through the rhodopsin-like family of receptors: P170 and P171 in helix 4, P215 in helix 5, P267 in helix 6, and P302 in helix 7. Moreover, additional discontinuities are created, or previously existing ones are reinforced, with the existence of other types of helix-disrupting residues such as glycines or residues that are able to form additional hydrogen bonds competing with the $i - i + 4$ interactions that from an ideal α -helix such as threonine, serine, and histidine.⁶⁵

Specifically, the only discontinuity found in helix 1 is caused by the nonconserved P53 and is reinforced with the neighboring G51. In helix 2, the main distortion appears close to two consecutive glycine residues (G89–90) which favor that three neighboring threonine residues (T92–94) can participate in backbone hydrogen bonds.¹⁷ In helix 3, the discontinuity is found also at two consecutive glycine residues (G120–121) that are close to E113, the counterion of the protonated Schiff base. The conserved P170 and P171 induce discontinuities at the cytoplasmic end of helix 4, and therefore, they are not considered as part of this helix according to the previous criteria. The main discontinuities in helix 5 are associated to the

TABLE 4: Analysis of Intrahelical Hydrogen Bonding^a

H1	FEAFQYYLAE	34	PWQFSMLAAYMFLILMIGFPINFLTLVTVQH	65	KK
DMFC	----3----	3	AAAAAAAAAAAAAAAA--AAAAAAAA-----3	3	3-
DPFC	----3----	3	AAAAAAAAA3AAAA--AAAAAAAA-----3	3	--
PLFC	----3----	3	3AAAAAAAAAAAAAAAA--AAAAAAAA-----3	3	--
POFC	----3----	3	3AAAAAAAAAAAAAAAA--AAAAAAAA-----3	3	--
H2	LRTF	72	LNYILLNLAVADLFMVFGGFTTLTSLHG	101	YF
DMFC	--33		3AAAAAAAAAAAAAAAA--3AAAAA----	3	-3
DPFC	--33		3AAAAAAAAAAAAAAAA--3AAAAA3---	3	-3
PLFC	--33		AA3AAAAA33A-PA--3AAAAA3---	3	-3
POFC	--33		AAAAAAAAA33AAAA--3AAAAA3---	3	-3
H3	VFG	107	PTGCNLEGFATLGGELALWSLVVLAIERVVVC	140	KPMS
DMFC	--3		3AAAAAAAAAAAAA-AAAA3AAAAA3AA3AA----	3	--3-
DPFC	--3		AAAAAAAAAAAAA-AAA33AAAAA3A3-3A----	3	--3-
PLFC	--3		AAAA-AAAAAAAA-AAAA33AAAA33A--AA----	3	--3-
POFC	--3		AAAAAAAAAAAAA-AAAA333AAA33333A----	3	----
H4	NFRF	149	GENHAIMGVAFITWVMALCAA	169	PPLVGSRYI
DMFC	----		AAAAAA33AAAAAAA--3	A3	-----
DPFC	----		A-33AAA333AAAA3AA--3	A	-----
PLFC	----		A-3AAA-333AAAA3AA--3	A3	-----
POFC	----		AAAAAAA3AAAAA3AA--3	A	-----
H5	YYTPHEETNN	201	ESFVIYMFVVFHFIPLIVIFFCYGQLVFTVKEA	233	AAQQQ
DMFC	----33--33		3AAAAAAPP--AA3AAAAA33--3--PP-3-A	A3	----
DPFC	----33--33		AAAAAAAPP--A3333AAAAA-AA--3A---A	A3	----
PLFC	----33--3A		AAAAAAAPP--AAAAAAAAAAAAA-33A3A--3	33	----
POFC	----33--3		AAAAAAAPP--A33AAAAAAAAAAAAAAAAA3-A	A	----3
H6	ESATT	244	QKAEKEVTRMVIIMVIAFLICMLPYAGVAFYIFTHQ	279	GSDF
DMFC	-3A3A		A-33A333AAAAAAA-3A--AAAAAAAAA3--3-		----
DPFC	-3---		AAAAAA-3AAAAAAA--A--AAAAAAAAAAAA--3-		----
PLFC	-3AA-		A--3A333AAAAAAA--3--AAAAAAAAAAAA--3-		----
POFC	--333		AA3AAA33AAAAA3AA-3A--AAAAA3AAAA--3-		----
H7	GPIF	288	MTIPAFFAKTSAVYNPVIYIM	308	
DMFC	---3		AAAA3---3A--333AAA---		
DPFC	---3		AAAA3---3A--3-3AAA---		
PLFC	3A3-		AAAA3---3A--333AAA---		
POFC	AA33		AAAA3---3A--333AAA---		
sH8	309		MNKQFRNCMVTI	320	LCCGKNPLGD
DMFC			AAAA-3AA3---		-----
DPFC			AAAAAAA3---		-----33
PLFC			AAAA-AA3---		-----
POFC			AAAA-33A---		-----

^a 3, A, and P account for $i - i + 3$, $i - i + 4$, and $i - i + 5$ interactions, respectively. The fragments in bold show the consensus transmembrane segments including residues up to $i + 4$.

conserved P215 and also to H211. The conserved P267 together with the strongly retinal-coupled⁶⁶ W265 are responsible for the pronounced kink at the center of helix 6. Finally, T297 and S298, on one hand, and the conserved P303, on the other, induce the two discontinuities in helix 7. Interestingly, in all systems, helix 7 is by far the least ideal α -helix, with only eight pairs of $i - i + 4$ interactions among the 18 pairs. Moreover, this helix exhibits a strong propensity to form $i - i + 3$ interactions, with five pairs on average.

Some TM segments exhibit additional irregularities on relatively unstructured regions when comparing to an ideal α -helix which are lipid type dependent, affecting preferably the cytoplasmic sides of the helices. Accordingly, we observe alterations in some residues because of either the absence of intrahelical hydrogen bonds or the appearance of $i - i + 3$ interactions as the predominant ones which differ from one simulation to another. In helix 3, it involves a region close to W126 and another one around amino acids E134, R135, and Y136, which are part of the E(D)RY motif critical for activation. Interestingly, residues of the ERY motif lie at the cytoplasmic

end of this helix, exhibiting hydrogen bonds with the preceding $i - 3$ or $i - 4$ residues in all cases and with the following $i + 3$ and $i + 4$ only for some systems. A central region of helix 4 around G149, N151, H152, and G156 is also affected. Moreover, the differences are more important when looking at the cytoplasmic sides of both helices 5 and 6, consistent with the differences between the crystal structures available. The present results show that these regions are dynamic and that they alternate between $i - i + 4$, $i - i + 3$, $i - i + 5$, and no intrahelix interactions. Specifically, the region with irregularities in helix 5 is around G224 and T229 and in helix 6 around E247, which interacts with the R135 of the E(D)RY motif. Interestingly, within the segment corresponding to residues 244–252, there are no helix-disrupting amino acids, pointing to the existence of five charged residues on this segment (see Table 4) as responsible for the alterations on the secondary structure.

Another important feature of the analysis reported in Table 4 is the existence of structured segments at the boundary between the TM segments and loops. This can be clearly

TABLE 5: Percentage of Occurrence of Salt Bridges between Rhodopsin Residues in the Different Bilayer Systems Using a Cutoff of 0.4 nm

− residue	+ residue	DMPC	DPPC	PLPC	POPC
E5	NT R177 I2	0	24	64	13
E25	NT R21 NT	15	100	75	51
E113	H3 K296 H7	100	100	100	100
E134	H3 R135 H3	99	99	100	98
E150	H4 R147 C2	0	100	100	98
D190	I2 R177 I2	100	100	100	100
E232	C3 K231 C3	20	0	0	29
E232	C3 K245 H6	0	0	98	0
E239	C3 K248 H6	0	0	0	95
E239	C3 K141 C2	93	0	99	0
E247	H6 R135 H3	94	100	86	68
E249	H6 R252 H6	100	100	99	97
D330	CT R314 H8	59	0	0	0
D330	CT K311 H8	0	0	59	0
D331	CT K67 C1	0	0	94	0
D331	CT K311 H8	26	99	2	100
D331	CT R314 H8	46	0	0	0
E332	CT K311 H8	0	2	0	93
E341	CT K325 CT	40	1	0	0
A348	CT R147 C2	100	78	1	93

observed between residues 169–171 in helix 4 for all lipid types. The results indicate that the existence of these consecutive turns at these positions complements the short length of this helix, significantly smaller than the other helices and shorter than the one provided by the static crystal structures. Similar features can be observed in the regions of the third cytoplasmic loop closer to the cytoplasmic ends of helices 5 and 6, but the differences from one lipid type to another become larger.

In summary, the stable parts of the α -helices over the trajectory are not affected by the lipid type. On the contrary, those regions where the helices are less stable, that is, those with higher propensity to form $i - i + 3$, and to a less extent $i - i + 5$, or even to lose the intrahelical backbone hydrogen bond, are more sensitive to the lipid type and particularly to the specific conformations adopted by the lipid acyl chains.

Salt Bridges within Rhodopsin. The evolution of all feasible salt bridges in rhodopsin was monitored using a cutoff of 0.3 nm after identification of all possible polar residues involved. The results shown in Table 5 indicate that only 5 out of 20 pairs exhibit significant interactions independently of the bilayer type: E113-K297, E134-R135, D90-R177, E247-R135, and E249-R252. Interestingly, all these residues lie in the TM segments except the pair D90-R177, which involves two residues at the second intradiscal loop. Furthermore, most of

these interactions are structurally important: E113-K297 involves the protonated Schiff base and its counterion, and both E134-R135 and E247-R135 are known to play a key role in the activation of most GPCRs.⁶⁷ It is important to outline that the latter interaction exhibits different residence times within each system, suggesting the role of lipids in modulating rhodopsin structure and activation.

From all the interactions listed in Table 5, only three of them involve the intradiscal loops or the N-terminus. In contrast, the cytoplasmic loops together with the C-terminus are involved in 13 salt bridges. This asymmetry explains the larger root-mean-square fluctuations (rmsf) reported previously for the cytoplasmic side of rhodopsin than for the intradiscal.^{20,32} Moreover, the existence or not of interactions involving residues either at the second or the third cytoplasmic loops or at the C-terminal, the most flexible parts of the protein, has effects on the rmsf (data not shown). This has important implications since the regions that exhibit the largest rmsd between the average structures with the different systems (see Figure 5) correspond also to those with the largest rmsf. Specifically, the absence of the interaction between the charged C-terminal residue A348 and R147 at the second cytoplasmic loop in the PLPC simulation seems responsible for the larger deviations found in this region for this system. Similarly, the lower persistence of contacts between E247 at H6 and R135 at H3 in POPC may be responsible of the larger rmsf at the third cytoplasmic loop observed in simulation. Despite that the interactions involving residues at the C-terminus are not shared within the different systems, important interactions between the short helix 8 and the C-terminus can be observed in all cases. Specifically, the interactions involve two proximal positively charged residues in helix 8 (K311 and R314) and three consecutive negatively charged residues at the C-terminus (D330, D331, and E332). Therefore, the possible combinations of ionic pairs available allow the existence of multiple distinct conformations which can have functional implications. Similarly, the rmsd on the second cytoplasmic loop is smaller in the simulations exhibiting the interaction E150–R147. Moreover, the existence of an ionic lock between the second and the third cytoplasmic loops seems to retain the conformation of the former.

The analysis of the salt bridges in rhodopsin indicates that those observed in the cytoplasmic loops and the C-terminal segment are sensitive to the specific lipid bilayer, whereas the salt bridges buried in the protein core remain relatively unaltered. Moreover, the results suggest a possible role of lipids in the

TABLE 6: Tilt Angles for the Protein as a Whole and Tilt and Kink Angles for Each Specific Helix (H1–H7) in the Simulations and in the Crystal Structure 1GZM^a

tilts	H1 34–65	H2 72–101	H3 107–140	H4 149–169	H5 201–233	H6 244–279	H7 288–309	overall bundle
1GZM	25	19	24	12	23	16	20	
DMPC	21	17	21	14	20	13	19	8
DPPC	24	21	22	9	24	15	21	8
POPC	24	19	22	12	23	16	21	7
PLPC	22	19	22	13	23	13	20	16
kinks	H1 34–53–65	H2 72–92–101	H3 107–115–140	H4 149–160–169	H5 201–214–233	H6 244–264–279	H7 288–296–309	
kinks	15	25	8	6	11	34	29	
DMPC	17	11	7	6	11	39	23	
DPPC	19	10	15	6	25	48	30	
POPC	19	11	10	6	22	44	26	
PLPC	16	14	11	7	17	47	28	

^a Reference 17. The intervals indicate the residues considered.

modulation of the electrostatic lock at the cytoplasmic side of helices 3 and 6. The results support the idea that the different lipid–protein interactions provided by each bilayer type can modulate protein structure and function.

Protein Rigid-Body Motions. There is evidence that lipid composition and specifically the bilayer thickness can modulate the rigid-body orientation of the protein as a whole as well as the individual helices (or parts of it) relative to the direction perpendicular to the bilayer. Moreover, in lipid bilayers with a thickness shorter than the hydrophobic width of the protein, tilt is known to be a mechanism to improve the hydrophobic matching.^{5,68–70} To compare the effect of the different lipidic environments on the rigid-body motions of rhodopsin, the evolution of the protein tilt from the direction perpendicular to the bilayer has been computed for all the simulations. Specifically, the overall protein tilt was measured from the vector obtained by averaging the positions of the last eight residues of each TM helix on the two sides of the protein. The average tilt values shown in Table 6 range between 7 and 16°. These results indicate that there is a small change in the orientation as a consequence of the different lipidic environments. The largest tilt is observed for the PLPC system, consistent with the largest lipid–protein interaction energies described above.

The tilt angles for each individual helix were calculated from the vectors obtained considering the positions of the last eight residues at each TM helix end and were measured from the vector resulting after averaging the seven helices. The results, shown in Table 6, reveal small or negligible differences both between the average values in each simulation and when compared with the angles obtained in the crystal structure.¹⁷ Differences are always below 5°, indicating that lipids almost do not affect the orientation of the helices. Additionally, the kink angles were computed for each helix by defining two vectors analogously to tilts, on the basis of the discontinuities in the secondary structure described below, considering three residues at each helix end and three residues centered at the main discontinuity. The results indicate that some kinks are sensitive to the lipidic environment. Specifically, in all simulations, helices 2 and 6 exhibit differences when compared to the crystal structure (up to 15°), suggesting that the conditions required for the crystallization may affect the native conformation of these kinks. Moreover, despite that in some simulations helices 3, 5, and 7 exhibit kink angles similar to those in the crystal structure, the values differ up to 6–14° when comparing the simulations performed with different lipid types. Finally, the kinks in helices 1 and 4 remain in all cases relatively unaltered and close to the values of the crystal structure.

The largest tilt for the protein as a whole observed for the bi-unsaturated PLPC lipids is in good agreement with recent results from both experiments and MD simulations that evidenced the existence of lipid specificity on rhodopsin and that suggest a tight packing of the polyunsaturated chains to the helices.^{25,71} Moreover, despite recent MD simulations of model transmembrane peptides that suggest that under positive mismatch the system alleviates it predominantly by tilting the peptide and to a lower extent increasing lipid order in the vicinity of the peptide, the case of rhodopsin is different. Specifically, the system exhibiting the largest membrane–protein hydrophobic mismatch (DMPC) does not exhibit the largest tilt angles either for the protein or for the helices. This suggests a different mechanism for alleviating the positive mismatch in the case of proteins than for small peptides. It has been shown below that the polar protein residues involved in hydrogen bonds with the lipid oxygens are located on two rings on each side of the protein

(see Figures 4 and 5). Roughly speaking, if we consider that both peptides and GPCRs can be approximated by cylinders, the much larger radius of rhodopsin would fail to allocate properly the ring of polar residues for large tilt angles without losing the hydrogen bonds with the lipid oxygens. On the contrary, the negligible radius of an α -helix peptide when compared to a seven- α -helix bundle membrane spanning protein such as rhodopsin allows keeping these interactions independently of the tilt angle. Thus, the results suggest that, despite that the contribution of the LJ term to the lipid–protein interactions is the largest, the electrostatic one is responsible for restraining the relative orientation of the protein to the bilayer.

Conclusions

The present work addresses the effect of lipid composition on the structural features of rhodopsin. For this purpose, four 20 ns MD trajectories of different one-component lipid bilayers were carried out. The systems included four phospholipid types with a phosphatidylcholine head and different acyl chains. Specifically, two bilayers with saturated lipids, DMPC and DPPC, and two bilayers with unsaturated lipids, POPC and PLPC, were considered for the present study.

The results show that on the one hand, lipids can modulate the structure of rhodopsin by affecting the tilt of the protein as a whole and the rigid-body motions involving helix kinks. However, the helix tilts as well as the secondary elements of the protein are not much affected by the lipidic environment, with the TM helices remaining relatively unaltered, and with only the least structured elements showing sensitivity to the lipid type. On the other hand, the protein infers an ordering effect over the lipid bilayer that depends on the difference between the equilibrium thickness of the former and the hydrophobic thickness of the latter, as can be observed in the variation of the bilayer thickness with the distance from the protein. Moreover, lipids with saturated acyl chains exhibit a poorer adaptation to the protein than lipids with unsaturated chains. Similarly, short acyl chains also exhibit an impaired matching because of the extended conformations that are forced to adopt to accommodate to the hydrophobic protein surface.

The analysis of lipid–protein interaction energies together with the study of the specific protein–lipid contacts shows differences between the systems studied. Regarding the hydrophobic interactions, the analysis of the specific lipid–protein contacts revealed that almost a third of the rhodopsin residues participate in interactions with the surrounding lipids, including amino acids phenylalanine, leucine, isoleucine, and valine which exhibit the largest number of contacts. Regarding the electrostatic contribution, the analysis of hydrogen bonds between protein donors and lipid oxygens revealed the importance of these interactions for the anchoring of the protein to the membrane. In the four systems, residues R252, K339, Y96, Y274, H152, and T108—and to a lower extent K66, R69, Y136, Y223, and W35—are found to participate in hydrogen bonds with lipid molecules and, therefore, they can be considered to be putative hooks of the protein to the bilayer. Of remarkable interest is the finding that the localization of these interactions is asymmetric regarding the two halves of the protein, suggesting that the cytoplasmic side of the protein is much more sensitive to the lipidic environment. Moreover, the analysis of salt bridges in rhodopsin revealed that lipids modulate the conformations of the cytoplasmic loops as well as the C-terminus. The results suggest a role of the lipid composition in modulating the electrostatic lock on the cytoplasmic side of helices 3 and 6.

Acknowledgment. A.C. wishes to express his gratitude to the Technical University of Catalonia for a fellowship to undertake his doctoral studies. We thank to the Biocomputing group of Dr. Peter Tieleman, at the University Of Calgary, for sharing their structure and topology files for lipids. The Spanish Ministry of Science and Technology supported this work through Grant No. SAF2005-08148-C04-01.

References and Notes

- (1) White, S. H.; Wimley, W. C. *Annu. Rev. Biophys. Biomed.* **1999**, *28*, 319.
- (2) Singer, S. J.; Nicolson, G. L. *Science* **1972**, *175*, 720.
- (3) Engelman, D. M. *Nature* **2005**, *438*, 578.
- (4) Jensen, M. O.; Mouritsen, O. G. *Biochim. Biophys. Acta* **2004**, *1666*, 205.
- (5) Kandasamy, S. K.; Larson, R. G. *Biophys. J.* **2006**, *90*, 2326.
- (6) Goodyear, D. J.; Sharpe, S.; Grant, C. W.; Morrow, M. R. *Biophys. J.* **2005**, *88*, 105.
- (7) Nymeyer, H.; Woolf, T. B.; Garcia, A. E. *Proteins* **2005**, *59*, 783.
- (8) Leontiadou, H.; Mark, A. E.; Marrink, S. J. *J. Am. Chem. Soc.* **2006**, *128*, 12156.
- (9) Yandek, L. E.; Pokorny, A.; Floren, A.; Knoelke, K.; Langel, U.; Almeida, P. F. *Biophys. J.* **2007**.
- (10) Yeagle, P. L.; Bennett, M.; Lemaitre, V.; Watts, A. *Biochim. Biophys. Acta* **2006**.
- (11) Archer, E.; Maigret, B.; Escricuet, C.; Pradayrol, L.; Fourmy, D. *Trends Pharmacol. Sci.* **2003**, *24*, 36.
- (12) Ellis, C. *Nat. Rev. Drug Discovery* **2004**, *3*, 575.
- (13) Attwood, T. K.; Findlay, J. B. *Protein Eng.* **1994**, *7*, 195.
- (14) Palczewski, K.; Kumasaka, T.; Hori, T.; Behnke, C. A.; Motoshima, H.; Fox, B. A.; Le, Trong, I.; Teller, D. C.; Okada, T.; Stenkamp, R. E.; Yamamoto, M.; Miyano, M. *Science* **2000**, *289*, 739.
- (15) Teller, D. C.; Okada, T.; Behnke, C. A.; Palczewski, K.; Stenkamp, R. E. *Biochemistry* **2001**, *40*, 7761.
- (16) Okada, T.; Fujiyoshi, Y.; Silow, M.; Navarro, J.; Landau, E. M.; Shichida, Y. *Proc. Natl. Acad. Sci. U.S.A.* **2002**, *99*, 5982.
- (17) Li, J.; Edwards, P. C.; Burghammer, M.; Villa, C.; Schertler, G. F. *X. J. Mol. Biol.* **2004**, *343*, 1409.
- (18) Okada, T.; Sugihara, M.; Bondar, A. N.; Elstner, M.; Entel, P.; Buss, V. *J. Mol. Biol.* **2004**, *342*, 571.
- (19) Huber, T.; Botelho, A. V.; Beyer, K.; Brown, M. F. *Biophys. J.* **2004**, *86*, 2078.
- (20) Crozier, P. S.; Stevens, M. J.; Forrest, L. R.; Woolf, T. B. *J. Mol. Biol.* **2003**, *333*, 493.
- (21) Saam, J.; Tajkhorshid, E.; Hayashi, S.; Schulten, K. *Biophys. J.* **2002**, *83*, 3097.
- (22) Lemaitre, V.; Yeagle, P.; Watts, A. *Biochemistry* **2005**, *44*, 12667.
- (23) Feller, S. E.; Gawrisch, K.; Woolf, T. B. *J. Am. Chem. Soc.* **2003**, *125*, 4434.
- (24) Pitman, M. C.; Grossfield, A.; Suits, F.; Feller, S. E. *J. Am. Chem. Soc.* **2005**, *127*, 4576.
- (25) Grossfield, A.; Feller, S. E.; Pitman, M. C. *Proc. Natl. Acad. Sci. U.S.A.* **2006**, *103*, 4888.
- (26) Berman, H. M.; Westbrook, J.; Feng, Z.; Gilliland, G.; Bhat, T. N.; Weissig, H.; Shindyalov, I. N.; Bourne, P. E. *Nucleic Acids Res.* **2000**, *28*, 235.
- (27) Fahmy, K.; Jager, F.; Beck, M.; Zvyaga, T. A.; Sakmar, T. P.; Siebert, F. *Proc. Natl. Acad. Sci. U.S.A.* **1993**, *90*, 10206.
- (28) Sandberg, L.; Edholm, O. *Proteins* **1999**, *36*, 474.
- (29) Berendsen, H. J. C.; van der Spoel, D.; van Drunen, R. *Comput. Phys. Commun.* **1995**, *91*, 43.
- (30) Lindahl, E.; Hess, B.; van der Spoel, D. *J. Mol. Model.* **2001**, *7*, 306.
- (31) Lindahl, E.; Edholm, O. *Biophys. J.* **2000**, *79*, 426.
- (32) Cordomi, A.; Edholm, O.; Perez, J. J. *J. Comput. Chem.* **2007**, *28*, 1017.
- (33) Berendsen, H. J. C.; Postma, J. P. M.; DiNola, A.; Haak, J. R. *J. Chem. Phys.* **1984**, *81*, 3684.
- (34) Miyamoto, S.; Kollman, P. A. *J. Comput. Chem.* **1992**, *13*, 952.
- (35) Darden, T.; York, D.; Pedersen, L. *J. Chem. Phys.* **1993**, *98*, 10089.
- (36) Jorgensen, W. L.; Maxwell, D. S.; TiradoRives, J. *J. Am. Chem. Soc.* **1996**, *118*, 11225.
- (37) Berger, O.; Edholm, O.; Jähnig, F. *Biophys. J.* **1997**, *72*, 2002.
- (38) Nagle, J. F.; Tristram-Nagle, S. *Biochim. Biophys. Acta* **2000**, *1469*, 159.
- (39) Hofsass, C.; Lindahl, E.; Edholm, O. *Biophys. J.* **2003**, *84*, 2192.
- (40) Wohler, J.; Edholm, O. *Biophys. J.* **2004**, *87*, 2433.
- (41) Bachar, M.; Brunelle, P.; Tieleman, D. P.; Rauk, A. *J. Phys. Chem. B* **2004**, *108*, 7170.
- (42) Jorgensen, W. L.; Chandrasekhar, J.; Madura, J. D.; Impey, R. W.; Klein, M. L. *J. Chem. Phys.* **1983**, *79*, 926.
- (43) Hayashi, S.; Tajkhorshid, E.; Schulten, K. *Biophys. J.* **2002**, *83*, 1281.
- (44) Hofsäb, C.; Lindahl, E.; Edholm, O. *Biophys. J.* **2003**, *84*, 2192.
- (45) Kucerkä, N.; Liu, Y. F.; Chu, N. J.; Petrace, H. I.; Tristram-Nagle, S. T.; Nagle, J. F. *Biophys. J.* **2005**, *88*, 2626.
- (46) König, B.; Dietrich, U.; Klöse, G. *Langmuir* **1997**, *13*, 525.
- (47) Mukhopadhyay, P.; Monticelli, L.; Tieleman, D. P. *Biophys. J.* **2004**, *86*, 1601.
- (48) Anézo, C.; de Vries, A. H.; Holtje, H. D.; Tieleman, D. P.; Marrink, S. J. *J. Phys. Chem. B* **2003**, *107*, 9424.
- (49) Böckmann, R. A.; Grubmüller, H. *Angew. Chem., Int. Ed.* **2004**, *43*, 1021.
- (50) Böckmann, R. A.; Hac, A.; Heimburg, T.; Grubmüller, H. *Biophys. J.* **2003**, *85*, 1647.
- (51) Pandit, S. A.; Bostick, D.; Berkowitz, M. L. *Biophys. J.* **2003**, *84*, 3743.
- (52) Seelig, A.; Seelig, J. *Biochemistry* **1977**, *16*, 45.
- (53) Stillwell, W.; Wassall, S. R. *Chem. Phys. Lipids* **2003**, *126*, 1.
- (54) Holte, L. L.; Peter, S. A.; Sinnwell, T. M.; Gawrisch, K. *Biophys. J.* **1995**, *68*, 2396.
- (55) Klein-Seetharaman, J.; Reeves, P. J.; Loewen, M. C.; Getmanova, E. V.; Chung, L.; Schwalbe, H.; Wright, P. E.; Khorana, H. G. *Proc. Natl. Acad. Sci. U.S.A.* **2002**, *99*, 3452.
- (56) Deol, S. S.; Bond, P. J.; Domene, C.; Sansom, M. S. *Biophys. J.* **2004**, *87*, 3737.
- (57) Bond, P. J.; Sansom, M. S. *J. Am. Chem. Soc.* **2006**, *128*, 2697.
- (58) Mishra, V. K.; Palgunachari, M. N.; Segrest, J. P.; Anantharamaiah, G. M. *J. Biol. Chem.* **1994**, *269*, 7185.
- (59) Saiz, L.; Bandyopadhyay, S.; Klein, M. L. *J. Phys. Chem. B* **2004**, *108*, 2608.
- (60) Strandberg, E.; Killian, J. A. *FEBS Lett.* **2003**, *544*, 69.
- (61) Tieleman, D. P.; Forrest, L. R.; Sansom, M. S.; Berendsen, H. J. *Biochemistry* **1998**, *37*, 17554.
- (62) Grossfield, A.; Woolf, T. B. *Langmuir* **2002**, *18*, 198.
- (63) Faraldo-Gomez, J. D.; Forrest, L. R.; Baaden, M.; Bond, P. J.; Domene, C.; Patargias, G.; Cuthbertson, J.; Sansom, M. S. *Proteins* **2004**, *57*, 783.
- (64) Grossfield, A.; Feller, S. E.; Pitman, M. C. *Proteins* **2007**, *67*, 31.
- (65) Ballesteros, J. A.; Shi, L.; Javitch, J. A. *Mol. Pharmacol.* **2001**, *60*, 1.
- (66) Crocker, E.; Eilers, M.; Ahuja, S.; Hornak, V.; Hirshfeld, A.; Sheves, M.; Smith, S. O. *J. Mol. Biol.* **2006**, *357*, 163.
- (67) Ballesteros, J. A.; Jensen, A. D.; Liapakis, G.; Rasmussen, S. G.; Shi, L.; Gether, U.; Javitch, J. A. *J. Biol. Chem.* **2001**, *276*, 29171.
- (68) Killian, J. A. *FEBS Lett.* **2003**, *555*, 134.
- (69) Lee, A. G. *Biochim. Biophys. Acta* **2003**, *1612*, 1.
- (70) Venturoli, D.; Rippe, B. *Am. J. Physiol.: Renal* **2005**, *288*, F605.
- (71) Soubias, O.; Teague, W. E.; Gawrisch, K. *J. Biol. Chem.* **2006**, *281*, 33233.

Structural rearrangements of rhodopsin subunits in a dimer complex: a molecular dynamics simulation study

Cordomí A, Perez JJ

J Mol Graph Model., 2008 Submitted.

Structural rearrangements of rhodopsin subunits in a dimer complex: a molecular dynamics simulation study

Arnau Cordermí and Juan J. Perez*

Dept d'Enginyeria Química, Technical University of Catalonia (UPC), ETS d'Enginyeria Industrial, Av. Diagonal 647, 08028 Barcelona, Spain;

ABSTRACT

The present work reports a 0.1 μ s molecular dynamics simulation of a bovine rhodopsin dimer based on a recently reported semi-empirical model obtained by fitting two monomers from the crystal structure to atomic force microscopy maps [Fotiadis et al. *Curr. Op. Struct. Biol.* 16:252, 2006]. The simulation provides a refined arrangement of the dimer for the model that takes into account the adaptations on the structure because of the direct exposure between the trans-membrane helices TM4 and TM5 in the context of a realistic environment with the use of explicit water molecules and a dipalmitoyl phosphatidylcholine lipid bilayer. Additionally, the comparison with an additional 0.1 μ s simulation of a single monomer allows the study the subunit-subunit interactions on the dimer interface together with the possible structural effects associated to the dimer formation. The present study describes the dimer interface at an atomistic level including an analysis of the energy contributions to the interaction of each part of the protein involved. We also compare the differences in the structure of the single monomer with those of the dimer subunits with the aim of understanding the changes required for the dimer formation.

INTRODUCTION

Rhodopsin is a key photoreceptor protein involved in the signaling process that eventually converts a photon into visual response. It belongs to one of the largest family of proteins in the human genome embodying about 2 % of the genes expressed: the G-protein coupled receptors (GPCR). These proteins play a key role in the transmission of cell signals and in the regulation of basic physiological processes. GPCR are embedded in the cellular membrane and are arranged in a characteristic seven helix bundle structure that defines a site for binding specific ligands that trigger the receptor activation process. In the case of rhodopsin, this site is occupied by a chromophore, the 11-*cis* retinal, which is covalently linked to residue K296 of transmembrane (TM) helix 7 via a protonated Schiff base. Photoactivation of the receptor by light absorption induces isomerization of the 11-*cis*-retinal to its all-*trans* configuration resulting in a conformational change of the receptor that originates a cascade of biochemical reactions known as visual phototransduction: the main molecular mechanism of the visual process.

Being the only member of the family with an atomistic structure available,¹⁻³ bovine rhodopsin has become the prototype GPCR and therefore, it has been largely studied. Early biophysical experiments described rhodopsin as a mobile monomer^{4,5} in line with the classical view of a freely diffusing particle in a fluid membrane model.⁶ However, in recent years there has been increasing evidence suggesting that GPCR may exist and function as homo- and heterodimers/oligomers⁷ as is discussed in many recent re-

ports.⁷⁻¹⁷ Indeed, the crystal structures of rhodopsin^{3,18,19} were solved as a dimer, although in a non-physiological orientation.²⁰ The most direct demonstration about the propensity of GPCR to form dimers is the recent atomic force microscopy (AFM) study of native disk membranes from rod outer segments, which provided large paracrystalline arrays of subunits under native conditions.^{21,22} By fitting the crystal structure of rhodopsin to the AFM map, the authors obtained an atomistic semi-empirical model of a rhodopsin oligomer in groups of two subunits interacting through their TM4 and TM5 helices. These and other domains involved in the dimerization reported for a variety of GPCR have recently been reviewed.⁸ Nevertheless, with the recent finding that each rhodopsin molecule binds its own signaling protein,²³ it is yet unclear whether the oligomerization is required or not for a proper function and signaling.^{11,23-30}

Despite the importance of the availability of several atomistic structures of rhodopsin, since they have been obtained using x-ray diffraction studies, it cannot be inferred from the structure the role of its natural environment. Thus, the study of rhodopsin with other techniques that can provide structural information in conditions closer to its native environment is of great interest. An emerging group of such methods applied in this context is represented by

keywords: membrane protein, GPCR, dimerization, MD simulations, lipid bilayers, GROMACS.

title running head: Adaptation between rhodopsin dimer subunits

abbreviations: AFM: atomic force microscopy; CT: C-terminus; Cx: cytoplasmic loop x; Ex: extracellular loop x; GPCR: G-protein coupled protein receptor; LJ: Lennard Jones, MD: molecular dynamics; NT: N-terminus; TM: transmembrane.

*To whom correspondence should be addressed. Phone: +34 934016679. Fax: +34 934017150. E-mail: juan.jesus.perez@upc.edu;

computer simulations^{31,32} and more specifically, molecular dynamics (MD) applied to sampling proteins embedded on different model lipid bilayers.^{33,34} Several recent reports based on MD calculations of the rhodopsin monomer have successfully provided information on the structural features of the protein and about its dynamical behavior that cannot be deduced from experimental data.³⁵⁻⁴² Therefore, it is reasonable to expect that MD can be useful in the study of the conformational arrangement of the dimer and provide information about the local rearrangement between subunits. In this direction, the first simulations of rhodopsin dimers and oligomers embedded in model membranes have been reported, including a 0.5 ns trajectory of an hexamer soaked in a stearyl-docosahexenoyl phosphatidylcholine lipid bilayer (SDPC) with and implicit solvent⁴³ and a 45 ns simulation of a dimer embedded in a palmitoyl-oleoyl phosphatidylcholine (POPC) with explicit water molecules.⁴⁴ In the present work we report the analysis of a 0.1 μ s atomistic MD simulation of a rhodopsin dimer embedded in a dipalmitoyl phosphatidylcholine (DPPC) lipid bilayer with water and electrolytes. These results have been compared with an additional trajectory of a rhodopsin monomer run in parallel using the same protocols. The results reported in the present work may provide new insights into the understanding of the dimer interface at an atomistic level as well as in the structural effects of the dimer formation.

METHODS

Molecular system

The coordinates of each rhodopsin molecule were taken from the first subunit of entry 1GZM² of the Protein Data Bank.⁴⁵ In addition, coordinates of the atoms of some missing C-terminal (CT) residues were taken from a different source¹⁸ and adapted by superposition of the α -carbon skeleton of both protein structures. Accordingly, the starting protein structure contained the whole sequence including the acetyl group of the N-terminus (NT). With the aim of assessing the putative role of two palmitoyl chains bonded to cysteines 322 and 323 as membrane anchoring point, they were included only in one of the monomers. All possibly charged amino acids were considered as charged except D83 and E122, since there is experimental evidence that these residues are protonated.⁴⁶ Moreover, these residues are located in the hydrophobic core and have no counter charge available in their neighborhood. The initial structure of the dimer was generated by superposing the structure of two monomers to a recently reported semi-empirical dimer model²¹ deposited in the Protein Data Bank with entry 1N3M, constrained to exhibit TM4 and TM5 helices in the protein-protein interface.

The protocol used to construct the monomer has been described in a previous report.⁴² In the case of the dimer, a larger box was required with initial dimensions 11.3x15.3x11.4 nm³. Specifically, it was embedded into a previously equilibrated rectangular box containing 570 DPPC lipids, 37300 water molecules and sodium and chloride ions, to obtain the physiologic ion concentration of 0.2 M in NaCl. Such box was obtained by replicating a DPPC bilayer with water and salt from a previous work,⁴² which had been derived from the results of a pure bilayer.⁴⁷ The procedure used for placing the protein and the subse-

quent removal of lipid and water molecules has been described elsewhere.^{41,42} In a subsequent step the balance between sodium and chloride ions was adjusted in order to obtain a totally electro neutral system by replacing water molecules by sodium and chloride ions according to the strongest electrostatic potential, taking the net charge of the dimer (-6) into account. In the case of the dimer the final system ended with 35400 water molecules, 451 lipids and 130 sodium and 124 chloride ions. Although the system is intended to reproduce physiologic ion concentrations, it should be stressed that in simulations with a single bilayer and periodic boundary conditions it is not possible to have different intra- and extra-cellular ionic concentrations as in biological organisms.

MD simulations

MD simulations were performed using a parallel version of the GROMACS 3.2 package.^{48,49} The all-atom OPLS force field⁵⁰ currently implemented in GROMACS 3.2 was used for all molecules of the system except for DPPC lipids, that were modeled using the Berger set of parameters previously,⁵¹ which reproduce most properties of pure bilayer. Water molecules were modeled using the TIP3P set of parameters.⁵² Retinal charges were taken from quantum chemical calculations⁵³ and have already been used satisfactorily in other rhodopsin MD simulations.^{36,41,42} For palmitoylated cysteines, fractional charges were computed from electrostatic potential calculations at HF/6-31G* level and further adapted to neutral group charges in a similar manner to standard amino acids in the OPLS-AA force-field.

All systems were subjected to periodic boundary conditions in the three directions of the Cartesian space. Simulations were performed at 323 K so that the DPPC lipids remained above the gel/liquid crystalline phase transition temperature. The temperature was kept constant using separate thermostats for protein, water, ions and lipids, respectively.⁵⁴ Although this temperature is higher than the physiological, it does not alter significantly protein structure since longer times than nanoseconds of simulation would be required for this purpose.^{41,42} The coupling time constants for all thermostats were 0.1 ps, except for water that was 0.01 ps. The integration of motion equations was performed using the leap frog algorithm with a time step of 2 fs. All bonds in the protein and lipids were frozen using the LINCS⁵⁵ algorithm. Bond lengths and angles for water were held constant using the analytical SETTLE method.⁵⁶ A plain cutoff of 1.0 nm was used to compute Lennard-Jones interactions and the PME method in the case of the electrostatic interactions,⁵⁷ with the neighbor list was updated every 10 steps. Prior to the production runs each system was energy minimized, and the gap between the protein and lipid and water molecules was removed running a 500 ps MD simulation, with protein coordinates strongly restrained to the initial structure.

Analysis of trajectories

The analysis of trajectories has been performed using the tools included in GROMACS package together with our own programs and scripts. For the determinations of helix tilts and kink angles, each helix or fragment was considered as an independent axis (1 for tilts and 2 for kinks) defined by the center of mass of 8 or 3 C α at their ends for tilts and kinks, respectively. The bundle tilt of each rhodopsin relative to the direction per-

pendicular to the bilayer was determined by considering the centers of mass of the last 8 C α on the two sides of each TM helix. The kink points were chosen according to a previous work as TM1:53, TM2:92, TM3:115, TM4:160, TM5:214, TM6:264, TM7:296.⁴²

Helix definitions

Two different criteria are used in order to define the lengths of the helices along this report. For the computation of geometrical features -including distances, tilts and kinks- helix limits were taken from the maximum common segments between the single monomer and dimer subunits A and B according to a secondary structure analysis analogous to a previous one⁴² as TM1:35-65, TM2:73-101, TM3:109-136, TM4:149-169, TM5:201-226, TM6:249-277 and TM7:288-308. However, since these limits are somehow strict, for the computation of energies of interaction they were enlarged up to the segments defined in the crystal structure² as TM1:34-65, TM2:71-101, TM3:106-140, TM4: 149-173, TM5:200-230, TM6:241-277, TM7: 286-309 and short helix 8:311-321. The locations of residues in all tables and figures refer to the second numbering.

RESULTS AND DISCUSSION

Global stability of the protein

The structure of the dimer at the end of the 0.1 μ s MD trajectory is shown in Figure 1 A. Interestingly, the quaternary structure of the dimer did not change much from the initial structure, i.e.: the semi-empirical model based on the paracrystal and the X-ray structure for the monomer.²² Specifically, each of the TM4 helices remains in close contact with the intradiscal segment of TM5 and with the cytoplasmic segment of TM3 of the complementary subunit. Additionally, the C2 and the E2 loops of the two subunits remain in close contact. This result indicates that protein packing is preserved in the environment of a DPPC lipid bilayer, similarly to what has already been reported in recent MD simulations of rhodopsin dimers or oligomers with one-component lipid bilayers.^{43,44}

The superposition of the C α chains between each of the dimer subunits A and B and that of the isolated monomer is depicted pictorially in Figure 1 B, showing that all the structures are similar except for the third cytoplasmic loop (C3) together with the adjacent cytoplasmic ends of the neighboring helices TM5 and TM6. However, it is precisely this region that exhibits the largest discrepancies between the different crystal structures available.^{2,3,18,19} Furthermore, subunits A and B exhibit a remarkable asymmetry in the conformation of C3, although within the conformational space covered by the crystal structures. These results stress the effect of the different environment provided by lipids, detergent molecules and other subunits.

Time evolution of the root mean square deviation (rmsd) as measured from the C α skeleton, taking the starting structure as reference is shown in Figure 2 A. The CT segment 322-348 has been omitted in the calculations due to its high mobility that would create noise to the results. In regard to the dimer simulation, the plot shows that the rmsd computed for each subunit separately reach a steady value of about 0.25 nm after 40 ns of simulation, indicating that the tertiary

structure is well preserved during the entire simulation. In contrast, the value for the dimer reaches a steady value later, after 60 nm of the simulation and is much higher: about 0.40 nm, indicating additional small changes in the relative orientation between the subunits. However, the arrangement of the helix bundles is qualitatively close to the initial model (see Figure 1 A). These values of rmsd are in agreement with the results of a recent simulation of the rhodopsin dimer in a POPC bilayer.⁴⁴ The rmsd of the protein in the single monomer simulation exhibits a larger value than the dimer subunits, providing a clear evidence of some stabilization of the protein structure with the dimer formation.

For a clearer monitoring of the deviations, Figure 2 B displays the rmsd computed for each C α . As can be seen, the largest deviations are located on the CT, the cytoplasmic loops C3 and C2 and finally, parts of the intradiscal loop E2 and of the NT -in decreasing importance- both in the dimer subunits and in the monomer. The profile of rmsd found agrees well with the reported in other simulations of rhodopsin monomers with different model lipid bilayers.^{37,42} The peak corresponding to the C3 loop has a clear asymmetry in the localization of the maximum in the dimer, which is clearly related to the different conformations obtained. This appears to be driven by small fluctuations on the conformation of the third cytoplasmic loops (C3) due to the direct interaction between the C2 loops (see insets in Figure 1 B). The cumulative rmsd deviations obtained by integrating the area under the peaks is shown in the bottom panel of Figure 2 B and helps to characterize those regions with the largest differences from one subunit to another. Thus, whereas dimer subunits A and B exhibit a similar profile, the single monomer exhibits clearly much larger deviations in the C3 loop and in the CT. It is interesting to note that the existence (in subunit A) or absence (in subunit B) of the palmitoylated cysteines at positions 322 and 323 (see methods) provides no difference in the rmsd, suggesting that, although these moieties are important for anchoring the protein to the bilayer, their might not be necessary to maintain the protein folding.

Finally, the root mean square fluctuations (rmsf) per residue during the last half of the simulation, computed from an average structure obtained from the same time of simulation are shown in Figure 2 C, indicating that the mobility of the protein is sensitive to the dimer formation. This is significant in the case of the C3 loops, which fluctuate in the dimer structure due to a destabilizing effect associated with the C2-C2 interaction that alters the C2-C3 contacts of the single monomer. The dimerization provided also decreased peaks in the NT and E2 regions of subunit A together with a larger E2 peak in subunit B which are probably related to the E2-E2 interactions between subunits. The B-factors of the x-ray structures exhibit two prominent peaks in the region of the C2 and C3 loops^{2,3,18,19} which coincided with the rmsf from recent 20 ns simulations of rhodopsin monomers.⁴¹ However, with the larger length of the present simulations the peak corresponding to C2 either for the monomer or for both dimer subunits is much lower than previously described. On the contrary larger fluctuations are observed at the NT region with the maximum at residues 16-18.

The time-evolution of the intra-helix backbone interactions (Figure 3) reveals no significant differ-

ences in the secondary structure when comparing each of the dimer subunits with the monomer. Each system exhibits about 185 pairs of residues forming $i,i+n$ interactions (with $n=3, 4$), 115 of $i,i+4$ type and 70 of $i,i+3$ type (consecutive $i,i+4$ or $i,i+3$ would give an α - or 3^{10} -helix, respectively). However, the results indicate a reduction of the number of backbone interactions associated with helical structures and also a decrease in the number of $i,i+4$ interactions with a consequent increase of those of $i,i+3$ type. This indicates that the protein exhibits shorter and less 'ideal' TM helices when embedded in a DPPC bilayer than observed in the crystal structure.^{2,3,18} Specifically, small changes can be observed in the cytoplasmic parts of segments TM3, TM5 and TM6 as it is shown in Figure 1 B. Similar results were obtained in a previous work.⁴¹

For each subunit, the internal salt bridges observed within a cutoff of 4.0 nm during the last 50 ns of the corresponding trajectories are listed in Table 1 A. The interactions exhibiting the longest interaction times are those previously observed in MD simulations of rhodopsin monomers⁴²: E113-K296, E134-R135, R135-E247, R177-D190 and E249-R252. However, interactions involving residues located in the C2 and C3 loops or in the CT exhibit large differences from one system to another, indicating that their formation depends on the different conformation of each of the rhodopsin monomers. These results suggest that the dimerization can favor the formation of specific salt-bridges not observed in the single monomer -such as E232-K248 and D330-R134-, but also generates an asymmetry between the two subunits in regard to these interactions. Finally, an important result obtained is that dimerization modulates the formation of salt-bridges that are associated to the GPCR activation such as E134-R135 and R135-E247 (see ref. 58,59 and therein), providing a direct evidence of a possible cooperative mechanism involving protein activation. A similar effect has also been described associated with the nature of lipids surrounding the protein.⁴² Furthermore, both E134 and E247 participate in additional salt-bridges involving subunit B (E134-R147 and E247-R147) that are not observed (or significantly enhanced) either in the isolated monomer or in subunit A of the same dimer.

Rigid-body movements

There is evidence that the environment of a membrane protein -including lipids, detergents and the formation of dimers or oligomers- can modulate the orientation of the protein as a whole as well as to the individual helices (or parts of it) when considered as rigid-body elements. Therefore, these features have been analyzed in the present work and compared to previous simulations of rhodopsin monomers or to the different crystal structures. Figure 4 displays the time-evolution of the relative distances between the centers of mass of the two subunits and between helices TM4 and TM5. The distance between subunits fluctuates between 3.7 and 3.8 nm along the simulations, reaching an average value of 3.73 ± 0.03 nm, that is only 0.14 nm lower than the value proposed in the semi-empirical model and is in even better agreement with the centre-to-centre distance between protrusions reported both in AFM topography measurements¹¹ or in the refined model produced from MD.⁴³ Regarding to the helix-to-helix distances (see methods), the TM4(A)-TM4(B) distance exhibits a final average value of 1.65 which, despite an initial decrease, remains

close to the initial value of 1.70 nm. Distances between TM4(A)-TM5(B) and TM5(A)-TM4(B) exhibit a more pronounced decrease from 1.75 to 1.30 and 1.50 nm, respectively. These values respond to the asymmetric arrangement of helices TM4 and TM5 as reported previously.⁴⁴ Similarly, despite an initial increase, the TM5(A)-TM5(B) distance decreases from 2.50 to 2.30 nm. Considering only the first 45 ns of the simulation we observe a similar trend than has recently been reported for the dimer in a POPC bilayer⁴⁴ in a simulations of that length. However, the present results suggest that with longer simulation times the larger changes observed in the previous study are reduced and therefore provide a better agreement to the experimental measurements. It should be noted, however, that the preceding and the present work used different starting structures for the protein (see methods), which could bias the results. Additionally, it is reasonable to expect some structural differences associated to the effect of different model lipid bilayers similar to what has been reported for rhodopsin monomers.⁴²

The average values for the bundle tilt were computed excluding the first 10 ns of the simulation, which is the time required for the first step of the protein-lipid matching. For a single monomer, the average tilt is $8 \pm 3^\circ$ in good agreement with our previous estimate.⁴² However, in the case of the dimer, tilts for subunits A and B exhibit average values of $9 \pm 3^\circ$ and $7 \pm 3^\circ$, indicating a small asymmetry regarding their orientation relative to the membrane. Since the two subunits are tilted in opposite directions (as is can be seen in Figure 1A) and exhibit a collective movement, it is reasonable to expect that if the angle of one subunit increases that of the complementary unit must decrease. Time evolution of the tilt angle (data not shown) indicates that tilts exhibit oscillations during the trajectories ranging between $0-18^\circ$, in agreement with the values obtained for rhodopsin in various model lipid bilayers.⁴² These results suggest that rhodopsin has an intrinsic range of tilt angles that provide a proper matching with the lipid bilayer. However it is possible to modulate it either through the dimerization -and probably larger oligomerizations- or with the lipidic environment.

Individual helix tilts and kinks either from the monomer or each of the dimer subunits, averaged over the last 50 ns of their respective trajectories are summarized in Table 2. Roughly speaking, the results indicate only minor differences between subunits A and B, suggesting almost a lack of asymmetry regarding these structural features. However, larger differences can be observed when comparing these values with those of a single monomer or the crystal structure as discussed below. Since the dimer interface involves TM4, TM5 and in a less extent TM3, it is expected that the largest differences on tilts and kinks are experienced by these helices. Indeed, TM4 exhibits a smaller tilt angle in the dimer than in a monomer simulation. On the contrary, the main kink observed in this helix exhibits a larger angle in the monomer than in the dimer subunits. These values differ also from those measured in the X-ray structure² and clearly suggest a direct effect of the dimer formation in the rigid-body structure of TM4. In a similar fashion, TM5 exhibits a larger tilt and a smaller kink in the dimer structure than in the single monomer. Interestingly, values observed in the dimer are close to those found in the X-ray structure since the two monomers of the crystal structure exhibit strong (non-native) TM5-TM5

contacts that resemble the TM4-TM5 interactions present in the dimer model.²⁰ TM3 exhibits also a larger tilt angle in the dimer and similar to the X-ray structure found in the monomer. TM6 exhibits some differences between the monomer and the dimer, but most importantly, holds the largest asymmetry between subunit A and B within all TM helices both in tilt and kink angles. Such large effects may be due to the proximity of TM5 and TM3 and mainly of the C2 loop, and the asymmetry caused by the different conformation of the C3 loop reported above (see Figure 1 B). The remaining helices show non-negligible differences between the single monomer and the dimer that might be associated to the changes in helices TM3-6. It is interesting to observe that there is, in general, a better agreement between the crystal structure and the structure from the dimer simulation than for the monomer one, suggesting that the anti-parallel arrangement in the X-ray structure resembles some of the interactions present in the dimer.

The dimer interface

Time-evolution of the interaction energy between subunits A and B along the MD trajectory shows that the structures optimize their contact surface in the first 60 ns. The average interaction energy during the last 40 ns of simulation –time when it has reached a steady value– is around -500 kJ/mol, with a Coulombic contribution of -73 ± 6 kJ/mol and a Lennard-Jones (LJ) contribution of -426 ± 8 kJ/mol. While the first term accounts for the electrostatic interactions or hydrogen bonds, the second one reflects basically the dispersion contribution and can be used to evaluate the contact surface between monomers. Not surprisingly, present results indicate that the LJ contribution is basically responsible for the subunit-subunit interactions and it is almost 6 times larger than the electrostatic interactions. Figure 5 A displays the minimum distance between every residue in each subunit and any residue in the complementary one during the last 40 ns of simulation. The plot provides a first approximation of the regions and specific residues exhibiting important contributions to the stability of the dimer complex. The shortest distances are observed for the TM4, C2 and TM5 regions, but also for the cytoplasmic side of TM3 and the ends of E2. Additionally, other segments including parts of NT, C1, TM2, TM6 and CT are also close to the other subunit, although it will be shown below that these contacts are occasional. Figure 5 B monitors in more detail which specific residues form the closest contacts within the TM4-C2-TM5 region.

In order to get a better insight onto the nature of the subunit-subunit mutual dependence both, the interaction energies between different protein regions –including TM3, C2 TM4, E2 and TM5 motifs– and specific residue-residue hydrophobic contacts or hydrogen bonds were analyzed during the last 40 ns of the trajectory. Average energies of interaction considering the different contributions are reported in Table 3, and the percentage of time that specific hydrophobic contacts and electrostatic interactions are observed along the trajectory are shown in Tables IV and V, respectively. A cutoff of 0.4 nm was used as criterion to consider the presence or not of an interaction/contact between residues. An additional threshold of 0.3 nm was used to discriminate direct hydrogen bonds from water mediated ones.

Regarding hydrophobic contacts, they basically involve residues with aromatic and bulky aliphatic side

chains, although aliphatic regions of some polar side chains also make a contribution and have been considered. Only seven residues: N145, F146, F159, M163, W175, N199 and Y206 were identified to interact with their counterparts in the complementary subunit during more than 50% of the trajectory analyzed (see Table 4 A). All residues except N145 and N199 are displayed in Figure 1 A, where it can be observed that they are evenly distributed along the subunit-subunit interface. Some of these interactions had been already characterized in the original AFM based model²² or have more recently been reported in a refined structure.²⁷ Moreover, additional experimental evidence from site-directed mutagenesis on the involvement of W175 and Y206 in such interactions has recently been released.²⁴ However, other residues like N145, F159 and M163 were not within 0.4 nm in the original model, pointing to that in a long enough sampling the system is able to form/optimize novel interactions. Interestingly, the contact between the two M155 reported in the refined structure was not observed in the present simulation, in agreement with the original model. Six pairs of additional crossed A-B/B-A interactions in both monomers including residues I133, F146 R147, H152, M155, V162, V173, W175, I214 and S202 were identified (see Table 4 B). Similarly as described above, all pairs except F146-H152 and W175-S202 were not evident in the original or in the refined model. The remaining interactions are listed in Table 4 C and appear to be related to the conformations adopted by each subunit. Interestingly in both, the TM3-C2-TM4 and TM4-E2-TM5 regions, the B-A interactions are exhibited by residues with smaller sequence numbers than A-B interactions. Finally, no contacts involving the CT remain stable for at least half of the trajectory analyzed, suggesting that despite the CT of one subunit can be close to the other (see Figure 5), this happens only occasionally because of the large motions of the segment. This suggests that they do not play an important role in the dimer stabilization.

The analysis of the LJ contribution to the interaction energy between different motifs (see Table 3 A), permits the identification of the region C2(A)-C2(B) as the most important according to the large number of contacts between residues identified in this loop (see Table 4 A). Moreover, with a smaller number of contacts, the interaction E2(A)-E2(B) exhibits the second largest energy with a stacking between the two W175 residues as a relevant interaction. Finally, TM4 and –in a less extent– TM5 are involved in a number of significant interactions with different segments of the protein. The interaction energy computed for segments C2(A)-C2(B) and E2(A)-E2(B) reaches steady values when the distance between subunits has been stabilized, as soon as in 10 ns (see above). On the contrary, the remaining interactions require longer simulation times for a fully optimization of the contacts, suggesting that the strong C2(A)-C2(B) and E2-E2(B) interactions might drive the dimer formation with the optimization of the contacts involving helices TM3, TM4 and TM5 in a second step. This hypothesis is consistent with the multi-step mechanism for rhodopsin association obtained from recent coarse-grained simulations.⁶⁰

In regard to charge-charge interactions or hydrogen bonds as specific contributions to the electrostatic term, the percentage of time that they are observed along the simulation is small in all the cases, in agreement with the small electrostatic values shown in

Table 3 B. The interactions in Table 5 include charge-neutral and neutral-neutral side chain interactions as well as side chain-backbone hydrogen bonds. Additionally, the differences when using a cutoff of 0.3 or 0.4 nm indicates that most of them are water mediated. The only common direct interactions observed involve the two Y206 and T198 sampled only during a 10% of the trajectory. Interestingly, all residues involved are located in loops, at the lipid/water interface of the neighboring TM helices or at the CT. When the analysis is extended to include water mediated hydrogen bonding, W175-N199, G174-S202 and N145-R147 are the interactions with the longest time of occurrence, although they do not exhibit as a whole, a symmetric behavior in the two subunits. The lack of A-B/B-A common list of interaction suggests that the formation of intra-subunit hydrogen bonds occurs only as a result of the existence of neighboring hydrophobic contacts. Most of the hydrogen bonds involve residues 142-149 at C2 and 173-176/196-199 at E2. The first are associated mainly to the hydrophobic contacts N145-N145, F146-F146 and F146-R147, while the second to W175-W175 and N199-N199 (see Table 4 A). There is not a perfect agreement between the hydrogen bonds found here and those reported from a refined structure^{27,43} except for the C2-CT ones, supporting the secondary role of these interactions relative to the different hydrophobic contacts formed. Therefore the most relevant electrostatic contribution to the interaction energy corresponds to de segments C2(A)-C2(B) and E2(A)-E2(B), consistent with the larger presence of hydrophilic residues out of the TM segments (see Table 4) although TM3-TM4, TM5-TM5 and TM4(A)-C2(B) pairs exhibit also a small contribution. However, the values reported in Table 5 account, in most cases, more for the mere proximity of backbones than two the specific side-chains interactions in Table 3).

These results indicate that the dimer is stabilized mainly by the dispersion energy accounting for hydrophobic contacts, although there is a small contribution from the electrostatic term due to the interactions between loops or helix ends. Analysis of the total interaction energy points to TM4 as the centre of the dimer complex since it exhibits interactions with all the motifs studied. The relevance of the preceding results is that they support the previous indications of asymmetry in the rhodopsin dimer.⁴⁴ It is interesting the remarkable asymmetry in the dimer structure as clearly suggested from the analysis of the interactions, otherwise more symmetric matrices would be listed in Tables III, IV and V.

Lipid-protein interactions

Time evolution of the Coulomb and the Lennard-Jones (LJ) contributions to the lipid-protein interaction energy were investigated along MD trajectories using a cutoff of 1.0 nm for both of them. The results are shown in Figure 6, where energies are normalized to the number of proteins per system for the sake of comparison. Time evolutions exhibit a small but continuous energy drop and only the LJ term reaches a steady value after 65 ns, whereas that the Coulombic term has not converged in 100 ns. This indicates that the extension of the simulations to longer time-scales can help lipids in adapting to the protein surface and its specific electrostatic features.⁴² The present simulations point to a strong interaction between the protein and lipids both in the single monomer and in the dimer. The magnitude of the LJ contribution is much

larger than the electrostatic one, with a difference between these terms of about -1500 kJ/mol after 100 ns. Since this value is already smaller than reported for shorter simulations (-2200 kJ/mol after 20ns), one can expect it to be even smaller for longer times. Therefore, present results suggest that the electrostatic term exhibits a tendency to grow in longer simulations. However, longer simulations times, which may provide a better convergence, are currently only achievable using coarse-graining methods.⁶⁰ The comparison between the monomer and the dimer shows a 20 % and 30 % drop in the LJ and Coulombic term respectively, which account for the obvious reduction in the available surface for protein-lipid interactions because of the dimer formation. In other words, the association of the protein subunits compete with the lipids for the same hydrophobic surface.⁶⁰

There is experimental evidence that basic amino acids -lysine and arginine- or polar-aromatic ones -tyrosine, histidine and tryptophan- can act as anchoring hooks to the lipid bilayers.^{61,62} Therefore, specific lipid-protein hydrogen bond interactions between any donor in the protein and any lipid oxygen acceptor have been analyzed along the MD trajectory and are reported in Table 6. The purpose of this study is the evaluation of the effects of the dimer formation on the existence of a group of residues predicted as possible anchoring points of rhodopsin to the lipid bilayer for a single monomer.⁴²

A radius of 0.4 nm permitted the identification of direct as well as water mediated hydrogen bonds. Table 6 shows those interactions that are present in at least 50 % of the snapshots analyzed in any of the monomers. It can be seen that residues W35, K66, R69, Y96, T108, Y136, Y223, R252, Y274 and K339, proposed as anchoring points in a previous work,⁴² are present in the table. However, residue H152, reported also in that work, is not involved in lipid protein interactions due to its location at the protein-protein interface and even participating in contacts between subunits (see Table 4). Furthermore, the remaining residues listed in Table 6 have also been previously described to participate in lipid-rhodopsin interactions in DPPC or other model bilayers, although the interactions were not consistently observed in all the systems studied.⁴² It is possible that the longer time scales of the simulations reported in the present work helps in optimizing such interactions. The present results support that the majority of the hydrogen bonds identified between rhodopsin and the lipid oxygens lie in the cytoplasmic side as previously reported. Moreover, considering that the activation of GPCR involves the cytoplasmic loops bound to the G-proteins, present results suggest that the existence of specific lipid-protein hydrogen bonds can be important to modulate loop conformations and in turn, for the signal transduction process. While K339 has already been reported to be particularly relevant regarding the interactions with lipid molecules, both from experiments⁶³ and previous MD simulations,³⁵ the role of the remaining residues reported here and in our previous work still needs to be clarified.

CONCLUSIONS

In the present work we report the analysis of a 0.1 μ s MD simulation of a rhodopsin dimer embedded in a DPPC bilayer. The starting structure used for the simulation was retrieved from a semi-empirical model pre-

viously reported based on AFM studies.²² The structural features of the dimer have been analyzed together with those of a single monomer by comparing these results with those of a parallel calculation of a 0.1 μ s trajectory of a rhodopsin monomer in the same environmental conditions and protocol. Furthermore, dimer interface has been studied by characterizing the regions and residues that play the most important role for the stability of the dimer. The work makes use of the possibilities of MD as a tool to provide a refined relaxed structure of the dimer.

Measurements of the rmsd of the C α skeleton in regard to the starting structure provides the image that the tertiary structure achieves a steady state 40 ns after the beginning of the simulation, whereas the dimer achieves a steady state later, after 60 ns. After the MD trajectory the quaternary structure of the dimer does not change very much indicating that the original structure is preserved in the lipid environment. Moreover, the structure of each helix is conserved except for the C3 loops and the adjacent ends of the neighboring helices TM5 and TM6. The analysis of the structural hydrogen bonds that are responsible for the secondary structure show not many differences between the structure of the monomer and the two units of the dimer. However, helices TM3, TM5 and TM6 appear shorter in each of the sub-units of the dimer in regard to the monomer structure. Salt bridges are basically the same as observed in the monomer, although dimerization generates new ones, and specifically, a few that are associated with the electrostatic lock pointed as being involved in activation of GPCRs.

The most important subunit-subunit interactions in the dimer involve loops C2 and E2, and following these TM4 and TM5 although less important. Analysis of the subunit-subunit interface permitted to identify those residues responsible for the stability of the quaternary structure of the dimer. Interestingly, the analysis of the interaction energy shows that the dimer is mainly stabilized by the dispersion term, which accounts for hydrophobic contacts, although there is a small contribution due to the electrostatic term from interactions between loops or helix ends. In general, electrostatic interactions do not seem to play an important role in the dimer interaction and the lack of symmetrical A-B/B-A interactions suggest that the formation of intra-subunit hydrogen bonds occurs only as a result of the existence of neighboring hydrophobic contacts.

The analysis of the structure points to a certain asymmetry in the quaternary structure of the dimer due to the different conformation of the loops C2, C3 and E2 in the two subunits, creating subtle differences in the sidechain interactions between subunits and ultimately altering some tilt and kink angles. In regard to the lipid-protein interactions, the analysis carried out reflects the same features as previously reported from the monomer simulations.

Finally, the present results are in reasonable agreement with those obtained previously from a 45 ns simulation,⁴⁴ despite the different model membrane used (DPPC vs. POPC), a different choice of the crystal structure (1GZM vs. 1L9H) fitting the two subunits of the dimer model, the presence of a physiologic NaCl concentration here and the use or not of an all-atom forcefield (OPLS-AA vs. GROMACS). As more reports are available there is additional support for the ro-

bustness of the present methodology, although a larger knowledge of the specific details of the protocols are needed to avoid possible artifacts produced during the simulations.

Acknowledgment

AC wishes to express his gratitude to the Technical University of Catalonia for a fellowship to undertake his doctoral studies. The Barcelona Supercomputer Center is acknowledged for a generous allocation of computer time. The Spanish Ministry of Science and Technology supported this work through grant number SAF2005-08148-C04-01.

REFERENCES

1. Palczewski, K.; Kumasaka, T.; Hori, T.; Behnke, C. A.; Motoshima, H.; Fox, B. A.; Le Trong, I.; Teller, D. C.; Okada, T.; Stenkamp, R. E.; Yamamoto, M.; Miyano, M. *Science* 2000, 289(5480), 739-745.
2. Li, J.; Edwards, P. C.; Burghammer, M.; Villa, C.; Schertler, G. F. X. *J Mol Biol* 2004, 343(5), 1409-1438.
3. Okada, T.; Sugihara, M.; Bondar, A. N.; Elstner, M.; Entel, P.; Buss, V. *J Mol Biol* 2004, 342(2), 571-583.
4. Liebman, P. A.; Entine, G. *Science* 1974, 185(149), 457-459.
5. Cone, R. A. *Nat New Biol* 1972, 236(63), 39-43.
6. Singer, S. J.; Nicolson, G. L. *Science* 1972, 175(4023), 720-731.
7. Milligan, G. *Drug Discov Today* 2006, 11(11-12), 541-549.
8. Milligan, G. *Biochim Biophys Acta* 2007, 1768(4), 825-835.
9. Terrillon, S.; Bouvier, M. *Embo J* 2004, 23(20), 3950-3961.
10. Bulenger, S.; Marullo, S.; Bouvier, M. *Trends Pharmacol Sci* 2005, 26(3), 131-137.
11. Fotiadis, D.; Jastrzebska, B.; Philippsen, A.; Muller, D. J.; Palczewski, K.; Engel, A. *Curr Opin Struct Biol* 2006, 16(2), 252-259.
12. Park, P. S.; Filipek, S.; Wells, J. W.; Palczewski, K. *Biochemistry* 2004, 43(50), 15643-15656.
13. Gomes, I.; Jordan, B. A.; Gupta, A.; Rios, C.; Trapaidze, N.; Devi, L. A. *J Mol Med-Jmm* 2001, 79(5-6), 226-242.
14. Salahpour, A.; Angers, S.; Bouvier, M. *Trends Endocrinol Metab* 2000, 11(5), 163-168.
15. Angers, S.; Salahpour, A.; Bouvier, M. *Annu Rev Pharmacol Toxicol* 2002, 42, 409-435.
16. Gazi, L.; Lopez-Gimenez, J. F.; Strange, P. G. *Curr Opin Drug Discov Devel* 2002, 5(5), 756-763.
17. George, S. R.; O'Dowd, B. F.; Lee, S. P. *Nat Rev Drug Discov* 2002, 1(10), 808-820.
18. Okada, T.; Fujiyoshi, Y.; Silow, M.; Navarro, J.; Landau, E. M.; Shichida, Y. *Proc Natl Acad Sci USA* 2002, 99(9), 5982-5987.
19. Teller, D. C.; Okada, T.; Behnke, C. A.; Palczewski, K.; Stenkamp, R. E. *Biochemistry* 2001, 40(26), 7761-7772.
20. Filipek, S.; Stenkamp, R. E.; Teller, D. C.; Palczewski, K. *Annu Rev Physiol* 2003, 65, 851-879.
21. Liang, Y.; Fotiadis, D.; Filipek, S.; Saperstein, D. A.; Palczewski, K.; Engel, A. *J Biol Chem* 2003, 278(24), 21655-21662.
22. Fotiadis, D.; Liang, Y.; Filipek, S.; Saperstein, D. A.; Engel, A.; Palczewski, K. *Nature* 2003, 421(6919), 127-128.
23. Hanson, S. M.; Gurevich, E. V.; Vishnivetskiy, S. A.; Ahmed, M. R.; Song, X.; Gurevich, V. V. *Proc Natl Acad Sci U S A* 2007, 104(9), 3125-3128.
24. Kota, P.; Reeves, P. J.; Rajbhandary, U. L.; Khorana, H. G. *Proc Natl Acad Sci U S A* 2006, 103(9), 3054-3059.
25. Filizola, M.; Weinstein, H. *Curr Opin Drug Disc* 2005, 8(5), 577-584.
26. Modzelewska, A.; Filipek, S.; Palczewski, K.; Park, P. S. *Cell Biochem Biophys* 2006, 46(1), 1-15.

27. Fotiadis, D.; Liang, Y.; Filipek, S.; Saperstein, D. A.; Engel, A.; Palczewski, K. *FEBS Lett* 2004, 564(3), 281-288.
28. Lee, S. P.; O'Dowd, B. F.; George, S. R. *Life Sci* 2003, 74(2-3), 173-180.
29. Milligan, G. *Mol Pharmacol* 2004, 66(1), 1-7.
30. Jastrzebska, B.; Fotiadis, D.; Jang, G. F.; Stenkamp, R. E.; Engel, A.; Palczewski, K. *J Biol Chem* 2006, 281(17), 11917-11922.
31. Fanelli, F.; De Benedetti, P. G. *Chem Rev* 2005, 105(9), 3297-3351.
32. Ash, W. L.; Zlomislic, M. R.; Oloo, E. O.; Tieleman, D. P. *Biochim Biophys Acta* 2004, 1666(1-2), 158-189.
33. Tieleman, D. P.; Forrest, L. R.; Sansom, M. S.; Berendsen, H. J. *Biochemistry* 1998, 37(50), 17554-17561.
34. Tieleman, D. P.; MacCallum, J. L.; Ash, W. L.; Kandt, C.; Xu, Z. T.; Monticelli, L. *J Phys-Condens Mat* 2006, 18(28), S1221-S1234.
35. Huber, T.; Botelho, A. V.; Beyer, K.; Brown, M. F. *Biophys J* 2004, 86(4), 2078-2100.
36. Saam, J.; Tajkhorshid, E.; Hayashi, S.; Schulten, K. *Biophys J* 2002, 83(6), 3097-3112.
37. Crozier, P. S.; Stevens, M. J.; Forrest, L. R.; Woolf, T. B. *J Mol Biol* 2003, 333(3), 493-514.
38. Pitman, M. C.; Grossfield, A.; Suits, F.; Feller, S. E. *J Am Chem Soc* 2005, 127(13), 4576-4577.
39. Grossfield, A.; Feller, S. E.; Pitman, M. C. *Proc Natl Acad Sci USA* 2006, 103(13), 4888-4893.
40. Schlegel, B.; Sippl, W.; Holtje, H. D. *J Mol Model (Online)* 2005, 12(1), 49-64.
41. Cordoní, A.; Edholm, O.; Perez, J. J. *J Comput Chem* 2007, 28(6), 1017-1030.
42. Cordoní, A.; Perez, J. J. *J Phys Chem B* 2007, 111(25), 7052-7063.
43. Filipek, S.; Krzysko, K. A.; Fotiadis, D.; Liang, Y.; Saperstein, D. A.; Engel, A.; Palczewski, K. *Photochem Photobiol Sci* 2004, 3(6), 628-638.
44. Filizola, M.; Wang, S. X.; Weinstein, H. *J Comput Aided Mol Des* 2006, 20(7-8), 405-416.
45. Berman, H. M.; Westbrook, J.; Feng, Z.; Gilliland, G.; Bhat, T. N.; Weissig, H.; Shindyalov, I. N.; Bourne, P. E. *Nucleic Acids Res* 2000, 28(1), 235-242.
46. Fahmy, K.; Jager, F.; Beck, M.; Zvyaga, T. A.; Sakmar, T. P.; Siebert, F. *Proc Natl Acad Sci USA* 1993, 90(21), 10206-10210.
47. Lindahl, E.; Edholm, O. *Biophys J* 2000, 79(1), 426-433.
48. Berendsen, H. J. C.; van der Spoel, D.; van Drunen, R. *Comput Phys Commun* 1995, 91(1-3), 43-56.
49. Lindahl, E.; Hess, B.; van der Spoel, D. *J Mol Model* 2001, 7(8), 306-317.
50. Jorgensen, W. L.; Maxwell, D. S.; TiradoRives, J. *J Am Chem Soc* 1996, 118(45), 11225-11236.
51. Berger, O.; Edholm, O.; Jähnig, F. *Biophys J* 1997, 72(5), 2002-2013.
52. Jorgensen, W. L.; Chandrasekhar, J.; Madura, J. D.; Impey, R. W.; Klein, M. L. *J Chem Phys* 1983, 79(2), 926-935.
53. Hayashi, S.; Tajkhorshid, E.; Schulten, K. *Biophys J* 2002, 83(3), 1281-1297.
54. Berendsen, H. J. C.; Postma, J. P. M.; DiNola, A.; Haak, J. R. *J Chem Phys* 1984, 81, 3684.
55. Hess, B.; Bekker, H.; Berendsen, H. J. C.; Fraaije, J. G. E. M. *J Comput Chem* 1997, 18(12), 1463-1472.
56. Miyamoto, S.; Kollman, P. A. *J Comput Chem* 1992, 13(8), 952-962.
57. Darden, T.; York, D.; Pedersen, L. *J Chem Phys* 1993, 98(12), 10089-10092.
58. Ballesteros, J. A.; Jensen, A. D.; Liapakis, G.; Rasmussen, S. G.; Shi, L.; Gether, U.; Javitch, J. A. *J Biol Chem* 2001, 276(31), 29171-29177.
59. Ramon, E.; Cordoní, A.; Bosch, L.; Zernii, E. Y.; Senin, II; Manyosa, J.; Philippov, P. P.; Perez, J. J.; Garriga, P. *J Biol Chem* 2007.
60. Periole, X.; Huber, T.; Marrink, S. J.; Sakmar, T. P. *J Am Chem Soc* 2007, 129(33), 10126-10132.
61. Mishra, V. K.; Palgunachari, M. N.; Segrest, J. P.; Anantharamaiah, G. M. *J Biol Chem* 1994, 269(10), 7185-7191.
62. Strandberg, E.; Killian, J. A. *FEBS Letters* 2003, 544(1-3), 69-73.
63. Klein-Seetharaman, J.; Reeves, P. J.; Loewen, M. C.; Getmanova, E. V.; Chung, L.; Schwalbe, H.; Wright, P. E.; Khorana, H. G. *Proc Natl Acad Sci USA* 2002, 99(6), 3452-3457.

Table 1 - Salt bridges observed in each of the rhodopsin molecules (mon: single monomer, sub A/B: dimer subunits A or B). The four columns of the left identify the residue and its location in each subunit, whereas those on the right indicate the percentage of time that the interaction is found in the different rhodopsin molecules during the last 50 ns of the simulation. Results in italic correspond to the most important interactions observed in all molecules. Additionally those residues underscored indicate that at least one of the residues of a pair has described as involved in the so-called electrostatic lock between the cytoplasmic sides of helices TM3 and TM6.⁵⁸

- residue		+residue		mon	sub A	sub B
E 5	NT	R 177	E2	98	87	20
E25	NT	R21	NT	13	88	26
<i>E 113</i>	<i>H3</i>	<i>K296</i>	<i>H7</i>	<i>100</i>	<i>85</i>	<i>81</i>
<u>E 134</u>	<u>H3</u>	<u>R 135</u>	<u>H3</u>	<u>99</u>	<u>100</u>	<u>100</u>
<u>E 134</u>	<u>H3</u>	<u>R 147</u>	<u>C2</u>			<u>45</u>
E 150	H4	R 147	C2	58	85	
<i>D 190</i>	<i>E2</i>	<i>R 177</i>	<i>E2</i>	<i>100</i>	<i>100</i>	<i>100</i>
E 197	E2	R 177	E2			29
E 232	C3	K 231	C3	18		20
E 232	C3	K 248	H6		93	99
E 232	C3	R 252	H6		31	18
E 239	C3	K 141	C2	94		
E 239	C3	K 245	H6		62	18
E 239	C3	K 248	H6		45	22
E 239	C3	R 252	H6		100	
<u>E 247</u>	<u>H6</u>	<u>R 135</u>	<u>H3</u>	<u>100</u>	<u>84</u>	<u>94</u>
<u>E 247</u>	<u>H6</u>	<u>R 147</u>	<u>C2</u>	<u>8</u>		<u>45</u>
E 249	H6	K 245	H6	87		38
<i>E 249</i>	<i>H6</i>	<i>R 252</i>	<i>H6</i>	<i>100</i>	<i>79</i>	<i>62</i>
E 249	H6	K 311	H8			13
E 249	H6	R 314	H8			70
D 282	E3	K 16	NT			11
D 330	CT	K 311	H8			98
D 330	CT	R 314	H8		99	100
D 331	CT	K 311	H8	38	92	79
E 332	CT	K 311	H8	19		
E 341	CT	K 66	C1	49		84
E 341	CT	K 67	C1		48	18
A 348	CT	R 147	C2			25
A 348	CT	K 245	H6			24

Table 2 – Average TM helix tilt and kink angles (in degrees) for the last 50 ns of trajectory (see methods for details). X-ray: crystal structure 1GZM, mon: single monomer, sub A/B: dimer subunits A or B.

tilts	TM1	TM2	TM3	TM4	TM5	TM6	TM7
X-ray	23	17	27	12	26	16	20
mon	20 ± 1	18 ± 1	24 ± 1	16 2 1	23 ± 1	11 ± 2	18 ± 2
sub A	27 ± 1	20 ± 1	28 ± 1	7 1 1	27 ± 2	18 ± 1	21 ± 1
sub B	26 ± 1	21 ± 1	29 ± 1	8 1 1	28 ± 2	22 ± 1	24 ± 1

kinks	TM1	TM2	TM3	TM4	TM5	TM6	TM7
X-ray	13	25	0	9	37	26	20
mon	5 ± 3	11 ± 3	5 ± 2	19 ± 3	56 ± 4	23 ± 4	18 ± 3
sub A	14 ± 3	19 ± 3	8 ± 3	12 ± 3	37 ± 3	27 ± 3	21 ± 4
sub B	16 ± 3	16 ± 4	5 ± 2	12 ± 3	38 ± 3	21 ± 3	24 ± 4

Table 3 – Contributions to the interaction energy between monomers of different parts of each subunit during the last 50 ns of simulation. Panels A) and B) display the LJ and the electrostatic interactions, respectively, whereas C) is the sum of them. The grey boxes indicate the interactions between a motif and the same counterpart.

A

LJ	TM3 (B)	C2 (B)	TM4 (B)	E2 (B)	TM5 (B)
TM3 (A)		-5.2 ± 2.1	-48.1 ± 7.5		
C2 (A)	-0.7 ± 0.3	-90.4 ± 14.0	-20.6 ± 14.2		
TM4 (A)	-21.4 ± 6.1	-34.4 ± 12.3	-17.2 ± 3.7	-8.0 ± 4.4	-59.1 ± 11.5
E2 (A)			-5.2 ± 2.0	-57.7 ± 12.1	-7.5 ± 3.3
TM5 (A)			-26.8 ± 5.9	-20.5 ± 6.4	-5.7 ± 2.3

B

EL	TM3 (B)	C2 (B)	TM4 (B)	E2 (B)	TM5 (B)
TM3 (A)			-8.6 ± 4.2		
C2 (A)		-29.7 ± 16.0	-0.8 ± 1.3		
TM4 (A)	-7.4 ± 8.0	-7.0 ± 11.9			
E2 (A)				-12.6 ± 12.3	
TM5 (A)					-1.3 4.4

C

TOT	TM3 (B)	C2 (B)	TM4 (B)	E2 (B)	TM5 (B)
TM3 (A)		-5.2 ± 2.1	-56.7 ± 11.6		
C2 (A)	-0.7 ± 0.3	-120.1 ± 30.0	-21.4 ± 15.5		
TM4 (A)	-28.8 ± 14.1	-41.4 ± 24.1	-17.2 ± 3.7	-8.0 ± 4.4	-59.1 ± 11.5
E2 (A)			-5.2 ± 2.0	-70.3 ± 24.4	-7.5 ± 3.3
TM5 (A)			-26.8 ± 5.9	-20.5 ± 6.4	-7.0 ± 2.3

Table 4 – Hydrophobic contacts between subunits during the last 50 ns, using a cutoff of 0.4 nm. The columns on the left hand indicate the residues and their location and those on the right the percentage of time the interaction is found. The interactions not observed in more than 50% of the trajectory analyzed are not shown. A) Interactions between the same residues in both subunits B) crossed interactions observed in both subunits C) specific interactions of each subunit with the other.

A				B			
residue 1		residue 2		A-B	B-A		
N 145	C2	N 145	C2	54	54	I 133	TM3
F 146	C2	F 146	C2	100	100	M 155	TM4
F 159	TM4	F 159	TM4	95	95	F 146	C2
M 163	TM4	M 163	TM4	97	97	H 152	TM4
W 175	E2	W 175	E2	100	100	V 162	TM4
N 199	E2	N 199	E2	95	95	I 214	TM5
Y 206	TM5	Y 206	TM5	77	77	V 173	TM4
						W 175	E2
						S 202	TM5
						S 202	TM5

C							
residue 1		residue 2		A-B	B-A		
V 137	TM3	F 146	C2		88	P 170	TM4
W 126	TM3	F 159	TM4	86	2	V 173	TM4
I 133	TM3	H 152	TM4	70	4	F 159	TM4
Y 136	TM3	N 151	TM4	97		M 163	TM4
		H 152	TM4		100	N 151	TM4
V 137	TM3	M 155	TM4	84		F 221	TM5
		N 151	TM4	100		V 218	TM5
C 140	TM3	H 152	TM4	100		F 221	TM5
		R 147	C2	91		M 155	TM4
P 142	C2	F 148	C2	95		F 159	TM4
		S 144	C2	70		I 214	TM5
		N 145	C2	74		V 209	TM5
		F 146	C2	61		V 162	TM4
M 143	C2	R 147	C2	21	79	M 163	TM4
		F 146	C2	100	4	V 210	TM5
		R 147	C2	98	2	Y 206	TM5
N 145	C2			56		V 210	TM5
F 146	C2	F 148	C2	83	16	Y 206	TM5
		G 149	TM4		100	S 202	TM5
		E 150	TM4	61		V 210	TM5
P 142	C2	H 152	TM4	91		S 202	TM5
		G 149	TM4	60		Y 206	TM5
		N 151	TM4	79		N 200	TM5
M 143	C2	H 152	TM4	56		S 202	TM5
N 145	C2	G 149	TM4	65			

Table 5 – Hydrogen bond interactions between subunits within a cutoff of 0.4 nm and 0.3 nm, accounting for direct and water mediated interactions, respectively. The columns on the left hand indicate the residues and their location and those on the right the percentage of time the interaction is found.

residue 1	residue 2	0.3 nm		0.4 nm	
		A-B	B-A	A-B	B-A
Y 136 TM3	N 151 TM4				7
P 142 C2	R 147 C2	2		11	
N 145 C2	F 146 C2				2
	R 147 C2		4		30
S 144 C2	P 347 CT				4
	A 348 CT	16		17	
N 145 C2					9
N 145 C2	G 149 TM4				5
N 151 TM4	Q 225 TM5				2
V 173 TM4	S 202 TM5			8	10
G 174 E2	W 175 E2				15
W 175 E2	E 196 E2				2
	N 199 E2	5		47	
S 176 E2					2
E 196 E2					2
E 197 E2	T 198 E2		5		23
T 198 E2		9	9	12	12
	N 199 E2			3	5
G 174 E2	S 202 TM5		6	5	42
W 175 E2				3	
Y 206 TM5	Y 206 TM5	10	10	11	11

Table 6 – Residues interacting with the lipid oxygens during the last 50 ns of simulation. The first three columns display the residue type, name and location and the last two show the percentage of time that the interactions are observed. Interactions observed less than half of the trajectory analyzed in the two monomers have been omitted.

residue			A	B
R	69	C1	100	100
R	252	TM6	94	100
R	314	sH8	80	14
K	66	C1	97	89
K	231	C3	19	78
K	325	CT	100	83
K	339	CT	100	100
H	278	E3	98	11
W	35	TM1	88	76
Y	60	TM1	16	55
Y	74	TM2	88	94
Y	96	TM2	90	87
Y	136	TM3	100	55
Y	223	TM5	64	7
Y	274	TM6	99	93
T	108	TM3	43	92
T	340	CT	98	0

Figure 1 A – Rhodopsin structures after 100 ns of simulation. The rhodopsin single monomer is displayed in blue and the dimer subunits A and B are coloured in green and orange, respectively. A) Trace of the dimer arrangement oriented showing TM4(A) and TM5(B) at first sight; hydrophilic residues interacting with the same residue of the pair of the other subunit are shown. B) Trace superposition of the single monomers and the subunits A and B of the dimer. The insets show a zoom of regions close to loops C2 (126-162) and C3 (220-250), respectively.

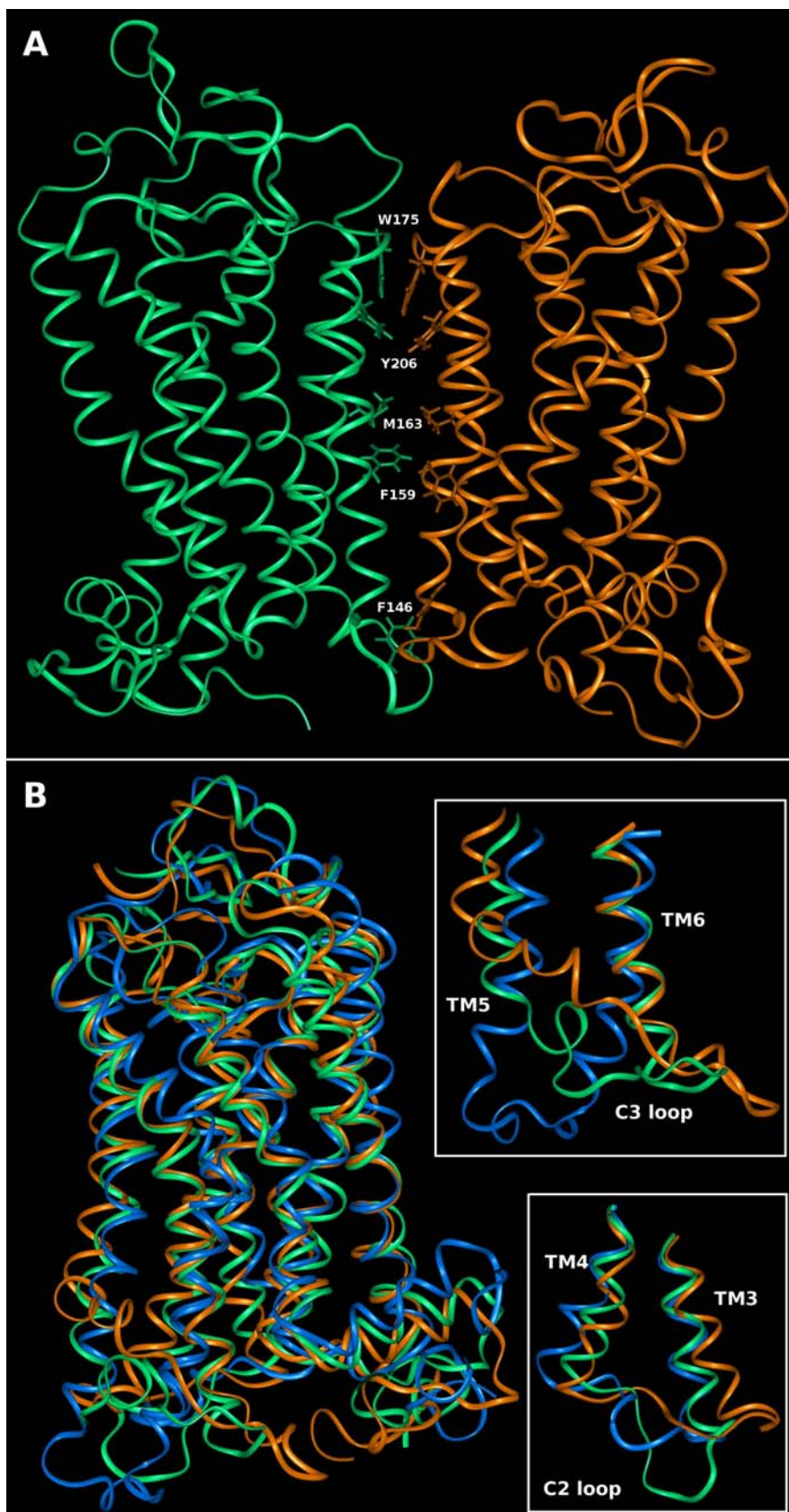
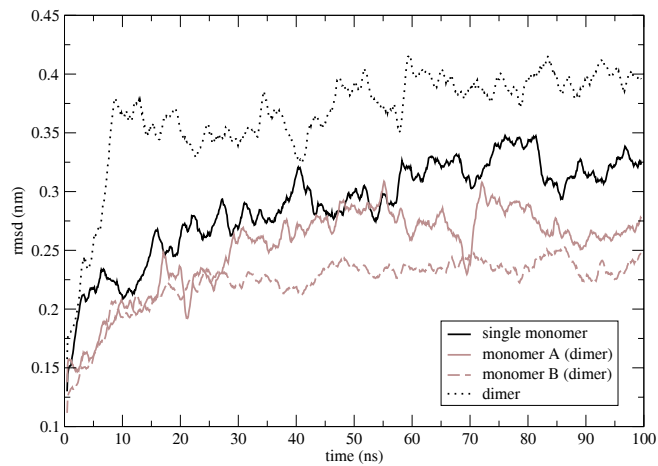
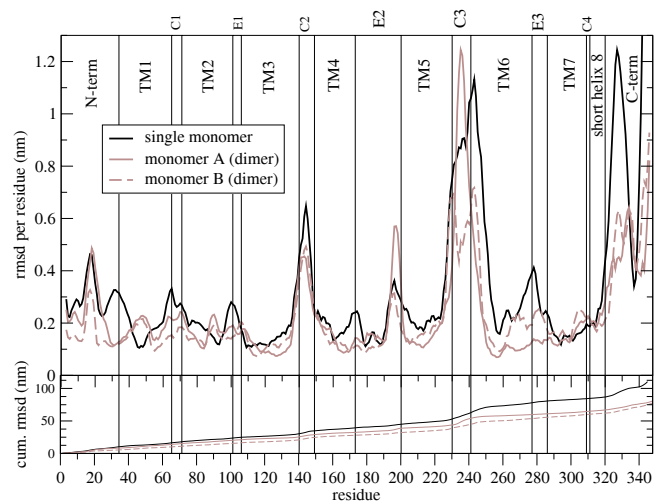


Figure 2 – A) Time evolution of the root mean square deviations (rmsd) for the rhodopsin monomers and for the dimer (excluding the CT residues 322-348). The values shown are a running average over 1 ns. B) Root mean square deviations from the initial structure; the bottom panel displays the cumulative deviations. The values shown are a running average over 5 residues. C) Root mean square fluctuations of the α -carbons computed from an average structure over the last 50 ns.

A



B



C

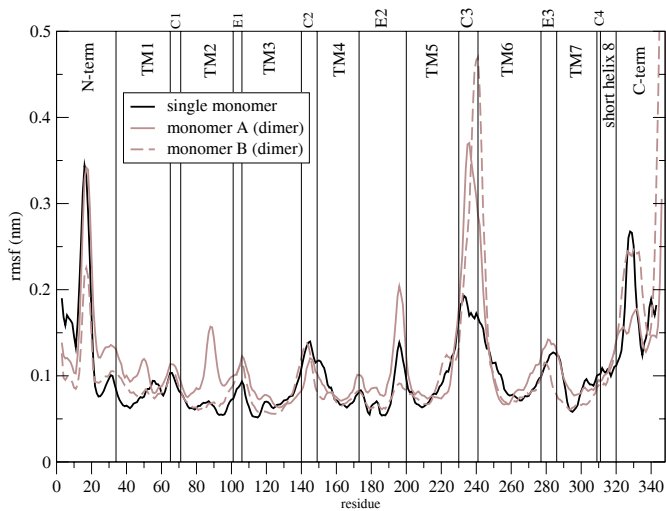


Figure 3 – Time evolution of the number of backbone intra-helical interactions in each rhodopsin molecule (monomer and dimer subunits).

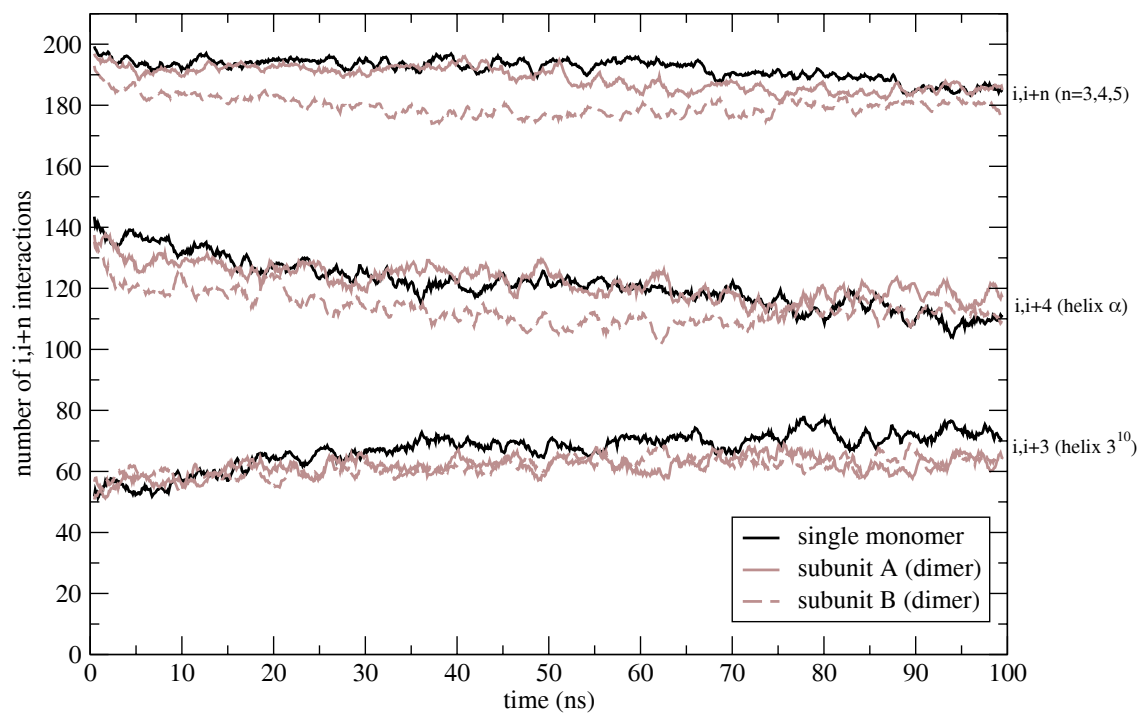


Figure 4 - Time evolution of the subunit-subunit and TM4/TM5(A)-TM4/TM5(B) distances. The dotted lines indicate the distance in the starting structure.

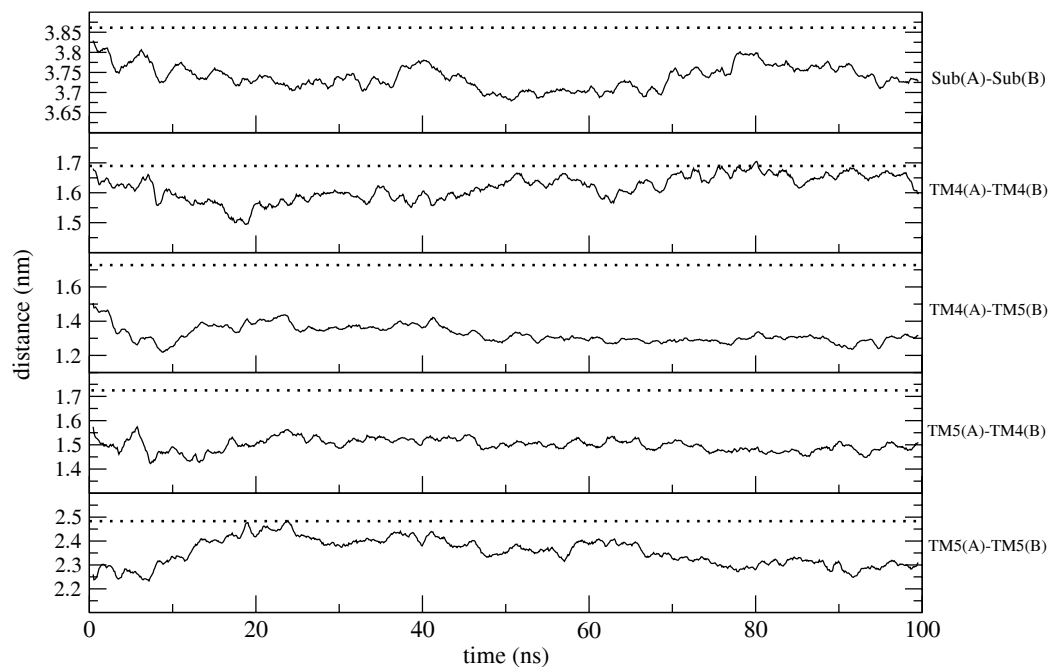
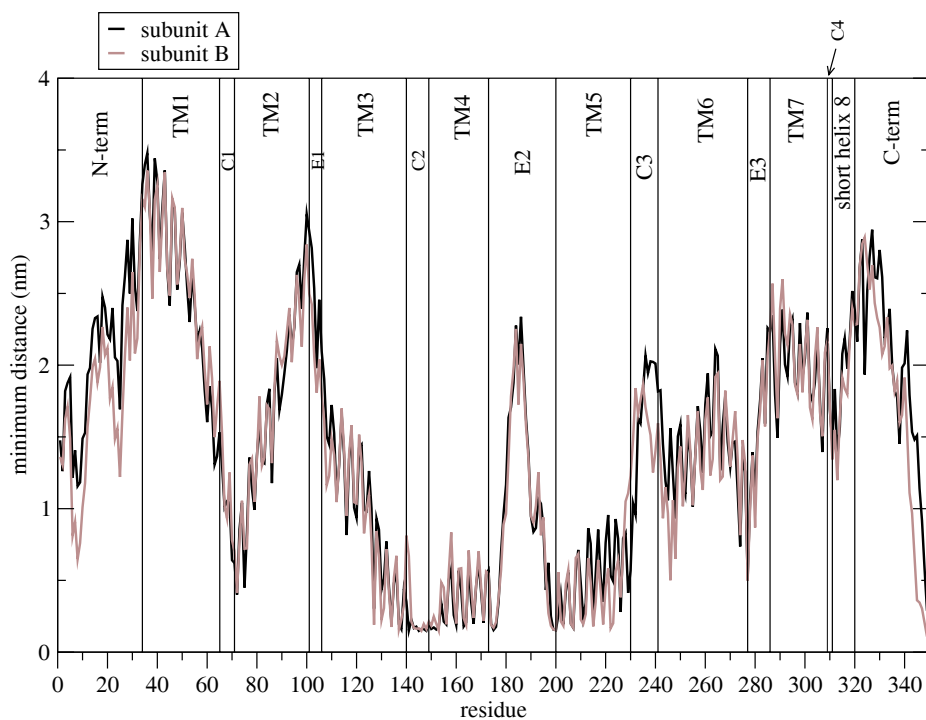


Figure 5 – Minimum distance between residues of subunits A/B with the corresponding subunit A) for the whole subunit B) for the segment TM3-C2-TM4-E2-TM5. The arrows point residues in Tables DI A and B.

A



B

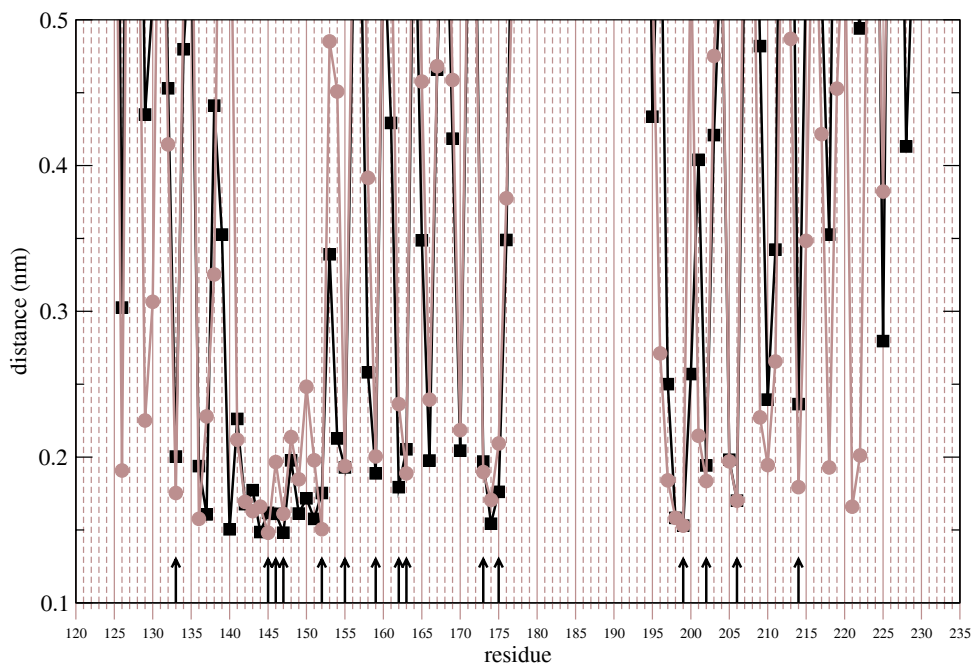
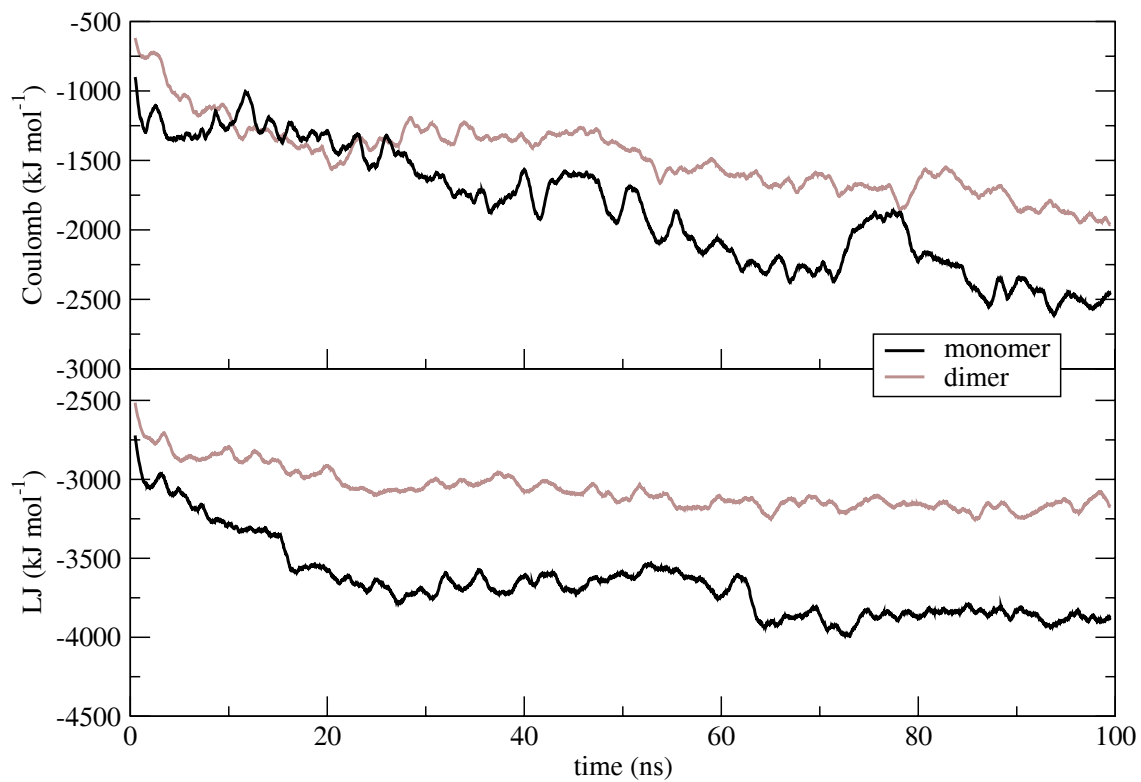


Figure 6 – Time-evolution of the Coulomb and LJ lipid-protein interactions normalized to the number of proteins per system.



The effect of ions on a dipalmitoyl phosphatidylcholine bilayer. A molecular dynamics simulation study

Cordomí A, Edholm O, Perez JJ

J Phys Chem B., 2008 15 Jan; Epub ahead of print.

Effect of Ions on a Dipalmitoyl Phosphatidylcholine Bilayer. A Molecular Dynamics Simulation Study

Arnau Cordermí,[†] Olle Edholm,[‡] and Juan J. Perez^{*,†}

Department of Chemical Engineering, Technical University of Catalonia (UPC), Av. Diagonal 647, 08028 Barcelona, Spain, and Theoretical Biological Physics, Royal Institute of Technology (KTH), SE-10691 Stockholm, Sweden

Received: May 20, 2007; In Final Form: October 26, 2007

The effect of physiological concentrations of different chlorides on the structure of a dipalmitoyl phosphatidylcholine (DPPC) bilayer has been investigated through atomistic molecular dynamics simulations. These calculations provide support to the concept that Li^+ , Na^+ , Ca^{2+} , Mg^{2+} , Sr^{2+} , Ba^{2+} , and Ac^{3+} , but not K^+ , bind to the lipid-head oxygens. Ion binding exhibits an influence on lipid order, area per lipid, orientation of the lipid head dipole, the charge distribution in the system, and therefore the electrostatic potential across the head-group region of the bilayer. These structural effects are sensitive to the specific characteristics of each cation, i.e., radius, charge, and coordination properties. These results provide evidence aimed at shedding some light into the apparent contradictions among different studies reported recently regarding the ordering effect of ions on zwitterionic phosphatidylcholine lipid bilayers.

Introduction

Biological membranes are not only essential for cell integrity, providing a barrier between the interior and the exterior of a cell, but also as a matrix and support for many types of proteins involved in important cell functions. Moreover, growing experimental evidence regarding the importance of the lipid membrane on protein function has recently attracted the interest of the scientific community.¹ However, the current knowledge about biological membranes is still scarce, due to the difficulties associated to the experimental techniques required. The present view of the membrane is based on the fluid mosaic model² where proteins are distributed in regions of biased composition with varying protein environment.

Atomistic molecular dynamics (MD) simulations of lipid bilayers provide a detailed microscopic picture of the interactions and processes in biological membranes that are not accessible by experimental methods. Still, the complexity of real membranes, containing many different proteins, lipids, and other molecules, are not affordable presently for atomic scale modeling. For this reason, the study of model one-component model lipid bilayers have been the focus of attention of a large number of reports published in recent years, which have been pivotal in order to provide new insights into this subject.^{3–9} The increasing computer power in recent years has offered the possibility to study more complicated systems such as phospholipid mixtures^{10–12} and/or the inclusion of other compounds such as cholesterol^{13–15} or ions.^{16–22}

Since membranes at physiological conditions are in contact with electrolyte solutions, their specific interactions with ions are a matter of substantial interest.²³ Experiments performed in the last few decades show that ions play an essential role not only in the structure, dynamics, and stability of membranes but also for the binding and insertion of proteins, membrane fusion, and transport across membranes.^{24–35} The specific binding of

ions to lipid bilayers has been studied in a variety of systems including both negatively charged and zwitterionic lipids. For charged lipids, the obvious role of ions is to compensate for the lipid charge.^{36,37} However, several studies have confirmed that ions interact in an analogous way as in zwitterionic lipid bilayers.^{18–22}

Despite experimental evidence that ions may alter the structural properties of lipid bilayers,^{38,39} the difficulties associated with precise experimental determinations still leave questions open. Thus, in a recent study of ion binding to a phosphatidylcholine (PC) bilayer the authors showed that certain ions, including different divalent ones and Li^+ , affect the gel to liquid-crystal transition.⁴⁰ In recent heat capacity measurements, the authors provided evidence that Na^+ reduces the area per lipid in bilayers of zwitterionic PC bilayers.²¹ Similarly, in a recent study, the differences observed in the nanomechanical properties of lipid bilayers with different electrolytes could only be explained as due to the increased lipid ordering originated by ion binding.⁴¹ Finally, in a recent X-ray diffraction study it was found that K^+ ions do not alter the structure of PC bilayers,⁴² showing an apparent differential behavior of potassium.

MD simulations of lipid bilayers with ionic solutions show that ions reduce the area per lipid for negatively charged lipids^{16,17,37,43} as well as for zwitterionic ones.^{18,21,22} Moreover, in a very recent MD study on ion penetration into PC bilayers almost no stable binding of K^+ ions to the lipid groups was observed, although the use of various force-fields yields different results.⁴⁴ The aim of this work is to understand the effect of different ions on the properties of the lipidic membrane and to analyze the differential behavior due to charge and size. For this purpose, eight 40 ns MD simulations of DPPC bilayers have been performed with a 0.2 M concentration of XCl_N , where $\text{X} = \text{Li}^+$, Na^+ , K^+ , Mg^{2+} , Ca^{2+} , Sr^{2+} , Ba^{2+} , and Ac^{3+} , and N is the cation charge. Despite the lack of biological interest in lithium, strontium, barium, and actinium, they were included to cover a larger range of ion parameters. Additionally, the effect

[†] Technical University of Catalonia (UPC).

[‡] Royal Institute of Technology (KTH).

of electrolyte concentration was tested by performing simulations with NaCl and KCl at 1 M concentration. The effects of the different ions were compared with a simulation of a pure DPPC bilayer in water that was used as reference. Present results indicate that ions Li^+ , Na^+ , Mg^{2+} , Ca^{2+} , Sr^{2+} , Ba^{2+} , and Ac^{3+} bind to the head-groups of DPPC and alter structural properties of the bilayer such as the area per lipid or the lipid head dipole orientation. However, potassium ions behave in a different manner, not binding to the head-groups and leaving the properties of the bilayer close to those of a bilayer in pure water. These results are consistent with all the experimental evidence available in the literature. However, because of the different results for potassium obtained in previous MD simulations, attributable to the force-field,⁴⁴ it cannot be excluded that, using a different force-field or longer simulation times, ions could penetrate the head-group without affecting structure and area per lipid of the bilayer. Further investigation of the effects of ion parameters to be used in simulations with lipid bilayers is needed.

Methods

Molecular Dynamics Simulations. All computer simulations were performed using the parallel version of the GROMACS 3.2 package.^{45,46} Each system was subject to periodic boundary conditions in the three coordinate directions. The temperature was kept constant at 323 K (well above the gel/liquid crystalline phase transition temperature of 314 K) using separate thermostats for lipids, water, and ions.⁴⁷ The time constant for the thermostats was set to 0.1 ps except for water, for which a smaller value of 0.01 ps was used. The pressure was kept at 0.1 MPa in the three coordinate directions using independent Berendsen barostats with a time constant of 1.0 ps.⁴⁷ A flexible cell geometry was chosen with the use of the NPT ensemble since other commonly used ones such as the NVT or the NP_{τ} -AT inherently fix the area per lipid.^{19,48,49} The equations of motion were integrated using the leapfrog algorithm with a time step of 4 fs. All bonds were kept frozen using the LINCS algorithm.⁵⁰ The bonds and the angle of the water molecules were fixed using the analytical SETTLE method. Lennard–Jones (LJ) interactions were computed with a cutoff of 1.0 nm, and the electrostatic interactions were treated with the Particle Mesh Ewald (PME) procedure.⁵¹ DPPC lipids were modeled using a variation of the force-field parameters described in ref 4, in which LJ parameters are computed as combinations of the single atomic ones according to the combinations rules of the OPLS-AA implementation in GROMACS. These parameters have been used in recent simulations of rhodopsin embedded in DPPC bilayers⁵² and equally reproduce the experimental area per lipid of pure DPPC bilayers in the liquid crystalline phase.^{4,13,53} Finally, ion parameters (listed in Table 1) were taken from the OPLS-AA force-field⁵⁴ currently implemented in GROMACS, and water molecules were treated using the TIP3P model.⁵⁵ Although different ion force-fields provide different results in specific properties,⁵⁶ the choice of the ion parameters does not appear to be critical for the purpose of the present work. Specifically, we computed the interaction energy between the different cation–oxygen pairs in the present work (data not shown), concluding that, first, differences in the cation–oxygen interactions for any oxygen type in the most commonly used force-fields are small, and second, the preceding differences for a specific cation are smaller than those between different cations. This suggests that cation–oxygen interaction energies follow the same trend independently of the parameters chosen even if combining different force-fields.

TABLE 1: Cationic Properties in the Present Study

ion	* σ (nm) ^a	* ϵ (kJ/mol) ^a	rdf cutoff (nm) ^b	est. radii (nm) ^c
Li^+	0.2126	0.0765	0.27	0.071
Na^+	0.3330	0.0116	0.31	0.103
K^+	0.4935	0.0014	0.36	0.143
Mg^{2+}	0.1644	3.6636	0.24	0.070
Ca^{2+}	0.2412	1.8826	0.30	0.103
Sr^{2+}	0.3103	4.9499	0.34	0.119
Ba^{2+}	0.3817	0.1972	0.33	0.141
Ac^{3+}	0.3473	0.2261	0.33	0.119

^a OPLS Lennard–Jones parameters with Gromacs version 3.2 used for the cations (file ffoplsaamb.itp). ^b Largest cation–oxygen distance for a water molecule in the first coordination shell taken from oxygen/cation RDF. ^c Estimate of the ionic radii is given as the position of the first peak of the oxygen/cation rdf less 0.137 nm (see text).

Starting Simulation Boxes. Binding of cations to a PC bilayer, starting from a random distribution of cations in the solvent, requires long simulation times since ions have to reach the water/lipid interphase region, a process that occurs in several tens of nanoseconds for some ions.²² With the aim of saving computer time, the starting boxes for the different simulations of the present work were generated from a previous simulation of a pure DPPC bilayer with water and sodium chloride.⁵² This system contained 256 lipids, $\sim 17\,000$ water molecules, corresponding to a hydration of 66 waters per lipid, and 61 sodium and 61 chloride ions, giving a concentration of sodium chloride of about 0.2 M. This box was generated in a simulation where electrostatic interactions were treated by using a twin cutoff of 1.0/1.8 nm and charge groups distributed in a way known to give artificially small areas in bilayers without ions.^{53,57,58} This procedure allows measurement of steady values for the area per lipid in less than 25 ns since the binding of cations to the lipid head-groups also reduces the area per lipid. This idea is supported by the fact that when ions are placed using a potential-based function, steady values of the area per lipid are obtained much faster than when using a random placing.⁵⁹ The initial size of the simulation boxes was $8.1 \times 8.1 \times 12.7 \text{ nm}^3$ (XYZ), the first two dimensions being those of the bilayer plane which corresponds to an area of 0.51 nm^2 per lipid.

Starting from the DPPC box containing 0.2 M NaCl, the remaining boxes with the same ion concentration were generated by replacing the sodium ions with the other cations. Moreover, the starting system containing NaCl is not in equilibrium when performing the simulations using the PME method. In the systems with divalent and trivalent ions, 61 or 122 water molecules were replaced by chloride ions to obtain an electro-neutral system. In the case of the simulations of NaCl and KCl at 1 M, 486 additional water molecules were substituted by 243 sodium and 243 chloride ions. In both cases, the ions were located at the most electrostatically favorable positions, using the GENION program from the GROMACS toolbox.

Results and Discussion

The present simulations show that with the exception of KCl, the rest of the systems exhibit the ions distributed in a double layer where the cations are closer to the bilayer than the chloride ions, generating a dipole in opposition to the one produced by the lipid head-groups. Moreover, cations are actually bound to the carbonyl or to the phosphate oxygens of the polar head-groups, whereas ions not bound are uniformly distributed in the water phase. Ion binding to the lipid molecules has effects on lipid order and results in a different charge distribution compared to the system with no electrolyte. Systems containing

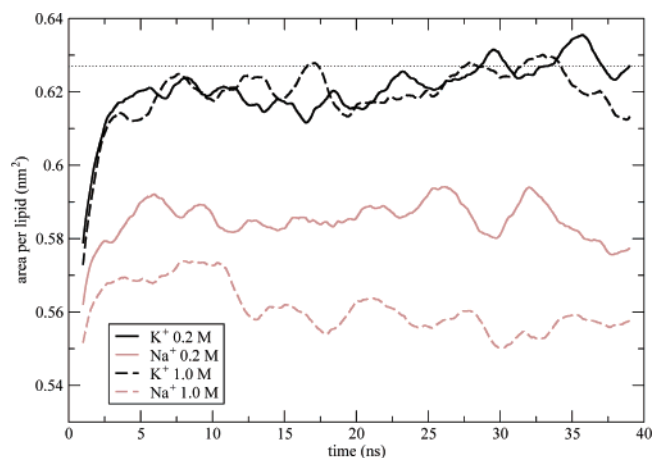


Figure 1. Time evolution of the area per lipid for the simulations with 0.2 M salt concentration and for the simulations with 0.2 and 1.0 M concentration of either NaCl or KCl. The curves are running averages over 2 ns. The straight dotted lines indicate the average area per lipid of the salt-free system.

KCl exhibit a differential behavior, showing no binding of potassium ions to the lipid head-group oxygens. A detailed analysis of these results is discussed below.

Figure 1 displays the time evolution of the area per lipid for the different simulations. The plot on the top displays the different systems with a 0.2 M saline concentration, whereas the one on the bottom shows a comparison of the simulations performed at 0.2 and 1 M concentration of sodium and potassium chlorides. As can be seen, in all cases the area per lipid reaches a plateau within 25 ns of simulation, indicating that the protocol used (see Methods) provided steady values for the areas much faster than usually required. The key point of the methodology used in the present work is to use a box of a DPPC bilayer and a 0.2 M NaCl aqueous solution generated using a cutoff to treat long-range interactions. In this conditions, ions,¹⁸ similarly to special group charges, artificially enhance lipid order.⁵⁸ Figure 2 shows the time evolution of the average number of ions bound per lipid, showing that, with the exception of the LiCl system, this parameter reaches a steady state within 5 ns. In the case of LiCl, the much longer simulation time required is related to the special behavior of the system, in which virtually all ions are bound to the bilayer at the end of the trajectory. This figure also shows that in the case of 1 M NaCl, as well as in the two simulations of KCl, the number of ions bound to the membrane decrease with time. This supports that the procedure used is robust enough to release the excess ions produced when sodium cations are mutated to different ones (see Methods). In contrast, Figure 3 displays the time evolution of the average number of lipids per ion, indicating that the system is not completely equilibrated for some polyvalent ions. Indeed, the equilibration process requires lateral rearrangement of lipids which is a rather slow process²² that has not yet converged in the present calculations. For this purpose, larger calculations are required that are beyond the scope of the present report.

Preferred Ionic Locations. Before discussing the effects of the ions upon the DPPC bilayer, we characterize the distribution of the important lipid head-group atoms. Plots of the number densities for the ions, phosphorus, and nitrogens are given in Figure 4 for systems with 0.2 M salt or no ions. The curves show average values over the two halves of the bilayer. In Table 2 we show positions of the maxima of the distributions and the distances between some of the maxima. The cations, except the potassium, are concentrated in a region 1.2–2.5 nm from the

center of the bilayer. The center of the distribution is located between the carbonyl and the phosphate oxygens of the lipids. In contrast, the potassium ions do not show a maximum in their distribution, suggesting that they are not bound to the bilayer. A closer inspection of the profiles shows minor differences (less than 0.2 nm) between the positions of the maxima in the other cation distributions.

The chloride ions are in all systems spread over a much wider region than the cations. There is a maximum in the distribution (except for KCl) but this is located just below 3 nm from the bilayer center, about 1 nm outside the maximum in the cation distribution. For the divalent and trivalent cations, the peaks become larger and wider with increasing charge because of the larger number of chloride ions present in the simulations. It is interesting to note that the chloride distribution in the system with MgCl₂ exhibits a shoulder at 2.3 nm. At this distance, chloride ions are necessarily coordinated to the cations bound to the membrane, suggesting a strong association between magnesium and chloride ions. A similar behavior is observed for the system with AcCl₃. In the system with KCl, the chloride density in the region below 4 nm from the bilayer center is even lower because there is no cationic charge density to be neutralized. The degree of chloride penetration to the membrane decreases in the following order for the different cations: Mg²⁺ > Ac³⁺ > Ca²⁺ ≈ Sr²⁺ ≈ Ba²⁺ > Li⁺ ≈ Na⁺ > K⁺. Further, the compensation of cation charge results in a stronger association between chloride and cations when the charge of the latter increases. As shown in Table 2, the distance between the maxima in the cation and the chloride distributions varies between 0.7 and 1.2 nm and indicates an inverse correlation with the total charge bound to the lipid head-groups (see below).

Number of Bound Ions. The computed radial distribution functions (rdf) of the water oxygens relative to the cations were used to define ion binding. Ions closer than the cutoff distance in column four of Table 1 were considered as bound. The first peak of the rdf, which lies between 0.20 and 0.30 nm, depending on ion size, contains the first coordination shell; that is, these ions are considered as directly bound. The average number of cations bound per lipid computed during the last 15 ns of each simulation is shown in Table 3. All systems at 0.2 M salt concentration except KCl and LiCl contained 0.16–0.18 bound cations per lipid which corresponds to about 70% of the cations. At 1 M concentration, the corresponding numbers were 0.32 and 25%. To better understand these values, two simple estimates were performed considering the coordination properties of each ion type reported. First, a lower limit was obtained considering the average number of lipids per ion computed from the simulations and assuming that a lipid can only be part of the first or the second coordination shell of only one ion at a time. Similarly the maximum number of ions that a bilayer can bind can be determined by dividing the number of lipid oxygens in the system by the average number of lipid oxygens participating in both the first and the second coordination shell. In all cases, the actual values in the simulations are within, or close to, the limits obtained from these approximations.

In the simulations performed at 0.2 M salt concentration, the largest number of lipid bound cations was found for LiCl. Further, the number of bound ions decreases with increasing radius for the single charged (alkali) ions. Contrary to this, the number of bound divalent and trivalent ions is almost equal, independent of the radius. The simulations performed at 1 M salt concentration still show no potassium binding while the number of bound sodium ions almost doubles due to the fivefold increase of total ionic concentration. This suggests that the ion

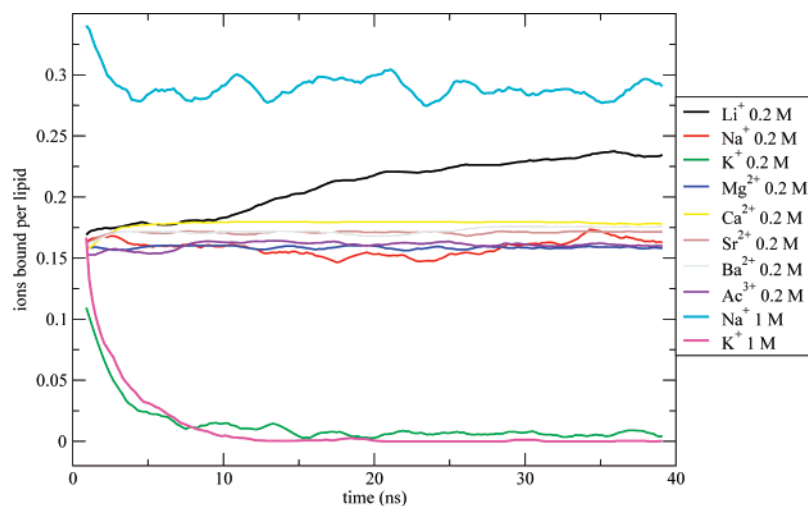


Figure 2. Time evolution of the number of ions per lipid bound to the lipid oxygen atoms.

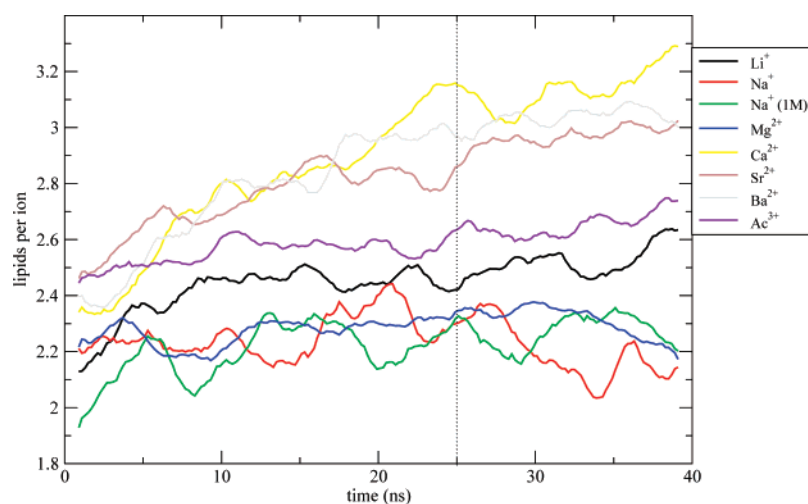


Figure 3. Time evolution of the number of lipids per ion.

binding is concentration dependent, although saturation can be achieved. As seen from Table 3, the maximum number of bound ions in the present simulations occurs with 1 M NaCl and is about one cation per three lipids. Even if we are starting to see saturation, it is still possible that this number could be slightly increased with salt concentrations beyond 1 M. The maximum bound positive charge per lipid is observed for 0.2 M AcCl_3 (about 0.5). Since we have not performed simulations with the divalent and trivalent ions at higher concentrations, we could not exclude that even more charge could bind to the membrane under such conditions. The present results also suggest that the bilayer might accommodate a larger number of lithium ions since they are smaller and bind in larger amounts to the bilayer at 0.2 M concentration. Moreover, it is also clear from the results for divalent and trivalent ions that the amount of charge provided by the monovalent ions is not limiting their binding.

Charge Distributions. The number density distributions of the phosphorus and the nitrogen atoms of the PC moiety are shown in Figure 4. The location of these atoms is crucial for the structure of the lipid bilayer. The distance between the peaks of these distributions directly reflect the tilt of the main part of the head-group dipole. A smaller contribution comes from the carbonyl dipoles. This affects directly the charge distribution perpendicular to the membrane surface and the dipole potential across the head-group region. The binding of cations in the lipid head-group region has a pronounced effect on the distribution of these groups. We observe that the maximum in the phos-

phorus density is shifted toward the water phase in the presence of all salts except KCl, in agreement with the increase in thickness (and decrease in the area per lipid) observed in previous simulations of PC lipids in sodium chloride.^{18,21,22} In all cases, this shift is accompanied by a reduction of the peak width, meaning that not only the bilayer thickness increases but also the lipid head positions become more well defined. This is related to the increased order of the system. The densities of both nitrogens and ester carbonyl oxygens (not shown) exhibit similar profiles as that of the phosphorus atoms and are affected in a similar way by the presence of ions. It can be seen in Table 2 that the locations of the oxygen atoms relative to the phosphorus are maintained in all cases. However, the presence of ions results in sharper distributions with reduced tails toward the water phase. The choline nitrogen distributions (Figure 4) are, in the presence of salts other than KCl, shifted toward the water phase (up to 0.35 nm) with the peak width relatively unaltered. This shift and the associated change of the charge distribution are due to the repulsive interactions between the choline nitrogens and the cations as well as due to the attractive forces between the anions and the PC groups.

The computed charge distributions perpendicular to the bilayer surface are shown in Figure 5 for the salt-free system and the systems with 0.2 M salt. Each system should, on average, be symmetric about the center of the membrane. Further, the existence of boundary conditions means that there could not be an electrostatic potential difference across the

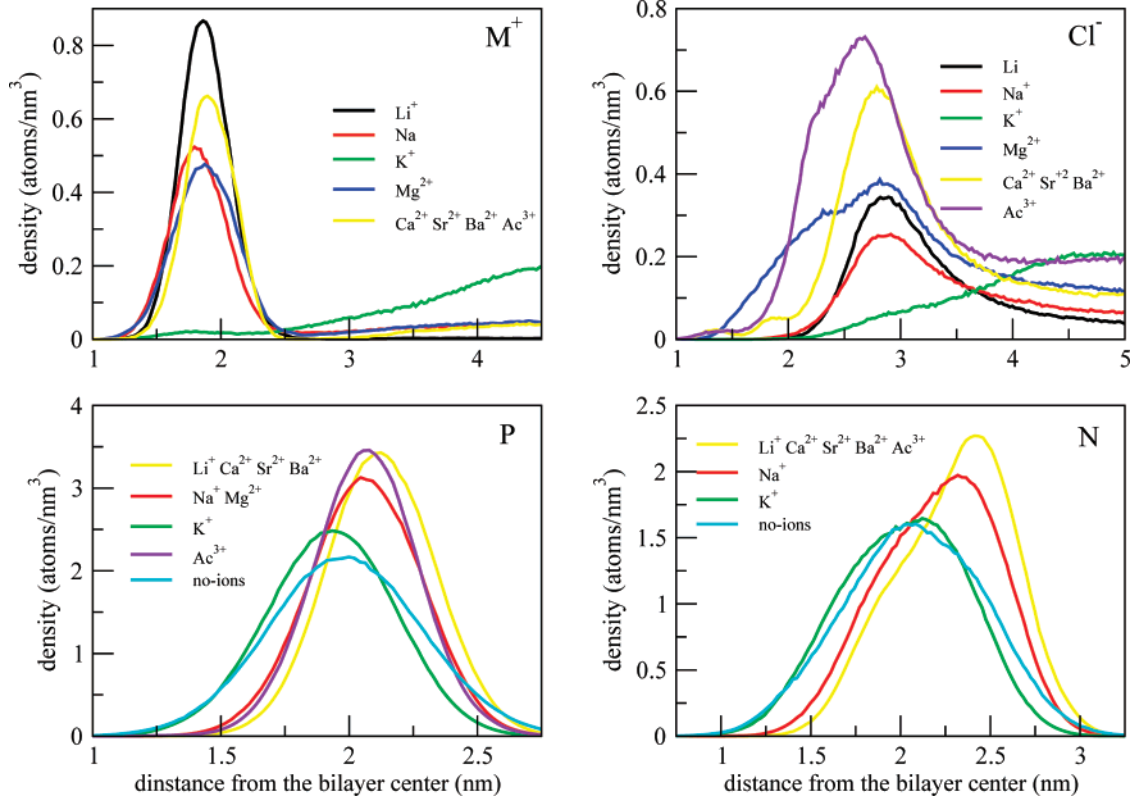


Figure 4. Partial number densities along the direction perpendicular to the bilayer plane for cations (top left), chloride ions (top right); the lipid phosphorus atoms (bottom left) and the nitrogen atoms (bottom right).

TABLE 2: The Position (nm) Relative to the Center of the Membrane of the Maxima in Different Number Density Profiles (left-hand side). The Distance (nm) between Some of the Peaks (right-hand side)^a

	density distributions maxima						distances between maxima				
	P	N	OP	OC	M	Cl	P-N	OP-M	OC-M	P-Cl	Cl-M
no ions	2.00	2.08	2.02	1.61			0.08				
Li ⁺	2.12	2.41	2.12	1.72	1.86	2.89	0.29	0.26	0.14	0.77	1.03
Na ⁺	2.04	2.32	2.09	1.68	1.79	2.91	0.28	0.30	0.11	0.87	1.12
K ⁺	1.93	2.12	1.97	1.54			0.19				
Mg ²⁺	2.06	2.33	2.10	1.69	1.87	2.82	0.27	0.23	0.18	0.76	0.95
Ca ²⁺	2.11	2.43	2.12	1.73	1.89	2.79	0.32	0.23	0.16	0.68	0.90
Sr ²⁺	2.11	2.39	2.11	1.73	1.92	2.78	0.28	0.19	0.19	0.67	0.86
Ba ²⁺	2.12	2.40	2.12	1.73	1.90	2.74	0.28	0.22	0.17	0.62	0.84
Ac ³⁺	2.08	2.40	2.08	1.71	1.92	2.68	0.32	0.16	0.21	0.60	0.76

^a P stands for phosphorus; N stands for nitrogen; OP stands for phosphate oxygens; OC stands for carbonyl oxygens; M stands for the different cations; and Cl for chloride ions.

periodic box. Therefore, the curves displayed are an average of both leaflets. The main feature of the charge distribution is consistent with the number densities of nitrogen and phosphorus atoms displayed in Figure 4. The charge distribution exhibits two regions with nonzero charge density: a negative one provided by the phosphate groups, and a positive one to the choline groups. Consequently, this charge distribution generates an electric dipole which is partially compensated by an opposing dipole generated by the polarized water molecules (see Figure 5). The result is a smooth total charge distribution, with maximum values about ± 0.1 charges/nm³. Three different types of charge distribution profiles can be identified: (1) the profile of the bilayer and water without ions; (2) the system containing KCl; (3) the systems with the remaining salts studied. The main difference between these profiles lies in the presence of a peak at 2.5 nm which occurs in all systems except those without salt or with KCl, originating from the shift of the choline groups toward the water phase driven by the binding of cations to the

bilayer. Both the salt-free system and that with KCl have single positive maxima close to the maximum of the phosphorus density distribution because in the latter, the potassium and the chloride ions are almost uniformly distributed. The systems with the remaining salts also exhibit differences in their charge density profiles since the location of the maxima in the charge distributions depends on charge and number of bound ions. The region with negative charge density is broader than that with positive charge, consistent with the broader distribution of chloride ions shown in Figure 4. Two major peaks with positive charge density are observed 2.0 and 2.5 nm from the bilayer center originating from the cations and choline nitrogens, respectively. In addition, a smaller maximum in the charge density can be observed at 1.3 nm originating from the ester carbons. This peak is not observed in the salt-free system, suggesting that the ions polarize the ester groups. On the other hand, minima in the charge density are found around 1.7, 2.2,

TABLE 3: Summary of the Computed System Properties

	ion/lipid			charge bound/lipid (e) ^d	dipole angle (deg)	area/lipid (nm ²) ^e	drop area lipid/ion lipid (nm ²)
	computed ^{a,b}	estimated minimum ^b	estimated maximum ^c				
no ions	0.00	—	—	0.097	14.7	0.627	—
Li ⁺ 0.2 M	0.23	0.17	0.28	0.184	28.5	0.557	0.300
Na ⁺ 0.2 M	0.17	0.18	0.28	0.161	23.8	0.585	0.247
Na ⁺ 1 M	0.32	0.18	0.28	0.186	28.0	0.556	0.222
K ⁺ 0.2 M	0.01	—	—	0.110	14.9	0.627	—
K ⁺ 1 M	0.00	—	—	0.109	16.0	0.623	—
Mg ²⁺ 0.2 M	0.17	0.17	0.31	0.184	28.6	0.583	0.258
Ca ²⁺ 0.2 M	0.18	0.14	0.21	0.208	33.0	0.548	0.440
Sr ²⁺ 0.2 M	0.17	0.14	0.20	0.205	32.4	0.555	0.419
Ba ²⁺ 0.2 M	0.18	0.14	0.20	0.206	32.2	0.557	0.399
Ac ³⁺ 0.2 M	0.16	0.15	0.22	0.221	35.0	0.561	0.402

^a Computed average number of ions bound per lipid. ^b See text. ^c Positive charge bound per lipid (including cations, chloride ions, and water). ^d Angle between the P–N vector and the bilayer plane. ^e Ration decrease area per lipid/ion per lipid.

and 2.5–3.0 nm due to the ester carbonyl oxygens, the phosphate oxygens, and the chloride ions, respectively.

As discussed above, the binding of ions to the lipid head-groups creates a charge dipole of cations and chloride ions which qualitatively resembles the charge dipole profile of polarized water molecules close to the bilayer head-groups. Interestingly, the magnitudes of the maxima in the charge densities provided by both the cations and the chloride ions are comparable or larger than those of the lipid head-groups in the system without ions. Furthermore, it is clear that the ionic charge densities alter the charge density distributions of lipid head-groups and water,

resulting in a different net distribution. From the plots in Figure 5, the cumulative charge, including the net ionic charge and that of the polarized water, is obtained by integration over the spatial dimension perpendicular to the bilayer from the center out to the box limits. Since the system is neutral, this net charge will vanish at some distance which typically is about 3.5 nm from the center. Then, the total positive charge bound to the bilayer is taken from the maximum of the integrated charge density, typically about 2.25 nm. From the number of ions per lipid listed in Table 3, it can easily be seen that the charge bound per lipid at 0.2 M ranges between 0.10 and 0.22, where the

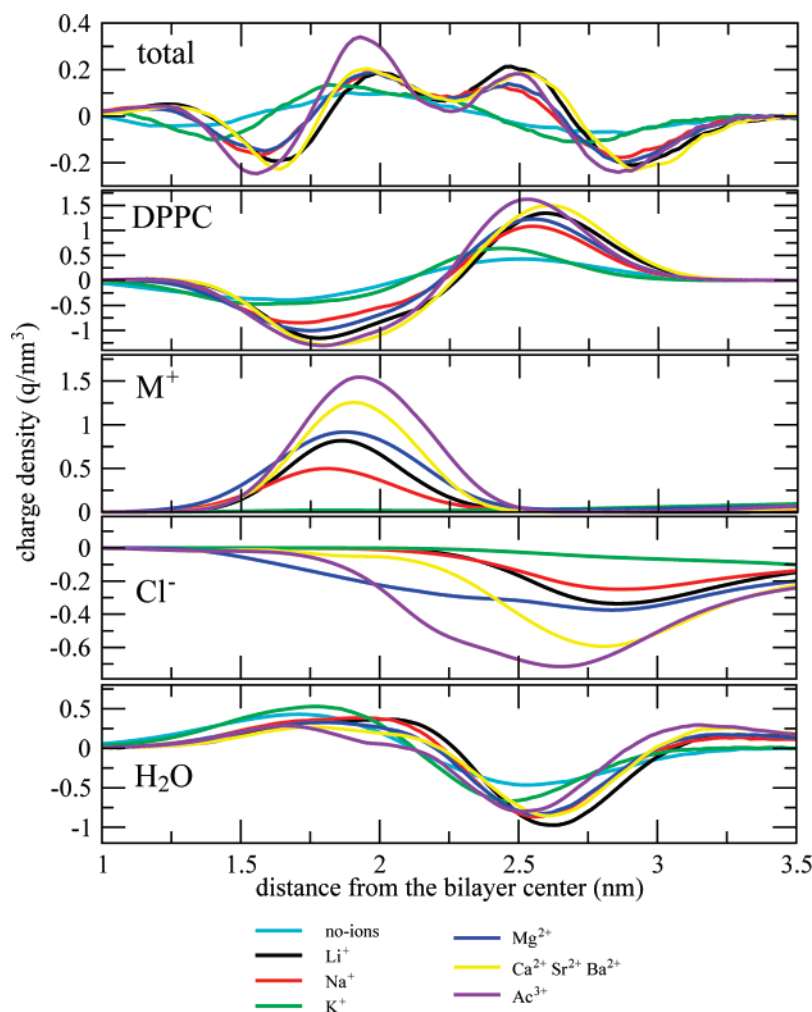
**Figure 5.** Charge densities in the direction perpendicular to the bilayer plane.

TABLE 4: Total Electrostatic Potential Difference (V) between the Center of the Water Layer and the Center of the Membrane, the Separate Contributions from Lipids, Ions, and Water, and an Approximate Result for the DPPC Head-Group Lipids^a

ion	total	DPPC	ions	H ₂ O	DPPC (dipole approx)
no ions	-0.55	4.95	0.00	-5.48	2.60
Li ⁺ 0.2 M	-0.73	9.35	-11.60	1.51	5.69
Na ⁺ 0.2 M	-0.66	7.79	-7.37	-1.06	4.55
Na ⁺ 1 M	-0.66	9.14	-9.36	-0.87	5.63
K ⁺ 0.2 M	-0.54	5.02	-0.41	-5.13	2.63
K ⁺ 1 M	-0.51	4.96	-0.09	-5.48	2.85
Mg ²⁺ 0.2 M	-0.73	9.06	-10.30	0.51	5.49
Ca ²⁺ 0.2 M	-0.75	10.50	-13.13	1.83	6.70
Sr ²⁺ 0.2 M	-0.71	10.15	-12.39	1.49	6.52
Ba ²⁺ 0.2 M	-0.73	10.15	-12.55	1.65	6.40
Ac ³⁺ 0.2 M	-0.69	10.32	-12.39	1.32	6.97

^a The DPPC head-groups are represented by a positive electron charge and a negative electron charge located at each end of a vector of length 0.36 nm forming the angle with the membrane plane given in Table 3.

lowest values correspond to the system without salt or with KCl. Interestingly, these results suggest that the total bound charge does not increment much upon ion binding, indicating that there are other changes in the system that smooth the additional charge, specifically in the lipid bilayer, the chloride, and the water distributions.

The electrostatic potential was computed by integrating the one-dimensional Poisson equation twice:

$$\frac{\partial^2 \phi}{\partial z^2} = \frac{\rho(z)}{\epsilon_0} \quad (1)$$

where Φ is the electrostatic potential, the charge density $\rho(z)$ is taken from Figure 5, and ϵ_0 is the dielectric permittivity of vacuum. For boundary conditions, we put the potential and its derivative to zero in the center of bilayer. The resulting total potential is shown in Table 4 together with the individual contributions of each part of the system. Consistent with the results reported in previous simulations,^{23,53} the total potential difference across the membrane/water interface in the system without ions is -0.55 V, resulting from a lipid contribution of +4.95 V and a water contribution of -5.48 V. The two simulations with KCl exhibit similar values, with a minor decrease in the system with the highest salt concentration. Further, it can be seen that the net potential difference from the potassium and chloride ions is small or negligible in these systems.

For the systems containing salts other than KCl, the total potential difference across the bilayer/water interface may be up to 50% larger than for the salt-free system. However, these net values are small compared to the potential difference created just by the ions, which ranges between 8 and 12 V in the present systems, because the lipid head-group and the water molecules shield it.²¹ The ionic distribution corresponds to an electric dipole with its positive end oriented toward the membrane, whereas the dipole from the lipid head-groups is oppositely oriented. The results indicate that the ions induce a change in head-group tilt that increases the size of the lipid dipole, and of the potential, almost by a factor two. Additionally, the positive end of the net dipole from water, that pointed toward the membrane in the salt-free system, changes to the opposite direction with the presence of salt. Therefore, in addition to the 7.5–10.5 V potential from the lipid head-group, water

provides about +1.5 V in the same direction which compensates most of the ionic potential.

Effects on the Lipid Head-Group. The cations bound to lipid head-group oxygens exert a repulsive force on the choline groups, pushing them further out into the water environment in agreement with early experimental results.³² This observation is consistent with the role of lipid head-groups as charge sensors which was pointed out in early works^{60,61} and in recent reports based on MD simulations. More precisely, a change in the orientation of the lipid head-groups can alleviate the charge provided by the bound ions.^{18,19,21,22,48} The average lipid head-group dipole tilts obtained from the present calculations, measured from the bilayer plane, are reported in Table 3. The average angle of the dipole in a system without ions is 15°, in good agreement with other results of different PC bilayers, which ranged between 10 and 20°.^{17–21}

Inspection of the table indicates that this angle may increase by up to 20° depending on ion type and salt concentration. The values obtained are in qualitative agreement with similar studies with bilayers with NaCl^{20,21} and 0.2 M CaCl₂²² despite that the results cannot be directly compared because of the different concentrations and waters/lipid and ions/lipid ratios. In the simulations with NaCl an increased dipole angle is observed with increasing salt concentration, consistent with the larger number of ions bound to the bilayer. In contrast, KCl results in a negligible effect on the dipole angle, which remains very close to that of the salt-free system both at 0.2 and 1 M salt concentration. The simulations indicate that in the present interval of bound charges (0–0.5 positive charges per lipid), the dipole angle with respect to the membrane plane increases with about 40° per positive charge and lipid.

The tilt angle correlates well with the bound ionic charge per lipid integrated from the sum of the charge distributions of the ions and the water molecules described in the preceding section (see Table 2). These results support the idea of lipid head-groups being charge sensors suggested in early experimental work. The electrostatic potential change across the lipid/water interface can be calculated by integrating the charge density from lipids, ions, and water twice in the Poisson equation. Using the charge neutrality of the system one may show that:

$$\Delta\phi = \frac{1}{\epsilon_0} \frac{P}{A}$$

where P/A is the total dipole moment per unit area, defined from the charge distribution or the positions of the individual charges as:

$$\frac{P}{A} = \int z\rho(z) dz = \frac{1}{A} \sum_i q_i z_i$$

For the lipid part of this dipole, one has to include all the fractional charges of the lipids including the carbonyl dipoles and the actual charge distribution between phosphates, oxygen, nitrogen, and hydrocarbon groups. A common simplified model is to consider the head-group as consisting of one full negative charge at the position of the phosphorus and one full positive charge at the position of the nitrogen or still simpler as a full negative and positive charge at a distance of 0.36 nm. This corresponds to a dipole of 5.76×10^{-29} C m = 17.3 debye. In such a model, the contribution to the electrostatic potential change across the lipid/water interface from the lipids is entirely

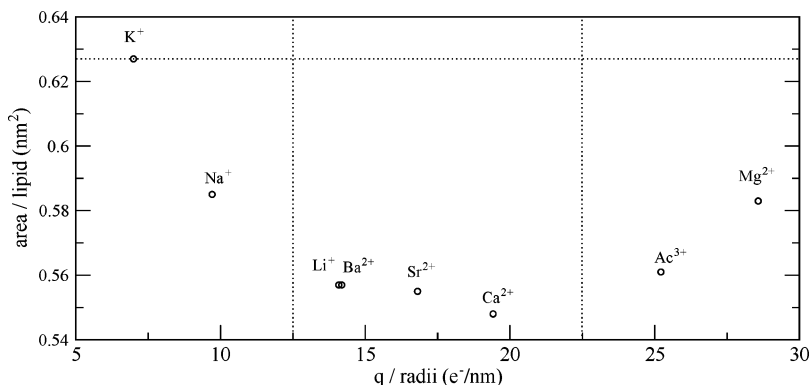


Figure 6. Area per lipid versus the ratio of charge/radii for the cations in the simulations at 0.2 M chloride salt concentration.

given by the tilt angle θ of this dipole and the area per lipid, A , as:

$$\Delta\phi = \frac{1}{\epsilon_0} \frac{P}{A} \sin \theta$$

The potential change in this dipole approximation has been calculated and is shown in the last column of Table 4. These values are smaller than those calculated from the full actual charge distribution, but there is a good correlation as $\Phi = 1.34\Phi_{\text{dip}} + 1.47$, indicating that the actual charge distribution has, in addition to this simplified model, contributions that increase the total dipole perpendicular to the bilayer with a constant value as with a dipole that is parallel to the PN dipole. The main contribution to this comes from the carbonyl region.

Ordering of the Lipid Molecules. The ordering in a lipid bilayer may be characterized by NMR order parameters, from fraction *trans* bonds, or from the area per lipid. All these measures are fairly well correlated. Although the area per lipid is not easily accessible experimentally, it is easy to calculate from simulations. Average values from the present simulations (shown in Table 3) provide clear evidence that the binding of cations to the lipid head-groups exerts an effect on the area per lipid. The bilayers exhibit in most cases smaller areas per lipid and larger thicknesses in agreement with previous results.^{18,21} The latter can be easily monitored from the density distributions of the lipid phosphate moieties shown in Figure 4. In the system without salt each monolayer exhibits the maximum number density centered about 1.9 nm from the bilayer center, while the simulations with salts other than KCl have the maximum shifted toward the water environment on each monolayer. Moreover, the ions induce a narrowing of the distribution width, suggesting that the induced lipid order is associated with a less fluctuating distribution of the phosphate moiety relative to the bilayer center. In spite of the almost negligible number of ions bound to the PC moieties in the potassium-containing systems, density distribution exhibits an equally pronounced narrowing of the peak, which seems to be the reason for the small shift of the maximum toward the bilayer center.

The area per lipid for the salt-free DPPC bilayer is $0.627 \pm 0.005 \text{ nm}^2$ in the present simulations, in good agreement with the experimental value of $0.64 \pm 0.02 \text{ nm}^2$ reported for a pure fully hydrated DPPC bilayer in the liquid crystalline phase.⁶² In contrast, the area per lipid computed from the simulations with salts other than KCl exhibit smaller values, as it is also reported in recent MD studies performed on Na^+ -DPPC¹⁸ and $\text{Na}^+/\text{Ca}^{2+}$ -POPC^{21,22} systems. Contrary to this, the area per lipid for the systems with both concentrations of KCl is similar to that of the salt-free system, which is consistent with our observation that potassium ions do not bind to the lipid head-

groups and with recent experimental results for KBr.⁴² Sodium exhibits a decrease in the average area per lipid, which gets slightly more pronounced at the highest concentration, similarly to the results reported in ref 21. The results for monovalent ions show a correlation between ordering effect, number of bound ions, and inverse ionic radii. For the same number of bound ions per lipid, the ordering effect upon the bilayer is larger for polyvalent than for monovalent ions.

Ion Features Contributing to the Area per Lipid. Present results indicate that each bound cation per lipid reduces the area per lipid, typically about 0.3 nm^2 (see Table 3), with differences depending on the ion type and with the largest effect observed for calcium. Moreover, the simulations at different concentrations of NaCl suggest that we are starting to see saturation of the number of bound ions as also reflected in the area per lipid. A fivefold increase in the ion concentration results in a doubling of the amount of bound ions, but the effect of this doubling of the amount of bound ions on the area is less than half the effect of the first ions. All cations studied, except potassium, bind to the lipid oxygens, modify the tilt of the lipid dipole, induce rearrangements around lipid head-groups, and affect the order of the acyl chains. Thus, it is reasonable to hypothesize that the ordering effect produced by a cation will depend on the number of ions bound to the lipid molecules and on specific cation features such as the radii charge, coordination number (CN), and energy of hydration.

The effect upon the area per lipid from binding of cations can be rationalized in terms of the charge/radius ratio as shown in Figure 6. The ionic radii were computed by subtracting the water oxygen radius (assumed to be constant) from the maximum of the radial distribution function (rdf) of the water oxygens around the ion, according to the procedure described in a previous work.⁴⁰ This approximation avoids the uncertainties in ionic radii when bound to the membrane since they depend on the CN they exhibit. A value of 0.137 nm for the water oxygen radius gives the best fitting to the experimental radii⁶³ based on the actual CN for the ions when bound to the lipids obtained from the present calculations (see Table 1).

The plot of the area per lipid versus the charge/radius can be divided into three parts: First, monovalent ions with ratios between 0 and 14 exhibit a drop on the area from the value of the pure system up to the maximum decrease observed. Second, for divalent ions with ratios between 14 and 20 the drop is much smaller. Finally, for Mg^{2+} and Ac^{3+} ions, with ratios larger than 25, the behavior of the area per lipid changes and starts increasing again. There are different sources for this behavior as discussed below.

The strength of the interactions between the ions and the bilayer are of importance in order to explain the effects of ions

on lipid order. Recently, it has been shown that changes on the phase transition temperature of PC bilayers exhibit a linear correlation with the electrostatic free energy of the ions in water.⁴⁰ Thus, one would expect that the present results can be understood from the differences in ion/oxygen interaction potentials. In the present work the interaction between a cation and a water/lipid oxygen atom is the combined effect of the Coulombic and the Lennard–Jones (LJ) terms. These combine into a potential well that may be described by a depth and the position of the minimum. Since the Coulombic term is attractive and the LJ repulsive at shorter distances, for the same valence a cation with a larger radius exhibits a shallow minimum in the potential curve. The present results suggest that the K^+ well is so shallow that ions do not bind to the lipid head-groups. Despite the different ion force-fields available, the minimum has a similar energy in the commonly used force-fields (data not shown). Additionally, to the present simulation using the OPLS-AA force-field for ions, very recent results have shown a similar effect using GROMACS and CHARMM.⁴⁴ Moreover, the result shown in Figure 6 can be used as a predictive tool for other ions not present in this study. It is reasonable to expect that monovalent ions that are larger than potassium, e.g., rubidium and cesium, behave similarly, not binding to the lipid head-groups. Because of its shallow well, sodium exhibits the largest fluctuations in the number of ions bound (see Figure 2), suggesting that mean lifetime for a sodium–lipid complex is shorter than for other cations. In contrast, polyvalent ions exhibit a deeper well even for the largest ions studied since the larger Coulombic term compensates for the penalty on the well depth because of the radius.

A larger cation radius provides larger CN and therefore an additional number of binding possibilities to the lipid oxygens. Therefore, the computation of the CN for each ion type is necessary to understand the present results. The CN for the first shell were computed for cations coordinated either only to water oxygens or to the lipid oxygens in any extent. The cutoffs considered were taken from the positions where the first peaks in the rdf vanish (see Table 1). Additionally, the CN for the second shells were computed from the second peak in the rdf, which provides a cutoff approximately 0.25 nm larger than the first shell. According to the present simulations, the average CN for the first shell for the cations bound to at least one lipid atom range between 4 and 9, as shown in Table 5A. The average values are similar to those obtained in pure water and are in reasonable agreement with those recently reported in the literature for metal hydrates obtained either from experiments or *ab initio* calculations (see ref 64 and references therein). The magnesium ion is the only ion exhibiting a significantly different coordination than experimentally determined. However, a strong association with chloride, reflected in a large peak at 2.5 nm in the pair correlation function with the chloride ions, is observed (not shown) and may explain this behavior. A similar peak is observed at 3.0 nm for the lithium ion, but the larger distance seems to be the reason for the minor effect on the CN.

The CNs observed in the simulations for a specific ion may differ, as seen from the relative populations displayed in Figure 7a. For the cations with the same valence, a larger radius produces a shift of the most populated CN toward larger values, in agreement with experimental evidence and recent MD simulations.²² The relatively wide distribution for potassium reflects the lower binding energy exhibited by this cation. Ions bound to the lipid head-groups are not completely surrounded by lipid oxygens and remain partially hydrated. Therefore, it may be better to use the actual number of lipid oxygens

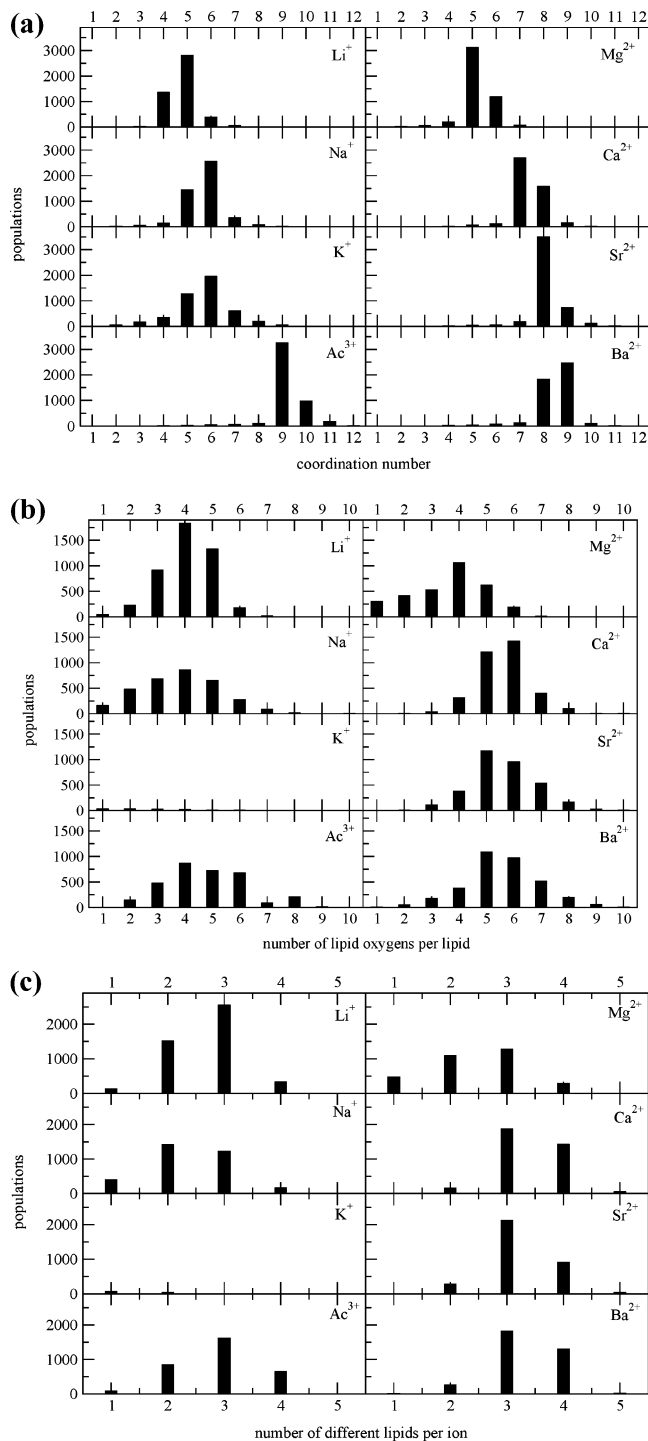


Figure 7. Populations for (a) the CN of the ions when bound to one or more lipid oxygen atoms. The coordinating atoms include water and lipid oxygens and chloride ions. (b) The number of lipid oxygens per cation. (c) The number of different lipids per cation.

coordinated to an ion instead of using the CNs given previously. Present simulations indicate that all cations, except potassium, have 3–5 lipid oxygens in the first coordination shell and 8–13 in the second (Table 5A), resulting in 11–18 lipid oxygens per cation in total. Each ion exhibits, however, a wide range of possible coordinations as can be seen from the populations displayed in Figure 7b.

These results suggest that ions can modulate lipid order by acting as cement between the neighboring lipids. If this is true, the modulation should depend on the number of different lipids

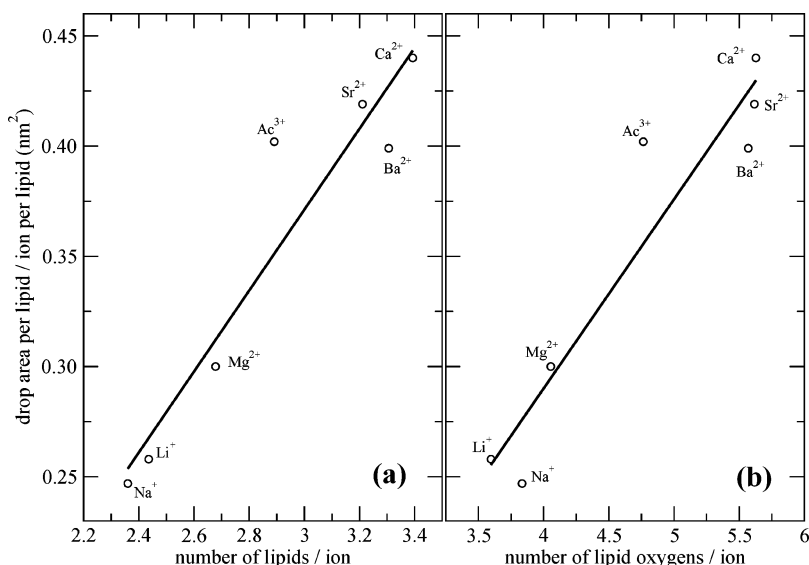


Figure 8. Drop in the area per lipid/ion per lipid ratio versus (a) the average number of different lipids bound per ion and (b) the average number of oxygens per ion, in the first coordination shell.

TABLE 5: Coordination Properties of Each Atom Type

A.									
ion	coordination no. (CN) ^a			no. of lipid oxygens ^b			no. of lipids ^c		
	water	DPPC	water exp ^d	LipO ^{1st}	LipO ^{2nd}	Lip O ^{tot}	1st CS	2nd CS	total
Li ⁺	4.7	4.8	4–5	4.1	10.3	14.3	2.7	3.1	5.8
Na ⁺	5.2	5.8	4–6	3.8	10.4	14.1	2.4	3.3	5.6
Na ⁺ (1 M)	5.8	5.8	4–6	3.5	9.6	13.1	2.3	3.1	5.4
K ⁺	5.6	5.5	4–6	–	–	–	–	–	–
Mg ²⁺	4.8	5.4	6	3.6	9.2	12.8	2.4	3.4	5.8
Ca ²⁺	7.7	7.2	6–8	5.6	13.8	19.4	3.4	3.8	7.2
Sr ²⁺	8.0	8.2	7–8	5.6	14.5	20.2	3.2	3.8	7.0
Ba ²⁺	8.4	8.5	7–9.5	5.6	14.5	20.1	3.3	4.0	7.3
Ac ³⁺	9.0	9.2	–	4.8	13.2	17.9	2.9	3.9	6.8

B.									
ion ^e	no. of oxygens in the first coordination shell ^f				no. of oxygens in the second coordination shell ^f				
	free PO ₄ ²⁻	ester PO ₄ ²⁻	free COO-R	ester COO-R	free PO ₄ ²⁻	ester PO ₄ ²⁻	free COO-R	ester COO-R	
Li ⁺	1.9	0.1	1.9	0.1	4.1	4.2	2.8	3.2	
Na ⁺	1.4	0.2	1.9	0.1	3.8	3.5	3.3	3.4	
Na ⁺ (1 M)	1.4	0.2	1.8	0.1	3.7	3.4	2.9	3.0	
Mg ²⁺	1.6	0.1	1.9	0.0	4.1	3.4	2.8	2.2	
Ca ²⁺	3.0	0.0	2.5	0.1	6.3	6.2	3.4	3.5	
Sr ²⁺	2.9	0.1	2.5	0.1	6.2	6.0	3.9	4.1	
Ba ²⁺	2.8	0.1	2.6	0.0	6.3	6.0	4.0	3.8	
Ac ³⁺	2.6	0.1	2.0	0.0	6.2	5.5	3.5	2.8	

^a CN–exp represents the experimental CN in metal hydrates. ^b LipO^{1st}, LipO^{2nd}, and Lip O^{tot} refer to the average number of lipid oxygens present in the first, second, or both coordination shells, respectively. ^c Number of different lipids per cation in the first and second coordination spheres. ^d From Tables 4 and 6 of ref 64. ^e K⁺ has not been included since the values are not meaningful due to the small number of ions bound to the bilayer. ^f CN–bound and –free indicate if the CN has been calculated for ions bound or free, respectively, to the lipid oxygens.

linked by a single ion. Therefore, an analysis of the average number of lipids per cation in the present trajectories has been performed. The results indicate that on average each ion interacts with 5.6–7.4 lipids of which 2.4–3.4 are in the first and 3.1–4.0 the second coordination shell. This indicates that despite differences in the average CN, the number of lipids that a cation can link increases only slightly for ions with larger CN. However, the results in Figure 3 suggest that longer simulations may provide slightly larger oxygens per ion for some polyvalent ions, as this parameter is not fully converged in 40 ns. Indeed, a recent MD study of the binding of Ca²⁺ ions to POPC bilayers observed about 4 lipids per ion.²² However, although it is true that longer simulations would provide slightly larger values than

reported in Table 5 A, they would still be smaller than 4 lipids as reported in the preceding reference. One possibility is that such differences arise from the force-field used for the ions, although it is also possible that they are due to the fact that the ratio ions/lipid is almost eight times larger in the present work, and therefore there are less free lipids. The histogram of the number of lipids per ion shown in Figure 7c reflects the wide range of possibilities. Moreover, ions exhibiting low CN require less lipid oxygens, and therefore the maximum number of ions that the bilayer can bind is larger.

The relative preference of the different cations for each of the four oxygen types present in a PC lipid is shown in Table 5B. This shows that the first coordination shell involves mainly

free (nonesterified) oxygens, either from the carbonyl or phosphate groups. The number densities shown in Figure 4 reveal that the cations are located in an intermediate region between the carbonyl and the phosphate oxygens. Table 5B shows that, in general, there is little difference in ion preference for different coordinating oxygens. The situation differs, however, if we look at each cation separately. Lithium interacts equally with both oxygen types, sodium and magnesium prefer the phosphate oxygens, and calcium, strontium, barium, and actinium prefer the carbonyl oxygens. Similar results are obtained from the rdf between cations and oxygen atoms (not shown). Regarding the second coordination shell, the present results suggest that the non-free oxygens are important as anchoring points for the water molecules that are part of the first coordination shell, specifically the esterified phosphate oxygens.

A recent study outlined the existence of discrepancies regarding the localization of cations within simulations.¹⁹ Ion penetration must be sensitive to the strength of the interactions between hydrocarbon lipid tails and to the balance between LJ and electrostatic interactions in the different force-fields used. To our knowledge, there are three lipid force-fields that have been used in studies of cation–lipid interactions, the one implemented in CHARMM,⁶⁵ the one developed by Berger et al.⁴ for GROMACS,^{45,46} and the one designed by Smondyrev et al.⁷ for AMBER.⁶⁶ In the present work we have used the parameters of Berger et al. in the context of the OPLS-AA implementation in GROMACS (see Methods), a widely used combination in membrane protein simulations.⁶⁷ With the lack of experimental information about the cation localization, none of these force-fields can *a priori* be considered better than the other for the present purposes. When more experimental information about specific binding of cations to lipid bilayers becomes available, it will be important to validate the different force-fields against that information, including ion parameters.⁵⁶

The analysis performed above suggests that the coordination properties have effects, though small, on the reduction of the area per lipid per binding ion. The decrease in area per lipid (see Table 4) shows a reasonable linear correlation with the average number of lipid oxygens being part of the first coordination sphere of a cation (Figure 8a). A similar tendency is observed for the average number of lipid molecules linked by the same cation (Figure 8b). These results are of considerable importance since some of the ions included in this study, e.g., K^+ , Na^+ , Ca^{2+} , and Mg^{2+} , are abundant in the aqueous solution surrounding biological membranes.

Conclusions

The effect of including different chloride salts in the water surrounding a DPPC bilayer has been studied in the present work by means of MD simulations. For this purpose, 40 ns simulations of DPPC bilayers in 0.2 M chloride salts with the cations Li^+ , Na^+ , K^+ , Mg^{2+} , Ca^{2+} , Sr^{2+} , Ba^{2+} , and Ac^{3+} were performed and analyzed. For sodium and potassium chlorides, additional simulations at a 1.0 M concentration allowed checking for concentration effects. A simulation without salt was also included and used as reference.

It is known that simulations of this kind of system require long sampling equilibration times. In order to reduce these times, the present calculations were carried out using a biased starting box generated using a treatment of the electrostatics that exaggerates lipid order and reduces area per lipid (see Methods). Since the presence of ions also favors small areas, the required

times to obtain a steady state for the area per lipid, once the system is lifted from these conditions, is reduced. These results suggest that the procedure is robust enough to provide reliable simulations; however, the equilibration times are still larger since reaching a steady value for the area per lipid does not guarantee that lipid molecules have completed the process of adaptation around the cations.

The simulations indicate that most ions actually do bind to the lipid head-groups, being distributed in the lipid–water interface generating a double layer, organized in such a way that the positive ions sit closer to the bilayer interface. Potassium chloride is one exception that exhibits a differential behavior not showing any binding to the lipid head-groups. All the systems at 0.2 M salt concentration contained 0.16–0.18 bound cations per lipid except the systems with KCl and LiCl. Moreover, for the alkaline cations, this number decreases with size, whereas for the rest of the ions, the number is almost identical. For the system containing 1 M NaCl, only a moderate increase of the number of bound cations from 0.17 up to 0.32 is observed, suggesting that there is a limit for the number of cations, or cation charges, that each lipid can bind.

The charge density profile of the system has contributions from lipid head-groups, ions, and water. Each contribution gives rise to a change of the electrostatic potential across the membrane/water interface. The different contributions tend to compensate for each other and result only in a small net potential drop when passing from the membrane to the water. This is, however, increased from about 0.5 V to about 1 V in the presence of ions. The lipid dipoles point toward the water and would give rise to an increased electrostatic potential of the order of 5 V without the water. Without ions, the water will overshield the head-groups and result in a net potential change of -0.5 V. The ionic distribution contributes with a potential change of about -10 V, but because of a larger tilt of the head-groups the contribution from the lipids will double and cancel this almost totally. Additionally, the water polarization will change sign and be reduced considerably compared to that in the salt-free system, resulting in a net potential change of about -1 V. The maximum contribution observed from the lipid heads is about $+10$ V, suggesting that there is a limit for this value given by a maximum value at which the head-group dipoles may tilt out of the membrane plane. This could then determine the maximum number of possible bound ions that would not give rise to excessive electrostatic fields.

With the exception of potassium, present simulations show that a large fraction of the cations are located around the carbonyl and phosphate oxygens of the lipid head-groups, whereas the chloride ions are located further out in the aqueous phase. The distance between the maxima observed in the cations and the chloride ions density distributions range between 0.7 and 1.2 nm for the different systems. Therefore, the ion distribution generates a dipole moment that opposes the dipole moment of the lipid head-groups modulated by the one created by the polarized water molecules in the opposite direction. However, the results reported in the present work regarding cation distributions need to be validated when more experimental information about specific binding of cations to lipid bilayers becomes available. Until then, it will be difficult to evaluate the strengths and weaknesses of the different force-fields including lipids, ions, and water molecules as well as the lack of computing the electronic polarizability in the currently available lipid force-fields. As recently stated,¹⁹ there are indeed

differences in the localization of cations between simulations using different force-fields^{19,21–23} that are waiting to be clarified.

The most important result of the present work is the observation of large differences between different ions depending on size and charge. Ion binding produces more ordered bilayers, i.e., thicker bilayers, and consequently smaller areas per lipid. However, to obtain good qualitative results, it is necessary to run very long simulations especially for the ions with higher valence. The results are sensitive to the force-field as shown in ref 44, and further investigation of the possible artifacts produced is necessary.

The present results have remarkable interest because many of the ions studied, specifically K^+ , Na^+ , Ca^{2+} , and Mg^{2+} , are present in biological membranes. Moreover, given that membranes are the natural barriers between electrolyte solutions with different concentrations, the results provide evidence that the ionic environment provides a contribution that may drive membrane asymmetry. We expect that the present results can shed light on the experimental results published in the literature regarding the differential behavior of alkaline ions in membranes.

Acknowledgment. A.C. wishes to express his gratitude to the Technical University of Catalonia for a fellowship to undertake his doctoral studies. The Spanish Ministry of Science and Technology supported this work through grant number SAF2005-08148-C04-01

References and Notes

- (1) White, S. H.; Wimley, W. C. *Annu. Rev. Biophys. Biomol. Struct.* **1999**, *28*, 319.
- (2) Singer, S. J.; Nicolson, G. L. *Science* **1972**, *175*, 720.
- (3) van der Ploeg, P.; Berendsen, H. J. C. *J. Chem. Phys.* **1982**, *76*, 3271.
- (4) Berger, O.; Edholm, O.; Jähnig, F. *Biophys. J.* **1997**, *72*, 2002.
- (5) Feller, S. E. *Curr. Opin. Colloid Interface Sci.* **2000**, *5*, 217.
- (6) Tieleman, D. P.; Marrink, S. J.; Berendsen, H. J. C. *Biochim. Biophys. Acta* **1997**, *1331*, 235.
- (7) Smondryev, A. M.; Berkowitz, M. L. *J. Comput. Chem.* **1999**, *20*, 531.
- (8) Lindahl, E.; Edholm, O. *Biophys. J.* **2000**, *79*, 426.
- (9) Feller, S. E.; Gawrisch, K.; MacKerell, A. D., Jr. *J. Am. Chem. Soc.* **2002**, *124*, 318.
- (10) Leekumjorn, S.; Sum, A. K. *Biophys. J.* **2006**, *90*, 3951.
- (11) Gurtovenko, A. A.; Patra, M.; Karttunen, M.; Vattulainen, I. *Biophys. J.* **2004**, *86*, 3461.
- (12) Pandit, S. A.; Bostick, D.; Berkowitz, M. L. *Biophys. J.* **2003**, *85*, 3120.
- (13) Hofsäβ, C.; Lindahl, E.; Edholm, O. *Biophys. J.* **2003**, *84*, 2192.
- (14) Pitman, M. C.; Suits, F.; Mackerell, A. D., Jr.; Feller, S. E. *Biochemistry* **2004**, *43*, 15318.
- (15) Pitman, M. C.; Grossfield, A.; Suits, F.; Feller, S. E. *J. Am. Chem. Soc.* **2005**, *127*, 4576.
- (16) Mukhopadhyay, P.; Monticelli, L.; Tieleman, D. P. *Biophys. J.* **2004**, *86*, 1601.
- (17) Pandit, S. A.; Berkowitz, M. L. *Biophys. J.* **2002**, *82*, 1818.
- (18) Pandit, S. A.; Bostick, D.; Berkowitz, M. L. *Biophys. J.* **2003**, *84*, 3743.
- (19) Sachs, J. N.; Nanda, H.; Petrache, H. I.; Woolf, T. B. *Biophys. J.* **2004**, *86*, 3772.
- (20) Gurtovenko, A. A. *J. Chem. Phys.* **2005**, *122*.
- (21) Böckmann, R. A.; Hac, A.; Heimburg, T.; Grubmüller, H. *Biophys. J.* **2003**, *85*, 1647.
- (22) Böckmann, R. A.; Grubmüller, H. *Angew. Chem., Int. Ed.* **2004**, *43*, 1021.
- (23) Berkowitz, M. L.; Bostick, D. L.; Pandit, S. *Chem. Rev.* **2006**, *106*, 1527.
- (24) Parsegian, V. A. *Ann. N. Y. Acad. Sci.* **1975**, *264*, 161.
- (25) Loosleymillman, M. E.; Rand, R. P.; Parsegian, V. A. *Biophys. J.* **1982**, *40*, 221.
- (26) Tatulian, S. A. *Eur. J. Biochem.* **1987**, *170*, 413.
- (27) Cunningham, B. A.; Gelerinter, E.; Lis, L. J. *Chem. Phys. Lipids* **1988**, *46*, 205.
- (28) Roux, M.; Bloom, M. *Biochemistry* **1990**, *29*, 7077.
- (29) Clarke, R. J.; Lupfert, C. *Biophys. J.* **1999**, *76*, 2614.
- (30) Akutsu, H.; Seelig, J. *Biochemistry* **1981**, *20*, 7366.
- (31) Altenbach, C.; Seelig, J. *Biochemistry* **1984**, *23*, 3913.
- (32) Brown, M. F.; Seelig, J. *Nature* **1977**, *269*, 721.
- (33) Lis, L. J.; Lis, W. T.; Parsegian, V. A.; Rand, R. P. *Biochemistry* **1981**, *20*, 1771.
- (34) Lis, L. J.; Parsegian, V. A.; Rand, R. P. *Biochemistry* **1981**, *20*, 1761.
- (35) Herbette, L.; Napolitano, C. A.; McDaniel, R. V. *Biophys. J.* **1984**, *46*, 677.
- (36) Elmore, D. E. *FEBS Lett.* **2006**, *580*, 144.
- (37) Zhao, W.; Rog, T.; Gurtovenko, A. A.; Vattulainen, I.; Karttunen, M. *Biophys. J.* **2007**, *92*, 1114.
- (38) Watts, A.; Harlos, K.; Marsh, D. *Biochim. Biophys. Acta* **1981**, *645*, 91.
- (39) Hauser, H.; Shipley, G. G. *Biochemistry* **1984**, *23*, 34.
- (40) Binder, H.; Zschornig, O. *Chem. Phys. Lipids* **2002**, *115*, 39.
- (41) Garcia-Manyes, S.; Oncins, G.; Sanz, F. *Biophys. J.* **2005**, *89*, 1812.
- (42) Petrache, H. I.; Tristram-Nagle, S.; Harries, D.; Kucerka, N.; Nagle, J. F.; Parsegian, V. A. *J. Lipid Res.* **2006**, *47*, 302.
- (43) Pedersen, U. R.; Leidy, C.; Westh, P.; Peters, G. H. *Biochim. Biophys. Acta* **2006**, *1758*, 573.
- (44) Gurtovenko, A. A.; Vattulainen, I. *Biophys. J.* **2007**, *92*, 1878.
- (45) Berendsen, H. J. C.; van der Spoel, D.; van Drunen, R. *Comput. Phys. Commun.* **1995**, *91*, 43.
- (46) Lindahl, E.; Hess, B.; van der Spoel, D. *J. Mol. Model.* **2001**, *7*, 306.
- (47) Berendsen, H. J. C.; Postma, J. P. M.; DiNola, A.; Haak, J. R. *J. Chem. Phys.* **1984**, *81*, 3684.
- (48) Gambu, I.; Roux, B. *J. Phys. Chem. B* **1997**, *101*, 6066.
- (49) Tieleman, D. P.; Berendsen, H. J. C. *J. Chem. Phys.* **1996**, *105*, 4871.
- (50) Miyamoto, S.; Kollman, P. A. *J. Comput. Chem.* **1992**, *13*, 952.
- (51) Darden, T.; York, D.; Pedersen, L. *J. Chem. Phys.* **1993**, *98*, 10089.
- (52) Cordomi, A.; Edholm, O.; Perez, J. J. *J. Comput. Chem.* **2007**, *28*, 1017.
- (53) Wohlert, J.; Edholm, O. *Biophys. J.* **2004**, *87*, 2433.
- (54) Jorgensen, W. L.; Maxwell, D. S.; TiradoRives, J. *J. Am. Chem. Soc.* **1996**, *118*, 11225.
- (55) Jorgensen, W. L.; Chandrasekhar, J.; Madura, J. D.; Impey, R. W.; Klein, M. L. *J. Chem. Phys.* **1983**, *79*, 926.
- (56) Patra, M.; Karttunen, M. *J. Comput. Chem.* **2004**, *25*, 678.
- (57) Patra, M.; Karttunen, M.; Hyvonen, M. T.; Falck, E.; Vattulainen, I. *J. Phys. Chem. B* **2004**, *108*, 4485.
- (58) Patra, M.; Karttunen, M.; Hyvonen, M. T.; Falck, E.; Lindqvist, P.; Vattulainen, I. *Biophys. J.* **2003**, *84*, 3636.
- (59) Cordomi, A.; Perez, J. J. *J. Phys. Chem. B* **2007**, *111*, 7052.
- (60) Seelig, J.; Macdonald, P. M.; Scherer, P. G. *Biochemistry* **1987**, *26*, 7535.
- (61) Akutsu, H.; Nagamori, T. *Biochemistry* **1991**, *30*, 4510.
- (62) Nagle, J. F.; Tristram-Nagle, S. *Biochim. Biophys. Acta* **2000**, *1469*, 159.
- (63) Shannon, R. D. *Acta. Crystallogr. Sect. A: Found. Crystallogr.* **1976**, *32*, 751.
- (64) Tunell, I.; Lim, C. *Inorg. Chem.* **2006**, *45*, 4811.
- (65) Brooks, B. R.; Brucoleri, R. E.; Olafson, B. D.; States, D. J.; Swaminathan, S.; Karplus, M. *J. Comput. Chem.* **1983**, *4*, 187.
- (66) Pearlman, D. A.; Case, D. A.; Caldwell, J. W.; Ross, W. S.; Cheatham, T. E.; Debolt, S.; Ferguson, D.; Seibel, G.; Kollman, P. *Comput. Phys. Commun.* **1995**, *91*, 1.
- (67) Tieleman, D. P.; MacCallum, J. L.; Ash, W. L.; Kandt, C.; Xu, Z. T.; Monticelli, L. *J. Phys. Condens. Matter* **2006**, *18*, S1221.

Critical role of electrostatic interactions of amino acids at the cytoplasmic region of helices 3 and 6 in rhodopsin conformational properties and activation

Ramon E, Cordero A, Bosch L, Zernii EY, Senin II, Manyosa J, Philippov PP, Perez JJ, Garriga P

J Biol Chem., 2007 May 11;282(19):14272-82

Critical Role of Electrostatic Interactions of Amino Acids at the Cytoplasmic Region of Helices 3 and 6 in Rhodopsin Conformational Properties and Activation*

Received for publication, December 4, 2006, and in revised form, February 5, 2007. Published, JBC Papers in Press, February 23, 2007, DOI 10.1074/jbc.M611091200

Eva Ramon^{†1}, Arnau Cordomí^{‡2}, Laia Bosch^{§2}, Eugeni Yu. Zernii[¶], Ivan I. Senin[¶], Joan Manyosa^{||}, Pavel P. Philippov[¶], Juan J. Pérez[§], and Pere Garriga^{‡3}

From the [†]Centre de Biotecnologia Molecular, Departament d'Enginyeria Química, Universitat Politècnica de Catalunya, 08222 Terrassa, Catalonia, Spain, [§]Centre de Biotecnologia Molecular, Departament d'Enginyeria Química, Universitat Politècnica de Catalunya, 08028 Barcelona, Catalonia, Spain, the [¶]Department of Cell Signalling, A. N. Belozersky Institute of Physicochemical Biology, M.V. Lomonosov Moscow State University, 119992 Moscow, Russia, and ^{||}Unitat de Biofísica, Departament de Bioquímica i de Biologia Molecular and Centre d'Estudis en Biofísica, Universitat Autònoma de Barcelona, 08193 Bellaterra, Catalonia, Spain

The cytoplasmic sides of transmembrane helices 3 and 6 of G-protein-coupled receptors are connected by a network of ionic interactions that play an important role in maintaining its inactive conformation. To investigate the role of such a network in rhodopsin structure and function, we have constructed single mutants at position 134 in helix 3 and at positions 247 and 251 in helix 6, as well as combinations of these to obtain double mutants involving the two helices. These mutants have been expressed in COS-1 cells, immunopurified using the rho-1D4 antibody, and studied by UV-visible spectrophotometry. Most of the single mutations did not affect chromophore formation, but double mutants, especially those involving the T251K mutant, resulted in low yield of protein and impaired 11-*cis*-retinal binding. Single mutants E134Q, E247Q, and E247A showed the ability to activate transducin in the dark, and E134Q and E247A enhanced activation upon illumination, with regard to wild-type rhodopsin. Mutations E247A and T251A (in E134Q/E247A and E134Q/T251A double mutants) resulted in enhanced activation compared with the single E134Q mutant in the dark. A role for Thr²⁵¹ in this network is proposed for the first time in rhodopsin. As a result of these mutations, alterations in the hydrogen bond interactions between the amino acid side chains at the cytoplasmic region of transmembrane helices 3 and 6 have been observed using molecular dynamics simulations. Our combined experimental and modeling results provide new insights into the details of the structural determinants of the conformational change ensuing photoactivation of rhodopsin.

Rhodopsin is the leading model for the G-protein-coupled receptor (GPCR)⁴ superfamily, which includes over 1000 membrane proteins (1). The three-dimensional structure of rhodopsin, characterized by seven transmembrane helices and a conserved disulfide bridge at the extracellular region, has been determined by x-ray crystallography (2–4). Upon rhodopsin activation by light absorption, the native chromophore 11-*cis*-retinal, bound through a protonated Schiff base linkage to Lys²⁹⁶, is isomerized to its all-*trans* configuration. This photochemical reaction causes a conformational change in the protein that leads to the formation, through a series of short lived photointermediates, of the active state metarhodopsin II. Structures of some of these intermediates have been recently determined (5–8). Most of these changes are concentrated on the transmembrane domain of the protein involving amino acids in the binding pocket of the retinal chromophore, which are efficiently transmitted to the cytoplasmic domain. The structural connection among several regions of rhodopsin (in the transmembrane and cytoplasmic domains) allows the interaction to its G-protein, transducin (Gt), which is activated, and initiates the visual transduction cascade (9, 10). The structural details underlying the signal transmission process, going from retinal isomerization to G-protein activation, have not been determined and still remain for the most part a main scientific question to be answered.

Based on the proposed existence of a common activation mechanism, which has been correlated with the presence of a set of conserved residues among the GPCR superfamily, nomenclature has been established for an easy comparison among their amino acid sequences (11). The highly conserved triplet Glu¹³⁴–Arg¹³⁵–Tyr¹³⁶ (corresponding to 3.49–3.50–3.51 according to this general numbering code), in the C-terminal part of helix 3, plays a critical role in the rhodopsin photoactivation process (12, 13). In particular, the Glu¹³⁴–Arg¹³⁵ ionic couple has been shown to be very important for the activation of Gt (14), and any changes in this interaction can alter

* This work was supported in part by Spanish Ministry of Education Grants SAF2005-08148-C04-01 (to J. J. P.) and SAF2005-08148-C04-02 (to P. G.) and in part by NATO Scientific Programme, INTAS Grant 03-51-4548 (to I. I. S., J. M., and P. G.), FEBS fellowship program (to E. Yu. Z.), and Russian Foundation for Basic Research Grants 06-04-48018, 04-04-04001 (to P. P. P.), and 06-04-48761 (I. I. S.). The costs of publication of this article were defrayed in part by the payment of page charges. This article must therefore be hereby marked "advertisement" in accordance with 18 U.S.C. Section 1734 solely to indicate this fact.

¹ Present address: Center for Membrane Biology, Dept. of Biochemistry and Molecular Biology, University of Texas Health Science Center, Houston, TX 77030.

² Recipient of doctoral fellowship from the Universitat Politècnica de Catalunya.

³ To whom correspondence should be addressed. Tel.: 34-937398998; Fax: 34-937398225; E-mail: pere.garriga@upc.edu.

⁴ The abbreviations used are: GPCR, G-protein-coupled receptors; Gt, transducin; UV-Vis, UV-visible; DM, dodecyl maltoside; MD, molecular dynamics; 9-mer, peptide corresponding to the last nine amino acids of the C-terminal region of rhodopsin; WT, wild type; DPPC, dipalmitoylphosphatidylcholine; GTP γ S, guanosine 5'-O-(3-thiotriphosphate).

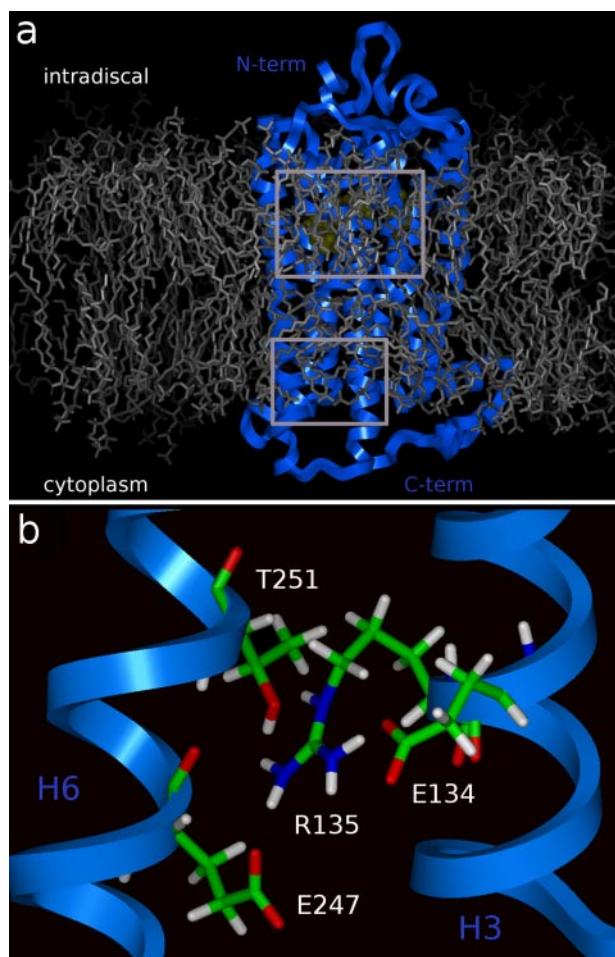


FIGURE 1. *a*, lateral view of bovine rhodopsin in a DPPC membrane; boxes show the retinal pocket and the region where the network of electrostatic residues between helices 3 and 6 are located; lipids are shown in gray, the protein in blue, and retinal and Lys²⁹⁶ in yellow; water molecules and Na⁺ and Cl⁻ ions have been omitted for clarity. *b*, detail of the network of electrostatic residues between helices 3 and 6 extracted from a representative snapshot of the WT simulation. Arg¹³⁵ interacts with Glu¹³⁴, Glu²⁴⁷, and Thr²⁵¹.

both the activation of the G-protein and other structural features like the glycosylation of rhodopsin (15–17). The crystal structures of rhodopsin reveal that several amino acids near the triplet are part of a network of electrostatic interactions between helices 3 and 6 (2, 3, 18, 19). Specifically, there are mainly four residues that are involved in this electrostatic lock in rhodopsin as follows: Glu¹³⁴ (3.49), Arg¹³⁵ (3.50), Glu²⁴⁷ (6.30), and Thr²⁵¹ (6.34), as shown in Fig. 1. The importance of positions 3.49 and 3.50 has been reported previously, and conformational changes causing constitutive activity of some GPCR have been described upon mutation of these residues. Examples of these receptors are rhodopsin (20–22), α_1 -adrenergic receptor (23), histamine-H₂ receptor (24), β_2 -adrenergic receptor (25), and the thyrotropin receptor (26). Similarly, these positions have been shown to be involved in the expression, activation, and internalization of the gonadotropin-releasing hormone receptor (27) and the stabilization and expression of the μ -opioid receptor (28). Specifically protonation of the carboxylic side chain of the amino acid at position 3.49 has been suggested to release the ionic lock that constrains the receptor in its inactive conformation, by means of a network of

electrostatic interactions, and to facilitate the movements of helices 3 and 6 necessary for the receptor to reach its active state (15, 23, 29).

On the other side, positions 6.30 and 6.34 have been studied in other receptors, such as β_2 -adrenergic (30), thyrotropin receptor (31), α_{1b} -adrenergic (32), human lutropin/choriogonadotropin receptor (33), μ -opioid receptor (34), and 5-hydroxytryptamine 2A serotonin receptor (35). In rhodopsin, single point mutations at Glu¹³⁴ and Glu²⁴⁷ have been studied because of the importance of the three cytoplasmic loops in Gt activation (14, 36), but no combination of mutations at the sites of helices 3 and 6 has been reported so far to address the role of the electrostatic network involving these two helices in the conformational and functional properties of the receptor.

In this work, the study of this electrostatic network, involving positions Glu¹³⁴, Arg¹³⁵, Glu²⁴⁷, and Thr²⁵¹, has been undertaken. Specifically, single and double mutants involving Glu¹³⁴ in helix 3 and Glu²⁴⁷ and Thr²⁵¹ in helix 6 have been constructed, purified, and characterized spectroscopically, functionally, and through molecular modeling. The results presented here provide experimental evidence for an important role of these amino acids in the functional status of the visual photoreceptor rhodopsin. Some of the double mutants show clear activity in dark conditions, particularly E134Q/T251A, and point to a key role of Thr²⁵¹ in the electrostatic network. The results provide experimental evidence, for the first time, for the involvement of Thr²⁵¹ in the conformational changes accompanying rhodopsin activation and highlight the importance of this residue in the structure and function of rhodopsin. The results are discussed in terms of the dynamic behavior of the different models of a selected subset of mutants as compared with the behavior of wild-type (WT) rhodopsin through molecular dynamics (MD) simulations.

The complementary study of the experimental and modeling features of the mutants provides new insights into the nature of the electrostatic network that keeps rhodopsin in its inactive conformation, allowing the dissection of the individual role of Glu¹³⁴, Glu²⁴⁷, and Thr²⁵¹ in the cytoplasmic domain of rhodopsin.

EXPERIMENTAL PROCEDURES

Materials—All buffers and chemicals were purchased from Panreac and Sigma. Oligonucleotides were obtained from Operon (Qiagen). Enzymes for site-directed mutagenesis by PCR were purchased from Stratagene and rho-1D4 antibody from the National Cell Culture Facilities. Cyanogen bromide-4B-Sepharose and phenylmethylsulfonyl fluoride were obtained from Sigma, and all restriction endonucleases were from Amersham Biosciences and New England Biolabs. Dodecyl maltoside (DM) was purchased from Anatrache. 11-*cis*-Retinal was synthesized at Moscow State University. The nonapeptide corresponding to the last nine residues of the C-terminal region of rhodopsin (9-mer) was synthesized in the Laboratori de Síntesi de Peptids (Universitat de Barcelona).

Buffers are defined as buffer A (1.8 mM KH₂PO₄, 10 mM Na₂HPO₄, 137 mM NaCl, 2.7 mM KCl, pH 7.2), buffer B (buffer A + 1%DM + 100 μ M phenylmethylsulfonyl fluoride), buffer C (buffer A + 0.05%DM), buffer D (2 mM NaH₂PO₄ + 0.05%DM,

Cytoplasmic Regions of Helices 3 and 6 of Rhodopsin

pH 6.0), and buffer D + the nonapeptide (buffer D + 100 μM 9-mer) for protein elution from the chromatographic column.

Construction, Expression, and Purification of Rhodopsin Mutants—For single mutations, site-directed mutagenesis was performed using cassette-based strategy replacing the PstI/MluI fragment of pMT4 (36) for an oligonucleotide containing the single mutation E134Q, E247A, and E247Q. PCR was used for obtaining single mutants at position Thr²⁵¹ and double mutants. Plasmid DNA was analyzed by restriction analysis (using EcoRI and MluI) and followed by DNA sequencing using the dideoxy chain-terminated method (constructed rhodopsin mutants are shown in Table 1). WT and mutant opsin genes were expressed in transiently transfected COS-1 cells as described (37). Transfected cells were harvested between 60 and 72 h after the addition of DNA and washed twice with buffer A. The cells were then incubated with 20 μM 11-*cis*-retinal for 5 h for reconstitution, solubilized in buffer B for 1 h, and finally centrifuged at 35,000 rpm for 35 min. All these procedures were carried out at 4 °C. Rhodopsin was purified from the supernatant using rho-1D4-Sepharose and incubated overnight at 4 °C. Sepharose was subsequently washed twice with buffer C and twice with buffer D and finally was incubated with buffer D + the nonapeptide for 30 min at 4 °C for rhodopsin elution. Rhodopsin concentration was determined by using a molar extinction coefficient value ϵ_{500} of 40,600 $\text{M}^{-1} \text{cm}^{-1}$.

UV-visible (UV-Vis) Absorption Spectroscopic Assays—All measurements were made on a Cary 1E spectrophotometer (Varian, Australia), equipped with a water-jacketed cuvette holder connected to a circulating water bath. Temperature was controlled by a Peltier accessory connected to the spectrophotometer. All spectra were recorded, in the 250–650 nm range, with a bandwidth of 2 nm, a response time of 0.5 s, and a scan speed of 180 nm/min. For the photobleaching and acidification of rhodopsin, samples were bleached by using a 150-watt power source with a 495 nm cutoff filter. Dark-adapted rhodopsin samples were illuminated for 20 s to ensure complete photoconversion to 380-nm absorbing species. Acidification was carried out by addition of 2 N H_2SO_4 (1% of the sample volume), immediately after photobleaching, and the absorption spectrum was recorded 2 min later.

Rhodopsin thermal stability in the dark was followed by monitoring the loss of A_{max} in the visible region as a function of time, at constant temperature (45 °C). Complete spectra were recorded every 5 min. Spectra were normalized and fitted to single exponential functions using SigmaPlot version 8.02 to derive the $t_{1/2}$ values. Hydroxylamine treatment was performed by adding hydroxylamine (pH 7.0) to the samples at a final concentration of 30 mM at 20 °C.

Gt Activation Assay—Gt activation levels were determined by incorporation of radioactive $\text{GTP}\gamma^{35}\text{S}$ in Gt molecules induced by WT rhodopsin or its mutants essentially as described previously (38). Briefly, the reaction mixture, containing 1 μM Gt, 20 nM rhodopsin, 10 mM Tris-HCl (pH 7.4), 100 mM NaCl, 5 mM MgCl_2 , 2 mM dithiothreitol, 0.012% DM, and 3 μM $\text{GTP}\gamma^{35}\text{S}$, was bleached for 30 s by using a 150-watt power source with a 495 nm cutoff filter. Samples were incubated at room temperature for 1 h, and the reactions were stopped by addition of 10 mM Tris-HCl (pH 7.4), 100 mM NaCl,

and 10 mM EDTA. The dark activity of the proteins was determined in exactly the same way but without illumination. The unbound $\text{GTP}\gamma^{35}\text{S}$ was removed by microfiltration. The amount of $\text{GTP}\gamma^{35}\text{S}$ bound to Gt was determined by Cerenkov counting using a TRI-CARB 2100TR scintillation counter from Packard Instrument Co.

MD Simulations—Atomic coordinates of rhodopsin were retrieved from the Protein Data Bank (entry 1GZM) (18). In contrast to other previously published crystal structures (2–4), this structure contains the coordinates of all the amino acids of the intradiscal and cytosolic loops of rhodopsin. The N-terminal acetyl group and the two palmitoyl chains at the cytoplasmic end of the receptor that are covalently linked to two consecutive cysteine residues were also included in the present model. In contrast, the C-terminal region after the palmitoylated cysteines, at the end of the short helix 8, was not included. Side chains of all the amino acids were considered in the protonation state they exhibit as free amino acids in water at pH 7, with the exception of Asp⁸³ and Glu¹²² that were treated as protonated and neutral, respectively, according to experimental evidence (39).

The process of protein embedding was performed as reported elsewhere (40). Specifically, the protein was placed in a box containing a mixture of DPPC lipids and water molecules generated and equilibrated according to the procedure described previously (41). The simulation box had an initial size of $10.3 \times 8.0 \times 10.2 \text{ nm}^3$ (*xyz*), and organized in such a way that the first two dimensions corresponded to the bilayer plane. The area per lipid was 0.64 nm^2 . Before protein insertion, the box contained 256 lipids and $\sim 17,000$ water molecules. After the protein was inserted in the center of the box, all water molecules with oxygen atoms closer to 0.40 nm from a non-hydrogen atom of the protein and all lipid molecules with at least one atom closer to 0.25 nm from a non-hydrogen atom of the protein were removed, resulting in a final system that contained 198 lipids and $\sim 16,000$ water molecules. Removal of these atoms introduces small voids between the protein and water or lipid molecules that are easily removed during the first step of the equilibration process (see below), in which a progressive adjustment of the lipid bilayer and water molecules to the protein takes place. Next, in the system with WT rhodopsin, 113 water molecules were selected randomly and replaced by 57 sodium and 56 chloride ions, providing a neutral system with a concentration of about 0.2 M of both sodium and chloride ions (fairly similar to that found in biological organisms). For the simulations of mutants, single water molecules were converted to ions when necessary, to keep the electroneutrality of the system.

All the computer simulations reported in this study were performed using a parallel version of the GROMACS 3.2 package (42, 43). The system was subjected to periodic boundary conditions in the three coordinate directions. Temperature was kept constant at 323 K (well above the gel/liquid crystalline phase transition temperature of 314 K) using separate thermostats for the protein, water, ions, and lipid molecules (44). The time constant for the thermostats was set to 0.1 ps except for water, for which a smaller value of 0.01 ps was used. The pressure in the three coordinate directions was kept at 0.1 MPa

TABLE 1

Mutant rhodopsins constructed to study the importance of Glu¹³⁴, Glu²⁴⁷, and Thr²⁵¹ on the stability and activity of rhodopsin

Single mutants were constructed using cassette mutagenesis, and double mutants were obtained by PCR.

Single mutants	Double mutants	
E134Q	E134Q/E247A	E247A/T251A
E247A	E134Q/E247Q	E247A/T251K
E247Q	E134Q/T251A	E247Q/T251A
T251A	E134Q/T251K	E247Q/T251K
T251K		

using independent Berendsen barostats with a time constant of 1.0 ps. The equations of motion were integrated using the leap-frog algorithm with a time step of 2 fs. All bonds within the protein and lipid molecules were kept frozen using the LINCS algorithm (45). The bonds and the angle of the water molecules were fixed using the analytical SETTLE method. Lennard-Jones interactions were computed with a cutoff of 1.0 nm, and the electrostatic interactions were treated using a twin cutoff of 1.0/1.8 nm, being the interactions in the interval 1–1.8 nm updated every 10 time steps.

The all-atom optimized potential for liquid simulations force field (46) currently implemented in GROMACS was used for all molecules of the system, except for the DPPC molecules, which were modeled using force field parameters previously described in the literature (47). Nonbonded pair interactions were computed as combinations of single atomic parameters to account for protein-lipid interactions. These parameters reproduce the experimental area per lipid of pure DPPC in the liquid crystalline phase (47–49). Water molecules were modeled using the TIP3P model (50). Fractional charges of retinal atoms were taken from quantum chemical calculations (51) and have already been used in other MD simulations of rhodopsin (52).

The structure of WT rhodopsin was energy-minimized and equilibrated in successive MD simulations at 6.5 ns long. First, 500 ps were run using the NPT ensemble, allowing the system to change the box dimensions, with protein coordinates strongly restrained to the initial structure. During this step, voids between the protein and lipid and water molecules vanished. At that point the simulation was continued for 500 ps in the NVT ensemble with the same positional restraints on the protein. In the last equilibration step, when the bilayer and water around the protein were equilibrated, restraints on the protein were released, and the system was equilibrated for 5.5 ns. The final structure obtained was used, first to continue the compute MD trajectory of the WT up to 10 ns, and second, to construct the different mutants by side-chain replacement and to subsequently perform a 5-ns MD trajectory on each of them.

RESULTS

Expression, Purification, and Spectral Characterization of Rhodopsin Mutants—The rhodopsin mutants obtained at the cytoplasmic boundaries of helices 3 and 6 (Table 1) were expressed in COS-1 cells, immunopurified with the monoclonal rho-1D4 antibody, and spectrophotometrically characterized by means of UV-Vis spectroscopy (Fig. 2). The A_{280}/A_{500} spectral ratios, which reflect chromophore regeneration and protein yield after purification, are shown in Table 2. All mutants studied showed no hydroxylamine sensitivity in the

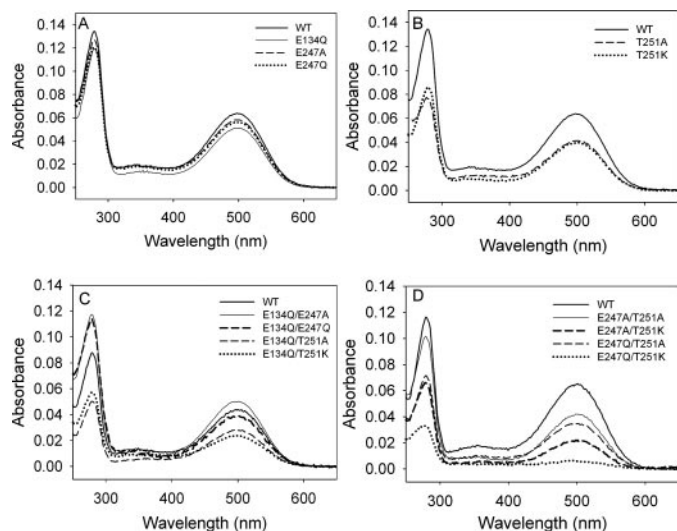


FIGURE 2. UV-Vis absorption spectra of single and double mutants. WT and mutant rhodopsins were expressed in COS-1 cells, regenerated with 11-*cis*-retinal, and purified in buffer C. Spectra were recorded at 20 °C. UV-Vis absorption spectra of WT, E134Q, E247A, and E247Q are shown in A; spectra of WT, T251A and T251K are shown in B; spectra of WT, E134Q/E247A, E134Q/E247Q, E134Q/T251A, and E134Q/T251K are shown in C; and spectra of WT, E247A/T251A, E247A/T251K, E247Q/T251A, and E247Q/T251K are shown in D.

TABLE 2

Spectral A_{280}/A_{500} ratio of rhodopsin mutants normalized to that of WT rhodopsin taken as 1.00

WT rhodopsin and mutants were transfected, regenerated with 11-*cis*-retinal, and purified in Buffer C + 0.05% DM as described (see "Experimental Procedures"). All spectra were recorded at 20 °C.

Rhodopsin	A_{280}/A_{500} ($n = 3$)
WT	1.00
E134Q	1.22 ± 0.10
E247A	0.98 ± 0.10
E247Q	1.00 ± 0.03
T251A	1.09 ± 0.07
T251K	1.19 ± 0.15
E134Q/E247A	1.29 ± 0.07
E134Q/E247Q	1.54 ± 0.13
E134Q/T251A	0.98 ± 0.04
E134Q/T251K	1.11 ± 0.10
E247A/T251A	1.42 ± 0.08
E247A/T251K	1.54 ± 0.15
E247Q/T251A	1.16 ± 0.06
E247Q/T251K	2.92 ± 0.10

dark, and their photobleaching and acidification properties were very similar to those of WT rhodopsin (data not shown).

Mutations E134Q, E247A, E247Q, E134Q/E247A, and E134Q/E247Q—These mutants were expressed to an extent similar to that of WT rhodopsin according to their absorbance spectra (Fig. 2, A and C). All mutants were regenerated with 11-*cis*-retinal to form a chromophore with spectral features similar to those of WT (λ_{max} at 500 nm). E247A and E247Q showed a chromophore formation similar to WT rhodopsin, whereas E134Q and E134Q/E247A showed some differences judged from the A_{280}/A_{500} ratios (Table 2). On the other hand, the double mutant E134Q/E247Q displayed impaired 11-*cis*-retinal binding (Table 2). This reduction may be interpreted as lack of accessibility of the retinal to the binding pocket as a result of the mutations, to some slight degree of structural misfolding affecting the proper conformation of the ligand-accepting receptor or to a lower stability of the mutant in detergent

TABLE 3
Thermal stability of WT and mutant rhodopsins

Spectra of rhodopsin (either WT or mutants) in Buffer C + 0.05% DM were recorded every 5 min at 45 °C. $A_{500\text{ nm}}$ at different times were fitted to single exponential functions using SigmaPlot version 8.02, and the $t_{1/2}$ values were determined.

Rhodopsin	$t_{1/2}$ <i>min</i>
WT	65
E134Q	22
E247A	29
E247Q	13
E134Q/E247A	13
E134Q/E247Q	14

solution. In any case, this reduction does not reflect gross conformational perturbations and it may be assumed that the overall conformation of the mutants is similar to WT rhodopsin, as observed for the same maximum absorbance at $\lambda = 500\text{ nm}$ (Fig. 2).

The positions where the mutations have been introduced (3.49 and 6.30 according to a generic numbering system for GPCR (11)) were also studied in the β_2 -adrenergic receptor (30) and proposed to play a critical role in the conformational rearrangement involving helix 3 and helix 6 that is required for rhodopsin activation (12). The results obtained with the β_2 -adrenergic receptor suggested that ionic interactions between 3.49, 3.50, and 6.30 may constitute a common switch governing activation of rhodopsin-like receptors. Furthermore, the features of the mutants, with regard to charge neutralization and changes in electrostatic interactions, showed a good correlation with the extent of constitutive activity observed for the mutants (30). In this study, some degree of dark activity was detected for some of the mutants studied (see "Gt Activation of Rhodopsin Mutants").

The thermal stability of these mutants, in the dark, was measured at 45 °C (Table 3). The general observed trend is that the mutants are less stable than WT. Lack of hydroxylamine reactivity indicated that the mutants present a compact structure around the Schiff base linkage, as would be expected because of the far away location of the mutations referred to the Schiff base environment (data not shown).

Mutations T251A, T251K, E134Q/T251A, and E134Q/T251K—We explored for the first time the functional role of the polar amino acid Thr²⁵¹ (in helix 6) in the electrostatic interaction with Glu¹³⁴ and Glu²⁴⁷, in native rhodopsin structure and function, by introducing mutations at this site. The single mutants T251A and T251K were analyzed to determine the involvement of Thr²⁵¹ (6.34) in the rhodopsin activation mechanism. Protein yield after purification from COS-1 was about half that of the WT under the same conditions (Fig. 2B). This suggests that the mutant proteins are expressed in the COS-1 cell line to a lower extent than the WT. The mutant rhodopsins show spectroscopic features of the WT concerning the λ_{max} which is located at 500 nm, but their A_{280}/A_{500} ratios are slightly higher than those of the WT (Table 2).

Double mutants E134Q/T251A, and E134Q/T251K were constructed and spectroscopically analyzed. These mutants were purified in lower amounts than WT (Fig. 2C). The A_{280}/A_{500} ratios are different for both mutants as follows: in the case of E134Q/T251A, the ratio is similar to that of WT, whereas

TABLE 4
Gt activation of WT rhodopsin and the mutants determined under dark and light conditions

The Gt activation data were obtained as described under "Experimental Procedures." All values were normalized to light-activated rhodopsin taken as 100%.

Rhodopsin	Gt activation (mol GTP γ S/mol Rho)	
	Dark	Light-activated
Wild type	0.99 \pm 0.09	10.37
E134Q	1.32 \pm 0.12	13.17 \pm 1.08
E247A	2.02 \pm 0.05	13.12 \pm 1.34
E247Q	1.50 \pm 0.34	9.95 \pm 0.96
T251A	1.21 \pm 0.25	7.72 \pm 0.35
T251K	1.09 \pm 0.36	8.09 \pm 0.36
E134Q/E247Q	0.52 \pm 0.22	10.37 \pm 1.34
E134Q/E247A	2.04 \pm 0.85	13.32 \pm 2.95
E134Q/T251A	5.81 \pm 1.45	14.03 \pm 0.26
E134Q/T251K	0.91 \pm 0.49	23.69 \pm 0.98
E247A/T251A	1.38 \pm 0.33	5.60 \pm 0.47
E247Q/T251A	0.31 \pm 0.10	5.98 \pm 0.15
E247A/T251K	0.62 \pm 0.10	2.07 \pm 0.10

E134Q/T251K has a slightly higher ratio when compared with WT rhodopsin (Table 2).

Mutations E247A/T251A, E247A/T251K, E247Q/T251A, and E247Q/T251K—Double mutants replacing amino acids in the same helix 6 (at 247 and 251 positions, which are about one helical turn apart in this helix), E247A/T251A and E247A/T251K, were obtained and spectrally characterized (Fig. 2D). Both mutants were obtained at lower yields and showed impaired 11-*cis*-retinal binding with regard to WT rhodopsin. Similar features were also observed for mutants E247Q/T251A and E247Q/T251K (Fig. 2D). Specifically, the mutation E247Q/T251K produces the most destabilizing effect in the protein resulting in a higher A_{280}/A_{500} ratio, which is larger than that of mutant E247A/T251K (Table 2). This suggests that there is steric hindrance imposed by the bulkier Gln side chain at position 247, in contrast to the case of Ala substitution in the E247A/T251K, which appears to be better tolerated.

Gt Activation of Rhodopsin Mutants—The spectral characterization shows that most of the mutants studied can be expressed, purified, and regenerated with 11-*cis*-retinal to an extent not very different from WT rhodopsin. This suggests that the overall conformation of these mutants in the dark state is not dramatically altered. Therefore, it was of great interest to analyze the functional characteristics of these mutants in terms of their ability to activate Gt.

The Gt activation experiments were carried out with detergent-solubilized and purified WT and mutant rhodopsins by means of a classical radioactive assay. Samples were analyzed both under dark and light conditions in all cases, and the data reported correspond to the final activation (after 1 h) detected in the two conditions. The Gt activation data for all the mutants studied are summarized in Table 4.

Single Mutants E134Q, E247A, E247Q, T251A, and T251K—Fig. 3A shows the functional data for the single mutants as well as that of the WT for comparison (in all experiments WT rhodopsin was used as a control for comparison, thereby its light activity was taken as 100% for reference).

The Gt activation for WT rhodopsin in dark conditions, obtained under the current experimental conditions used, is about 10%, as also seen in previous reports (37). No activity was previously detected for purified WT rhodopsin in DM solution

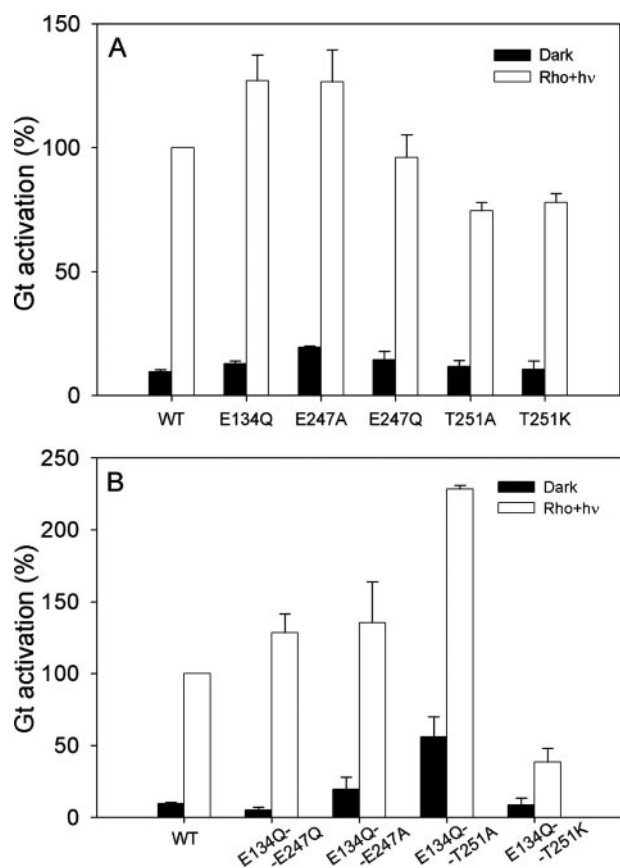


FIGURE 3. Gt activation by WT rhodopsin and representative mutants. A, single mutants; B, double mutants. WT and mutants in 10 mM Tris-HCl (pH 7.4), 100 mM NaCl, 5 mM MgCl₂, 2 mM dithiothreitol, 0.012% DM were bleached and incubated with 1 μ M Gt and 3 μ M GTP γ ^{35S} for 1 h at room temperature. The values were obtained as described under "Experimental Procedures." The complete values of Gt activation for all of the mutants studied in this study are given in Table 4.

in dark conditions (53). On the other hand, the activity of mutants in the content of COS-1 cell membranes was found to be lower than when they are purified in detergent solution (54). This may be due to an increased conformational flexibility of the mutants in the detergent-solubilized state that facilitates physical interaction with Gt in the recognition event that takes places in the activation mechanism.

In the case of the E134Q mutant, we found a small increase in dark activity as well as increased activity in light conditions (of ~30%) which was similar to that previously reported (54, 55). For the Glu²⁴⁷ mutations in helix 6, we found a different behavior for the E247A and E247Q. In the latter case, the light activation is not increased with regard to WT rhodopsin and in the dark appears to be only slightly above the E134Q level. In the case of E247A, the activity upon illumination is similar to that of E134Q, but in dark conditions it is clearly higher. It appears that mutations to Ala result in higher levels of dark activity, as will be discussed below. Mutations at Thr²⁵¹ result in a somehow lower activity with regard to WT under light conditions.

Double Mutants Involving Amino Acids of Helices 3 and 6 (Interhelical)—In the case of the double mutants (Fig. 3B and Table 4), a combined effect can also be observed. Addition of E134Q mutation to any of the single mutants in helix 6 (in the E134Q/E247A, E134Q/E247Q, E134Q/T251A, and E134Q/

T251K mutants) resulted in an increase of Gt activation in light conditions, except T251K which showed a clear decrease to about 40% of the WT activity. The E134Q/T251A double mutant shows a clear and definite synergistic effect when compared with the corresponding single mutants both in the dark (50%) and in the light (230%). This is the first time that experimental evidence is provided for the decisive involvement of Thr²⁵¹ in rhodopsin helix 6 in the electrostatic network at the cytoplasmic ends of helices 3 and 6.

A synergistic effect was observed previously for mutations in the transmembrane domain like G90D/M257Y (56) or E113Q/M257Y (57). In the case of the double mutant E134Q/M257A, this was proposed to have a 50% activity in the dark. We observe a similar effect for the E134Q/T251A double mutant. However, in our case this is the first time where mutations at the cytoplasmic boundaries show such dark activity. Mutations at the homologous position of Thr²⁵¹ in other GPCR were shown to be constitutively active (31, 58–60).

Double Mutants Involving Only Amino Acids of Helix 6 (Intrahelical)—We studied double mutants E247A/T251A, E247Q/T251A, and E247Q/T251K. All of these mutants showed reduced Gt activation under light conditions, particularly E247A/T251K which showed only 20% activity (Table 4).

In the case of the samples under light conditions, the possibility that different metarhodopsin II decay rates are in part responsible for the observed differences in transducin activation by the different mutants cannot be excluded.

Molecular Modeling Studies—The analysis of the crystal structure of rhodopsin (2–4, 17, 18) reveals that residues Glu¹³⁴, Glu²⁴⁷, and Thr²⁵¹ are part of a network of hydrogen bonds located at the cytoplasmic sides of helices 3 and 6 as shown in Fig. 1. The use of MD simulations allows a better characterization of these interactions, providing insight into the structural effects caused by the different mutations on WT rhodopsin and their effect on the activation process of the receptor.

The amino acid sequence corresponding to the cytoplasmic side of helices 3 and 6 is particularly abundant in charged residues (Table 5). Thus, it is expected that the structure is sensitive to alterations on the charge of the side chains (Table 6). Hydrogen bond interactions involving the residues on the cytoplasmic sides of helices 3 and 6, as well as on the second and third cytoplasmic loops, are listed in Table 7. A more detailed description of the molecular computations on the WT and mutants follows.

WT and E134Q, E247A, E247Q, and T251K Single Mutants—In native rhodopsin, the positively charged Arg¹³⁵ establishes strong interactions with residues Glu¹³⁴, Glu²⁴⁷, and Thr²⁵¹ along the entire simulation either with one of the negatively charged residues of helix 3 (Glu¹³⁴) or with one negatively charged and one polar residue of helix 6 (Glu²⁴⁷ and Thr²⁵¹). The involvement of Thr²⁵¹ is supported by the increased activity exhibited by the Thr²⁵¹ mutant reported in this study and the effect of an analogous residue in the β_2 -adrenergic receptor (30). A set of hydrogen bonds among residues at the boundary between helix 6 and the third cytoplasmic loop (involving Glu²³⁹, Ser²⁴⁰, Thr²⁴², Thr²⁴³, Gln²⁴⁴, and Lys²⁴⁸) was observed. The removal of the negative charge at position 134 in mutant

Cytoplasmic Regions of Helices 3 and 6 of Rhodopsin

TABLE 5

Sequence of bovine rhodopsin at the region of the cytoplasmic sides of helices 3 and 6

These parts of the sequence contain a large number of charged residues. The signs (*) and (·) indicate the charged and the polar residues, respectively. The lengths of the secondary motifs have been taken from Ref. 18. H3 and H6 account for helices 3 and 6, respectively; C2 and C3 for the second and the third cytoplasmic loops; Cyt and Int indicate whether the part of the sequence is located on the cytoplasmic or the intradiscal side, respectively.

H3	Int	106	GPTGCNLEGGFFATLGG EIALWSLVVLAIER YVVVC · · * · * · ** ·	140	Cyt
C2	Cyt	141	KPMSNFRF * · · *	148	Cyt
C3	Cyt	234	AAQQQES · · · * ·	240	Cyt
H6	Cyt	241	ATTQKAEKEVTRMVIIMVIAFLICWLPYAGVAFYIF · · · * * * * · *	276	Int

TABLE 6

The net charge at helices 3 and 6 and their average relative distances in the studied mutants compared to WT

The separations are given in nm and related to the value observed in WT.

	WT	E134Q	E247Q	T251K	E134Q/E247A	E134Q/T251A	E134Q/T251K	E247Q/T251K
Net charge H3	0	+1	0	0	+1	+1	+1	0
Net charge H6	0	0	+1	+1	+1	0	+1	+2
Net total charge	0	+1	+1	+1	+2	+1	+2	+2
H3-H6 separation		-0.8	-0.9	2.4	-0.3	-0.6	0.0	-0.9

E134Q has effects on the competition to form hydrogen bonding interactions between helices 3 and 6. Specifically, the E134Q mutation induces a remarkable preference of Arg¹³⁵ for residues located in helix 6. Thus, after a short simulation time, the interaction between residues Gln¹³⁴ and Arg¹³⁵ is lost, whereas Arg¹³⁵-Glu²⁴⁷ and Arg¹³⁵-Thr²⁵¹ interactions remain stable. Therefore, the interaction between the cytoplasmic side of helices 3 and 6 is stronger than in WT rhodopsin. Glu¹³⁴ forms a hydrogen bond with His¹⁵² on helix 4, with the drop of the Glu¹³⁴-Arg¹³⁵ interaction, during half of the time of the trajectory analyzed. Additionally, a Glu²³⁹-Lys²⁴⁵ interaction, at the boundary between the third cytoplasmic loop and helix 6, can be observed for a small amount of snapshots.

Removal of the negative charge at position 247, in the E247Q mutant, forces Arg¹³⁵ to exhibit a more favorable interaction with Glu¹³⁴ than with Gln²⁴⁷, just the opposite observed in the case of the E134Q mutant. Although the Arg¹³⁵-Gln²⁴⁷ interaction is maintained during the entire simulation, it is too weak to keep Arg¹³⁵ close to Thr²⁵¹. Thus, the Thr²⁵¹-Arg¹³⁵ interaction is lost, whereas the distance between Arg¹³⁵ and Glu¹³⁴ is clearly reduced after a short simulation time, inducing a displacement of Arg¹³⁵ side chain toward helix 3 moving away from helix 6. There are also two interactions as follows: Glu²³⁹-Ser²⁴⁰ and Ser²⁴⁰-Thr²⁴² at the boundary between the third cytoplasmic loop and helix 6, which can be observed during most part of the trajectory. These interactions are already present in the WT, although to a lower extent.

The T251K mutation provides an additional positive charge at the end of helix 6, a region with a large number of charged residues as follows: three positively charged residues (Lys²⁴⁵, Lys²⁴⁸, and Arg²⁵²) and two negatively charged ones (Glu²⁴⁷ and Glu²⁴⁹), as shown in Table 5. The presence of Lys²⁵¹ forces a rearrangement of the neighboring positively charged residues, driven by electrostatic repulsion. Consequently, the

Arg¹³⁵-Glu²⁴⁷ interaction vanishes after 2.5 ns, with Glu¹³⁴-Arg¹³⁵ the only remaining hydrogen bond interaction involving residue Arg¹³⁵. Therefore, the effect of this mutation is similar to that of E247Q, favoring the Arg¹³⁵-Glu¹³⁴ interaction. Lys²⁵¹ interacts mainly with Glu²³⁹ and Gln¹³⁷ on the third cytoplasmic loop, but also with Thr²²⁹ in helix 5. Moreover, Glu²⁴⁷ exhibits a hydrogen bond interaction with Gln³¹² at the short cytoplasmic helix 8 during a long time of the trajectory, not observed in any other simulation. As a consequence of these rearrangements induced by the new positively charged chain at position 251, a set of hydrogen bonds appears to be favored involving residues located either on helix 6 or on the third cytoplasmic loop (Glu²³², Gln²³⁶, Gln²³⁷, Glu²³⁹, Ser²⁴⁰, and Lys²⁴⁸). Nevertheless, the only hydrogen bond detected in WT rhodopsin is Glu²³⁹-Ser²⁴⁰, although for shorter times, as well as in the remainder of the mutants. These new interactions are a consequence of the positive charge density at the end of helix 6, suggesting that T251K can significantly alter the conformation of the cytoplasmic ends of helices 3 and 6 and the third cytoplasmic loop by modifying the hydrogen bond network between them. Because none of the mutants involving this single mutation (including the double ones) exhibited increased activation, neither in the dark nor in the light conditions, it may be regarded as a deleterious one in terms of protein function, probably by constraining the conformation of the receptor in a functionally defective state.

Double Mutants E134Q/E247A, E134Q/T251A, E134Q/T251K, and E247Q/T251K—The E134Q/E247A double mutation adds two net positive charges with regard to the WT and, more important, removes the two counter-charges of Arg¹³⁵ (Glu¹³⁴ and Glu²⁴⁷). As shown above, the hydrogen bond interactions with Arg¹³⁵ are kept in E247Q and lost in the E134Q single mutant, respectively. Similarly, in the double mutant the interaction Arg¹³⁵-Gln¹³⁴ is too weak to be kept without the

TABLE 7

Hydrogen bonds at the cytoplasmic sides of helices 3 and 6

Gray scale indicates percentage of trajectory present: 0–20% (white), 20–40% (light gray), 40–60% (medium gray), 60–80% (dark gray), and 80–100% (black). The limits of helices and loops are taken from Ref. 18. The analysis has been performed on the last 2 ns of each trajectory using a cutoff of 0.45 nm.

residue	number	motif	residue	number	motif	WT	E134Q	E247Q	T251K	E134Q/E247A	E134Q/T251A	E134Q/T251K	E247Q/T251K
E/Q	134	H3	R	135	H3	■		■	■			■	■
E/Q	134	H3	HIS	152	H4		■	■					
E/Q	134	H3	E/Q	247	H6								
E/Q	134	H3	T/K/A	251	H6								■
R	135	H3	E	150	H4								
R	135	H3	E/Q	247	H6	■		■			■	■	
R	135	H3	T/A	251	H6	■				■			
Y	136	H3	Q	225	H5	■				■	■		■
R	147	C2	E	239	C3			■					
Y	223	H5	K	248	H6								■
Y	223	H5	R	252	H6		■	■					■
T	229	H5	K	248	H6	■					■		
T	229	H5	T/K/A	251	H6				■				
E	232	C3	Q	236	C3				■				
Q	237	C3	K	248	H6						■		
Q	237	C3	T/K/A	251	H6				■				
E	239	C3	S	240	C3			■	■			■	■
E	239	C3	T	243	H6			■	■			■	■
E	239	C3	K	245	H6		■						
E	239	C3	K	248	H6				■				
E	239	C3	T/K/A	251	H6				■				
S	240	C3	T	242	H6	■		■		■		■	■
S	240	C3	T	243	H6	■				■		■	■
S	240	C3	K	248	H6				■				
Q	244	H6	K	248	H6	■							
Q	244	H6	T/K/A	251	H6							■	
E/Q	247	H6	E	239	C3								■
E/Q	247	H6	T/K/A	251	H6								■
E/Q	247	H6	Q	312	H8				■				
K	248	H6	E	249	H6			■					
E	249	H6	R	252	H6	■		■	■	■	■	■	■

Cytoplasmic Regions of Helices 3 and 6 of Rhodopsin

negative charge. The E247A mutation only allows the residue to interact with Arg¹³⁵ through its backbone carbonyl. As a consequence of this, both interactions vanish, destroying the ionic lock associated with the D(E)RY motif and keeping only the interaction Arg¹³⁵–Thr²⁵¹ when compared with WT, although exhibiting shorter residence times. The removal of two negative charges forces hydrogen bond donors on the third loop to be closer to the cytoplasmic end of helix 6 to compensate for the lack of the negative charge, similarly to the effect observed when a positive charge is added in the case of T251K. Therefore, a set of interactions involving residues Glu²³⁹, Ser²⁴⁰, and Thr²⁴² already observed in the WT are reinforced, specifically those involving Glu²³⁹ (Glu²³⁹–Thr²⁴³ and Glu²³⁹–Ser²⁴⁰), at the boundary between the third cytoplasmic loop and helix 6.

In the case of the E134Q/T251A double mutant, there are two simultaneous effects. On the one hand, as observed for the E134Q single mutant, removal of the negative charge at position 134 favors the Arg¹³⁵–Glu²⁴⁷ interaction, and on the other hand the T251A mutation removes the hydrogen bond between Arg¹³⁵ and residue 251. The present analysis shows a decrease of the fraction of trajectory where Arg¹³⁵ and Glu²⁴⁷ are interacting (about 25%). As a result of all these rearrangements, new hydrogen bonds between Lys²⁴⁸ on helix 6 and both Thr²²⁹ on helix 5 and Gln²³⁷ on the third cytoplasmic loop are formed and kept during most of the trajectory analyzed. Additionally, interactions involving Ser²⁴⁰ already present in WT are reinforced. The existence of these new hydrogen bonds and the reinforcement of others already existing in the WT may explain the high level of dark activity observed for this mutant (see Fig. 3 and Table 4).

The E134Q/T251K double mutant implies removal of the negative charge at position 134. This causes impaired interaction with Arg¹³⁵, although this interaction is still observed in about half of the snapshots analyzed. This situation is different from the other mutants containing Gln¹³⁴ studied (E134Q and E134Q/T251A), where the interaction is completely lost. The reason for this specific behavior can be associated with the net +2 charge of the mutant, which requires a large number of residues with negative charge density to be closer. In some snapshots, where Gln¹³⁴ does not interact with Arg¹³⁵, it is involved in a hydrogen bond with His¹⁵². Obviously, the absence of Thr²⁵¹ results in the loss of the interaction with Arg¹³⁵. Additionally, the presence of Lys²⁵¹ weakens the Glu²⁴⁷–Arg¹³⁵ interaction, because it competes with Arg¹³⁵ for Glu²⁴⁷, as in the other mutants containing T251K. Here, Lys²⁵¹ also interacts with Gln²⁴⁴. Although the interactions involving Arg¹³⁵ are significantly weakened or lost, when compared with the WT, a network of hydrogen bonds between residues at helix 6 and the third cytoplasmic loop, already present in the WT, is sensibly enhanced as follows: Glu²³⁹–Ser²⁴⁰, Glu²³⁹–Thr²⁴³, Ser²⁴⁰–Thr²⁴², and Ser²⁴⁰–Thr²⁴³.

Finally, the E247Q/T251K double mutant involves mutations of two amino acids in the same helix. In this case, the side-chain replacements introduce a net charge of +2 at helix 6, resulting in five positively charged residues within two helix turns with only a single negatively charged side chain (see Table 5). The suppression of the negative charge at position 247 and the introduction of an additional positively charged residue at

position 251 breaks the Arg¹³⁵–Gln²⁴⁷ interaction, leaving Lys²⁵¹–Gln²⁴⁷ as the predominant interaction. Additionally, Gln²⁴⁷ interacts with Glu²³⁹ on the third cytoplasmic loop. The results are somehow similar to those described for the single mutant E247Q, but the changes in the interaction patterns are larger because of the existence of an additional positive charge in the region. Arg¹³⁵ and Lys²⁵¹ share the same counter-ion (Glu¹³⁴) with the Arg¹³⁵–Glu¹³⁴ interaction being pre-dominant during the trajectory analyzed. The interactions involving Glu²³⁹, Ser²⁴⁰, Thr²⁴², and Thr²⁴³ at the boundary between helix 3 and the third loop become favored.

Distance between Helices 3 and 6—Table 6 shows the average relative distances between the cytoplasmic ends of helices 3 and 6 obtained from the simulations. Interestingly, the alterations on the hydrogen bond patterns described in the preceding section do not necessarily imply changes in the relative distances between helices. Specifically, the differences are smaller than 0.1 nm in all cases except for the T251K mutant. The results show that single mutants E134Q, E247Q, and T251K exhibit similar, shorter, or larger distances, respectively, compared with WT. Specifically, because residue 134 in helix 3 does not interact with helix 6, the removal of the negative charge with the E134Q mutation gives the smaller change. The results for E247Q clearly show that the loss of the electrostatic “lock” does not lead to a larger separation of the helices. On the contrary, here they even become slightly closer. T251K exhibits the largest separation between helices 3 and 6 because of the additional volume and/or charge at this position after the mutation. The different results observed for the double mutants, and specifically for those containing T251K, suggest that rhodopsin has mechanisms to rearrange the relative orientations of the helices. This can be done by rigid body motions of helices or helical fragments and lead to long range effects.⁵ Overall, the analysis performed here suggests that despite being important for maintaining the receptor in its inactive state, other residues, in addition to Glu¹³⁴, Glu²⁴⁷, and Thr²⁵¹, are involved in maintaining the cytoplasmic sides of helices 3 and 6 together. This is in agreement with the observation that Arg¹³⁵ is not critical for receptor function, but it is important for stabilizing receptors in the inactive conformation (61).

DISCUSSION

Previous studies have suggested that the cytoplasmic regions of transmembrane helices 3 and 6 of the GPCR are engaged in a network of electrostatic interactions that stabilizes their inactive states. In rhodopsin this would involve Arg¹³⁵ in helix 3. Thus, mutation at Arg¹³⁵, as in the R135Q mutant, could affect these interactions leading to a conformation that would have some features of the activated receptor. However, mutations at this site did not result in dark activity of the mutated rhodopsins (21, 54, 62). This suggested that the network of interactions was more complex than expected and stimulated our interest for other residues, such as Thr²⁵¹ in helix 6. Therefore, we have constructed and analyzed rhodopsins with mutations at other residues involved in this network (namely Glu¹³⁴,

⁵ A. Cordero, E. Ramon, P. Garriga, and J. J. Pérez, unpublished data.

Glu²⁴⁷, and Thr²⁵¹), but our discussion of the results takes into account the proposed role for Arg¹³⁵ in this specific set of interactions (although no mutant at this position was used in this study).

The detailed analysis of the structural and functional properties of mutants at the Glu²⁴⁷ and Thr²⁵¹ positions in helix 6, and combining these with the previously studied E134Q mutant in helix 3, provides experimental evidence for the importance of the electrostatic network around the cytoplasmic boundaries of helices 3 and 6 of rhodopsin in the conformational and functional properties of the receptor. Our results support the existence of such a network and indicate, for the first time, that Thr²⁵¹ plays a key role in it. A clear synergistic effect is found for the E134Q/T251A double mutant that shows a significant level of dark activity (as well as a large increase of activity in light condition) in comparison with the corresponding individual single mutants. Previous studies have also shown synergistic effects on Gt activation in rhodopsin, but in that case the amino acids were more deeply buried into the transmembrane domain. This is also the first time where such an effect is reported for amino acids clearly at the cytoplasmic domain in rhodopsin. The dark activity of the E134Q/T251A double mutant suggests that the combination of a neutral nonpolar side chain at position 251 (like in T251A) and a charge at position 247 leads to a rhodopsin conformation that permits activation of Gt in dark conditions and stresses the critical role of amino acid interactions in this region (possibly including residues in the cytoplasmic loop as detected in the MD simulations).

The analysis of the MD simulations performed in this study provides insight into the dynamic nature of the residue interactions within the protein structure, providing a basis for the interpretation of the experimental results of the mutants presented. The analysis outlines important differences, as a result of the side chain replacements, in terms of hydrogen bond patterns between residues in the region around the cytoplasmic sides of helices 3 and 6 and in the third cytoplasmic loop. Specifically, every mutant studied exhibits a different hydrogen bond profile and distinct to that found in WT. Moreover, the profile exhibited by double mutants cannot be predicted from the effects observed for the corresponding single mutants, suggesting that the protein is extremely sensitive to subtle conformational rearrangements. The network of interactions found in WT rhodopsin around the ERY motif becomes weakened in all the mutants studied, and this seems to be partly compensated with new hydrogen bonds involving helix 6 and the third loop.

In summary, the results presented in this study provide experimental evidence that the interaction among Glu¹³⁴, Arg¹³⁵, Glu²⁴⁷, and Thr²⁵¹, between helices 3 and 6, respectively, is crucial in keeping rhodopsin in the inactive state. Arg¹³⁵–Glu¹³⁴ interaction is important so that Arg¹³⁵ adopts the necessary conformation that favors the previous interaction. A clear new finding is that the additional hydrogen bond between helices 3 and 6 with Arg¹³⁵–Thr²⁵¹ contributes to the stabilization of the inactive state. Thus, removal of this interaction in the E134Q/T251A double mutant results in high levels of activity in dark and light conditions. Spectral and functional characterization and MD simulations taken together highlight

the importance of the so-called “ionic lock” at the cytoplasmic ends of helices 3 and 6 in rhodopsin, and allow the proposal of a key role for Thr²⁵¹ in this electrostatic network for the first time. Our results suggest that the mutants can affect the rhodopsin activation process as follows: (i) by alleviating the network of interactions in the region around the ERY motif, favoring rhodopsin activation, and/or (ii) by altering the conformation of the third loop, disrupting the interaction with the G-protein.

Acknowledgments—We thank Kevin Ridge for critical reading of the manuscript. We are grateful to Barcelona Supercomputer Center for the generous allocation of computer time granted to the project “Molecular Dynamics Simulations of G-protein-coupled Receptors.”

REFERENCES

1. Palczewski, K. (2006) *Annu. Rev. Biochem.* **75**, 743–767
2. Palczewski, K., Kumasaka, T., Hori, T., Behnke, C. A., Motoshima, H., Fox, B. A., Le Trong, I., Teller, D. C., Okada, T., Stenkamp, R. E., Yamamoto, M., and Miyano, M. (2000) *Science* **289**, 739–745
3. Teller, D. C., Okada, T., Behnke, C. A., and Palczewski, K. (2001) *Biochemistry* **40**, 7761–7772
4. Okada, T., Fujiyoshi, Y., Silow, M., Navarro, J., Landau, E. M., and Shichida, Y. (2002) *Proc. Natl. Acad. Sci. U. S. A.* **99**, 5982–5987
5. Salom, D., Lodowski, D. T., Stenkamp, R. E., Le Trong, I., Golczak, M., Jastrzebska, B., Harris, T., Ballesteros, J. A., and Palczewski, K. (2006) *Proc. Natl. Acad. Sci. U. S. A.* **103**, 16123–16128
6. Salgado, G. F., Struts, A. V., Tanaka, K., Krane, S., Nakanishi, K., and Brown, M. F. (2006) *J. Am. Chem. Soc.* **128**, 11067–11071
7. Ruprecht, J. J., Mielke, T., Vogel, R., Villa, C., and Schertler, G. F. (2004) *EMBO J.* **23**, 3609–3620
8. Nakamichi, H., and Okada, T. (2006) *Proc. Natl. Acad. Sci. U. S. A.* **103**, 12729–12734
9. Shichida, Y., and Morizumi, T. (March 1, 2006) *Photochem Photobiol.* 10.1562/2006-3-22-IR-854
10. Oldham, W. M., and Hamm, H. E. (2006) *Q. Rev. Biophys.* **39**, 117–166
11. Ballesteros, J. A., and Weinstein, H. (1995) *Methods Neurosci.* **25**, 366–428
12. Farrens, D. L., Altenbach, C., Yang, K., Hubbell, W., and Khorana, H. G. (1996) *Science* **276**, 768–770
13. Patel, A. B., Crocker, E., Eilers, M., Hirshfeld, A., Sheves, M., and Smith, S. O. (2004) *Proc. Natl. Acad. Sci. U. S. A.* **101**, 10048–10053
14. Franke, R. R., König, B., Sakmar, T. P., Khorana, H. G., and Hofmann, K. P. (1990) *Science* **250**, 123–125
15. Arnis, S., Fahmy, K., Hofmann, K. P., and Sakmar, T. P. (1994) *J. Biol. Chem.* **269**, 23879–23881
16. Jansen, J. J., Mulder, W. R., De Caluwe, G. L., Vlaskov, J. M., and DeGrip, W. J. (1991) *Biochim. Biophys. Acta* **1089**, 68–76
17. Kaushal, S., Ridge, K. D., and Khorana, H. G. (1994) *Proc. Natl. Acad. Sci. U. S. A.* **91**, 4024–4028
18. Li, J., Edwards, P. C., Burghammer, M., Villa, C., and Schertler, G. F. X. (2004) *J. Mol. Biol.* **343**, 1409–1438
19. Okada, T., Sugihara, M., Bondar, A. N., Elstner, M., Entel, P., and Buss, V. (2004) *J. Mol. Biol.* **342**, 571–583
20. Fahmy, K., Sakmar, T. P., and Siebert, F. (2000) *Biochemistry* **39**, 10607–10612
21. Cohen, G. B., Yang, T., Robinson, P. R., and Oprian, D. D. (1993) *Biochemistry* **32**, 6111–6115
22. Kim, J. M., Altenbach, C., Thurmond, R. L., Khorana, H. G., and Hubbell, W. L. (1997) *Proc. Natl. Acad. Sci. U. S. A.* **94**, 14273–14278
23. Scheer, A., Fanelli, F., Costa, T., De Benedetti, P. G., and Cotecchia, S. (1996) *EMBO J.* **15**, 3566–3578
24. Alewijnse, A. E., Timmerman, H., Jacobs, E. H., Smit, M. J., Roovers, E., Cotecchia, S., and Leurs, R. (2000) *Mol. Pharmacol.* **57**, 890–898

Cytoplasmic Regions of Helices 3 and 6 of Rhodopsin

25. Samama, P., Cotecchia, S., Costa, T., and Lefkowitz, R. J. (1993) *J. Biol. Chem.* **268**, 4625–4636
26. Ringkanaanont, U., Van Durme, J., Montanelli, L., Ugrasbul, F., Yu, Y. M., Weiss, R. E., Refetoff, S., and Grasberger, H. (2006) *Mol. Endocrinol.* **20**, 893–903
27. Arora, K. K., Cheng, Z., and Catt, K. J. (1997) *Mol. Endocrinol.* **11**, 203–212
28. Li, J., Huang, P., Chen, C., de Riel, J. K., Weinstein, H., and Liu-Chen, L. Y. (2001) *Biochemistry* **40**, 12039–12050
29. Rasmussen, S. G., Jensen, A. D., Liapakis, G., Ghanouni, P., Javitch, J. A., and Gether, U. (1999) *Mol. Pharmacol.* **56**, 175–184
30. Ballesteros, J. A., Jensen, A. D., Liapakis, G., Rasmussen, S. G., Shi, L., Gether, U., and Javitch, J. A. (2001) *J. Biol. Chem.* **276**, 29171–29177
31. Parma, J., Duprez, L., Van Sande, J., Cochaux, P., Gervy, C., Mockel, J., Dumont, J., and Vassart, G. (1993) *Nature* **365**, 649–651
32. Greasley, P. J., Fanelli, F., Rossier, O., Abuin, L., and Cotecchia, S. (2002) *Mol. Pharmacol.* **61**, 1025–1032
33. Kosugi, S., Mori, T., and Shenker, A. (1998) *Mol. Pharmacol.* **53**, 894–901
34. Huang, P., Li, J., Chen, C., Visiers, I., Weinstein, H., and Liu-Chen, L. Y. (2001) *Biochemistry* **40**, 13501–13509
35. Shapiro, D. A., Kristiansen, K., Weiner, D. M., Kroeze, W. K., and Roth, B. L. (2002) *J. Biol. Chem.* **277**, 11441–11449
36. Franke, R. R., Sakmar, T. P., Oprian, D. D., and Khorana, H. G. (1988) *J. Biol. Chem.* **263**, 2119–2122
37. Oprian, D. D., Molday, R. S., Kaufman, R. J., and Khorana, H. G. (1987) *Proc. Natl. Acad. Sci. U. S. A.* **84**, 8874–8878
38. Senin, I. I., Bosch, L., Ramon, E., Zernii, E. Y., Manyosa, J., Philippov, P. P., and Garriga, P. (2006) *Biochem. Biophys. Res. Commun.* **349**, 345–352
39. Fahmy, K., Jager, F., Beck, M., Zvyaga, T. A., Sakmar, T. P., and Siebert, F. (1993) *Proc. Natl. Acad. Sci. U. S. A.* **90**, 10206–10210
40. Cordomi, A., Edholm, O., and Perez, J. J. (2007) *J. Comp. Chem.* **28**, 1017–1030
41. Lindahl, E., and Edholm, O. (2000) *Biophys. J.* **79**, 426–433
42. Berendsen, H. J. C., van der Spoel, D., and Vandrunen, R. (1995) *Comput. Phys. Commun.* **91**, 43–56
43. Lindahl, E., Hess, B., and van der Spoel, D. (2001) *J. Mol. Model.* **7**, 306–317
44. Berendsen, H. J. C., Postma, J. P. M., DiNola, A., and Haak, J. R. (1984) *J. Chem. Phys.* **81**, 3684–3690
45. Miyamoto, S., and Kollman, P. A. (1992) *J. Comput. Chem.* **13**, 952–962
46. Jorgensen, W. L., Maxwell, D. S., and Tirado-Rives, J. (1996) *J. Am. Chem. Soc.* **118**, 11225–11236
47. Berger, O., Edholm, O., and Jähnig, F. (1997) *Biophys. J.* **72**, 2002–2013
48. Hofsäsa, C., Lindahl, E., and Edholm, O. (2003) *Biophys. J.* **84**, 2192–2206
49. Wohler, J., and Edholm, O. (2004) *Biophys. J.* **87**, 2433–2445
50. Jorgensen, W. L., Chandrasekhar, J., Madura, J. D., Impey, R. W., and Klein, M. L. (1983) *J. Chem. Phys.* **79**, 926–935
51. Hayashi, S., Tajkhorshid, E., and Schulten, K. (2002) *Biophys. J.* **83**, 1281–1297
52. Saam, J., Tajkhorshid, E., Hayashi, S., and Schulten, K. (2002) *Biophys. J.* **83**, 3097–3112
53. Han, M., Lou, J., Nakanishi, K., Sakmar, T. P., and Smith, S. O. (1997) *J. Biol. Chem.* **272**, 23081–23085
54. Acharya, S., and Karnik, S. S. (1996) *J. Biol. Chem.* **271**, 25406–25411
55. Sakmar, T. P., Franke, R. R., and Khorana, H. G. (1989) *Proc. Natl. Acad. Sci. U. S. A.* **86**, 8309–8313
56. Kim, J. M., Altenbach, C., Kono, M., Oprian, D. D., Hubbell, W. L., and Khorana, H. G. (2004) *Proc. Natl. Acad. Sci. U. S. A.* **101**, 12508–12513
57. Han, M., Smith, S. O., and Sakmar, T. P. (1998) *Biochemistry* **37**, 8253–8261
58. Van Sande, J., Parma, J., Tonacchera, M., Swillens, S., Dumont, J., and Vassart, G. (1995) *J. Clin. Endocrinol. Metab.* **80**, 2577–2585
59. Ren, Q., Kurose, H., Lefkowitz, R. J., and Cotecchia, S. (1993) *J. Biol. Chem.* **268**, 16483–16487
60. Kjelsberg, M. A., Cotecchia, S., Ostrowski, J., Caron, M. G., and Lefkowitz, R. J. (1992) *J. Biol. Chem.* **267**, 1430–1433
61. Flanagan, C. A. (2005) *Mol. Pharmacol.* **68**, 1–3
62. Shi, W., Sports, C. D., Raman, D., Shirakawa, S., Osawa, S., and Weiss, E. R. (1998) *Biochemistry* **37**, 4869–4874

**Molecular dynamics simulations of rhodopsin point mutants
at the cytoplasmic side of helices 3 and 6.**

Cordomí A, Ramon E, Garriga P, Perez JJ

J. Biomol. Struct. Dyn., 2008, In press.

Molecular dynamics simulations of rhodopsin point mutants at the cytoplasmic side of helices 3 and 6

Arnau Cordoní¹, Eva Ramón^{2,&}, Pere Garriga² and Juan J. Perez^{1,}*

¹Laboratori d'Enginyeria Molecular, Departament d'Enginyeria Química, Universitat Politècnica de Catalunya, Barcelona, Spain.

²Centre de Biotecnologia Molecular, Departament d'Enginyeria Química, Universitat Politècnica de Catalunya, Terrassa, Spain.

[&]Present address: Centre for Membrane Biology, Department of Biochemistry and Molecular Biology, The University of Texas Health Science Center, Houston, Texas.

ABSTRACT

The present work reports on a structural analysis carried out through different computer simulations of a set of rhodopsin mutants with differential functional features in regard to the wild type. Most of these mutants, whose experimental features had previously been reported [Ramon et al. *J. Biol. Chem.* 282: 19. 14272-14282, 2007], were designed to perturb a network of electrostatic interactions located at the cytoplasmic sides of transmembrane helices 3 and 6. Geometric and energetic features derived from the detailed analysis of a series of molecular dynamics simulations of the different rhodopsin mutants, involving positions 134(3.49), 247(6.30) and 251(6.34), suggest that the protein structure is sensitive to these mutations through the local changes induced that extend further to the secondary structure of neighboring helices and, ultimately, to the packing of the helical bundle. Overall, the results obtained highlight the complexity of the analyzed network of electrostatic interactions where the effect of each mutation on protein structure can produce rather specific features.

INTRODUCTION

Rhodopsin is a key photoreceptor protein involved in the signaling process that eventually converts a photon into a visual response. This protein is a member of the G-protein coupled receptors (GPCR) superfamily, a family of proteins that plays a key role in the transmission of cell signals and in the regulation of basic physiological processes, being one of the largest families of proteins of the human genome and covering about 2% of the genes expressed. These proteins are embedded in the cell membrane and are arranged in a characteristic seven helix bundle structure that defines a site for specific binding of ligands that trigger the receptor activation process. In the case of rhodopsin, this site contains the chromophore molecule 11-*cis*-retinal that is covalently linked to K296 in transmembrane (TM) helix 7 via a protonated Schiff base linkage. Photoactivation of the receptor by light absorption induces isomerization of the 11-*cis*-retinal chromophore to its all-*trans* configuration, which results in a conformational change in the receptor that starts a cascade of biochemical reactions known as visual phototransduction that is the main molecular mechanism of the visual process.

Amino acids at the cytoplasmic sides of helices TM3 and TM6 (see Fig. 1) were shown to be involved in the activation mechanism of rhodopsin (1-6). Site-directed mutagenesis studies provided experimental evidence about the relevance of a set of interactions around R135(3.50), often referred to as the electrostatic lock. This region is highly conserved throughout the members of the GPCR superfamily and was considered as a putative molecular switch involved in a common activation mechanism of most GPCR (7-9). Different studies have addressed the effect of mutating either

R135(3.50) (7, 8, 10, 11), E134(3.49) (7, 8, 12), E247(6.30) (9, 13), or T251(6.34) (14) in different GPCR. Particularly, protonation of E134(3.49) or the mutation of either E134(3.49), E247(6.30) or T251(6.34) to residues lacking their charged/polar groups have been shown to increase either the dark activity of the receptor (with retinal bound in the 11-*cis* form), or the activity in the absence of ligand (constitutive activity) (1-6). These studies have great significance in clarifying several aspects of GPCR function; however the molecular interpretation of these functional effects is sometimes difficult and may be based in inaccurate hypothesis.

Knowledge of the 3D structure of rhodopsin at atomic resolution provides a unique opportunity to carry out structure-function studies aimed at shedding light into the mechanism of rhodopsin activation. The different crystal structures of rhodopsin reported in its dark-state (7-11) clearly provide support to the fact that residues E134(3.49), R135(3.50), E247(6.30) and T251(6.34) are involved in a network of hydrogen bond interactions, being R135(3.50) simultaneously hydrogen-bonded to E134(3.49), E247(6.30) and T251(6.34) as shown in Fig. 2. These interactions are believed to stabilize rhodopsin in its inactive form. Accordingly, mutations that weaken the hydrogen bond network will facilitate the transition to a partially activated state and consequently enhance the activity of the receptor. Although these interactions are believed to be present in other GPCR, only the interaction between R131(3.49) and D130(3.50) is present in the recently reported crystal structures of different engineered chimeras of the human β 2 adrenergic receptor (12-14). However, the proximity of the engineered added motifs to the protein seem to favor the interaction of E268(6.30) either with K267(6.29) or with the

T4L motif, despite the former remains close to R131(3.49).

Computational methods and specifically, molecular dynamics (MD) simulations can provide useful information about the structural features of a protein and about its dynamical behavior, not available from X-ray diffraction data. Moreover, combining site-directed mutagenesis and MD simulations has already been shown to be a useful approach to explore the molecular mechanisms underlying GPCR activation (1,15,16). Currently, simulations of rhodopsin embedded in a lipid bilayer can be carried out for several tens or even hundreds of nanoseconds, providing data in a realistic environment. In this direction, several MD studies of rhodopsin performed on different model lipid molecules have been recently reported (17-24).

In the present study we focus on the region of the electrostatic network around the cytoplasmic edges of helices TM3 and TM6 through the comparison of the structural features of wild type (WT) rhodopsin with those of different single and double mutants at positions 134(3.49), 247(6.30) and 251(6.34) using MD as a tool. Accordingly, nine different 5 ns MD simulations of WT rhodopsin and a set of single and double mutants including E134Q, E247Q, T251K, E134Q/E247A, E134Q/T251A, E134Q/T251K, E134Q/T251E, and E247Q/T251K, were performed and analyzed. Most of these mutants were recently reported to have activation profiles that could be attributable to different conformational states (3). The present work is an extension of a preliminary theoretical analysis carried out to provide structural support to site-directed mutagenesis experiments (3). The results reported in the present work provide evidence that the mutations produce subtle local changes in the hydrogen bond patterns that subsequently affect the secondary structure of helices TM3, TM4, TM5 and TM6 and eventually perturb the structural properties of the helix bundle as a whole. Our results suggest a cooperative mechanism which allows the protein to respond to a specific mutation through the rearrangement of the structure that extends far from the local area where mutations have been introduced.

METHODS

Rhodopsin structure

Rhodopsin coordinates were taken from the first monomer of entry 1GZM (10) of the Protein Data Bank (25). This structure differs from those previously published (7,8,11) in that all the residues of the extracellular and cytoplasmic loops are included in the structure. In addition, all residues of the N-terminal segment, including the acetyl group are present in our model. However, it does not include the C-terminal part beyond the palmitoylated cysteines at the end of the short cytoplasmic helix 8. The two palmitoyl chains bonded to two cysteine residues that are believed to be important for the membrane anchoring point were also included. All possibly charged amino acids in the WT as well as in all mutants were charged except D83 and E122, since there is experimental evidence that these residues are protonated and neutral (26). Additionally, both residues are located in the hydrophobic

core, and have no counter charge in their neighborhood. Despite the mutations performed involve variations of the total charge, no changes in the protonation state of the neighboring residues were considered since the net charge compared to the WT is always positive, in favor of the charged form or the protein already observed for the WT (2).

Membrane model and embedding

Rhodopsin was embedded into a previously equilibrated rectangular box containing both DPPC lipids and water molecules (27). The initial box contained 256 lipid and 17044 water molecules, giving the dimensions 10.3x8.0x10.2 nm³ before protein insertion. Although DPPC is not the predominant lipid type in the rod cell outer membranes it was selected because it is the best characterized PC lipid both experimentally (28) and from MD simulations (27,29-33). Additionally, it was previously shown that the hydrophobic thickness of a DPPC bilayer matches the thickness of rhodopsin (23,34).

After introducing the receptor in the box, all water molecules having the oxygen atom closer than 0.40 nm and all lipid molecules having a heavy atom closer than 0.25 nm from a heavy atom of the protein were removed. This process was used to eliminate steric hindrances between the protein and both DPPC or water molecules, but introduced small voids between the protein and water and lipid molecules that were removed during the equilibration period of the MD simulations. Depending on the total charge of each system, about 100 water molecules in the box were randomly chosen and replaced by either sodium or chloride ions to obtain the physiologic ion concentration of 0.2 M in NaCl, fairly similar to the concentrations in biological organisms. The balance between sodium and chloride ions was adjusted to obtain a totally electro-neutral system taking the net charge of the protein into account. In the simulations with a single bilayer and periodic boundary conditions both sides exhibit the same concentrations. However, water solutions in real membranes exhibit different intracellular and extracellular ionic concentrations.

MD simulation protocol

All simulations were performed using a parallel version of GROMACS 3.2 package (35,36). All systems were subject to periodic boundary conditions in three directions of the Cartesian space. Simulations were performed at 323 K so that DPPC lipids remained above the gel/liquid crystalline phase transition temperature. The temperature was kept constant using separate thermostats for protein, water, ions and lipids (37). Although this temperature is slightly higher than the physiological one, it is used because otherwise considerably longer time than the order of some nanoseconds of simulation would be required to significantly alter the protein structure (17,24). The coupling time constants for all thermostats were 0.1 ps, except for water that was 0.01 ps. The integration of motion equations was performed using a leap frog algorithm with a time step of 2 fs. All bonds in the protein and lipids were frozen using the LINCS (38) algorithm. For water, bonds and angles were held constant using the analytical SETTLE method (39). A cutoff of 1.0 nm was used for Lennard-Jones interactions and a twin cutoff of 1.0/1.8 nm for electrostatic interac-

tions, with the neighbor list was updated every 10 steps. Although it is known that truncation of long range interactions may lead to some artifacts in the lipid bilayer (29,32,40-44), we have recently shown that sampling in the NVT ensemble together with a large cutoff for the electrostatics is suitable for simulating bovine rhodopsin embedded in a DPPC lipid bilayer (45), in agreement with previous results regarding alamethicin channel forming peptides (46). Specifically, the fixed volume restrains the bilayer thickness whereas the membrane acts as a physical restraint that stabilize the protein structure from possible long-range electrostatic artifacts (45).

The all-atom OPLS force field (47) currently implemented in GROMACS 3.2 was used for all molecules in the system except for DPPC lipids, that were modeled with a previously described force field (33), which reproduces most properties including areas per lipid of pure lipid bilayer systems. TIP3P model was used for water molecules (48). Retinal charges were taken from quantum chemical calculations (49) and have already been used in other rhodopsin MD simulations (19). For palmitoylated cysteines, fractional charge were computed from electrostatic potential calculations at HF/6-31G* level and further adapted to neutral group charges in a similar manner to standard amino acids in the OPLS-AA force-field.

WT rhodopsin was energy minimized and equilibrated in successive MD simulations extending up to 6.5 ns in total. First, 500 ps were run using the NPT ensemble, allowing the system to change the box dimensions, with protein coordinates strongly restrained to the initial structure. During this step, the gap between the protein and lipid and water molecules was removed. Then, 500 ps were run using the NVT ensemble with the same position restraints in the protein. In the last equilibration step, when the bilayer and water around the protein had stabilized, the restraints on the protein were released and the system was run for 5.5 ns. From this point, production runs of 5 ns were started with WT rhodopsin and all mutants studied. Mutants were constructed by replacement of residue side-chains in the equilibrated WT structure. In order to keep the electro-neutrality of the system, single water molecules were converted to Na⁺ or Cl⁻ ions when necessary.

Analysis of trajectories

The analysis of trajectories has been performed using the tools included in GROMACS package together with our own programs. Lengths of the helices considered in this report were taken from the consensus secondary structure (Table I) as follows: TM1:34-61, TM2:72-101, TM3:107-134, TM4:151-169, TM5:201-225, TM6:248-278, and TM7:288-310. For the determinations of tilt and kink angles, each helix was considered as an independent axis defined by 8 C α at every helix end, and divided in two axes across the center of mass of 3 C α centered at the main kink points: TM1:53, TM2:92, TM3:115, TM4:160, TM5:214, TM6:264, TM7:296 as reported in ref. (24). Interaction energies were computed from the electrostatic and Lennard-Jones (LJ) contributions corresponding to different parts of the system studied. For the computation of specific residues or TM helices, all atoms -including hydrogen atoms and those being part of the back-

bone- were taken into account. Particularly, the cytoplasmic segments of TM3 and TM6 were chosen as 121-139 and 244-264, respectively.

RESULTS

The different mutants selected in the present work had been designed to alter the network of the hydrogen bonds and electrostatic interactions in the cytoplasmic side of helices TM3 and TM6. The analysis of MD trajectories described in the present section is intended to underline exclusively the structural effects induced by the mutations. The results indicate that the different mutations produce subtle structural alterations in the network of electrostatic interactions that, in turn, induce alterations on the secondary motifs of helices TM3 and TM6 and ultimately, on the rigid-body motions of the protein.

The link between the cytoplasmic sides of TM3 and TM6

The interactions network

The so-called electrostatic lock of rhodopsin is a network of electrostatic interactions that stabilizes the receptor in its inactive conformation. It involves R135(3.50) as a key piece, exhibiting interactions with E134(3.49), E247(6.30) and T251(6.34) simultaneously, constituting the four residues of the lock. A close up look into this region, showing the hydrogen bonding and electrostatic interactions in the different mutants, taken from representative snapshots of the last section of the corresponding MD trajectories, is displayed in Fig. 2. For a more quantitative analysis Table IIA lists the interaction energies between the specific pairs of residues involved in the electrostatic lock, namely residues 134, 135, 247 and 251. In order to assess the strength of the TM3-TM6 interaction, the last column of this Table refers to the interaction energy between helices TM3 and TM6 computed from the different contributions of these residues, taking into account the particular helix where they are located. Additionally, interaction energies between segments 121-139 (TM3) and 244-264 (TM6) were computed for the different mutants, which exhibit values ranging from -560 kJ/mol to -30 kJ/mol (Table IIB). Such differences are basically attributable to the coulombic contribution since the LJ term is rather constant, suggesting that the contact surface between the two helices is very similar in all cases. Values reported in Table IIB exhibit a parallel trend with those of the last column of Table IIA (excluding the double mutant E247Q/T251K, which exhibits the largest standard deviations; see below), suggesting that the four residues of the electrostatic network analyzed above account for most of the interaction energy between helices TM3 and TM6 at this region.

In WT rhodopsin, the structural features of the residues involved in the electrostatic lock that can be observed in the X-ray structures are preserved along the MD trajectory, in agreement with previous simulations (18-20). Specifically, R135(3.50) exhibits two ionic interactions with E134(3.49) of TM3 and E247(6.30) of TM6, respectively, in addition to a hydrogen bond with residue T251(6.34) of TM6, during the whole trajectory. Values for the interaction energies (see Table IIA)

are -550 kJ/mol, -400 kJ/mol and -50 kJ/mol, respectively. Interestingly, whereas a direct residue-residue hydrogen bonding interaction is observed for E247(6.30) and T251(6.34), the interaction with E134(3.49) is sometimes direct and sometimes mediated through a water molecule, a finding also compatible with a previous study (19).

Single mutants

E134Q is characterized by the loss of one of the ionic pairs of R135(3.50) and therefore, for the lack of competition -observed in the WT- between E134(3.49) and E247(6.30) for the latter residue. This leads to a strengthening of the interaction R135-E247 and, consequently, between TM3 and TM6, giving a interaction energy that is about twice the obtained for the WT rhodopsin. The opposite effect is found in the mutant E247Q, where the interaction with R135(3.50) weakens. More important is the fact that visual inspection of the structures suggests that the mutants favor the displacement of R135(3.50) side-chain towards helix TM3 moving away from TM6. The preceding results reveal that the removal of the negative charge at positions 134 and/or 247 reduces the interaction with R135 by a half or even disappearing in some cases.

Mutant T251K exhibits an additional positive charge located at the beginning of TM6, a region already containing a large number of charged residues including three positively charged ones K245, K248 and R252, and two negatively charged ones E247(6.30) and E249. Replacement of a threonine residue for a lysine not only affects the charge of the system but also increases steric hindrance due to the presence of a bulkier side chain. This strongly affects the original network forcing a rearrangement of the neighboring positively charged residues. Particularly, R135(3.50) feels electrostatic repulsion from K251, which ends up with a weakening of the interaction R135(3.50)-E247(6.30). This situation forces a rearrangement of the different residues to form new interactions in other directions. Thus, K251(6.34) forms hydrogen bonds with residues E239 and Q237, located in the third cytoplasmic loop (3), with T229 in helix TM5 and with solvent water molecules and chloride ions. Similarly, E247(6.30) exhibits a hydrogen bond interaction with Q312 (not observed in any other simulation) at the short cytoplasmic helix 8 during a long fraction of the MD trajectory as well as with solvent water molecules and sodium ions. As a consequence, the mutant exhibits a weaker interaction between TM3 and TM6 than in the WT. Moreover, the similar interaction energies between mutants E247Q and T251K suggest that the effect of removing the negative charge of residue 247 is analogous to introducing a positive one at position 251.

Double mutants

The interactions observed in double mutants are not always predictable from the behavior observed for the corresponding single mutants. Specifically, in the case of E134Q/E247A, mutation of E134 and E247 not only represents a loss of interactions but the removal of the two counter-charges of R135(3.50). On the one side A247(6.30) is not able to establish a hydrogen bond with R135(3.50),

whereas on the other side the R135(3.50)-Q134(3.49) interaction is much weaker than in the single mutant. As a consequence, the R135(3.50)-T251(6.34) is the only interaction present in the WT that is preserved. Therefore, the electrostatic network associated to the D(E)RY motif is almost lost as it is underlined by the 60% drop in the interaction energy between TM3-TM6, giving the smallest value within the systems studied. The results suggest that mutation E134Q has no effect in stabilizing the interaction between TM3 and TM6 if residue E247(6.30) is not present.

The two replacements in mutant E134Q/T251A disturb the native direct interactions R135(3.50)-T251(6.34) and R135(3.50)-E134(3.49). Not only the interaction energy between R135(3.50)-T/A251(6.34) drops to a fifth of the native one but also induces a small decrease on the R135(3.50)-E247(6.30) interaction, suggesting that T251(6.34) helps in stabilizing the latter. Therefore, the E134Q/T251A double mutant exhibits a interaction energy about 50 kJ/mol lower than the energy exhibited by the single mutant E134Q. The double mutant E134Q/T251K combines some of the features of both single mutations. On the one hand, E134Q/T251K results in a drop in the interaction energy between residues R135(3.50)-E134(3.49), similar to that found in the single mutant E134Q(3.49), though smaller, and on the other, the pair K251(6.34)-R135(3.50) exhibits an unfavorable interaction energy similar to that in the T251K single mutant. However, K251(6.34) weakens the interaction E247(6.30)-R135(3.50) more than observed in the single mutant, due to the competition between the former and R135(3.50) for E247(6.30). In contrast, the main difference with the single mutant is the favorable interaction energy between E247(6.30) and K251(6.34). However, since both residues are in the same helix this interaction does not produce a net stabilization between TM3 and TM6, resulting in a similar interaction energy. The E247Q/T251K double mutant has five positively charged residues within two helix turns with only a single negatively charged side-chain. Specifically, the mutation impairs the native interaction R135(3.50)-E/Q247(6.30) as in the E247Q single mutant, although there are larger alterations due to the existence of the additional positive charge. The interaction energy between TM3 and TM6 is larger than in the remaining mutants containing T251K due to the stronger salt bridge between E134(3.49) and K251(6.34) and the smaller repulsion between E134(3.49) and Q247(6.30) (see Table II). The conformational change of R135, moving apart from the helix, reduces the repulsion with other charged residues at TM6 that are able to better explain the gain in the interaction energy between the cytoplasmic sides of TM3 and TM6 (Table IIB) than merely considering the four residues of the lock (last column of Table IIA).

In the double mutant E134Q/T251E both mutations favor the interactions between residues contributing to hold TM3 and TM6 helices together at expenses of a loss in the intra-helix interactions -a drop in the interaction energy between E134Q(3.49) and R135(3.50) and a significant increase in the repulsion between E247(6.30) and E251(6.34)-. The E134Q(3.49) mutation prevents the competition between residues E134(3.49) and

E247(6.30) for residue R135(3.50), and additionally there is a new ionic interaction between R135 and E251, which favors the interaction between helices. Not surprisingly, the mutant exhibits the largest interaction energy among the proteins studied -more than twice the energy of the WT- (see Table II).

Interactions with the solvent (water molecules, ions and lipids)

A detailed analysis of Fig. 1 and 2 shows that most residues of the electrostatic lock are solvent accessible, mostly E/Q134, E/Q247, E/K251 and R135, to a lesser extent. Therefore, for a complete picture of the structural changes produced on the system, it is necessary to consider the interactions of the protein with water and ions that damp those within residues (18). Furthermore, protein-solvent/ion interactions are likely to rearrange not only because some specific atoms of the WT are missing, but also as a response to the different net charge in the mutants studied. The results show that the strength of the interactions with water molecules and ions is sensitive to how buried the side chains are. Whereas sodium ions are mostly found close to negatively charged residues E134(3.49) and E247(6.30) -and E251(6.34) in E134Q/T251E mutant-, chloride ions stay close to R135(3.50) -and mostly K251(6.34) in mutants K251, E134Q/T251K and E247Q/T251K-. Regarding water molecules, the proteins where native interactions are removed (E134Q or E247Q/A) exhibit a tendency to adopt more compact structures, that is, replacing protein-protein water mediated interactions by direct ones. Furthermore, when new charged residues are added (mutants containing T251K or T251E) the electrostatic lock becomes more open and accessible to water molecules and ions. Specifically, whereas the side-chain of T251 is not solvent accessible, both K251 and E251 are pushed away from the protein core. Finally, recent studies suggest that interactions with lipid oxygen atoms may also help to stabilize the charges of the receptor, in particular residues Y136, K248 and R252 (24).

Distances between TM3 and TM6

The average distance between the centers of mass of the cytoplasmic sides of TM3 and TM6 is reported in the last column of Table II B. In the WT this is 11.2 Å and the value for the different systems differ less than 1 Å in all cases except for T251K that is larger (see Fig. 2). The separation between helices in the latter is almost 2 Å larger than the in WT, but becomes smaller in the double mutants involving K251(6.34). Distances between the cytoplasmic faces of TM3 and TM6 do not follow the same trends as the interaction energies, suggesting that the packing of these fragments is independent of the local effects at the cytoplasmic side of these helices.

Protein stability and secondary structure

The analysis of the MD trajectories performed indicates that no major changes in the protein tertiary structure occur in the mutants studied. However, there are local effects on the structure that can be identified by measuring the root mean square deviations (rmsd) of the protein α -carbons along the

MD trajectory. Thus, rmsd time evolution exhibits a plateau after 3 ns for all systems, with asymptotic values between 0.25-0.30 nm for all systems including WT rhodopsin (data not shown), compatible with previous simulations of similar systems (17,24). E134Q/T251E represents an exception, exhibiting a larger value of 0.35 nm, due to the necessary rearrangements experienced, necessary for E251(6.34) to become the main counterion of R135(3.50). As expected, the TM regions exhibit lower rmsd values, whereas the second and the third cytoplasmic loops are the regions exhibiting the larger deviations, in agreement with recent simulations of WT rhodopsin performed under different conditions (17,24). The computation of the rmsd for the cytoplasmic segments of TM3 and TM6 (residues 121-139 and 244-264, respectively) normalized to the WT shows that the majority of mutants do not exhibit deviations in these regions. Exceptions are E247Q and E247Q/T251K that exhibit rmsd values of 0.13 and 0.09 nm at TM3, and T251K and E134Q/T251E that exhibit rmsd values of 0.18 and 0.15 nm at TM6.

Although recent work indicated that the conserved D(E)RY and NPxxY motifs exhibit a strong correlation with retinal (50), the analysis of the rmsd values indicate that the deviations around the protonated Schiff Base are of the order of 0.05 nm after 5 ns in all systems including the WT, suggesting that the different mutants do not directly affect the retinal conformation. Finally, despite we and others have recently hypothesized that the mutants studied in the present work may have an effect in the conformation of the neighboring loops (3), a detailed analysis is beyond the scope of the present calculations, since loops are not properly sampled in simulations of the length of the present ones (51,52).

In order to analyze the effect of the mutations on the secondary structure of the different TM regions, an analysis of the intra-helical hydrogen bonds ($i,i+n$; $n=3,4,5$) in each of the helices was performed. Indeed, the existence of helix breaks and turns of type 310 ($i,i+3$) at the end of the helices is critical since they produce larger rmsd in the second and third cytoplasmic loops. Table I shows the secondary structure of the average from the last 2 ns of trajectory for each of the mutants. These results suggest that the helical structure is well preserved in all cases, although they show subtle differences in regard to the length and stability of the cytoplasmic regions of both TM3 and TM6. Hydrogen bonds involving the carbonyl groups of residues 131-136 in the region of the D(E)RY motif in TM3, exhibit deviations from an ideal α -helix that are also found in the WT. Moreover, the secondary structure at the cytoplasmic side of TM3 is sensitive to the interaction with TM6 since either the lack of a negative charge at position 247(6.30), or the existence of a positive one at position 251(6.34) provides larger distortions, with additional breaks and/or a larger number of $i,i+3$ interactions. In any case, alterations are small and local as can be graphically observed in Fig. 2. In contrast, larger alterations are observed in the region 151-158 at the cytoplasmic side of TM4, in particular in the mutants T251K and E134Q/E247Q. The cytoplasmic region of TM5 - including the carbonyl groups of residues 221-228- exhibits similar intra-helical interactions than in the WT in most

cases analyzed, suggesting that the lack of interaction between helices might stabilize the secondary structure of residues in this region. The fragment of TM6 containing the carbonyl groups of residues 247-255 is destabilized in T251K, E134Q/E247A, E134Q/T251K and E134Q/T251E as depicted in Fig. 2. Particularly, the helix break in T251K reflects a tilt of the 251-247 fragment and the destabilization observed in E134Q/E247A is due to the larger distance between residues 247 and 251. The breakage of E134Q/T251K interactions is necessary for the formation of E247(6.30)-K251(6.34). Finally, E134Q/T251E exhibits 6 consecutive $i,i+3$ interactions which appear because E251(6.34) becomes the counterion of R135(3.50) instead of E247(6.30). Overall, the results suggest that the effects on the secondary structure are small and locally related to the cytoplasmic sides of helices TM3 and TM6 and the neighboring TM4 and TM5 connected through the second and the third cytoplasmic loops, respectively.

Analysis of the helix bundle

The analysis of the effects of the different mutations on the packing of the helix bundle is based on the study of rigid body motions of the helices, taken as independent objects (see Material and Methods section). In this case, the analysis performed includes the in-plane and perpendicular motions relative to the bilayer plane as well as the helix tilts and kinks. The first two structural features exhibit differences smaller than 1 Å, and even below 0.4 Å, in most mutants when compared to the WT, indicating that these parameters are not sensitive to the mutations performed. However, the values for the average tilt and kink angles over the last 1 ns of each trajectory reveal significant differences in some cases (Table III). The major differences are observed for TM4, TM5 and TM6, which are adjacent to the second and third cytoplasmic loops and close to residues 134, 135, 247 and 251. The reason why TM3 is not listed here is that it interacts strongly with many helices -TM2, TM4, TM5 and TM6- that act as a physical constraint.

Time evolution of certain helix tilts and kinks exhibit clear differences in comparison with WT rhodopsin (Fig. 3). The results show that the angles of the rigid body motions begin from a common value -the same starting structure- and evolve to a slow but steady increasing divergence, which in some cases seems not to be finished in 5 ns. Other changes may occur although they overlap with their natural oscillations. Values of helix tilt do not change much from one system to another except in a few cases, and the differences are often in the range of the standard deviations. Therefore, the discussion below refers only to the cases where there is a clear difference between the values of the WT and the mutants (see Fig. 3). This is the case of TM4 for the mutants E134Q/E247A and E134Q, and TM6 for the mutants T251K, E247Q, E247Q/T251K and E134Q/E247A. The large deviation of 11° found in TM4 for the E134Q/E247A double mutant seems to arise from the absence of a counterion for residue R135(3.50). In contrast, the small differences observed in helix TM6 seem to correlate well with the charge exhibited by the helix, with mutants like E134Q providing smaller tilts than the WT and mutants like T251K exhibiting larger ones. A previous model for T251(6.34K) mutants on the μ -opioid receptor suggested a large

separation between TM3 and TM6 and effects on the neighbor helix TM5 motivated by the additional charge (4). The present MD simulations show a small separation between TM3 and TM6, for mutations including T251K, but larger alterations on tilt and kink angles of helices TM4, TM5 and TM6.

Some mutants exhibit also a clear deviation in the kink values in TM4, TM5 and TM6 from the corresponding values for the WT. The pronounced kink of TM4 for the mutants E134Q/E247A and E134Q suggest a direct implication of the E134Q mutation leading to differences of about 10°. Contrarily, TM5 shows significant but smaller differences in the time-evolution of kinks, but with E134Q/T251A and T251K providing less bended helices than the WT. Finally, the large bend of 40° in TM6 observed for the WT exhibits also large differences from one system to another which seem to be sensitive to the mutants involving alterations in the charge of residue 247(6.30) and/or 251(6.34) -with changes up to 15° for E247Q/T251K-, because of the +2 net charge localized in a small region.

DISCUSSION

The present study addresses an analysis by means of MD simulations of the structural effects produced by a set of mutations on the residues defining the region called *electrostatic lock*, at the boundaries of the cytoplasmic domain of rhodopsin, linking the cytoplasmic side of TM3 and TM6. For this purpose nine 5 ns MD simulations, in an explicit lipid bilayer, have been carried out, and the dynamical behavior of three single and five double mutations have been compared with that of WT rhodopsin. The results obtained provide new insights into the structural rearrangements caused by introducing point mutations at amino acid positions involved in the *electrostatic lock*, providing a theoretical basis for the recent study of the expressed and purified mutants (Ramon et al., 2007), in terms of the pre-disposition of the dark state structures to undergo relevant functional changes (53). The MD simulations clearly indicate that the protein structure is sensitive to side chain modifications involving the network of electrostatic interactions between the cytoplasmic sides of helices TM3 and TM6 that keep the receptor in its inactive conformation.

The results suggest that each mutant needs to be analyzed individually in terms of the conformational rearrangements induced. Moreover, the resulting electrostatic arrangements have to be carefully taken into account for a meaningful interpretation of the experimental results obtained by side-directed mutagenesis and functional assays. Furthermore, double mutants do not generally exhibit a behavior which can be easily predicted from that of the corresponding single ones. Thus, care should be taken when analyzing the results from a set of given mutations because the structural properties in each particular mutant are very sensitive to specific details of the particular side chain interactions adopted.

Changes are described in the hydrogen bond network involving R135(3.50) and E134(3.49), E247(6.30) and T251(6.34), defining the electrostatic network between the cytoplasmic ends of helices TM3 and TM6. The rearrangement of the

structure due to the mutations is fast, typically occurring in less than 0.5 ns. At this time the secondary structure of helices TM3, TM4, TM5 and TM6 starts being altered to compensate the newly formed interactions. These changes are transmitted to the second and third cytoplasmic loops and to small, but not negligible changes in the tilt and kink angles of helices TM4, TM5 and TM6 –extending for more than 5 ns in most cases- which, however, do not affect the global packing of the helical bundle. Although it has been possible to identify the initial structural changes induced by the side chain mutations, larger sampling times would be required for a full characterization.

One of the most striking result of the present study is that side chain mutations on rhodopsin –at the cytoplasmic side of the protein- not only have local effects but can induce changes in other helices than those containing the mutations, providing evidence that rhodopsin responds to local conformational changes in a global-cooperative manner. This highlights the exquisite conformational design of the protein and the sophisticated set of different interactions responsible for the formation of the correctly folded (and functionally optimized) rhodopsin molecule. Although all side chain mutations studied in this work are located on helices TM3 and TM6, and were designed in order to alter electrostatic interactions, they result in alterations of other features such as helix tilts and kinks up to 20° in TM6 but also in TM4 and to a lower extent in TM5. The rationale is that subtle local changes can be transmitted along the whole bundle of helices since every helix is tightly packed with the neighboring helices. These may be the structural determinants of the formation of the correctly folded rhodopsin molecule that is required for its main role in the visual phototransduction process.

The calculations corresponding to the mutants E247Q(6.30), and T251E(6.34), support the paradigm that a reduced interaction between helices TM3 and TM6 provides a larger dark activity of rhodopsin (3), supporting the *electrostatic lock* hypothesis. Similar results have also been obtained in other GPCR such as the β 2-adrenergic receptor (1) or the μ -opioid receptor (4). However, some mutants like E134Q or T251K do not provide full support to this hypothesis since they exhibit higher dark activity than WT rhodopsin (3) despite of exhibiting higher interaction energy between TM3 and TM6 than WT rhodopsin. It would seem that the local environment is also responsible for maintaining such interactions. In this context we suggest that the different interaction patterns observed in the recently reported crystal structures of different engineered chimeras of the human β 2 adrenergic receptor (12-14) could be due to the local effects in the *electrostatic lock* induced by the engineered added motifs. The enhanced activity for mutants E134Q and E134Q/T251A of rhodopsin (3) can be argued considering that E134(3.49) helps in maintaining the optimal conformation of R135(3.50) to hold TM3 and TM6 together (1,3), a role supported by the inhibition reported for E134D mutant (6). Moreover, a recent analysis of interaction correlation patterns from MD simulations revealed that this residue is strongly correlated with retinal, providing evidence that the residue regulates rhodopsin activity (50). On the other hand, despite that

the mutant T251K destabilizes the electrostatic network between TM3 and TM6 both in rhodopsin and in the μ -opioid receptor (4), in the latter case it exhibits an increased constitutive activity -following the paradigm-, but not in the former case (3), suggesting a combination of effects in a global mechanism. Additionally, the μ -opioid receptor does not exhibit dark activity despite that the WT lacks the residue equivalent to E247(6.30) (4). Present calculations suggest that the effect on the interaction energy between TM3 and TM6 of mutant E247Q is similar to that of T251K. According to the results of the present work, the possibility that the latter mutant –and maybe other ones- exhibits a defective folding in the region of G-protein binding should be considered. It is also possible that some of the mutants studied here may result in alterations of the NPxxY motif in TM7 as previously suggested (54). However, the present results provide support to previous studies which found that the conserved R135(3.50) side chain is not required for receptor function, but it is important for stabilizing receptors in the inactive conformation (55). Our results suggest an emerging picture where the so-called “electrostatic lock” would not be an on-off mechanism with a single molecular switch, but would form part of a concerted mechanism involving coupling of two protonation switches (56) other than the mere *electrostatic lock*, contributing to the observed mutant phenotypes with enhanced activities.

Acknowledgment

A.C. and E.R. are the recipients of fellowships from UPC and Generalitat de Catalunya, respectively. This work has been supported by grants from the Spanish Ministry of Education SAF2005-08148-C04-01 and SAF2002-04325-C03-01 (to JJP), and SAF2005-08148-C04-02 and SAF2002-04325-C03-02 (to PG).

REFERENCES

- Ballesteros, J. A.; Jensen, A. D.; Liapakis, G.; Rasmussen, S. G.; Shi, L.; Gether, U.; Javitch, J. A. *J Biol Chem* 2001, 276(31), 29171-29177.
- Periole, X.; Ceruso, M. A.; Mehler, E. L. *Biochemistry* 2004, 43(22), 6858-6864.
- Ramon, E.; Cordomí, A.; Bosch, L.; Zernii, E. Y.; Senin, II; Manyosa, J.; Philippov, P. P.; Perez, J. J.; Garriga, P. *J Biol Chem* 2007.
- Huang, P.; Visiers, I.; Weinstein, H.; Liu-Chen, L. Y. *Biochemistry* 2002, 41(40), 11972-11980.
- Li, J.; Huang, P.; Chen, C.; de Riel, J. K.; Weinstein, H.; Liu-Chen, L. Y. *Biochemistry* 2001, 40(40), 12039-12050.
- Cohen, G. B.; Yang, T.; Robinson, P. R.; Oprian, D. D. *Biochemistry* 1993, 32(23), 6111-6115.
- Palczewski, K.; Kumasaka, T.; Hori, T.; Behnke, C. A.; Motoshima, H.; Fox, B. A.; Le Trong, I.; Teller, D. C.; Okada, T.; Stenkamp, R. E.; Yamamoto, M.; Miyano, M. *Science* 2000, 289(5480), 739-745.
- Okada, T.; Fujiyoshi, Y.; Silow, M.; Navarro, J.; Landau, E. M.; Shichida, Y. *Proc Natl Acad Sci USA* 2002, 99(9), 5982-5987.
- Okada, T.; Sugihara, M.; Bondar, A. N.; Elstner, M.; Entel, P.; Buss, V. *J Mol Biol* 2004, 342(2), 571-583.
- Li, J.; Edwards, P. C.; Burghammer, M.; Villa, C.; Schertler, G. F. X. *J Mol Biol* 2004, 343(5), 1409-1438.
- Teller, D. C.; Okada, T.; Behnke, C. A.; Palczewski, K.; Stenkamp, R. E. *Biochemistry* 2001, 40(26), 7761-7772.
- Cherezov, V.; Rosenbaum, D. M.; Hanson, M. A.; Rasmussen, S. G.; Thian, F. S.; Kobilka, T. S.; Choi, H. J.; Kuhn, P.; Weis, W. I.; Kobilka, B. K.; Stevens, R. C. *Science* 2007.

13. Rosenbaum, D. M.; Cherezov, V.; Hanson, M. A.; Rasmussen, S. G.; Thian, F. S.; Kobilka, T. S.; Choi, H. J.; Yao, X. J.; Weis, W. I.; Stevens, R. C.; Kobilka, B. K. *Science* 2007.
14. Rasmussen, S. G.; Choi, H. J.; Rosenbaum, D. M.; Kobilka, T. S.; Thian, F. S.; Edwards, P. C.; Burghammer, M.; Ratnala, V. R.; Sanishvili, R.; Fischetti, R. F.; Schertler, G. F.; Weis, W. I.; Kobilka, B. K. *Nature* 2007.
15. Scheer, A.; Fanelli, F.; Costa, T.; De Benedetti, P. G.; Cotecchia, S. *Embo J* 1996, 15(14), 3566-3578.
16. Urizar, E.; Claeysen, S.; Deupi, X.; Govaerts, C.; Costagliola, S.; Vassart, G.; Pardo, L. *J Biol Chem* 2005, 280(17), 17135-17141.
17. Cordomi, A.; Edholm, O.; Perez, J. J. *J Comput Chem* 2007, 28(6), 1017-1030.
18. Huber, T.; Botelho, A. V.; Beyer, K.; Brown, M. F. *Biophys J* 2004, 86(4), 2078-2100.
19. Saam, J.; Tajkhorshid, E.; Hayashi, S.; Schulten, K. *Biophys J* 2002, 83(6), 3097-3112.
20. Crozier, P. S.; Stevens, M. J.; Forrest, L. R.; Woolf, T. B. *J Mol Biol* 2003, 333(3), 493-514.
21. Pitman, M. C.; Grossfield, A.; Suits, F.; Feller, S. E. *J Am Chem Soc* 2005, 127(13), 4576-4577.
22. Grossfield, A.; Feller, S. E.; Pitman, M. C. *Proc Natl Acad Sci USA* 2006, 103(13), 4888-4893.
23. Schlegel, B.; Sippl, W.; Holtje, H. D. *J Mol Model (Online)* 2005, 12(1), 49-64.
24. Cordomi, A.; Perez, J. J. *J Phys Chem B* 2007, 111(25), 7052-7063.
25. Berman, H. M.; Westbrook, J.; Feng, Z.; Gilliland, G.; Bhat, T. N.; Weissig, H.; Shindyalov, I. N.; Bourne, P. E. *Nucleic Acids Res* 2000, 28(1), 235-242.
26. Fahmy, K.; Jager, F.; Beck, M.; Zvyaga, T. A.; Sakmar, T. P.; Siebert, F. *Proc Natl Acad Sci USA* 1993, 90(21), 10206-10210.
27. Lindahl, E.; Edholm, O. *Biophys J* 2000, 79(1), 426-433.
28. Nagle, J. F.; Tristram-Nagle, S. *Biochim Biophys Acta* 2000, 1469(3), 159-195.
29. Patra, M.; Karttunen, M.; Hyvönen, M. T.; Falck, E.; Lindqvist, P.; Vattulainen, I. *Biophys J* 2003, 84(6), 3636-3645.
30. Smondyrev, A. M.; Berkowitz, M. L. *J Comput Chem* 1999, 20(5), 531-545.
31. Tieleman, D. P.; Berendsen, H. J. C. *J Chem Phys* 1996, 105(11), 4871-4880.
32. Anézo, C.; de Vries, A. H.; Holtje, H. D.; Tieleman, D. P.; Marrink, S. J. *J Phys Chem B* 2003, 107(35), 9424-9433.
33. Berger, O.; Edholm, O.; Jähnig, F. *Biophys J* 1997, 72(5), 2002-2013.
34. Cordomi, A.; Perez, J. J. *J Phys Chem B* 2007, 111(25), 7052-7063.
35. Berendsen, H. J. C.; van der Spoel, D.; van Drunen, R. *Comput Phys Commun* 1995, 91(1-3), 43-56.
36. Lindahl, E.; Hess, B.; van der Spoel, D. *J Mol Model* 2001, 7(8), 306-317.
37. Berendsen, H. J. C.; Postma, J. P. M.; DiNola, A.; Haak, J. R. *J Chem Phys* 1984, 81, 3684.
38. Hess, B.; Bekker, H.; Berendsen, H. J. C.; Fraaije, J. G. E. M. *J Comput Chem* 1997, 18(12), 1463-1472.
39. Miyamoto, S.; Kollman, P. A. *J Comput Chem* 1992, 13(8), 952-962.
40. Wohler, J.; Edholm, O. *Biophys J* 2004, 87(4), 2433-2445.
41. Klauda, J. B.; Brooks, B. R.; Pastor, R. W. *J Chem Phys* 2006, 125(14), 144710.
42. Venable, R. M.; Brooks, B. R.; Pastor, R. W. *J Chem Phys* 2000, 112(10), 4822-4832.
43. Tobias, D. J. *Curr Opin Struct Biol* 2001, 11(2), 253-261.
44. Patra, M.; Karttunen, M.; Hyvönen, M. T.; Falck, E.; Vattulainen, I. *J Phys Chem B* 2004, 108(14), 4485-4494.
45. Cordomi, A.; Edholm, O.; Perez, J. J. *J Comput Chem* 2007, 28(6), 1017-1030.
46. Tieleman, D. P.; Hess, B.; Sansom, M. S. P. *Biophys J* 2002, 83(5), 2393-2407.
47. Jorgensen, W. L.; Maxwell, D. S.; TiradoRives, J. J. *Am Chem Soc* 1996, 118(45), 11225-11236.
48. Jorgensen, W. L.; Chandrasekhar, J.; Madura, J. D.; Impey, R. W.; Klein, M. L. *J Chem Phys* 1983, 79(2), 926-935.
49. Hayashi, S.; Tajkhorshid, E.; Schulten, K. *Biophys J* 2002, 83(3), 1281-1297.
50. Kong, Y. F.; Karplus, M. *Structure* 2007, 15(5), 611-623.
51. Faraldo-Gomez, J. D.; Forrest, L. R.; Baaden, M.; Bond, P. J.; Domene, C.; Patargias, G.; Cuthbertson, J.; Sansom, M. S. *Proteins* 2004, 57(4), 783-791.
52. Grossfield, A.; Feller, S. E.; Pitman, M. C. *Proteins* 2007, 67(1), 31-40.
53. Isin, B.; Rader, A. J.; Dhiman, H. K.; Klein-Seetharaman, J.; Bahar, I. *Proteins-Structure Function and Bioinformatics* 2006, 65(4), 970-983.
54. Govaerts, C.; Lefort, A.; Costagliola, S.; Wodak, S. J.; Ballesteros, J. A.; Van Sande, J.; Pardo, L.; Vassart, G. *J Biol Chem* 2001, 276(25), 22991-22999.
55. Flanagan, C. A. *Mol Pharmacol* 2005, 68(1), 1-3.
56. Vogel, R.; Sakmar, T. P.; Sheves, M.; Siebert, F. *Photochem Photobiol* 2007, 83(2), 286-292.

Table I – Secondary structure features of the cytoplasmic segments involved in the electrostatic network. Results corresponding to TM3, TM4, TM5 and TM6 and loops C2 and C3 are presented in a color code display. Backbone interactions $i,i+4$ (α -helix) in blue; $i,i+3$ (310-helix) in red and $i,i+5$ (π -helix) in magenta. Random coil structures are shown in cyan.

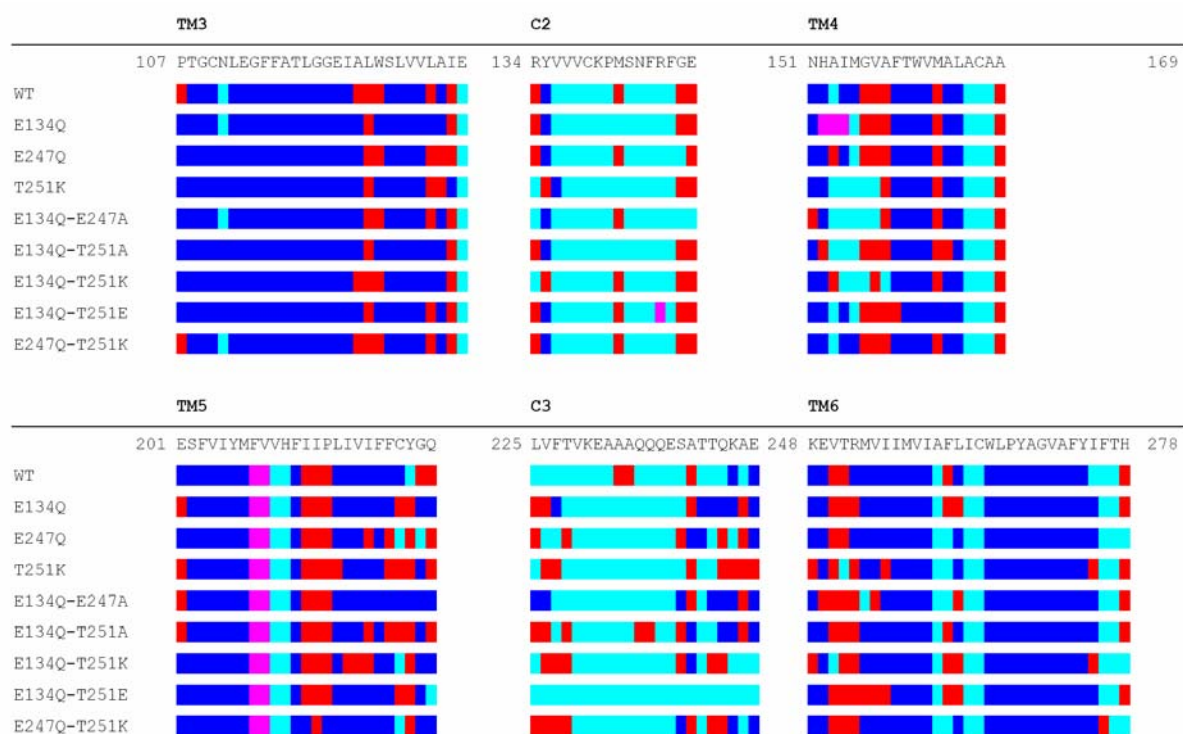


Table II – Average interaction energies (and standard deviations) in kJ/mol computed between A) pairs of critical residues involved in the electrostatic network and B) the whole cytoplasmic segments of TM3 and TM6. The last column in A shows the sum of pairs involving TM3-TM6 interactions, whereas the last three columns in B are the Gt activation in the dark, upon illumination, and the average distance between TM3 and TM6, respectively.

A

	134-135		134-247		134-251		135-247		135-251		247-251		TM3-TM6	
WT	-550	±70	210	±30	10	±0	-400	±30	-50	±10	-10	±10	-240	±70
E134Q	-220	±20	0	±10	0	±0	-410	±40	-50	±10	-10	±10	-460	±60
E247Q	-640	±30	20	±10	10	±0	-90	±20	-30	±20	-30	±10	-100	±50
T251K	-590	±20	170	±70	-120	±10	-290	±130	150	±20	-140	±20	-100	±230
E134Q-E247A	-230	±10	0	±0	0	±0	-20	±10	-40	±20	-20	±10	-60	±30
E134Q-T251A	-240	±10	10	±10	0	±0	-360	±90	-10	±10	-10	±10	-370	±110
E134Q-T251K	-270	±30	10	±0	-10	±0	-220	±90	140	±20	-270	±80	-80	±110
E134Q-T251E	-260	±40	0	±10	10	±10	-140	±30	-470	±40	170	±30	-600	±90
E247Q-T251K	-550	±70	10	±10	-180	±50	-20	±30	100	±20	-60	±30	-90	±110

B

	Coulomb		LJ		Total		Gt activation dark*		Gt activation light*		dist. (Å)
WT	-140	±10	-100	±5	-240	±15	0.99	±0.09	10.37		11.2
E134Q	-300	±15	-100	±5	-400	±20	1.32	±0.12	13.17	±1.08	11.5
E247Q	0	±20	-130	±10	-130	±30	1.5	±0.34	9.95	±0.96	10.7
T251K	-50	±40	-100	±10	-150	±50	1.09	±0.36	8.09	±0.36	12.9
E134Q-E247A	80	±15	-110	±5	-30	±20	2.04	±0.85	13.32	±2.95	11.8
E134Q-T251A	-230	±45	-110	±5	-350	±50	5.81	±1.45	14.03	±0.26	11.5
E134Q-T251K	-10	±35	-110	±5	-120	±40	0.91	±0.49	23.69	±0.98	11.6
E134Q-T251E	-480	±25	-80	±5	-560	±30	-	-	-	-	11.9
E247Q-T251K	-190	±90	-120	±10	-310	±100	-	-	-	-	11

* taken from ref (4).

Table III – Average tilt (A) and kink (B) angles (in degrees) computed from the last 1 ns of each trajectory. For each helix (TM1-TM7) the second column indicates the standard deviations. Average values for the last 5 ns of the WT simulation are shown as a reference.

A

Helix Tilts	TM1 34/61	TM2 72/101	TM3 107/134	TM4 151/169	TM5 201/214/225	TM6 248/278	TM7 288/310
WT (0-5ns)	22 ±2	21 ±1	25 ±1	11 ±2	23 ±2	14 ±1	17 ±2
WT (4-5ns)	22 ±1	21 ±1	24 ±1	9 ±2	21 ±1	14 ±1	18 ±1
E134Q	18 ±1	19 ±1	24 ±1	13 ±2	23 ±1	14 ±1	16 ±1
E247Q	19 ±1	19 ±1	24 ±1	11 ±2	20 ±1	13 ±1	15 ±1
T251K	21 ±1	21 ±1	25 ±1	10 ±1	23 ±1	16 ±1	15 ±1
E134Q/E247A	20 ±1	20 ±1	25 ±1	21 ±2	21 ±1	12 ±1	16 ±1
E134Q/T251A	20 ±1	21 ±0	25 ±1	14 ±2	23 ±1	14 ±1	15 ±1
E134Q/T251K	23 ±1	20 ±1	25 ±1	12 ±2	22 ±1	15 ±1	15 ±1
E134Q/T251E	22 ±1	21 ±1	24 ±1	9 ±1	23 ±1	15 ±1	17 ±1
E247Q/T251K	20 ±1	19 ±1	24 ±1	8 ±2	21 ±1	12 ±1	15 ±1

B

Helix Kinks	TM1 34/53/61	TM2 72/92/101	TM3 107/115/134	TM4 151/160/169	TM5 201/214/225	TM6 248/264/278	TM7 288/296/310
WT (0-5ns)	23 ±4	10 ±3	9 ±3	6 ±3	17 ±3	44 ±3	36 ±5
WT (4-5ns)	19 ±3	10 ±3	11 ±2	5 ±3	18 ±3	41 ±3	41 ±4
E134Q	18 ±2	12 ±2	14 ±2	17 ±3	15 ±3	40 ±2	32 ±3
E247Q	17 ±3	12 ±3	13 ±3	5 ±2	19 ±2	49 ±2	30 ±3
T251K	18 ±3	12 ±2	10 ±2	8 ±3	13 ±2	36 ±2	32 ±2
E134Q/E247A	14 ±2	13 ±2	10 ±2	14 ±5	20 ±3	51 ±2	37 ±3
E134Q/T251A	17 ±2	11 ±2	12 ±2	5 ±3	16 ±3	40 ±2	28 ±2
E134Q/T251K	19 ±3	14 ±2	12 ±2	6 ±3	14 ±3	44 ±3	29 ±3
E134Q/T251E	14 ±3	15 ±2	8 ±2	7 ±3	16 ±3	46 ±3	31 ±2
E247Q/T251K	21 ±3	11 ±2	13 ±3	8 ±4	17 ±3	55 ±3	33 ±2

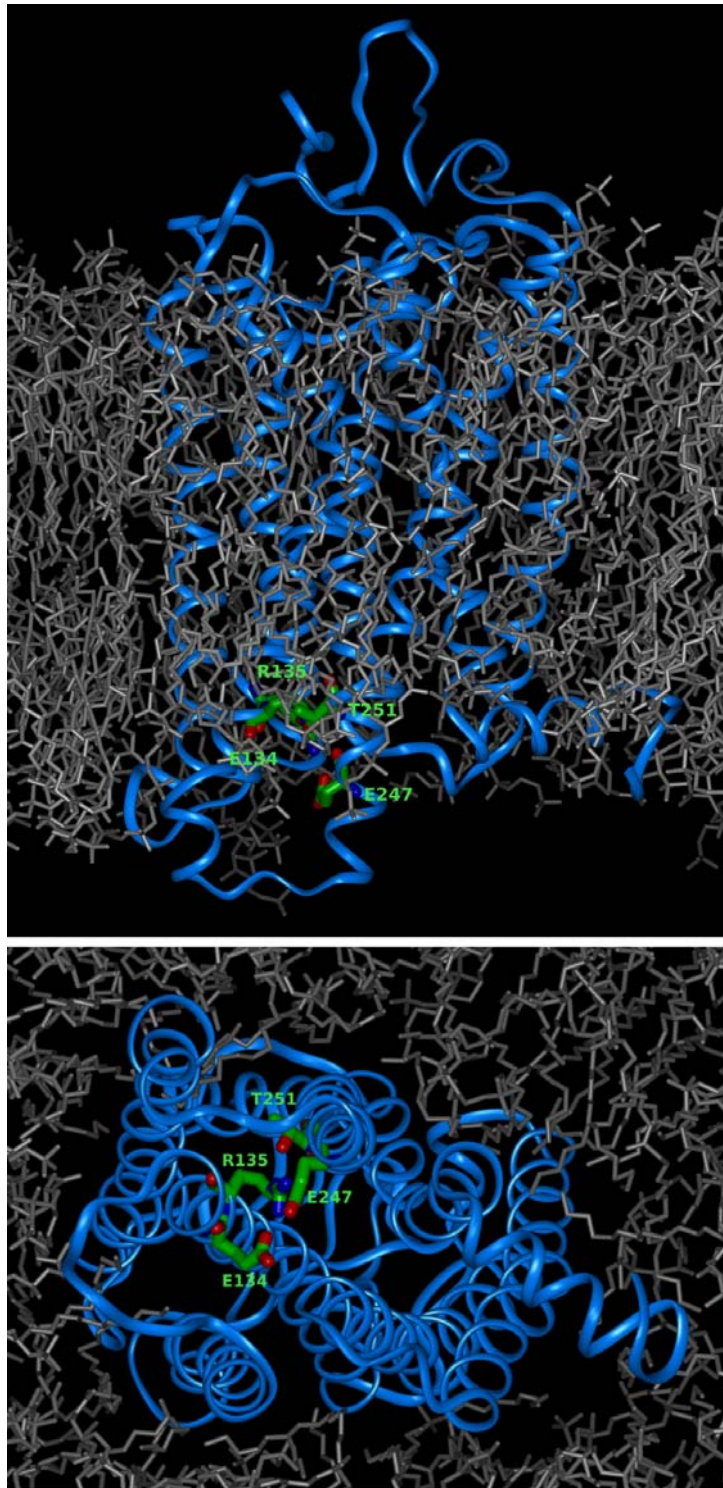


Fig. 1 – Lateral (top panel) and cytoplasmic (bottom panel) of WT bovine rhodopsin embedded in a DPPC bilayer. The protein is shown in a blue ribbon representation; amino acids E134, R135, E247 and T251 are colored by atom type and lipids are displayed in grey. Water molecules were omitted for clarity.

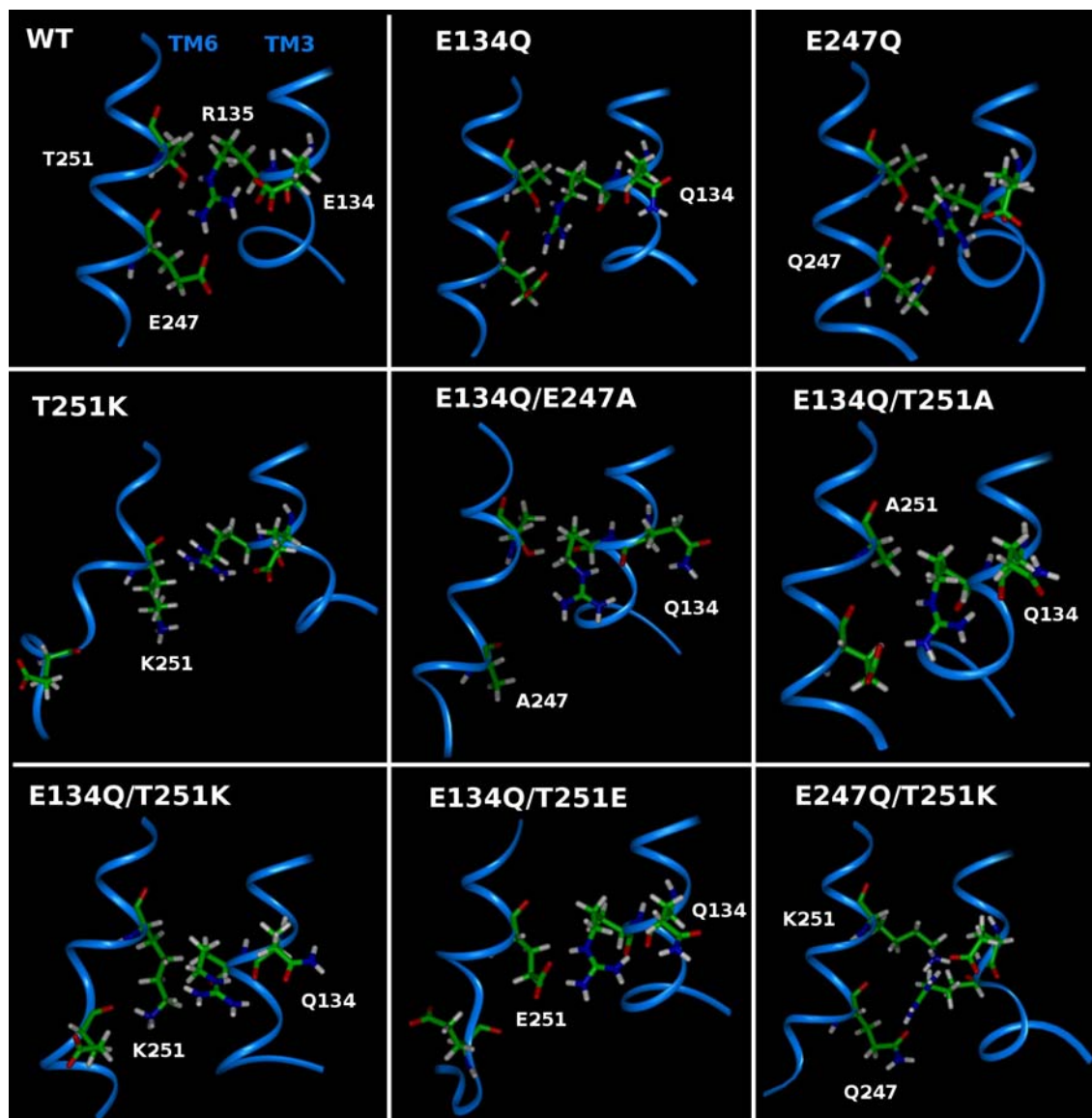


Fig. 2 – Representative interactions involving residues E/Q134(3.49), R135(3.50), E/Q/A247(6.30) and T/K/E251(6.34) at the cytoplasmic side of TM3 and TM6. The cytoplasmic segments of TM3 and TM6 are shown in a blue ribbon representation; amino acids E134, R135, E247 and T251 are colored by atom type.

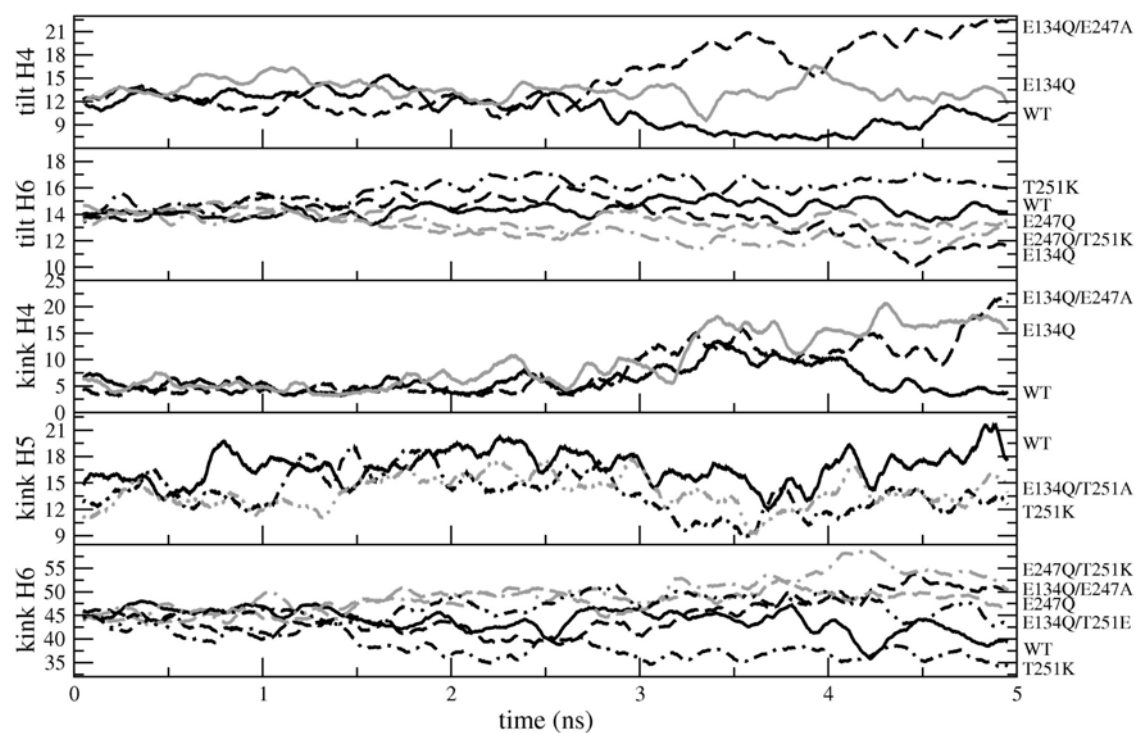


Fig. 3 – Time evolution of a selected group of the tilt and kink angles. Values for those mutants not shown in the Figure follow a profile which does not deviate much from that exhibited by the WT.

A methyl group at C7 of 11-cis-retinal allows chromophore formation but affects rhodopsin activation.

Bosch L, Cordero A, Dominguez M, Toledo D, Morillo M, Perez JJ, Alvarez R, de Lera AR, Garriga P

Vision Res., 2006 Dec;46(27):4472-81

A methyl group at C7 of 11-*cis*-retinal allows chromophore formation but affects rhodopsin activation

Laia Bosch^a, Arnau Cordoní^b, Marta Domínguez^c, Darwin Toledo^a, Margarita Morillo^a,
Juan J. Pérez^b, Rosana Alvarez^c, Angel R. de Lera^c, Pere Garriga^{a,*}

^a *Departament d'Enginyeria Química, Universitat Politècnica de Catalunya, 08222 Terrassa, Catalonia, Spain*

^b *Departament d'Enginyeria Química, Universitat Politècnica de Catalunya, 08028 Barcelona, Catalonia, Spain*

^c *Departamento de Química Orgánica, Facultad de Química, Universidade de Vigo, 36310 Vigo, Spain*

Received 14 June 2006; received in revised form 27 July 2006

Abstract

The newly synthesized 11-*cis*-7-methylretinal can form an artificial visual pigment with kinetic and spectroscopic properties similar to the native pigment in the dark-state. However, its photobleaching behavior is altered, showing a Meta I-like photoproduct. This behavior reflects a steric constraint imposed by the 7-methyl group that affects the conformational change in the binding pocket as a result of retinal photoisomerization. Transducin activation is reduced, when compared to the native pigment with 11-*cis*-retinal. Molecular dynamics simulations suggest coupling of the C7 methyl group and the β -ionone ring with Met207 in transmembrane helix 5 in agreement with recent experimental results.

© 2006 Elsevier Ltd. All rights reserved.

Keywords: Retinal analogues; Chromophore regeneration; Photobleaching; Rhodopsin photoactivation; Transducin activation

1. Introduction

The visual pigment rhodopsin (Rho), the prototypical G-protein-coupled receptor (GPCR) (Hargrave, 2001; Menon, Han, & Sakmar, 2001), is a 40 kDa protein consisting of 348 amino acids folded into seven transmembrane α -helices interconnected by hydrophilic extramembranous loops. Its chromophore, 11-*cis*-retinal (Fig. 1), is covalently bound as an inverse agonist at the ϵ -amino group of Lys296 (helix 7) via a protonated Schiff base, the counterion of which is Glu113 (helix 3).

Visual transduction, the process by which visual cells convert light into a neural signal transmitted to the brain along the optic nerve, is triggered by the absorption of a photon by the chromophore 11-*cis*-retinal. The photochemically induced isomerization to all-*trans*-retinal and subsequent

thermal relaxation of the pigment through a series of intermediates leads to the agonist-bound state termed metarhodopsin II (Meta II, $\lambda_{\max} = 380$ nm), with an unprotonated Schiff base. At this stage, the interaction of the extramembranous loops on the cytoplasmic side with transducin (G_T), a member of the G-protein superfamily, activates the enzymatic cascade leading to visual transduction. Hydrolysis of 10^5 molecules of cGMP to GMP, inactivation of Meta II by phosphorylation with rhodopsin kinase, closing of the cation-specific channels in the rod outer segment of visual cells and build up of electric potential, results in generation of the neural signal providing the sensation of vision (Stryer, 1991; Sakmar, Franke, & Khorana, 1989; Rando, 2001; McBee, Palczewski, Baehr, & Pepperberg, 2001).

The 11-*cis*-retinal chromophore is exquisitely designed to occupy the binding site of rhodopsin acting as an inverse agonist, and thus to abrogate its activity. This is most likely due to its distorted conformation around the C6–C7 and C12–C13 bonds because of the steric interactions between C5–CH₃/H8 and C13–CH₃/H10. Being adapted to the

* Corresponding author. Fax: +34 937398225.

E-mail address: pere.garriga@upc.edu (P. Garriga).

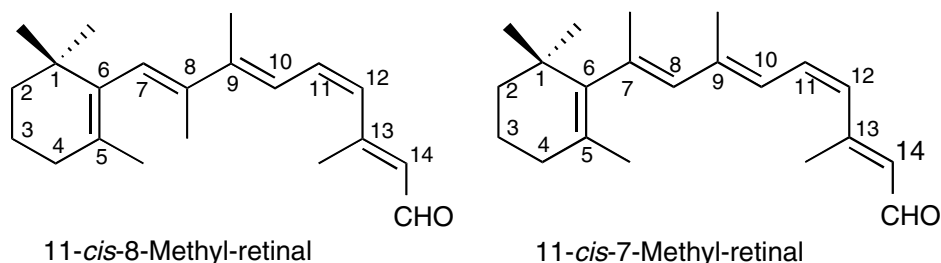


Fig. 1. 11-*cis*-8-Methylretinal and 11-*cis*-7-methylretinal chemical structures. The 8-methyl derivative was previously studied (Alvarez et al., 2003). The 7-methyl analogue of 11-*cis*-retinal used in the present study has been newly synthesized.

chiral binding pocket, these distortions in polyenes define an absolute sense of twist that affects the absorption maxima of the visual pigments and the movements of the chromophore after the initial photoisomerization.

There is an ongoing debate regarding the movements of the chromophore following the 11-*cis* to *trans* photoisomerization in Rho, in particular whether a ring flip of the C6–C7-*s-cis* to the C6–C7-*s-trans* conformation occurs and its effect in the activation step of the visual process (Albeck et al., 1989; Jang et al., 2001). Photocross-linking experiments by Nakanishi using (11*Z*)-3-diazo-4-oxo[15-³H]retinal suggested a flip-over of the ionone ring in the Batho to Lumi transition (Fishkin, Berova, & Nakanishi, 2004), which appears to be consistent with computations (Ishiguro, 2000). However, solid-state ¹³C NMR observations are compatible with intermediates retaining the chromophore in its original location in Rho up to the active Meta II state (Spooner et al., 2002; Spooner et al., 2003; Spooner et al., 2004).

The C6–C7 bond of retinal in native Rho was recently established to be in the *s*-conformation through binding studies of two enantiomeric 6-*s-cis*-locked analogues (*R*)-**3** and (*S*)-**3** (Fujimoto et al., 2001; Fujimoto et al., 2002). On the other hand, the 2.8 Å resolution X-ray structure (Teller, Okada, Behnke, Palczewski, & Stenkamp, 2001) indicates that the C12–C13-*s*-bond helicity is most likely positive (Chan, Nakanishi, Ebrey, & Honig, 1974; Rando, 1996), in keeping with recent theoretical analysis (Buss, Kolster, Terstegen, & Vahrenhorst, 1998; Buss, 2001), thus correcting earlier estimations of negative helicity (Kakitani, Kakitani, & Yomosa, 1977; Han & Smith, 1995; Lou, Hashimoto, Berova, & Nakanishi, 1997; Lou et al., 1999).

Artificial visual pigments, generated by treatment of the apoprotein opsin with synthetic analogues of retinal (Nakanishi & Crouch, 1995), in particular when combined with mutations of opsin, have been invaluable in the study of the role that conformational changes of the chromophore play in the visual cycle. We have recently reported the consequences of sterically perturbing the C6–C7-conformational equilibrium by incorporating methyl groups at the C8 position (Alvarez, Domínguez, Pazos, Sussman, & de Lera, 2003) (Fig. 1), with the finding that the perturbation extends to the C9–C10 bond, thus impairing reconstitution. It was considered that the methyl group at the C7 position could hinder the C6–C7 free rotation due to steric interactions with C1-2CH₃, thus becoming the non-locked

analogue of bicyclic systems, and allowing the examination of a region of the chromophore which has been shown previously to be important for the stability of early rhodopsin photointermediates (Randall et al., 1991; Lewis, Pinkas, Sheves, Ottolenghi, & Kligler, 1995).

We have now synthesized 11-*cis*-7-methylretinal (Fig. 1) and studied chromophore regeneration in binding experiments with native and mutated opsins. We find that opsin can be regenerated with the 7-methyl-Rho to a similar extent as with native 11-*cis*-retinal (Rho) and forms a chromophore that is blue-shifted to 490 nm. The spectroscopic properties of the dark-state of 7-methyl-Rho are similar to those of Rho except for a slightly lower thermal stability of the protein. In contrast, the photobleaching behaviour is clearly altered indicating an effect of the methyl group at C7 in the photoactivation pathway of rhodopsin. Molecular modelling studies suggest that this methyl group is in the vicinity of Met207 in transmembrane helix 5 of rhodopsin. Accordingly, this part of the retinal molecule, particularly the β-ionone ring, would come in close contact with Met207 after illumination in agreement with recent theoretical (Saam, Tajkhorshid, Hayashi, & Schulten, 2002) and experimental NMR studies (Crocker et al., 2006).

Our results, taken together with previous studies on other retinal analogues, reinforce the current model of rhodopsin function, where photoactivation is very effectively controlled by the tight molecular coupling between opsin and 11-*cis*-retinal. 11-*cis*-Retinal is a unique molecule with a chemical design that allows optimal interaction with the opsin apoprotein in its binding pocket, and this is essential for the formation of the light-activated conformation of the receptor.

2. Materials and methods

2.1. Stereoselective synthesis of 11-*cis*-7-methylretinal

The synthetic scheme we developed, for the synthesis of retinoids, is based on the direct attachment of the side-chain precursor to the hydrophobic ring using the Suzuki cross-coupling reaction of functionalized fragments (Dominguez, 2005), and will be described in detail elsewhere.

2.2. Protein expression, regeneration, and characterization

2.2.1. Purification of rhodopsin from ROS

ROS membranes, prepared by an ultracentrifugation method and using previously described conditions (del Valle, Ramon, Cañavate, Dias, & Garriga, 2003) were solubilized in buffer B (1.8 mM KH₂PO₄,

10 mM NaHPO₄, 137 mM NaCl, 2.7 mM KCl, pH 7.2, +1% DM) and passed through a Sepharose column that has the monoclonal Rho 1D4 antibody covalently attached. Rhodopsin bound to the antibody column is washed with buffer A (1.8 mM KH₂PO₄, 10 mM NaHPO₄, 137 mM NaCl, 2.7 mM KCl, pH 7.2) and eluted in buffer C (2 mM Na₂HPO₄, pH 6, +0.05% DM) containing 100 μM of a 9-mer corresponding to the last nine amino acids of the C-terminal tail of rhodopsin (TETSQVAPA).

2.2.2. Expression and purification of recombinant wild-type (wt) and mutant rhodopsin

Wt and mutant opsin genes were expressed in transiently transfected monkey kidney cells (COS-1) as described (Oprian, Molday, Kaufman, & Khorana, 1989). After the addition of 20 μM 11-*cis*-retinal or 11-*cis*-7-methylretinal in the dark, the transfected COS-1 cells were solubilized in 1% DM, and the proteins were purified by immunoaffinity chromatography using the Rho-1D4 monoclonal antibody (Oprian et al., 1989).

2.2.3. UV-vis absorption spectra of wt and mutant rhodopsin

UV-visible absorption spectra were performed with a Cary 100Bio Varian spectrophotometer equipped with water-jacketed cuvette holders connected to a circulating water bath with a Peltier accessory at 20 °C. All spectra were recorded with a bandwidth of 2 nm, a response time of 1 s, and a scan speed of 240 nm/min. Baseline correction was performed with buffer C (Na₂HPO₄ 2 mM, pH 6, +0.05% DM) in 150 μL quartz cuvettes and all experiments were carried out in a dark room under complete darkness or under dim red light using Kodak No2 filters (12.7–17.8 cm). For photobleaching experiments samples were illuminated with a Dollan-Jenner 150-W fiber optic light (Fiber-lite MI-150) equipped with a >495-nm long-pass filter for 10 s, and the corresponding spectra were recorded immediately after illumination. The hydroxylamine reactivity of wt and mutant rhodopsins in the dark was followed as a decay of the absorption visible band in the dark in the presence of 30 mM hydroxylamine. Thermal bleaching of rhodopsin was determined by following the decay of the visible chromophoric band in the dark at 55 °C as a function of time. In the case of pigment regeneration experiments, a rhodopsin/retinal 1:2 molar ratio was used. Retinal was added to purified rhodopsin and spectra were recorded after illumination for 10 s in a time course experiment. Regeneration experiments were followed by recording spectra every 5 min in the cycle mode of the spectrophotometer. In the acidification experiments, samples were acidified by addition of 1% concentrated H₂SO₄ solution (1.5 μL to a total of 150 μL) and spectra were recorded 30 s after acidification.

2.2.4. G_t activation assay

G_t was prepared from bovine rod outer segments as described (Ting, Goldin, & Ho, 1994). G_t activation was measured by means of fluorescence spectroscopy. The fluorescence technique has been previously applied to the study of rhodopsin mutants (Fahmy & Sakmar, 1993; Jager et al., 1994; Farrens, Altenbach, Yang, Hubbell, & Khorana, 1996). Fluorescence measurements were carried out with an Aminco SL spectrofluorometer with excitation and emission wavelengths of 295 nm (2-nm slit width) and 340 nm (16-nm slit width), respectively. Briefly, rhodopsin (40 nM) was added to a continuously stirred solution of G_t (250 nM) and GTPγS (5 μM) in 10 mM Tris-HCl, pH 7.4, 100 mM NaCl, 2 mM MgCl₂, and 0.012% DM. The reaction was initiated by illuminating the sample for 30 s with a 150 W-fibre optic light source through a 495-nm cut-off filter. The assay was carried out at a temperature of 20 °C. The relative initial rates of G_t activation were obtained from the slope of the fluorescence increase in the first 60 s after illumination and normalised to the value obtained for wt rhodopsin (Rho) taken as 1.00.

2.3. Molecular modelling

2.3.1. Rhodopsin structure and embedding into virtual lipid model

The rhodopsin model was built based on recent crystal structures (Li, Edwards, Burghammer, Villa, & Schertler, 2004; Okada et al., 2002). All amino acids were considered in the protonated state as they exhibit as free amino acids in water at pH 7, with the exception of Asp83 and Glu122, which were treated as protonated and neutral in accordance

with experimental evidence (Fahmy et al., 1993). Protein embedding in the bilayer was performed by placing the protein in a box containing a mixture of DPPC lipids, water molecules and ions generated and equilibrated according to a procedure described previously (Lindahl & Edholm, 2000). After the protein was placed in the center of the box, all ions and water molecules with the oxygen atoms closer than 0.40 nm to any non-hydrogen atom of the protein and all lipid molecules with at least one atom closer than 0.25 nm were removed. The resulting final system contained 195 lipids, 15,782 water molecules, 56 sodium, and 56 chloride ions.

2.3.2. Molecular dynamics (MD) simulations

All computer simulations were performed using the GROMACS 3.2 package (Berendsen, Vanderspoel, & Vandrunen, 1995; Lindahl, Hess, & van der Spoel, 2001). The system was subjected to periodic boundary conditions in the three coordinate directions. The temperature was kept constant at 323 K and the pressure was kept at 0.1 MPa in the three coordinate directions by independent barostats. All bonds of the protein and lipid molecules were kept frozen using the LINCS algorithm (Miyamoto & Kollman, 1992). The bonds and the angle of the water molecules were fixed using the analytical SETTLE method. The equations of motion were integrated using the leapfrog algorithm with a time step of 2 fs. Lennard-Jones interactions were computed with a cutoff of 1.0 nm and the electrostatic interactions were treated with the Particle Mesh Ewald (PME) technique (Darden, York, & Pedersen, 1993). The all-atom OPLS force field (Jorgensen, Maxwell, & TiradoRives, 1996) currently implemented in GROMACS was used for all molecules of the system, except for the DPPC molecules that were modeled using the force field parameters described previously (Berger, Edholm, & Jahnig, 1997). The procedure used for running the MD simulations is described below. Once rhodopsin was inserted in the bilayer, the system was energy minimized. Subsequently, the system was subjected to a 0.5 ns MD simulation to allow for the removal of voids present between the protein and the lipids or water, being the atomic coordinates of the protein restrained to their crystallographic positions. After that, a 10 ns simulation of rhodopsin with 11-*cis*-retinal in the dark-state was performed. Starting from the snapshot obtained after running 4 ns of the preceding simulation, the structure of 11-*cis*-retinal was modified to that of 11-*cis*-7-methylretinal and a subsequent 10 ns simulation was performed with the methylated derivative. Additionally, two more simulations were performed changing the torsion potential around the C11–C12 bond abruptly in both systems containing either 11-*cis*-retinal or 11-*cis*-7-methylretinal in order to force the isomerization from the 11-*cis* to all-*trans* configuration of the chromophore. These simulations were performed starting from the structures obtained after running 1 ns of the corresponding simulations with the 11-*cis* isomers. For all the simulations, coordinates were collected every 10 ps and stored for further analysis.

3. Results and discussion

3.1. ROS rhodopsin regeneration with 11-*cis*-7-methylretinal

Rhodopsin, purified from bovine rod outer segments (ROS) by immunoaffinity chromatography, was regenerated with 11-*cis*-7-methylretinal (7-methyl-Rho) (Fig. 2). The 11-*cis*-retinal analogue was added to the purified rhodopsin in dodecyl maltoside (DM) detergent solution and the sample was subsequently illuminated. Spectra of the regeneration process were recorded in a time course experiment (Fig. 2, inset). The initial spectrum in the dark shows the typical absorbance bands at 280 and 500 nm corresponding to native rhodopsin (with 11-*cis*-retinal, Rho) and a band at 376 nm corresponding to the free 11-*cis*-7-methylretinal added to the sample. After 10 s illumination with light of $\lambda > 495$ nm, rhodopsin was bleached and the chromophore band at 500 nm was converted to a species

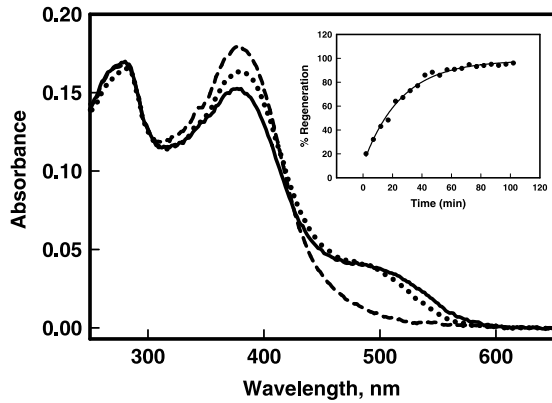


Fig. 2. Chromophore regeneration of purified rhodopsin from native ROS in DM detergent solution (buffer C). UV–vis absorption spectrum of dark ground-state rhodopsin regenerated with 11-*cis*-7-methylretinal plus free added 11-*cis*-7-methylretinal (—). Absorption spectrum of the rhodopsin sample after illumination for 10 s with light of $\lambda > 495$ nm (---). Absorption spectrum of the sample 2 h after illumination showing the regenerated visible chromophoric band (···). Temperature, 20 °C. (Inset) time course of the regeneration process of purified ROS rhodopsin with 11-*cis*-7-methylretinal.

absorbing at 380-nm. The spectrum recorded 2 h after illumination—the last one recorded after illumination—shows clear regeneration of the chromophoric band in the visible region in the vicinity of 500 nm. A small but definite blue-shift of the visible band to 490 nm can be detected.

3.2. Expression and characterization of 7-methyl-Rho

WT protein expressed in transiently transfected COS-1 cells and purified by immunoaffinity chromatography was regenerated with 11-*cis*-retinal (Rho) and 11-*cis*-7-meth-

ylretinal (7-methyl-Rho). The UV–vis absorption spectra in the dark, after illumination and acidification for these proteins are shown in Fig. 3. The 7-methyl-Rho formed normal chromophore and UV–visible absorption spectra in the dark with a λ_{\max} at 490 nm and a A_{280}/A_{490} 1.8, the same as the A_{280}/A_{500} of Rho indicating that the binding pocket is formed and able to accommodate the retinal analogue. This result is in agreement with what was observed in the case of the ROS rhodopsin regenerated sample (Fig. 2). The regeneration experiments indicate that, after incubation of opsin with 11-*cis*-7-methylretinal ($\lambda_{\max} = 368$ nm in MeOH), regeneration is observed with both native ROS and with purified recombinant wt rhodopsin, and the chromophoric yield is similar to that of 11-*cis*-retinal.

After 10 s illumination of 7-methyl-Rho, with light of $\lambda > 495$ nm, the visible band at 490 nm was not fully converted to Meta II species with maximum at 380 nm, but rather two bands of similar intensity are detected at 373 and 467 nm, respectively (Fig. 3B), indicating that the methyl group introduced at C7 in retinal causes a stability change in photointermediates. Acidification of the sample after illumination resulted in formation of a band with λ_{\max} at 427 nm with concomitant decrease in the bands at 373 and 467 nm. This indicates that the two bands, at 373 and 467 nm, correspond to species that are covalently linked to opsin through an unprotonated and protonated Schiff base linkage, respectively. An altered photobleaching behavior has been previously observed for rhodopsin mutants in the transmembrane domain and mutations associated with the degenerative disease of the eye retinitis pigmentosa, like G51V and G89D (Hwa, Garriga, Liu, & Khorana, 1997; Bosch, Ramon, del Valle, & Garriga, 2003). A similar alteration in the native photointermediate pathway formation

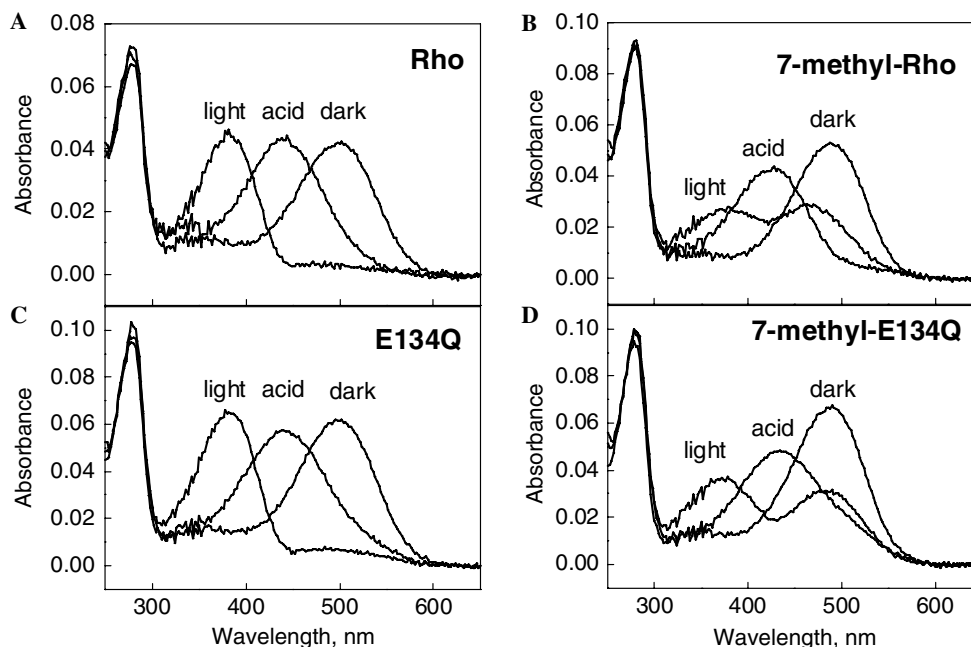


Fig. 3. UV–visible absorption spectra in the dark in buffer C (dark), after illumination for 10 s with light of $\lambda > 495$ nm, and acid denaturation (acid). (A) Rho; (B) 7-methyl-Rho; (C) E134Q; and (D) 7-methyl-E134Q. The spectra were recorded at a temperature of 20 °C.

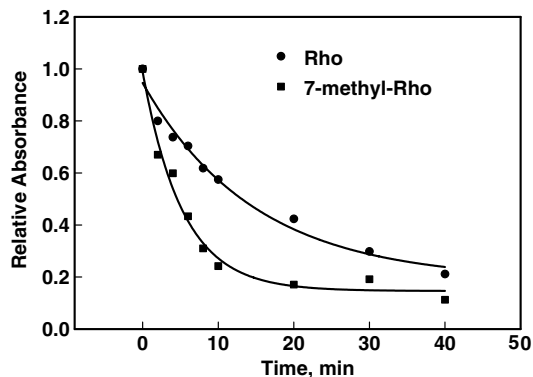


Fig. 4. Dark-state stability at 55°C of Rho (●) and 7-methyl-Rho (■) determined by measuring the decay of the absorbance band at 500 and 490 nm, respectively.

has been also recently reported for rhodopsin regenerated with other retinal analogues, like an acyclic retinal (Bartl et al., 2005) or polyene methylated retinals (Vogel et al., 2006).

Rho did not show hydroxylamine reactivity in the dark, indicating that hydroxylamine could not access the Schiff base linkage, and this reflects that the protein has a compact structure in the dark. A similar result was obtained for 7-methyl-Rho suggesting that 7-methyl-Rho has a compact structure around the Schiff base linkage like Rho. Thermal stability at 55°C of 7-methyl-Rho in the dark was reduced ($t_{1/2} = 4.6$ min, Rho $t_{1/2} = 13.1$ min), indicating that the dark-state was less stable when the protein is regenerated with the methylated analogue (Fig. 4). Spectra of the regeneration process were recorded in a time course experiment for Rho and 7-methyl-Rho and the total regeneration and regeneration kinetics of both proteins were similar (data not shown).

Further illumination of 7-methyl-Rho for 1 or 5 min only caused a small decrease in the 467 nm band with a concomitant slight increase in the 373 nm band (Fig. 5A). The altered photointermediate with λ_{\max} at 467 nm decayed with time to a species with λ_{\max} at 485 nm (Fig. 5B). The figure shows representative spectra at different times after illumination and the difference spectrum between those at

60 and 0 min (Fig. 5B, inset). It is interesting to note that two different Meta I photointermediates, Meta Ia and Meta Ib have been recently proposed to absorb at 485 and 465 nm, respectively (Shichida & Morizumi, 2006), very close to the absorbances observed in our experiments (Fig. 5B). In our case, the altered photointermediate pathway is a consequence of a methyl group introduced at the C7 position of 11-*cis*-retinal, causing a stability change in activation photointermediates.

We have also analyzed the E134Q mutant—Glu134 belongs to the D(E)RY triplet which is highly conserved through the GPCR superfamily—which mimics the protonated state in photo-activated rhodopsin and which facilitates the Meta II conformation (Vogel et al., 2006; Bartl et al., 2005; Fahmy, Sakmar, & Siebert, 2000). The UV-vis spectrum after illumination of E134Q mutant regenerated with 11-*cis*-7-methylretinal (7-methyl-E134Q) (490 nm band in the dark) showed two bands, one at 373 nm and the other at 485 nm. In this case, the E134Q mutation, in contrast to the results reported with other retinal structures (Bartl et al., 2005), could not facilitate light-induced Meta II formation (no shift of the protonated species at 485–380 nm was detected) (Fig. 3C and D). A summary of the data for the dark, light, and acidified spectra of WT Rho and the mutant E134Q is depicted in Table 1.

In order to elucidate if the different species formed in the light activation process are in equilibrium, 100 μ M of the high affinity peptide Gt α -HAA (VLEDLKSCGLF) was

Table 1
 λ_{\max} of the absorption bands in the UV-vis absorption spectra of rhodopsin proteins in the dark, and after illumination and acidification

Recombinant protein	λ_{\max} (dark) (nm)	λ_{\max} (light) (nm)	λ_{\max} (acid) (nm)	A_{280}/A_{500}^a
Rho	500	380	440	1.8
7-Methyl-Rho	490	373/467	427	1.8
E134Q	500	380	440	1.6
7-Methyl-E134Q	490	373/485	435	1.6

^a In the case of the 7-methyl-containing pigments, and because of the blue-shift observed for the visible band, the A_{280}/A_{490} ratio is used.

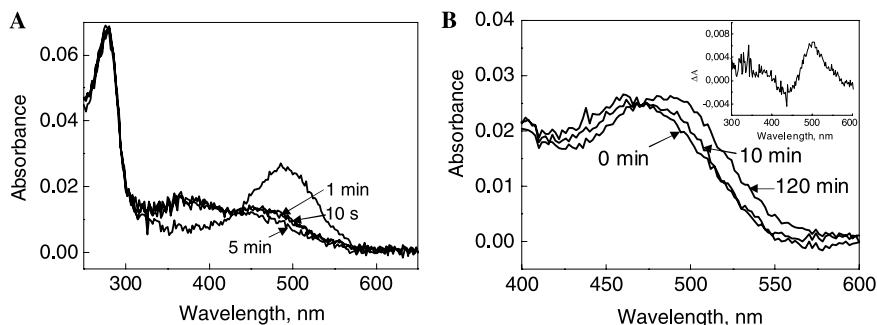


Fig. 5. Photobleaching and decay of the 467-nm species at a temperature of 20°C. (A) The photobleaching of 7-methyl-Rho was further explored by illuminating the sample for different time periods after the first initial 10 s illumination as indicated in the figure. (B). The band formed after 10 s illumination was allowed to decay in the dark at 20°C. The band decayed to form a new band at 485 nm as shown in the figure where representative spectral time points are depicted. The presence of an isosbestic point indicates a change between two distinct conformational states. The difference between the initial illuminated spectrum (after 10 s illumination) and that after 120 min shows a maximum at about 500 nm and a minimum at about 450 nm (inset).

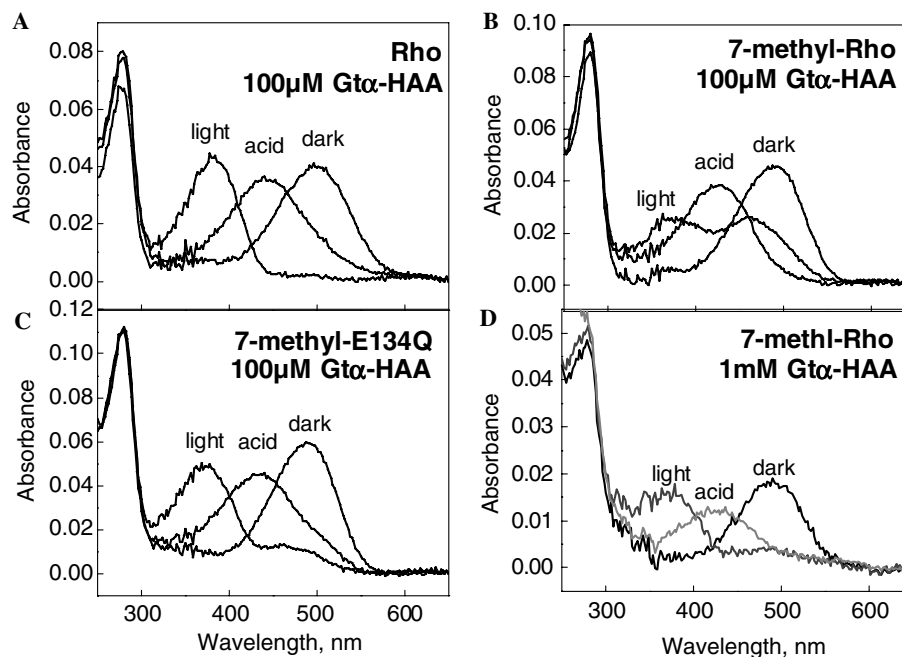


Fig. 6. UV-visible absorption spectra in the dark in buffer C (dark), after illumination for 10 s with light of $\lambda > 495$ nm, and acid denaturation (acid) of Rho, 7-methyl-Rho and 7-methyl-E134Q in the presence of different concentrations of the high affinity peptide Gt α -HAA (VLEDLKSCGLF), a peptide of the C-terminal domain of the α -subunit of G $_t$. (A) Rho with 100 μ M Gt α -HAA; (B) 7-methyl-Rho with 100 μ M Gt α -HAA; (C) 7-methyl-E134Q with 100 μ M Gt α -HAA; and (D) 7-methyl-Rho with 1 mM Gt α -HAA. The spectra were recorded at a temperature of 20 $^{\circ}$ C.

added before sample illumination (Bartl, Ritter, & Hofmann, 2000). No change in band formation or intensity could be appreciated after illumination of 7-methyl-Rho in the presence of the Gt α -HAA peptide (Fig. 6). Illumination of 7-methyl-E134Q in the presence of Gt α -HAA peptide shifted most of the 485 nm band to 373 nm. Higher concentration of peptide (1 mM Gt α -HAA) was required to shift most of the protonated band of 7-methyl-Rho to 373 nm (Fig. 6D). This suggests that the species formed after illumination of pigments regenerated with 11-*cis*-7-methylretinal are in equilibrium and that this equilibrium is shifted with the Gt α -HAA peptide to the 373-nm species.

3.3. G protein activation

The functionality of 7-methyl-Rho and E134Q-7-methyl-Rho was also determined by measuring the transducin activation by means of a fluorescence assay which monitors intrinsic tryptophan fluorescence changes in the G protein resulting from GTP γ S uptake. The initial rates of activation for 7-methyl-Rho and 7-methyl-E134Q are similar to those of the same proteins regenerated with the native 11-*cis*-retinal chromophore (Table 2). However, the total level of activation for the methylated proteins was reduced to about half of that of Rho. This result suggests that one of the two species formed (373nm or 467 nm band with similar intensities) is responsible for the total G $_t$ activation observed while the other species is not active. A first interpretation could be that the 373 nm corresponds to the active species and that the 467 nm band corresponds to an inactive Meta I-like species. However, it is tempting to speculate that the 373nm can

Table 2

G $_t$ activation measured, by a fluorescence assay as described in Section 2, of wt Rho and the E134Q mutant regenerated with 11-*cis*-retinal and with the 7-methyl analogue

Recombinant protein	Relative total G $_t$ activation ^a	Relative initial activation rate ^b
Rho	1.00	1.00
E134Q	0.95	0.95
7-Methyl-Rho	0.55	0.91
7-Methyl-E134Q	0.50	0.85

^a Relative total G $_t$ activation measured as the maximal fluorescence increase.

^b Initial activation rates derived from the first 60 s of the fluorescence curves.

be an inactive unprotonated Schiff base linked species—typically active Meta II conformation absorbs at 380 nm—while the 467 nm band could correspond to a protonated Schiff base linked species that may be active. There are previous reports of protonated Schiff base species capable of transducin activation, like G90D congenital night blindness mutant (Rao, Cohen, & Oprian, 1994; Fahmy, Zvyaga, Sakmar, & Siebert, 1996). Further experiments are required to clarify this point. It is also possible that the decreased ability to activate G $_t$ of the methylated protein is due to a faster rate of Meta II decay for the sample as has been experimentally observed (data not shown).

3.4. Molecular modelling

MD simulations were carried out to get further insight into the understanding of the experimental results

shape that characterizes the 11-*cis* configuration. This new “L”-type shape can no longer allow the β -ionone ring to be accommodated within the pocket formed by residues Trp265, Phe212, Leu125, and Glu122. In this way, the ring is forced to occupy other sub-pockets. Interestingly, the simulations performed with both Rho and 7-methyl-Rho in the all-*trans* configuration suggest a different localization of the β -ionone ring due to the conformational peculiarities of the methylated analogue. In Rho, the β -ionone ring interacts, after isomerization, with the hydrophobic residues Phe208, Phe212, Tyr191, and Met207, whereas in the 7-methyl-Rho the β -ionone ring interacts with Glu122, Cys167, His211, Thr118, Ile189, and Met207. Trp265 is in all cases moved apart from the β -ionone ring and becomes closer to the polyene chain. This is in accordance with a recent experimental study which proposed that the interaction of Trp265 with the retinal chromophore is responsible for stabilizing the inactive conformation in the dark, and that the motion of the β -ionone ring allows Trp265 and transmembrane helix H6 to adopt the active conformations upon illumination (Crocker et al., 2006). Moreover, it is important to highlight that the main difference between Rho and 7-methyl-Rho is that the β -ionone ring is located in opposite sides around Met207, suggesting the importance of the methylation at position C7 in the conformations achieved after the isomerization. Regarding the interactions of the methyl group at C7 in the methylated chromophore, in the dark-state the methyl group lies close to Glu122 and Met207, whereas after isomerization it becomes closer to Thr118 maintaining the interactions with Met207 (Fig. 7, bottom panels).

Significant changes regarding the orientations of the C19 and C20-methyl groups can be observed after retinal isomerization, not only because of the different configuration of the double bond itself, but also due to the different localization of the β -ionone ring that leads to a rearrangement of neighboring side-chains interacting with the polyene chain in both Rho and 7-methyl-Rho. Thus, the C20-methyl group interacts with Ala295 in the dark-state in all cases, and with Ala292 after isomerization. Positions of the C20-methyl group are similar in Rho and 7-methyl-Rho. That is not the case of the C19-methyl group which adopts a slightly different orientation, being closer to Thr118 in the case of Rho. The C19-methyl group, which is interacting with Ile189 and Thr118 in the dark in both Rho and 7-methyl-Rho is moved towards Tyr268 and Tyr191, occupying the space between them after isomerization. Another aromatic residue, Tyr268, exhibits a significant displacement due to the existence of both the C19 and C20-methyl groups pointing to the same side. This displacement is larger in the case of Rho because of the different location of the β -ionone ring.

3.5. Role of Met207 in the conformational change upon rhodopsin activation

The methyl group at C7 is positioned close to Met207 in transmembrane helix 5 of rhodopsin (Fig. 7). Interestingly,

Met207 has been proposed to come in close contact with the β -ionone of the retinal in the activated Meta II state both by molecular dynamics (Saam et al., 2002) and NMR studies (Crocker et al., 2006). In our case the observed altered photobleaching behaviour could be reflecting the steric constraint imposed by the added methyl group at C7. This methyl group is likely affecting the conformational change in the protein induced by the *cis*–*trans* isomerization of the retinal chromophore, and could be partially blocking the transition to the active Meta II conformation. This would result in a decreased G_t activation, as experimentally observed (see Table 2). Evidence of the important role of the β -ionone ring and its methyl groups in rhodopsin photoactivation, particularly in the Meta I–Meta II transition, has been obtained by using retinals with ring modifications in a recent FTIR study (Vogel, Siebert, Lüdeke, Hirshfeld, & Sheves, 2005).

Amino acid residues at the equivalent position of Met207 in rhodopsin, like Ser203 in the β -adrenergic receptor generally have strong propensities to mediate helix or ligand interactions (Liu, Eilers, Patel, & Smith, 2004; Patel et al., 2005). For instance, in the H2-histamine receptor, this position is occupied by an Asp that has been suggested to interact electrostatically with the positively charged histamine ligand (Birdsall, 1991). In addition, Met207 causes ADRP when mutated to Arg in the Met207Arg mutant (Farrar et al., 1992) and patients with this mutation show a severe clinical phenotype. It was recently found in a theoretical study that Met207Arg mutant has an altered pattern of light absorption based on quantum mechanical simulations (Padron-Garcia et al., 2004) but no molecular evaluation of the mutation has been reported so far.

We are currently constructing mutants at Met207 (the RP mutant Met207Arg and others) to further dissect the role of this residue in the coupling of opsin to the retinal and in the activation process. The specific study of Met207Arg mutation can provide new insights into the molecular defects associated with retinitis pigmentosa mutations in rhodopsin. Further work is also in progress to increase the size of the alkyl group at C7 that could hinder the rotation of the C6–C7 bond and thus affect the structural and functional behaviour of the native pigment. The combined study of Met207 mutants and other retinal analogues with bulkier substitutions at C7 should add relevant information to the unravelling of the detailed mechanism of the rhodopsin photoactivation process.

Acknowledgments

We thank Dr. O. Ernst and Prof. K.P. Hofmann for the gift of the Gt α -HAA peptide, and Prof. J. Manyosa for the spectrofluorometer facility. Supported by grants from Ministerio de Educación y Ciencia (SAF2004-07131 to A.R. de L.; FPU Fellowship to M.D.; SAF2005-08148-C02-04 to P.G., SAF2005-08148-C01-04 to J.J.P.), the European Community (QLK32002-02029; EPITRON Contract No.

518417), Xunta de Galicia (PGIDIT05PXIC31403PN), and for a UPC fellowship (from Universitat Politècnica de Catalunya) to L.B., A.C. and D.T.

References

- Albeck, A., Friedman, N., Ottolenghi, M., Sheves, M., Einterz, C. M., Hug, S. J., et al. (1989). Photolysis intermediates of the artificial visual pigment *cis*-5,6-dihydro-isorhodopsin. *Biophysical Journal*, *55*, 233–241.
- Alvarez, R., Domínguez, M., Pazos, Y., Sussman, F., & de Lera, A. R. (2003). (9Z)- and (11Z)-8-methylretinals for artificial visual pigment studies: stereoselective synthesis, structure, and binding models. *Chemistry-A European Journal*, *9*, 5821–5831.
- Bartl, F. J., Fritze, O., Ritter, E., Herrmann, R., Kuksa, V., Palczewski, K., et al. (2005). Partial agonism in a G protein-coupled receptor: role of the retinal ring structure in rhodopsin activation. *Journal of Biological Chemistry*, *280*, 34259–34267.
- Bartl, F. J., Ritter, E., & Hofmann, K. P. (2000). FTIR spectroscopy of complexes formed between metarhodopsin II and C-terminal peptides from the G-protein alpha- and gamma-subunits. *FEBS Letters*, *473*, 259–264.
- Berendsen, H. J. C., Vandespoel, D., & Vandrunen, R. (1995). Gromacs—a message—passing parallel molecular-dynamics implementation. *Computer Physics Communications*, *91*, 43–56.
- Berger, O., Edholm, O., & Jahnig, F. (1997). Molecular dynamics simulations of a fluid bilayer of dipalmitoylphosphatidylcholine at full hydration, constant pressure, and constant temperature. *Biophysical Journal*, *72*, 2002–2013.
- Birdsall, N. J. (1991). Cloning and structure–function of the H-2 histamine-receptor. *Trends in Pharmacological Sciences*, *12*, 9–10.
- Bosch, L., Ramon, E., del Valle, L. J., & Garriga, P. (2003). Structural and functional role of helices I and II in rhodopsin. A novel interplay evidenced by mutations at Gly-51 and Gly-89 in the transmembrane domain. *Journal of Biological Chemistry*, *278*, 20203–20209.
- Buss, V. (2001). Inherent chirality of the retinal chromophore in rhodopsin—a nonempirical theoretical analysis of chiroptical data. *Chirality*, *13*, 13–23.
- Buss, V., Kolster, K., Terstegen, F., & Vahrenhorst, R. (1998). Absolute sense of twist of the C12–C13 bond of the retinal chromophore in rhodopsin—semiempirical and nonempirical calculations of chiroptical data. *Angewandte Chemie International Edition in English*, *37*, 1893–1895.
- Chan, W. K., Nakanishi, K., Ebrey, T. G., & Honig, B. (1974). Properties of 14-methylretinal, 13-desmethyl-14-methylretinal, and visual pigments formed therefrom. *Journal of the American Chemical Society*, *96*, 3642–3644.
- Crocker, E., Eilers, M., Ahuja, S., Hornak, V., Hirshfeld, A., Sheves, M., et al. (2006). Location of Trp265 in metarhodopsin II: implications for the activation mechanism of the visual receptor rhodopsin. *Journal of Molecular Biology*, *357*, 163–172.
- Darden, T., York, D., & Pedersen, L. (1993). Particle mesh Ewald—an $N \log(N)$ method for Ewald sums in large systems. *Journal of Chemical Physics*, *98*, 10089–10092.
- del Valle, L., Ramon, E., Cañavate, E., Dias, P., & Garriga, P. (2003). Zinc-induced decrease of the thermal stability and regeneration of rhodopsin. *Journal of Biological Chemistry*, *278*, 4719–4724.
- Domínguez, M. (2005). PhD Thesis, University of Vigo.
- Fahmy, K., Jager, F., Beck, M., Zvyaga, T. A., Sakmar, T. P., & Siebert, F. (1993). Protonation states of membrane-embedded carboxylic-acid groups in rhodopsin and Metarhodopsin-II—a Fourier-transform infrared-spectroscopy study of site-directed mutants. *Proceedings of the National Academy of Sciences of the United States of America*, *90*, 10206–10210.
- Fahmy, K., & Sakmar, T. P. (1993). Regulation of the rhodopsin-transducin interaction by a highly conserved carboxylic acid group. *Biochemistry*, *32*, 7229–7236.
- Fahmy, K., Sakmar, T. P., & Siebert, F. (2000). Transducin-dependent protonation of glutamic acid 134 in rhodopsin. *Biochemistry*, *39*, 10607–10612.
- Fahmy, K., Zvyaga, T. A., Sakmar, T. P., & Siebert, F. (1996). Spectroscopic evidence for altered chromophore–protein interactions in low-temperature photoproducts of the visual pigment responsible for congenital night blindness. *Biochemistry*, *35*, 15065–15073.
- Farrar, G. J., Findlay, J. B., Kumar-Singh, R., Kenna, P., Humphries, M. M., Sharpe, E., et al. (1992). Autosomal dominant retinitis pigmentosa: a novel mutation in the rhodopsin gene in the original 3q linked family. *Human Molecular Genetics*, *1*, 769–771.
- Farrens, D. L., Altenbach, C., Yang, K., Hubbell, W. L., & Khorana, H. G. (1996). Requirement of rigid-body motion of transmembrane helices for light activation of rhodopsin. *Science*, *274*, 768–770.
- Fishkin, N., Berova, N., & Nakanishi, K. (2004). Primary events in dim light vision: a chemical and spectroscopic approach towards understanding protein/chromophore interactions in rhodopsin. *The Chemical Record*, *4*, 120–135.
- Fujimoto, Y., Fishkin, N., Pescitelli, G., Decatur, J., Berova, N., & Nakanishi, K. (2002). Solution and biologically relevant conformations of enantiomeric 11-*cis*-locked cyclopropyl retinals. *Journal of the American Chemical Society*, *124*, 7294–7302.
- Fujimoto, Y., Ishihara, J., Maki, S., Fujioka, N., Wang, T., Furuta, T., et al. (2001). On the bioactive conformation of the rhodopsin chromophore: absolute sense of Twist around the 6-*s-cis* bond. *Chemistry-A European Journal*, *7*, 4198–4204.
- Han, M., & Smith, S. O. (1995). NMR constraints on the location of the retinal chromophore in rhodopsin and bathorhodopsin. *Biochemistry*, *34*, 1425–1432.
- Hargrave, P. A. (2001). Rhodopsin structure, function, and topography. The Friedenwald lecture. *Investigative Ophthalmology and Visual Science*, *42*, 3–9.
- Hwa, J., Garriga, P., Liu, X., & Khorana, H. G. (1997). Structure and function in rhodopsin: packing of the helices in the transmembrane domain and folding to a tertiary structure in the intradiscal domain are coupled. *Proceedings of the National Academy of Science of the United States of America*, *94*, 10571–10576.
- Ishiguro, M. (2000). A mechanism of primary photoactivation reactions of rhodopsin: modeling of the intermediates in the rhodopsin photocycle. *Journal of the American Chemical Society*, *122*, 444–451.
- Jager, F., Jager, S., Krautle, O., Friedman, N., Scheves, M., Hofmann, K. P., et al. (1994). Interactions of the beta-ionone ring with the protein in the visual pigment rhodopsin control the activation mechanism. An FTIR and fluorescence study on artificial vertebrate rhodopsins. *Biochemistry*, *33*, 7889–7897.
- Jang, G. F., Kuksa, V., Filipek, S., Barti, E., Ritter, E., Gelb, M., et al. (2001). Mechanism of rhodopsin activation as examined with ring-constrained retinal analogues and the crystal structure of the ground state protein. *Journal of Biological Chemistry*, *276*, 26148–26153.
- Jorgensen, W. L., Maxwell, D. S., & TiradoRives, J. (1996). Development and testing of the OPLS all-atom force field on conformational energetics and properties of organic liquids. *Journal of the American Chemical Society*, *118*, 11225–11236.
- Kakitani, H., Kakitani, T., & Yomosa, S. (1977). Molecular mechanism for the initial process of visual excitation. II. Theoretical analysis of optical activity in rhodopsin and bathorhodopsin. *Journal of the Physical Society of Japan*, *42*, 996–1004.
- Lemaitre, V., Yeagle, P., & Watts, A. (2005). Molecular dynamics simulations of retinal in rhodopsin: from the dark-adapted state towards lumirhodopsin. *Biochemistry*, *44*, 12667–12680.
- Lewis, J. W., Pinkas, I., Sheves, M., Ottolenghi, M., & Kliger, D. S. (1995). Structural changes in early photolysis intermediates of rhodopsin from time-resolved spectral measurements of artificial pigments sterically hindered along the chromophore chain. *Journal of the American Chemical Society*, *117*, 918–923.
- Li, J., Edwards, P. C., Burghammer, M., Villa, C., & Schertler, G. F. X. (2004). Structure of bovine rhodopsin in a trigonal crystal form. *Journal of Molecular Biology*, *343*, 1409–1438.

- Lindahl, E., & Edholm, O. (2000). Mesoscopic undulations and thickness fluctuations in lipid bilayers from molecular dynamics simulations. *Biophysical Journal*, *79*, 426–433.
- Lindahl, E., Hess, B., & van der Spoel, D. (2001). GROMACS 3.0: a package for molecular simulation and trajectory analysis. *Journal of Molecular Modeling*, *7*, 306–317.
- Liu, W., Eilers, M., Patel, A. B., & Smith, S. O. (2004). Helix packing moments reveal diversity and conservation in membrane protein structure. *Journal of Molecular Biology*, *337*, 713–729.
- Lou, J., Hashimoto, M., Berova, N., & Nakanishi, K. (1999). Enantioselective binding of an 11-*cis*-locked cyclopropyl retinal. The conformation of retinal in bovine rhodopsin. *Organic Letters*, *1*, 51–54.
- McBee, J. K., Palczewski, K., Baehr, W., & Pepperberg, D. R. (2001). Confronting complexity: the interlink of phototransduction and retinoid metabolism in the vertebrate retina. *Progress in Retinal Eye Research*, *20*, 469–529.
- Menon, S. T., Han, M., & Sakmar, T. P. (2001). Rhodopsin: structural basis of molecular physiology. *Physiological Reviews*, *81*, 1659–1688.
- Miyamoto, S., & Kollman, P. A. (1992). Settle—an analytical version of the shake and rattle algorithm for rigid water models. *Journal of Computational Chemistry*, *13*, 952–962.
- Nakanishi, K., & Crouch, R. (1995). Application of artificial pigments to structure determination and study of photoinduced transformations of retinal proteins. *Israel Journal of Chemistry*, *35*, 253–272.
- Okada, T., Fujiyoshi, Y., Silow, M., Navarro, J., Landau, E. M., & Shichida, Y. (2002). Functional role of internal water molecules in rhodopsin revealed by X-ray crystallography. *Proceedings of the National Academy of Sciences of the United States of America*, *99*, 5982–5987.
- Okada, T., Sugihara, M., Bondar, A. N., Elstner, M., Entel, P., & Buss, V. (2004). The retinal conformation and its environment in rhodopsin in light of a new 2.2 angstrom crystal structure. *Journal of Molecular Biology*, *342*, 571–583.
- Oprian, D. D., Molday, R. S., Kaufman, R. J., & Khorana, H. G. (1989). Expression of a synthetic bovine rhodopsin gene in monkey kidney cells. *Proceedings of the National Academy of Sciences of the United States of America*, *84*, 8874–8878.
- Padron-Garcia, J. A., Crespo-Otero, R., Hernandez-Rodriguez, E. W., Garriga, P., Montero, L. A., & Garcia-Pineiro, J. C. (2004). Patterns of retinal light absorption related to retinitis pigmentosa mutants from in silico model structures of rhodopsin. *Proteins*, *57*, 392–399.
- Palczewski, K., Kumasaka, T., Hori, T., Behnke, C. A., Motoshima, H., Fox, B. A., et al. (2000). Crystal structure of rhodopsin: A G protein-coupled receptor. *Science*, *289*, 739–745.
- Patel, A. B., Crocker, E., Eilers, M., Hirshfeld, A., Sheves, M., & Smith, S. O. (2004). Coupling of retinal isomerization to the activation of rhodopsin. *Proceedings of the National Academy of Sciences of the United States of America*, *101*, 10048–10053.
- Patel, A. B., Crocker, E., Reeves, P. J., Getmanova, E. V., Eilers, M., Khorana, H. G., et al. (2005). Changes in interhelical hydrogen bonding upon rhodopsin activation. *Journal of Molecular Biology*, *347*, 803–812.
- Randall, C. E., Lewis, J. W., Hug, S. J., Björling, S. C., Eisner-Shanas, I., Ottolenghi, M., et al. (1991). A new photolysis intermediate in artificial and native visual pigments. *Journal of the American Chemical Society*, *113*, 3473–3485.
- Rando, R. (1996). Polyenes and vision. *Chemistry and Biology*, *3*, 255–262.
- Rando, R. R. (2001). The biochemistry of the visual cycle. *Chemical Reviews*, *101*, 1881–1896.
- Rao, V. R., Cohen, G. B., & Oprian, D. D. (1994). Rhodopsin mutation G90D and a molecular mechanism for congenital night blindness. *Nature*, *367*, 639–642.
- Rohrig, U. F., Guidoni, L., & Rothlisberger, U. (2002). Early steps of the intramolecular signal transduction in rhodopsin explored by molecular dynamics simulations. *Biochemistry*, *41*, 10799–10809.
- Saam, J., Tajkhorshid, E., Hayashi, S., & Schulten, K. (2002). Molecular dynamics investigation of primary photoinduced events in the activation of rhodopsin. *Biophysical Journal*, *83*, 3097–3112.
- Sakmar, T. P., Franke, R. R., & Khorana, H. G. (1989). Glutamic acid-113 serves as the retinylidene Schiff base counterion in bovine rhodopsin. *Proceedings of the National Academy of Sciences of the United States of America*, *86*, 8309–8313.
- Shichida, Y., & Morizumi, T. (2006). Mechanism of G-protein activation by rhodopsin. *Photochemistry and Photobiology* [Epub ahead of print].
- Spooner, P. J. R., Sharples, J. M., Goodall, S. C., Bovee-Geurts, P. H. M., Verhoeven, M. A., Lugtenburg, J., et al. (2004). The ring of the rhodopsin chromophore in a hydrophobic activation switch within the binding pocket. *Journal of Molecular Biology*, *343*, 719–730.
- Spooner, P. J. R., Sharples, J. M., Goodall, S. C., Seedorf, H., Verhoeven, M. A., Lugtenburg, J., et al. (2003). Conformational Similarities in the β -ionone ring region of the rhodopsin chromophore in its ground state and after photoactivation to the metarhodopsin-I intermediate. *Biochemistry*, *42*, 13371–13378.
- Spooner, P. J. R., Sharples, J. M., Verhoeven, M. A., Lugtenburg, J., Glau-bitz, C., & Watts, A. (2002). Relative Orientation between the β -ionone ring and the polyene chain for the chromophore of rhodopsin in native membranes. *Biochemistry*, *41*, 7549–7555.
- Stryer, L. (1991). Visual excitation and recovery. *Journal of Biological Chemistry*, *266*, 10711–10714.
- Tan, Q., Lou, J., Borhan, B., Karnaukhova, E., Berova, N., & Nakanishi, K. (1997). Absolute sense of twist of the C12–C13 bond of the retinal chromophore in bovine rhodopsin based on exciton-coupled CD spectra of 11,12-dihydroretinal analogues. *Angewandte Chemie International Edition in English*, *36*, 2089–2093.
- Teller, D. C., Okada, T., Behnke, C. A., Palczewski, K., & Stenkamp, R. (2001). Advances in determination of a high-resolution three-dimensional structure of rhodopsin, a model of G-protein-coupled receptors (GPCRs). *Biochemistry*, *40*, 7761–7772.
- Ting, T. D., Goldin, S. B., & Ho, Y. K. (1994). In P. A. Hargrave (Ed.), *Methods in neurosciences* (Vol. 15, pp. 1800–1895). San Diego, CA: Academic Press, Inc.
- Vogel, R., Ludeke, S., Siebert, F., Sakmar, T. P., Hirshfeld, A., & Sheves, M. (2006). Agonists and partial agonists of rhodopsin: retinal polyene methylation affects receptor activation. *Biochemistry*, *45*, 1640–1652.
- Vogel, R., Siebert, F., Ludeke, S., Hirshfeld, A., & Sheves, M. (2005). Agonists and partial agonists of rhodopsin: retinals with ring modifications. *Biochemistry*, *44*, 11684–11699.

**X-ray absorption and molecular dynamics study of cation
binding sites in the purple membrane**

Sepulcre F, Cordoní A, Proietti MG, Perez JJ, Garcia J, Querol E,
Padros E

Proteins. 2007 May 1;67(2):360-74

X-ray Absorption and Molecular Dynamics Study of Cation Binding Sites in the Purple Membrane

Francesc Sepulcre,^{1*} Arnau Cordoní,² M. Grazia Proietti,³ Juan J. Perez,² Joaquin García,³ Enric Querol,⁴ and Esteve Padrós⁵

¹Departament d'Enginyeria Agroalimentària i Biotecnologia, Escola Superior d'Agricultura de Barcelona, Universitat Politècnica de Catalunya, Barcelona, Spain

²Departament d'Enginyeria Química, ETS d'Enginyeria Industrial, Universitat Politècnica de Catalunya, Barcelona, Spain

³Instituto de Ciencia de los Materiales de Aragón, CSIC-Universidad de Zaragoza, Saragossa, Spain

⁴Institut de Biotecnologia i Biomedicina, Universitat Autònoma de Barcelona, Barcelona, Spain

⁵Unitat de Biofísica, Departament de Bioquímica i Biologia Molecular and Centre d'Estudis en Biofísica, Universitat Autònoma de Barcelona, Barcelona, Spain

ABSTRACT The present work describes the results of a study aimed at identifying candidate cation binding sites on the extracellular region of bacteriorhodopsin, including a site near the retinal pocket. The approach used is a combined effort involving computational chemistry methods (computation of cation affinity maps and molecular dynamics) together with the Extended X-Ray Absorption Fine Structure (EXAFS) technique to obtain relevant information about the local structure of the protein in the neighborhood of Mn²⁺ ions in different affinity binding sites. The results permit the identification of a high-affinity binding site where the ion is coordinated simultaneously to Asp212⁻ and Asp85⁻. Comparison of EXAFS data of the wild type protein with the quadruple mutant E9Q/E74Q/E194Q/E204Q at pH 7.0 and 10.0 demonstrate that extracellular glutamic acid residues are involved in cation binding. *Proteins* 2007;67:360–374. © 2007 Wiley-Liss, Inc.

Key words: bacteriorhodopsin; Mn-EXAFS; Mn-XANES; Mn K-edge; quick EXAFS; proton pumping

INTRODUCTION

Bacteriorhodopsin (BR) is the only membrane protein constituent of the purple membrane (PM) of the *Halobacterium salinarum*, whose function is to act as a light-driven proton pump, through the generation of a proton gradient across the cellular membrane. BR is a 26 kDa chromophoric transmembrane protein, whose structure consists of a bundle of seven helices connected through interhelical loops. In addition, the protein contains a prosthetic group consisting of a retinal molecule covalently linked to Lys216 via a protonated Schiff base. When BR absorbs a photon, the protein undergoes a photochemical cycle during which retinal isomerizes from the *all-trans* to a *13-cis* configuration. This cascade of events induces protein conformational changes that result in the translocation of a proton from the intra- to extracellular side, followed by a subsequent return of

both, the retinal molecule and the protein to their initial states. In this way BR converts the energy of light into an electrochemical proton gradient used by bacteria to produce ATP by means of the ATP-synthases (for reviews see Refs. 1 and 2).

Purple membranes are isolated as sheets of about 0.5 μm diameter formed by BR (75% w/w) and phospholipids (25% w/w),³ plus 4 mols of Ca²⁺, and 1 mol of Mg²⁺ per mole of protein.^{4,5} Removal of the endogenous cations by different methods^{4–6} leads to a deionized form of the membrane that exhibits a λ_{max} centered at about 605 nm at a mild acid pH, in contrast with the purple form (568 nm), being the proton pumping activity also affected.^{4,5,7} The purple form can be regenerated by adding a wide variety of mono-, di-, or trivalent cations.^{4,7–9}

The location of the cation binding sites in BR is uncertain at present. Some groups postulate that cation interaction occurs via non-specific binding sites,^{10–13} although the majority of the works seem to favor a specific binding. Thus, Tuzi et al. using ¹³C NMR techniques proposed the existence of a cation binding site located on the loop between helices F and G,¹⁴ Eliash et al. have shown a Mn²⁺-specific binding site on the extracellular part of the membrane,¹⁵ and Sanz et al. established Glu194 and Glu204 as residues involved in cation binding.¹⁶ In addition, a high-affinity binding site located near the retinal pocket had also been suggested by several authors.^{17–24}

Assuming similar binding behavior to Ca²⁺ due to its high relative mass and electronic properties, Mn²⁺ is a

The Supplementary Material referred to in this article can be found at <http://www.interscience.wiley.com/jpages/0887-3585/suppmat/>

Grant sponsor: Spanish Ministry of Science and Technology; Grant numbers: SAF2002-04325-C03-01, BMC2003-04941; Grant sponsor: INFN-CICYT Cooperation Project; Grant number: 2254-121-2005.

*Correspondence to: Francesc Sepulcre, Departament d'Enginyeria Agroalimentària i Biotecnologia, Escola Superior d'Agricultura de Barcelona, Universitat Politècnica de Catalunya, Barcelona, Spain. E-mail: francesc.sepulcre@upc.edu

Received 30 May 2006; Revised 1 August 2006; Accepted 15 September 2006

Published online 31 January 2007 in Wiley InterScience (www.interscience.wiley.com). DOI: 10.1002/prot.21273

useful experimental probe to analyze the structural role of bound cations as well as their localization in BR. In particular, Mn^{2+} regenerated BR has been studied using electron spin resonance (ESR),⁷ Fourier transform infrared spectroscopy (FTIR),²⁵ magnetic susceptibility,²⁰ and extended x-ray absorption fine structure (EXAFS) measurements^{21,26} to analyze the structural role, as well as the possible localization of the bound cations. The binding of the Mn^{2+} cations to the deionized membrane consist of a high-affinity site, three sites of medium, and one site of low affinity.⁷

Based on this, the present study addresses the identification of candidate cation binding sites on the extracellular segment of BR, including a site near the retinal pocket. For this purpose we combine the use of Molecular Dynamics (MD) simulations and the Extended X-Ray Absorption Fine Structure (EXAFS) technique to obtain information about the local structure around the Mn^{2+} ions in the different affinity binding sites of BR. The EXAFS technique has the advantage of being chemically selective and not requiring crystalline samples. The local structural properties of the system (interatomic distances, coordination numbers, and Debye–Waller factors) can be obtained by comparing the EXAFS oscillation either with an experimental or with a theoretical model.

With the aim of searching the local environment of the high and medium-affinity binding sites of Mn^{2+} in purple membrane, we have measured the X-ray absorption spectra of deionized blue membrane regenerated with 1 Mn^{2+} and 5 Mn^{2+} per mole of BR, in order to fill only the high and medium affinity binding sites, respectively.

The methodology used in the present work has been the following: first, we identified the affinity sites for Mn^{2+} and Ca^{2+} by computing the affinity maps of each of the cations on the protein, using the GRID program. Second, we perform for each of the sites identified a MD simulation in order to obtain structural details about Mn^{2+} clusters, using a MD simulation of a Mn^{2+} ion in water solution as a reference. Finally, the results obtained in the simulations were used as a starting point to fit the experimental EXAFS spectra.

MATERIALS AND METHODS

Purple Membrane Preparation

Purple membrane was isolated from *Halobacterium salinarum* strain S9, as described previously.²⁷ Cations were removed from the purple membrane by an extensive dialysis using a cation-exchange Dowex AG-50W resin. In each case, a separated aliquot of deionized membrane was used for pH and spectroscopic controls to avoid any contamination. Regeneration was done at pH 5 by adding Mn^{2+} at a molar ratio of 1:1 or 5:1 (Mn^{2+} :BR) and checked by UV-Vis spectroscopy, verifying that the absorption band shifts were located, as expected, from 600 nm to 580–590 nm.

Site-Directed Mutagenesis on BR

The quadruple mutant E9Q/E74Q/E194Q/E204Q (4Glu) was obtained as follows: the gene encoding BR, *bop* gene,

subcloned in pUC119 as a 1.2 kb BamHI/HindIII fragment (a gift from Dr. R. Needleman), was used as a template for mutagenesis. Single mutants were obtained by PCR site-directed mutagenesis²⁸ and amplified in the *Escherichia coli* TG1 strain. Screening of the mutants was performed by DNA sequencing. 4Glu mutant was constructed by cloning single mutants together, taking advantage of unique restriction sites. 4Glu mutant was transformed and expressed in the *H. salinarum* L33 strain with help of the shuttle plasmid pXLNovR. Membrane was grown and purified by standard methods. Mutations were confirmed from *H. salinarum* transformants by sequencing the *bop* gene from isolated DNA.

Recording of EXAFS Spectra

EXAFS of the Mn^{2+} /BR samples were carried out at 280 K in fluorescence mode at the Mn K-edge, at the beam-line ID26 of the European Synchrotron Radiation Facility (ESRF). The final concentration of the protein was about 2–3 mM. To minimize the sample exposure to radiation we used a quick scan method,^{29–31} consisting in data acquisition during a continuous energy scan of the crystal monochromator. The individual energy scans lasted about 1 min. The sample was moved automatically every five scans and the results we show correspond to an average over about 10–12 h. Radiation damage or photo-reduction can be excluded by checking the sample color changes associated to retinal bleaching. No alteration was observed for overall 5 min exposition. A monochromatic beam was obtained by means of a Si(111) double crystal, with an energy resolution $\Delta E/E = 1.4 \cdot 10^{-4}$. The fluorescence signal at the Mn K-edge was detected by a multi-element Silicon-drift solid state detector. The absorption spectrum of Mn^{2+} in water was also recorded as a reference system.

Computational Methods

Starting model

BR coordinates were taken from the Protein Data Bank³² (entry 1C3W).³³ The structure has a resolution of 1.55 Å and contains a homotrimer of BR in the ground state. This structure lacks four amino acids at the N-terminus and five residues from 157 to 161 on the third cytosolic loop. The model used consisted of a single monomer including a retinal molecule linked to Lys216 via a Schiff base. All amino acids were modeled in the protonation state they would have as free amino acids in water at pH 7 with the exception of Asp96 and Asp115, which were treated as protonated and neutral in accordance with experimental evidence.^{33,34} All lipid molecules and fragments in the crystal structure were removed.

GRID probes

Interaction energy (IE) maps were computed by means of the GRID program^{35,36} using Ca^{2+} and Mn^{2+} probes, respectively. All crystallographic water molecules were kept in the computation of the maps since they may interact favorably with the probes. The maps were computed at a

resolution of 0.5 Å. All protein atoms of the 1c3w structure were held fixed according to the crystallographic structure.

MD Simulations

The goal of the MD simulations performed was to collect sets of coordinates of the atoms within a very short radius around each Mn^{2+} ion to be used to compute the EXAFS spectra. All MD simulations were run using the AMBER 5.0 package.^{37,38} Specifically, the parm99 set of parameters³⁹ was used for all atoms in the system except for Mn^{2+} ions, whose parameters were taken from Bradbrook et al.⁴⁰ These parameters describe a free ion without explicit consideration of its coordination capabilities.⁴¹ A recent study supports that such approximation is able to predict accurately geometries of the first coordination shell of divalent metal cations and to describe properly the hydration free energies.⁴² The rationale of using such a simplified set of parameters for the present study is based on: first, their capability to reproduce accurately the coordination geometry of Mn^{2+} found in the crystal structure of Concanavalin-A; second, because Mn^{2+} ions play a similar role as Ca^{2+} or other divalent atoms such as Mg^{2+} in the BR photocycle, suggesting that the binding sites may be the same; and third, because these simulations are intended to find prospective binding sites and, consequently, the procedure needs to avoid the use of any *a priori* assumption. Therefore, even the covalent contribution of Mn^{2+} may be important in terms of IE, it is considered being not important to reproduce correct geometries. However, it is important to stress that all the geometries extracted from the MD simulations are further optimized during the EXAFS fitting.

The TIP3 model was used to represent water molecules,⁴³ and retinal charges were taken from *ab initio* calculations.⁴⁴ All MD simulations were performed at 300K and temperature was kept constant using the Berendsen's algorithm.⁴⁵ Since both bond and angle vibrations may be of importance at the Mn^{2+} environment for interpreting EXAFS spectra, their vibration was considered explicitly and therefore the time step used in the calculations was set to 1 fs. A cutoff of 12 Å was used to treat long-range interactions.

Hydrogen atoms were automatically added to the coordinate file using the AMBER package and the resulting model was minimized using harmonic restraints of 100 kcal/mole on all heavy atoms. All crystallographic water molecules that were used in the GRID calculations were removed, and only some internal water molecules were explicitly reintroduced based on a previous model of coordination.²⁰

The system was simulated without including the lipid bilayer and therefore the protein structure was subjected to restraints as it is described below. After insertion of Mn^{2+} ions based on the GRID results, the system was energy minimized with 100 kcal/mol restrictions on alpha carbons of all protein residues and on Mn^{2+} atoms. After that, each system was progressively heated during 100 ps from 0 to 300 K at intervals of 30 K every 10 ps with the same position restraints. At that point, the restraints

were removed and every system was equilibrated for 50 ps before starting the production run, which was performed for 1 ns. System coordinates were saved every 1 ps for further analysis.

MD simulation of extracellular sites

Three independent simulations were performed for every Mn^{2+} ion, starting from the positions predicted from GRID calculations. A 22 Å radius sphere of water molecules was introduced surrounding solvent exposed residues at the protein extracellular part where metal binding sites were located. Only the motion of residues lying inside or close to the cap of water molecules was considered in the calculations. Thus, only BR residues 1–14, 56–86, 118–142, and 184–212 plus all water molecules and ions were allowed to move. The position of the rest of the atoms in the system was kept restrained.

MD simulation of an internal site

For the simulation of a Mn^{2+} ion in the internal site between Asp85⁻ and Asp212⁻ an initial interaction model was taken from a previous work.²⁰ The authors reported a model cluster where a Mn^{2+} ion was coordinated to these two aspartic acid residues and three internal water molecules. Our starting structure was obtained by superposition of coordinates from the model work based on proposed aspartic side chains, to Asp85⁻ and Asp212⁻ side chains in our protein structure. The Mn^{2+} ion initial position was also consistent with our GRID results. Harmonic restraints were applied on water molecules interacting with the Mn^{2+} ion only during the heating process, and the restraints were removed during the production run.

MD simulation of a Mn^{2+} ion in water

An additional MD simulation with a single Mn^{2+} ion in water was performed with the aim to compare differences with protein clusters of solvent exposed sites. A Mn^{2+} ion was set in a 22 Å sphere of water molecules and the simulation was performed without restrictions during the heating process.

Determination of Representative Cluster of Atoms for EXAFS Analysis

The cluster of atoms used contain only the environment of each metal, i.e. the Mn^{2+} ion plus the seven closest protein residues or water molecules to each Mn^{2+} ion. With the aim of summing up the whole information of the MD trajectories in a single structure, so that there was no need to calculate the spectra for every single conformation stored during the simulation, representative structures were selected. These structures should be something similar to an average structure but without being actually that since the high mobility of water molecules makes it physically unrealistic. Thus, two different criteria to establish representative structures for every cluster were defined: Root Mean Square Displacement (RMSD) and interaction energy (IE). According to the RMSD criterion,

the representative structure of a cluster was the structure having the lowest RMSD value including only residues directly involved in the interaction with each Mn^{2+} ion and excluding all the mobile water molecules. We considered mobile water molecules as those not lying inside the protein and being part of the solvent. This criterion was reasonable for clusters interacting mainly with protein residues, but was inadequate for a Mn^{2+} ion interacting mainly with water molecules. Thus, we introduced the IE criterion where the representative structure was chosen as the structure having the IE value closest to the average value. The IE of every Mn^{2+} ion with the remaining system was calculated as the sum of the electrostatic and the van der Waals terms involving the Mn^{2+} ion.

RESULTS

GRID Maps

GRID calculations allow the prediction of specific non-covalent interactions of a ligand with a target molecule of known three-dimensional structure. Therefore, it can be considered as an appropriate approach to identify possible metal binding sites on BR. Because of the little information available regarding the charge of the different residues, the protein was modeled with all the residues charged except for those the specific information is available. However, this does not represent any problem for the validity of the results, since if in any of the binding sites, the protonation state of any of the residues may be different, the procedure would actually locate the site, although the relative minima order may be altered.

Computed maps using the Mn^{2+} ion probe are displayed in Figure 1. The maps exhibit similar affinity zones for both Mn^{2+} and Ca^{2+} probes, in agreement with the experimental observation that suggests common binding sites for both metals. Both probes show high affinity sites for BR, especially at the vicinity of Asp and Glu amino acids, and more specifically for those lying on internal sites.

According to the relative IE listed in Table I, two medium/high affinity metal binding sites have been identified: one between Glu194 and Glu204, and another one between Asp85 and Asp212. Seven additional low energy sites have also been found, three of them at the cytoplasmic surface side, lying between Asp36 and Asp38 and in the environment of Asp102 and Asp104, two on the extracellular surface side close to Glu9 and to Glu74, and two internal near Asp115 and Asp96. When comparing Ca^{2+} and Mn^{2+} maps, both show a similar minima location and general shape demonstrating that both probes share the same affinity patterns for both ions.

According to the present calculations, the highest affinity zones are clearly located in internal sites. This was expected, since as pointed out in the methods section, the presence of unpaired charges in internal protein sites is unfavorable. Interestingly, both Ca^{2+} and Mn^{2+} GRID maps, exhibit their absolute minimum between two negatively charged amino acids, Glu194 and Glu204 within helices C, F, and G, at the extracellular limit of the trans-

membrane section. Although the site can be considered as internal, these residues are partially accessible to the solvent since they are located near the protein surface. Despite the existence of water molecules near the ion for this cluster in the crystal structure, none of these molecules has been found to interact directly with it. The next prospective sites in increasing energy are two internal regions close to Asp212 and between Asp85 and Asp212. All these residues are buried in the protein core in the central region of the transmembrane helices and, accordingly, they are not exposed to the solvent. However, some water molecules have been found in crystal structures close to Asp85 and Asp212 that may interact with the metallic probes. Interestingly, two different minima close to Asp212 have been observed, one is located between this residue and Asp85 and the other close to the aromatic residues Trp86, Tyr185, and Phe208. These minima overlap when displaying the maps at higher contour energies. GRID calculations also yield low-affinity sites in the other internal sites, near Asp115 and Asp96. Although both side chains are neutral, they exhibit enough polarity in the internal medium to act potentially as low-affinity binding sites. The extracellular sites are located between Asp36 and Asp38 at the first intracellular loop, close to Glu9 at the beginning of the first helix, between Asp102 and Asp104 second intracellular loop, near Glu74 at the first cytoplasmic loop and close to Glu166 at the extracellular end of helix F.

MD Simulations

MD has been used to sample the geometries of atoms in the environment of each ion. The current study is focused on the prospective binding sites located in the extracellular part and therefore, simulations involve only ions located in this region. From the results of the GRID maps the environment of four different Mn^{2+} sites in the protein has been studied: two high-affinity sites and two low-affinity sites. We refer as cluster 1 to the internal high affinity site, close to Glu194 and Glu204 in the extracellular side. Clusters 2 and 3 are defined as to the low affinity extracellular sites, highly exposed to the solvent and close to Glu74 and to Glu9, respectively. Finally, cluster 4 corresponds to the internal high affinity site formed by residues Asp85 and Asp212 near the chromophore. Additionally, a simulation of a single Mn^{2+} ion in water has also been performed as a reference (cluster W).

With the aim of analyzing residues involved in the coordination of each Mn^{2+} ion, the Mn^{2+} -O distances between atoms participating in the coordination have been computed. In the following analysis, any residue with any of its atoms lying within a distance cutoff of 2.5 Å to the Mn^{2+} ion has been considered to be directly coordinated to the ion. For every cluster, the number of snapshots with an atom inside the cutoff sphere, as well as their average distance to the ion along the corresponding MD simulation, is shown on Tables IIA-VA, IIB-VB, and VI, respectively. All Mn^{2+} -O distances lie within 2.2 and 2.5 Å, and clearly the average distance depends on the oxygen type (hydroxyl,

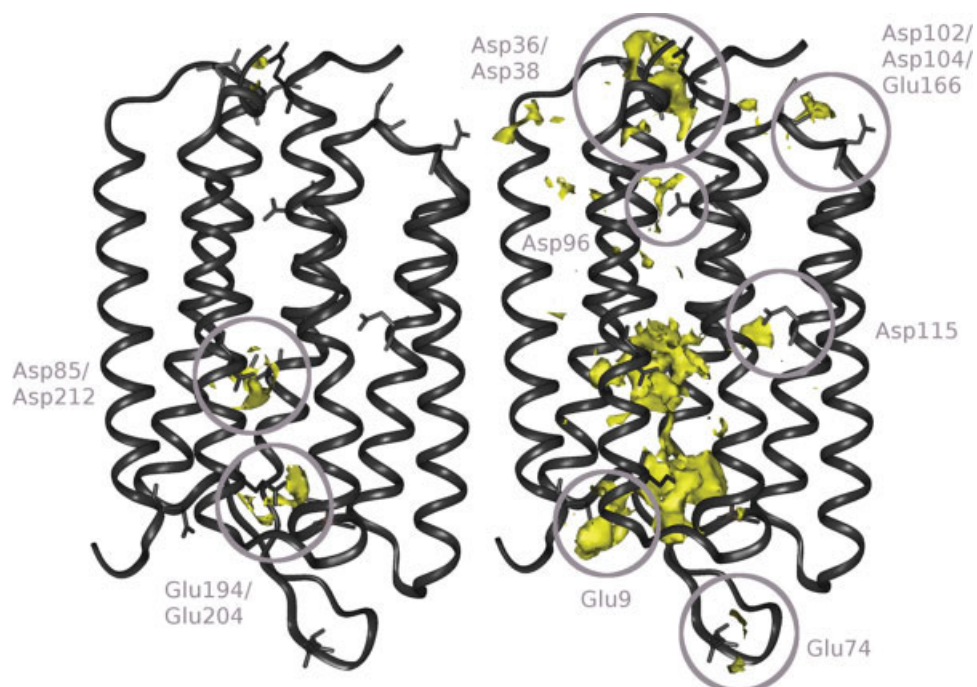


Fig. 1. Affinity regions for the Mn^{2+} probe obtained applying the GRID program to the BR structure 1c3w.³³ The maps are shown at +40 kcal/mol (left) and +75 kcal/mol (right) relative to the absolute minimum.

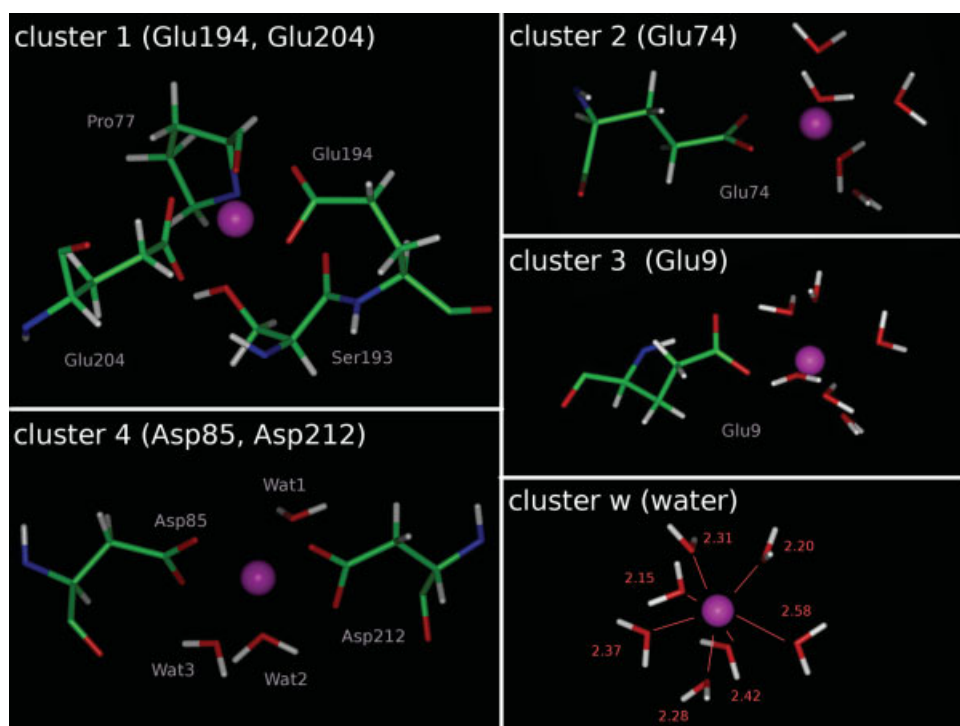


Fig. 2. Representative structures of MD simulations of each cluster according to the IE criterion (snapshots at 213, 110, 55, 462, and 704 ps for cluster 1, 2, 3, 4, and W respectively). Only residues having an atom within 3 Å from Mn^{2+} ion are displayed. Protein residues and water molecules are colored by atom element (Mn^{2+} ion appears in magenta). Starting structure, 1c3w.³³

TABLE I. Relative Energies of the Metal Binding Sites Predicted for Ca²⁺ and Mn²⁺ GRID Probes

Residues	Energy Mn ²⁺ (kcal/mol)	Energy Ca ²⁺ (kcal/mol)
1 Glu194 ⁻ /Glu204 ⁻	0	0
2 Asp85 ⁻ /Asp212 ⁻	30	30
3 Asp36 ⁻ /Asp38 ⁻	40	40
4 Glu9 ⁻	50	45
5 Asp115	55	50
6 Asp96	60	55
7 Asp102 ⁻ /Asp104 ⁻	65	60
8 Glu74 ⁻	65	60
9 Glu166 ⁻	75	70

TABLE II. Cluster 1; A: % of Snapshots Where an Atom of a Certain Residue is Within 2.5 Å of the Mn²⁺ ion; B: Average Distances of Coordinating Atoms With the Mn²⁺ Ion and Their Standard Deviations

A. Residue	d(Mn) < 2.5 Å
Pro77 (backbone oxygen)	98.5%
Ser193 (hydroxyl)	97.4%
Glu194 (carboxyl)	100.0%
Glu204 (carboxyl)	100.0%
B. Atom	Distance/Å (SD)
Pro77 O	2.22 (0.08)
Ser193 OG	2.38 (0.10)
Ser193 O	2.52 (0.26)
Glu194 OE1	2.22 (0.07)
Glu194 OE2	2.23 (0.07)
Glu204 OE1	2.21 (0.07)
Glu204 OE2	2.32 (0.15)

carboxylic, carbonylic or water). As it will be shown below, the average Mn²⁺-O distance is longer than in the EXAFS experiments. On the other hand, the standard deviation of these distances provides a measure of the importance of these interactions. Thus, the most stable interactions have low standard deviations (between 0.07 and 0.10 Å) that increase as an interaction is weaker.

Cluster 1 (Glu194/Glu204)

The Mn²⁺ ion of this cluster lies between the cytoplasmic side of helices C, F, and G, the first cytoplasmatic loop at the limit with helix C and the third cytoplasmatic loop that connects helices F and G (Fig. 2). From the analysis of the MD simulation, it could be established that the four carboxylic oxygens of residues Glu194⁻ and Glu204⁻, the hydroxyl oxygen of Ser193 and the backbone oxygens of residues Pro77 and Ser193 are part of the first coordination shell, as shown in Figure 2 (see also Table II). Distances and deviations of these interactions show that the main coordination points are three carboxylic oxygens of glutamic acid residues Glu194⁻ and Glu204⁻ and the backbone oxygen of Pro77, since their oxygen atoms have average distances about 2.2 Å from Mn²⁺ ion and standard deviations below 0.10 Å. On the

TABLE III. Cluster 2; A: % of Snapshots Where an Atom of a Certain Residue is Within 2.5 Å of the Mn²⁺ Ion; B: Average Distances of Coordinating Atoms With the Mn²⁺ Ion and Their Standard Deviations

A. Residue	d(Mn) < 2.5 Å
Glu74	99.9%
Wat900	25.1%
Wat438	24.0%
Wat691	23.0%
Wat1022	22.7%
Wat888	20.9%
B. Atom	distance (SD) (Å)
Glu74 OE1	2.48 (0.54)
Glu74 OE2	2.42 (0.47)
Wat778 O	2.33 (0.13) ^a
Wat900 O	2.33 (0.13) ^b
Wat438 O	2.40 (0.42) ^c

^a39 < t < 400 ps.

^b723 < t < 1000 ps.

^c400 < t < 666 ps.

TABLE IV. Cluster 3; A: % of Snapshots Where an Atom of a Certain Residue is Within 2.5 Å of the Mn²⁺ Ion; B: Average Distances of Coordinating Atoms With the Mn²⁺ Ion and Their Standard Deviations

A. Residue	d(Mn) < 2.5 (Å)
Glu9	100%
Wat788	79.4%
Wat818	61.0%
Wat1146	52.7%
Wat867	45.6%
Wat771	44.1%
Wat1128	31.4%
Wat1126	26.7%
Wat876	21.7%
B. Atom	Distance (SD) (Å)
Glu9 OE1	3.74 (0.30)
Glu9 OE2	2.19 (0.06)
Wat788 O	2.31 (0.10) ^a
Wat818 O	2.30 (0.09) ^b
Wat1146 O	2.31 (0.10) ^c

^a47 < t < 870 ps.

^b76 < t < 705 ps.

^c451 < t < 1000 ps.

other hand, the other interacting atoms: the hydroxyl and backbone oxygens of Ser193 and the remaining carboxyl oxygen of Glu204⁻, exhibit both larger distances and standard deviations than other oxygens. Finally, although there are some water molecules close to the site and interacting with residues Glu194⁻ and Glu204⁻, no water molecules were detected to be in the Mn²⁺ first coordination shell during the simulation.

Cluster 2 (Glu74)

The Mn²⁺ ion of this cluster is located close to Glu74⁻, at the most solvent exposed section of the first cytoplas-

TABLE V. Cluster 4; A: % of Snapshots Where an Atom of a Certain Residue is Within 2.5 Å of the Mn²⁺ Ion; B: Average Distances of Coordinating Atoms With the Mn²⁺ Ion and Their Standard Deviations

A. Residue	d(Mn) < 2.5 Å
Asp85	100.0%
Asp212	100.0%
Wat229	99.3%
Wat230	98.5%
Wat231	98.8%
B. Atom	Distance (SD) (Å)
Asp85 OD1	2.24 (0.07)
Asp85 OD2	2.25 (0.07)
Asp212 OD1	2.25 (0.07)
Asp212 OD2	2.26 (0.07)
Wat229	2.30 (0.07)
Wat230	2.32 (0.08)
Wat231	2.29 (0.07)

matic loop. During the MD simulation, the Mn²⁺ ion exhibits a distorted octahedral coordination, similar to that observed in the simulation in pure water, with the difference that two water molecules have been substituted by two carboxylic oxygen atoms from Glu74⁻. The representative structure according to the IE criterion (Fig. 2) exhibits five water molecules with different coordinating distances. Some of them have longer distances than the average, because of a water exchange occurring in the first coordination shell. From the analysis of the MD simulation it can be established that the first coordination shell of Mn²⁺ involves on average two oxygen atoms of Glu74⁻ and four additional water molecules (see Table III). None of these water molecules remain coordinated to the Mn²⁺ ion during the trajectory. However, this is an artifact due to the parameterization for Mn²⁺ used in the present work that shows computed residence times for water molecules in the first coordination shell similar to those of alkaline ions, and those to be expected for a Mn²⁺, that are in the microsecond scale.⁴⁶ This is not a problem for the purpose of the present work, since in this way the space of configurations can be adequately sampled within 1 ns with the corresponding save of computer time. It is interesting to point out that some molecules remain in the first coordinated shell of Mn²⁺ for a short time, whereas others exhibit longer residence times. This is related to the ordering of water molecules close to Mn²⁺ ion as it is discussed below. The evolution of Mn²⁺-O distances involving carboxylic oxygens of Glu74⁻ shows alternation of single/double interactions. Thus, when only a single oxygen interacts directly with the Mn²⁺ ion, a fifth water molecule becomes part of the first coordination shell.

Cluster 3 (Glu9)

The Mn²⁺ ion of this cluster lies close to Glu9⁻, at the boundary between the N-terminal region and helix A. The environment of this site includes the first and the third

TABLE VI. Cluster W. Average Distances of Coordinating Atoms With the Mn²⁺ Ion and Their Standard Deviations

Atom	Distance (SD) (Å)	Snapshots observed (ps)
Wat949	2.32 (0.10)	202–233, 549–824
Wat1113	2.33 (0.11)	309–603
Wat830	2.34 (0.11)	1–241
Wat434	2.33 (0.11)	309–365, 373–603

extracellular loops together with the N-terminal segment. During the simulation, the Mn²⁺ ion shows a distorted octahedral coordination geometry similar to that found in cluster 2 (Fig. 2). Water molecules exhibiting longer distances to Mn²⁺ than the average can be identified due to the process of water exchange. In general, the first six neighbors are five water molecules and a carboxylic oxygen atom of Glu9⁻. Interestingly, the other Glu9⁻ carboxylic oxygen is part of the second coordination shell and it is used as an anchoring point for water molecules that are part of the first coordination shell of the Mn²⁺ ion. Thus, this water molecule acts as a bridge between Glu9⁻ carboxylic oxygen and the Mn²⁺ ion. Although some water molecules remain coordinated to Mn²⁺ ion for long times (up to near 800 ps), similarly to what has been described for cluster 2, none of them remains in the first coordination shell during the simulation. The number of snapshots for residues and water molecules with the largest residence times, and the average distances and their standard deviations are shown in Table IV.

Cluster 4 (Asp85/Asp212)

The Mn²⁺ ion of this cluster lies in the protein core between helices B, C, and G. From the MD simulation analysis we established that the first coordination shell of Mn²⁺ ion involves residues Asp85⁻ and Asp212⁻ together with three internal water molecules (Table V(A)). All aspartic carboxyl oxygens on the site show short Mn²⁺-O distances and small standard deviations, indicating that they all remain strongly coordinated during the whole trajectory (Table V(B)). Interestingly, the internal water molecules have additional anchoring points that help to keep their position. Thus, a water molecule (Wat229) interacts with the backbone carbonyl oxygen of Val49, a second water (Wat230) acts as a bridge between the side chain nitrogen atom of Trp86 and the backbone carbonyl oxygen of Arg82 and a third (Wat231) has its hydrogen atoms interacting with the Schiff base nitrogen atom (Lys216) and with the Thr89 hydroxyl group. These results are in agreement with the initial coordination model used.²⁰

Cluster W (Mn-Water)

To properly understand the results involving Mn²⁺-protein interactions described previously, the results of a MD trajectory of a Mn²⁺ ion soaked in pure water is a necessary reference. Several events of water exchange have been observed in the analysis of this trajectory, showing the dynamic nature of the first coordination

shell of Mn^{2+} . It is important to stress that, due to the parameterization used for Mn^{2+} in the present work, the 1 ns trajectory can be understood to provide a number of events relative to water exchange similar to what it is expected to be observed in a longer trajectory. Specifically, the residence time for a water molecule in the first coordination shell is that of an alkaline or alkaline-earth metal, which is about three orders of magnitude shorter than the experimentally known for Mn^{2+} .

An average coordination number of 6 is observed, considering a cutoff between 2.35 and 2.40 Å. In general, an octahedral coordination geometry is observed with an average Mn^{2+} -oxygen distance of 2.33 ± 0.11 Å. This distance is longer than the optimum interaction distance between a Mn^{2+} ion and a water molecule in an octahedral complex of about 2.15–2.20 Å,^{21,26} as deduced from our previous measurements. However, the former value has an implicit correction due to the water exchange process. More specifically, the analysis of the MD trajectories in detail, reveals that in every snapshot there is an average of four water molecules with distances to Mn^{2+} ion close to this value (between 2.10 and 2.35 Å), that can be considered strongly coordinated to the metal, plus some additional molecules with larger distances that exhibit a weaker interaction with Mn^{2+} . These differences in distances support the idea of a continuous exchange of water molecules in the first coordination shell, so that in every snapshot there is a coexistence of water molecules that were already coordinated to Mn^{2+} in the previous snapshot, together with other that are either entering or escaping from the first coordination sphere. A representative configuration of the simulation of a Mn^{2+} ion in water according to the IE criterion is shown in Figure 2. In this figure, all water molecules with the oxygen atom within 3.0 Å from Mn^{2+} ion, are shown. From the seven water molecules within this distance (ranging from 2.10 to 2.60 Å), a distorted octahedral can be observed with three water molecules at distances lower than 2.35 Å and four water molecules at longer distances, one of them out of the first coordination shell.

Water Exchange Inside the Clusters

A general feature that can be deduced from the present results is that the larger the neighboring protein surface close to the metal, the least the coordination shell changes along the MD simulation. Moreover, changes in the coordination sphere are faster in bulk water or in very water exposed sites. Specifically, since in clusters 2 and 3 there is only one or two protein oxygens in the first coordination shell and all the remaining coordination positions are filled with water molecules, these simulations are easier to compare with that of cluster W. The percentage of water molecules with residence times of 10% or longer among the total number of waters observed to interact with the Mn^{2+} ion along the MD trajectory are: 22%, 42% and 13% in clusters 2, 3 and W, respectively. In Figure 3 it is possible to follow the evolution of water molecules with longer residence times. Interest-

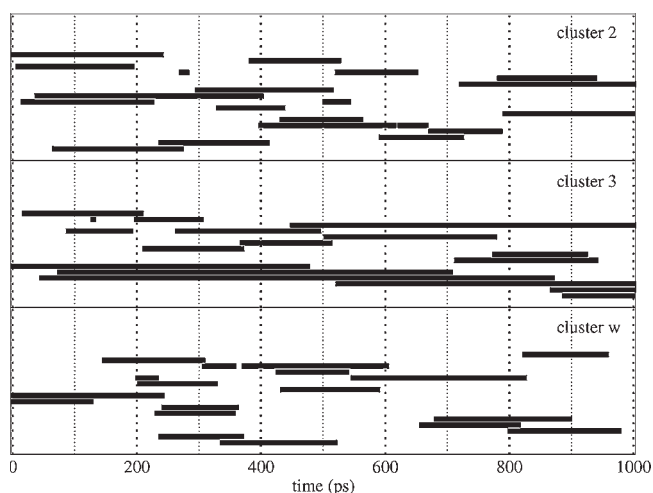


Fig. 3. Evolution along the MD simulation of long time coordinating water molecules. Each line represents a water molecule coordinated with the Mn^{2+} .

ingly, first, at any time there is always at least one long time residence molecule interacting with the Mn^{2+} ion and second, some of these molecules are even able to escape from the first coordination sphere and return later. The residence times as well as the number of water molecules with long residence time grow in proportion to the protein surface surrounding the site. Figure 4 represents a plot of the coordination times for the 15 water molecules with the longest residence times for each cluster. The results show that when there is a protein anchoring point in a cluster, the coordination times of the water molecules increase significantly. This is expected since in protein clusters, water molecules compete for a smaller number of coordinating sites (6 in cluster W, 5 in cluster 3 (Glu9⁻) and 4 in cluster 2 (Glu74⁻)) and furthermore, there is an excluded volume for water molecules in protein sites that is occupied by the remaining protein structure. Clearly the available volume affects the ease of a water molecule to enter or escape from the first coordination sphere. Comparison of clusters 3 and 2, suggests that there is a correlation between the available volume around the ion and the coordination time of water molecules. Thus, cluster 3 has more protein environment than 2 and water molecules exhibit longer coordination times. Finally, in addition to the effect of having less accessible volume, the existence of protein residues close to the ion increases the chances for specific hydrogen bond interactions that result in a stabilization of particular conformations involving water molecules in the first or second coordination shell of the Mn^{2+} ion, like the interaction between a water molecule and a Glu9⁻ carboxyl oxygen in cluster 3.

EXAFS Results

In the EXAFS technique, the fine structure oscillations showing up in the extended energy region above the absorption edge are analyzed. The k-space frequency, am-

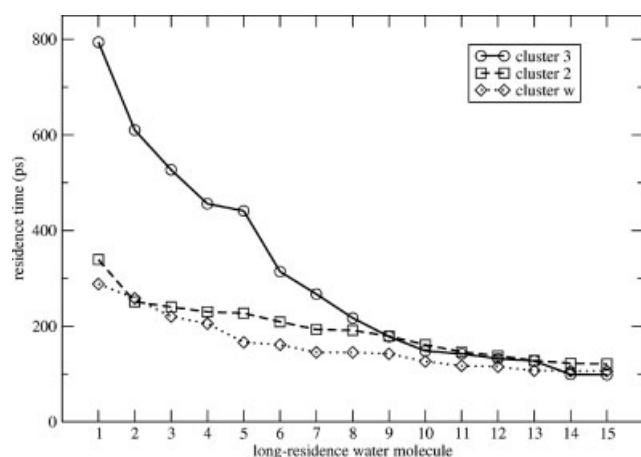


Fig. 4. Water molecules with the longest coordination times for clusters 2, 3, and W.

plitude and phase of the EXAFS oscillations, are directly related to interatomic distances and number and type of scatterers around the absorber.

Quantitative analysis of the EXAFS signals is performed by fitting the experimental spectra to theoretical signals calculated by means of phases and amplitudes generated by the FEFF8 code.⁴⁷ The fitting procedure is carried out by means of the Ifeffit code⁴⁸ implemented by the Artemis package.⁴⁹ We use the geometry of the extracellular clusters obtained from the MD calculations to obtain theoretical EXAFS signals and compare them with the EXAFS data obtained for the high-affinity binding site (i.e., WT regenerated with 1 Mn^{2+} /BR molecule). The atoms coordinates of the different clusters were extracted from MD simulations snapshots following the two criteria (RMSD and IE) as described above, in the Materials and Methods section. We consider the scattering paths with $R \leq 4\text{\AA}$.

Purple Membrane WT Regenerated With 1 Mn^{2+} /BR: Influence of pH on the High-Affinity Binding Site

Figure 5(A) shows the Mn-K edge normalized XANES spectra corresponding to WT BR regenerated with 1 Mn^{2+} , at pH 7 and 10. The spectra show a characteristic 1s-3d peak centered at 6540 eV followed by an intense absorption edge with a peak maximum of 6550 eV. The edge shapes are similar showing that no major changes take place in the Mn^{2+} environment of the bound high-affinity cation between pH 7 and 10.

The EXAFS signal, $\chi(k)$, of WT regenerated with 1 Mn^{2+} at pH 7 and 10 are shown in Figure 5(B). They are very similar to each other confirming that the symmetry and/or the atoms bounded to the cation are the same for the two pH values. Their Fourier transforms (FT) are reported in Figure 6(A,B). They were calculated in the range 2.5–9.4 \AA^{-1} . The main contribution at about 1.8 \AA is due to the Mn–O scattering paths, which dominate the EXAFS signal (note that the average R -value of

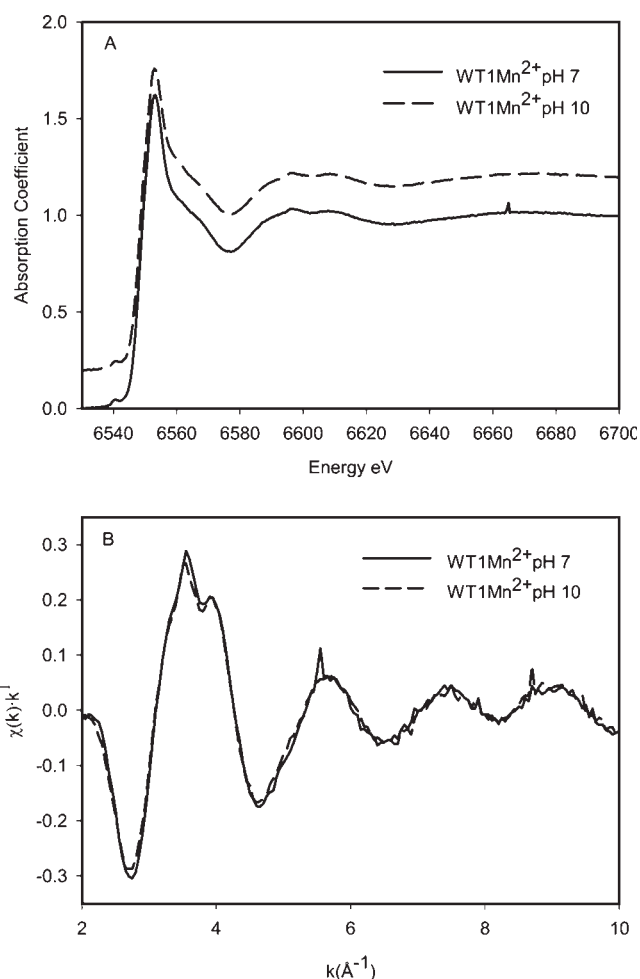


Fig. 5. Mn K-edge X-ray absorption spectra of the complex WT BR regenerated with 1 Mn^{2+} per mole of protein, measured at pH 7.0 (solid line) and pH 10.0 (dashed line). Absorption spectra are presented in (A) and EXAFS spectra in (B).

the Mn–O distances is not corrected in the figure for the central atoms phase shift). We performed quantitative analysis of the EXAFS data by comparing the experimental signals with theoretical signals calculated for the different clusters obtained by the MD simulations as described in previous section. The parameters let free to vary to minimize the χ^2 (R -factor) values were E_0 (origin value of the photoelectron energy) and the interatomic Mn–O distances (R_i). The overall inelastic losses factor S_0^2 was fixed to a standard value of 0.8, and the EXAFS data were fitted in k -space in the range 2.5–9.4 \AA^{-1} .

The interatomic Mn–O distances were all allowed to vary with the same ΔR variation in such a way to produce a rigid contraction or expansion of the cluster as a whole, i.e. without changing the cluster geometry as determined by MD. Indeed, EXAFS is not directly sensitive, as XANES, to the cluster geometrical details and its shape is essentially determined, in this kind of system, by the coordination numbers and distances distribution of the Nearest Neighbors (NN) atoms.

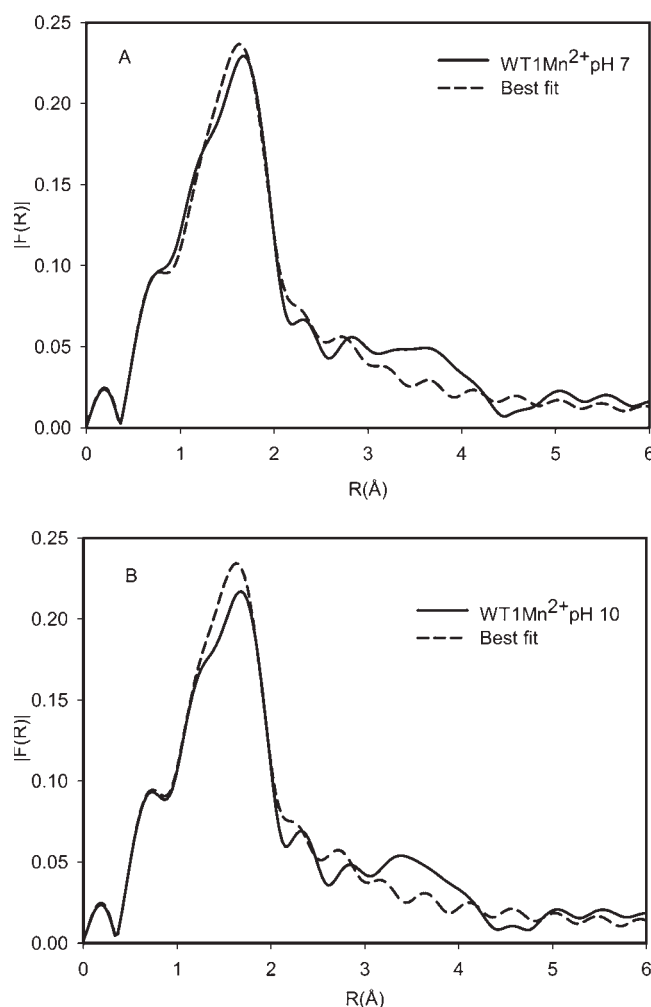


Fig. 6. Fourier transforms of the EXAFS data shown in Figure 5 and the best fit (dashed line) at pH 7.0 (A) and pH 10.0 (B).

The Debye–Waller factors, which describe both static and dynamic fluctuations in interatomic distances, were calculated by the correlated Debye model implemented in IFFEFIT and described by Sevillano et al.,⁵⁰ in which the only two parameters required are the experimental temperature and the Debye temperature of the cluster (Θ_D).

The Debye temperatures (Θ_D) of the different clusters were calculated according to: $\Theta_D = h\nu/K$, where h and K are respectively the Planck constant and the Boltzmann constant, and ν is the experimental vibrational mode of Mn–(H₂O) and Mn–carboxylate bonds.⁵¹ For simplicity, we have considered the average value of these frequency regions ($\nu = 600 \text{ cm}^{-1}$). This gives an average value for $\Theta_D = 936 \text{ K}$.

The theoretical signals (EXAFS and FT) are compared with each other and with the experimental signal for sample WT1Mn²⁺pH 7, in Figure 7. The difference among the different clusters is quite evident; the cluster which better fit the experimental EXAFS is the RMSD Asp85⁻/Asp212⁻. The geometry and coordination distances, of all clusters considered, are described in the previ-

ous section and reported in Figure 2 and Tables II–IV. We show here in Table VII the best fit procedure results. We report the R -factor (χ^2 residuals), for samples WT1Mn²⁺ pH 7 and pH 10 compared with the RMSD and EI clusters. We tested all the clusters calculated by MD but, for sake of clarity, we only report those giving the lowest R values.

We can see that cluster RMSD Asp85⁻/Asp212⁻ gives the best fit result for WT BR regenerated with 1 Mn²⁺/BR molecule (WT1Mn²⁺ sample). In this case we performed a further best fit letting the Θ_D temperature, i.e. the DW factors, free to vary and we obtained the same results within the statistical errors.

The structural parameters of the manganese ion environment, as determined by the least-square fit, are summarized in Table VIII for the first 6 single scattering paths that correspond to Mn–O coordination. We find here a very similar average value for the Mn–O distance (2.18 Å for pH 7 and 2.17 Å for pH 10), and a Debye–Waller factor of 0.004 Å² for both the pH values studied.

These values are consistent with the results found in our previous work²¹ for the high-affinity binding site studied at pH 5 (2.17 Å and 0.005 Å²). From the structural/geometrical point of view, the fits obtained for WT at pH 7 and 10, and pH 5 are very similar,²¹ suggesting that the coordination of the Mn²⁺ ion in the high-affinity binding site of BR is not affected by a pH increase from 5 to 10. This is a further confirmation that this kind of site is located in the internal protein region. Moreover, we can discriminate among the different possibilities provided by MD showing that the Asp85⁻/Asp212⁻ site is the best approximation of the experimental results.

Purple Membrane WT and 4Glu Regenerated With 5Mn²⁺/BR: Influence of pH on High and Medium-Affinity Binding Site

In this section, a qualitative analysis of the pH influence on the Mn environment in native and mutated proteins is presented, in which both the low and high affinity sites are involved.

Figure 8 displays the raw absorption spectra of the WT purple membrane (A) and the 4Glu sample (B) (WT5Mn²⁺ and 4Glu5Mn²⁺, respectively), regenerated with 5Mn²⁺/BR molecule. The solid lines represent the samples at pH 7 and the dotted lines those at pH 10. The overall shape and position of the edges (6550 eV) of the WT5Mn²⁺ and 4Glu5Mn²⁺ samples at pH 7 are very similar to each other and also to the WT1Mn²⁺ (see Fig. 5). As in the previous case (WT1Mn²⁺ sample) all the spectra show a pre-edge structure at 6540 eV. All the samples, except WT5Mn²⁺ at pH 10, have a pronounced absorption edge with peak maximum at about 6550 eV. In case of sample WT5Mn²⁺ at pH 10, instead, the edge is dramatically altered, i.e., it has a significantly lower maximum at 6560 eV and a different overall shape. The EXAFS spectra are reported in Figure 9(A) (WT) and Figure 9(B) (4Glu) for both pH values. For the 4Glu samples the EXAFS spectra for pH 7

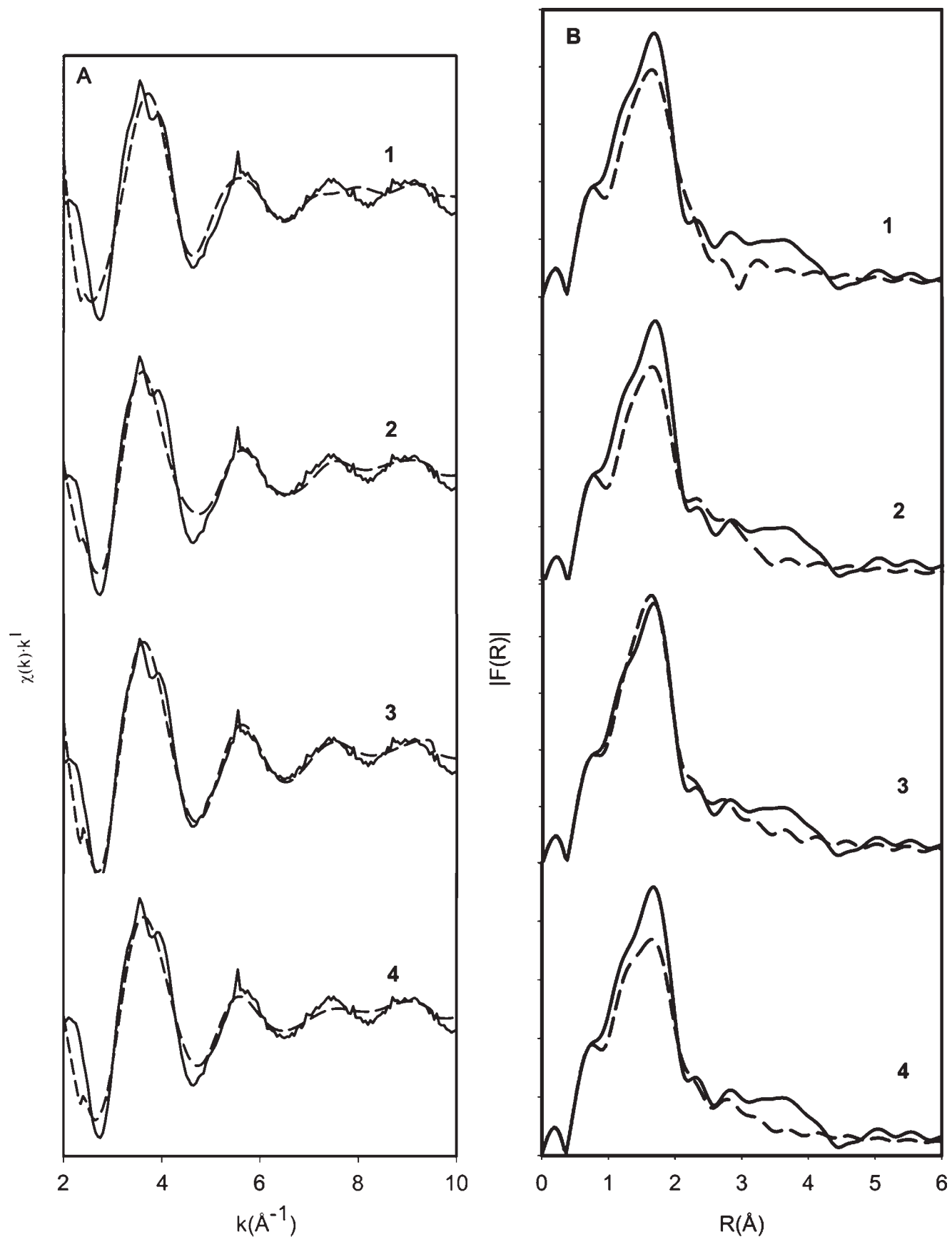


Fig. 7. A comparison between the background-subtracted k-space EXAFS data (A) and their Fourier transform (B) of the WT1Mn²⁺ pH7 sample (solid line) and the best fit (dashed line) for clusters 1:Glu194⁻/Glu204⁻ (RMSD); 2: Glu74⁻ (RMSD); 3: Asp85⁻/Asp212⁻ (RMSD) and 4: Glu9⁻ (EI).

TABLE VII. Fit Parameters Corresponding to the Fits on the Putative BR-Clusters and WT Bacteriorhodopsin Regenerated With 1Mn²⁺ Per Mole of Protein

Parameter → Sample & cluster	R-factor (χ^2)	ΔE_0 (eV)	ΔR (Å)	σ^2 (Å ² × 10 ⁻³) (fix) ($\Theta_D = 936$ K)
Glu194 ⁻ /Glu204 ⁻ (RMSD)				
WT1Mn ²⁺ pH7	0.078	-5 ± 4	-0.04 ± 0.02	4
WT1Mn ²⁺ pH10	0.069	-7 ± 4	-0.05 ± 0.02	4
Mn ²⁺ -solution	0.184	-4 ± 10	-0.03 ± 0.05	4
Glu74 ⁻ (RMSD)				
WT1Mn ²⁺ pH7	0.067	-6 ± 3	-0.04 ± 0.02	4
WT1Mn ²⁺ pH10	0.061	-7 ± 2	-0.04 ± 0.01	4
Mn ²⁺ -solution	0.177	-7 ± 7	-0.04 ± 0.04	4
Glu9 ⁻ (EI)				
WT1Mn ²⁺ pH7	0.053	-10 ± 3	-0.07 ± 0.02	4
WT1Mn ²⁺ pH10	0.048	-11 ± 3	-0.07 ± 0.02	4
Mn ²⁺ -solution	0.175	-11 ± 9	-0.07 ± 0.05	4
Asp85 ⁻ /Asp212 ⁻ (RMSD)				
WT1Mn ²⁺ pH7	0.029	-6 ± 1	-0.02 ± 0.01	4
WT1Mn ²⁺ pH10	0.036	-7 ± 2	-0.03 ± 0.01	4
Mn ²⁺ -solution	0.096	-6 ± 4	-0.02 ± 0.02	4

The RMSD and IE criteria are described in the text.
 E_0 and R were iterated ($S_0^2 = 0.8$).

TABLE VIII. Interatomic Distances (R) and Debye-Waller Factors (σ^2) for the First 6 Paths (Mn–O) Corresponding to the Best Fit for WT Bacteriorhodopsin-Mn²⁺ at a Molar Ratio of 1:1 at pH 7 (A) and pH 10 (B)

	R (Å)	σ^2 (Å ² × 10 ⁻³)
A. WT1Mn ²⁺ pH7		
Path 1	2.07	4
Path 2	2.12	4
Path 3	2.16	4
Path 4	2.20	4
Path 5	2.24	4
Path 6	2.27	4
B. WT1Mn ²⁺ pH10		
Path 1	2.06	4
Path 2	2.11	4
Path 3	2.15	4
Path 4	2.20	4
Path 5	2.23	4
Path 6	2.26	4

and 10 are quite similar to each other, whereas for WT BR a strong change is found as for XANES.

We did not perform any best fit analysis due to the present lack of information about the low and medium affinity sites environment. Indeed, the MD calculations provide different possibilities for the external sites (Glu9⁻, Glu74⁻, Glu194⁻/204⁻) that can be simultaneously occupied by four out of the five regenerating Mn ions. Therefore performing a quantitative analysis would not lead to any pertinent information due to the lack of selectivity in the mutation process.

It should be noted that a change in the Mn oxidation state induced by the different pH can be discarded due to the very tiny change in the Mn edge position between pH 7 and 10 (about 0.5–1.0 eV) in comparison with the val-

ues obtained by Subías et al.,⁵² and also to the high similarity of the 4Glu spectra at both pH values.

As a last point, we performed for comparison the best fit analysis of the reference sample of Mn²⁺ water solution, using a regular octahedral cluster to generate the theoretical signal. We obtained the results shown in Table IX, finding an average Mn²⁺-O distance of 2.14 Å, in good agreement with a previous EXAFS study²¹ and with the typical distance for a Mn–O bond in Mn–OH₂ complexes, which is about 2.10 Å.⁵³ Therefore, as stated above, distances obtained from the present MD according to parameterization used for Mn²⁺ (see Tables I–VI) are slightly overestimated.

DISCUSSION

In this work we have combined theoretical calculations with experimental EXAFS data in order to obtain structural information about the local environment around cation binding sites in BR. First, calculations were applied to predict specific interaction sites between BR and Mn²⁺ or Ca²⁺ by using the GRID program. Second, MD calculations were applied to the sites located in the extracellular region of BR to obtain structural details about Mn²⁺ clusters. Finally, the results of these calculations were used as starting points to fit the experimental EXAFS data.

This paper represents the extension of previous works about x-ray absorption studies of Mn²⁺ and Ca²⁺ binding to the purple and bleached membranes at pH 5.^{21,22,26} Now we present results for pH values 7.0 and 10.0 and we also analyze the 4Glu mutant.

Although Mn²⁺ is not found as a physiological cation in purple membrane, it is known that deionized BR can be regenerated with a variety of cations.^{4,5,7,8} In particular Duñach et al.⁵⁴ have found that both stoichiometry and apparent affinity constants for radioactive Ca²⁺ in deion-

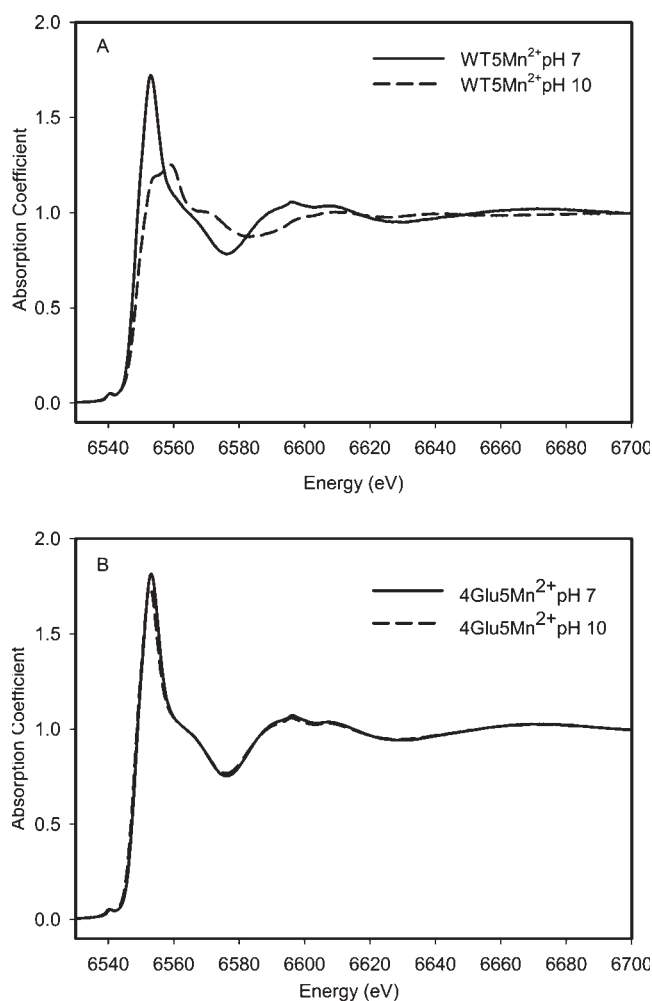


Fig. 8. A comparison of the pH effect on the X-ray absorption spectra of the complex WT BR-Mn²⁺ (A) and 4Glu-Mn²⁺ (B) at a molar ratio of 1:5 (protein: Mn²⁺). Measurements were made at pH 7.0 (solid line) and pH 10.0 (dashed line).

ized BR were almost identical to those found for Mn²⁺. In agreement with these results, we find in this work that the calculated GRID maps for metallic Mn²⁺ and Ca²⁺ ions probes show very similar affinity zones for Mn²⁺ and Ca²⁺, suggesting that the metal binding sites are essentially the same for both metals.

We compare here the cation binding in four different clusters of BR found in the GRID map and located in the extracellular region of the protein (external sites: Glu74⁻, Glu9⁻, and Glu194⁻/Glu204⁻) and a site near the retinal pocket (Asp85⁻/Asp212⁻). The local environment of Mn²⁺ in all these putative clusters is formed by carboxyl side-chains of Asp and Glu residues that had already been proposed as candidates for cation binding in BR.^{16,17,23,55,56}

From the comparison of the GRID maps for the four clusters, we find that minimum energy value is given by the cluster formed by Glu194⁻/Glu204⁻. However, since the energy difference between this site and the Asp85⁻/Asp212⁻ site is quite small, a dynamic equilibrium

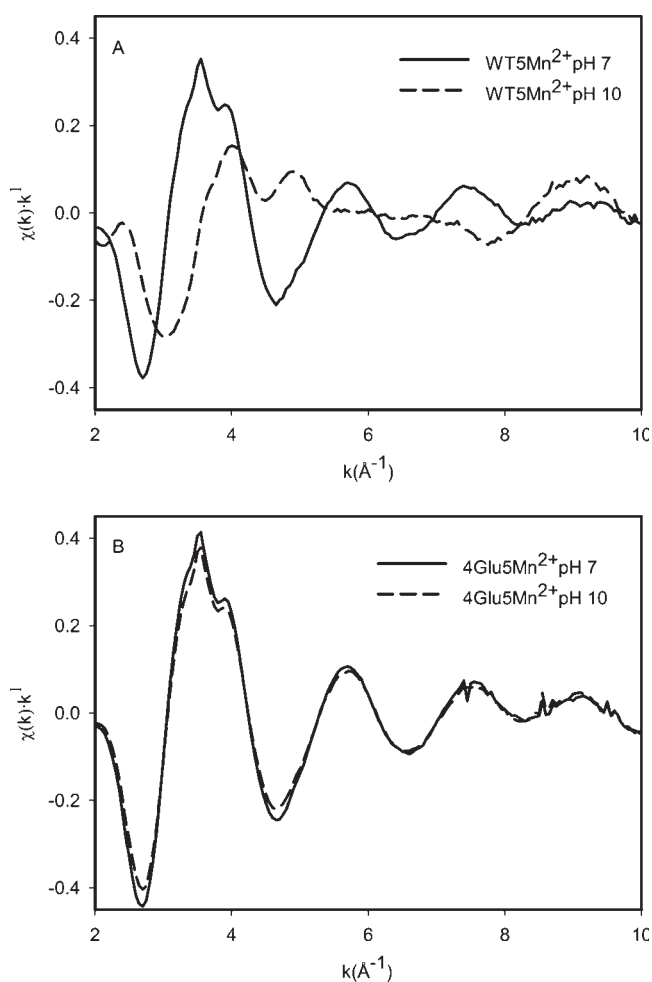


Fig. 9. EXAFS spectra $\chi(k)$ of the data shown in Figure 8. (A) WT BR-Mn²⁺ and (B) 4Glu-Mn²⁺ at a molar ratio of 1:5 (protein: Mn²⁺), at pH 7.0 (solid line) and pH 10.0 (dashed line).

TABLE IX. Interatomic Distance (R) and E_0 Factor of the First Shell of Mn²⁺ in Water

	S_0^2 (fix)	ΔE_0 (eV)	R (\AA)	σ^2 ($\text{\AA}^2 \times 10^{-3}$) (fix) ($\Theta_D=936$ K)
Mn solution	0.8	-14 ± 2	2.14 ± 0.01	3

between these sites may be envisaged to explain the cation binding in BR. That is not to say that these binding sites are nonspecific. Yet, a relationship among the cations located in the extracellular region could be necessary in order to maintain the native structure and the hydrogen bonded-network of this part of the protein.

As a matter of fact, the EXAFS fittings results for PM regenerated with 1 Mn²⁺ per BR molecule are consistent with the high-affinity binding site being located between Asp85⁻ and Asp212⁻, for both pH values studied. For this site we find a quite similar average Mn—O distance for the two pH values of 7 and 10 (2.18 and 2.17 \AA , respectively), indicating that there is no change in the metal first coordination shell upon a pH increase. The av-

erage Mn—O distance found for Mn^{2+} in the protein shows a difference of 0.03–0.04 Å with respect to the Mn—O distance for Mn^{2+} in water solution found here, which is a significant difference considering the same coordination number of 6. This implies that the first coordination shell for the metal atom is different when it is bound to the protein or is solvated by water molecules.

Comparison of EXAFS results at pH values of 7 and 10 for all the studied samples (WT1Mn^{2+} ; WT5Mn^{2+} ; 4Glu5Mn^{2+}) gives valuable information about the location of cation binding sites and on involvement of the mutated Glu residues. First, there is a strong similarity between the behavior of 4Glu5Mn^{2+} and WT1Mn^{2+} : the EXAFS spectra are similar and both show insensitivity on pH change. This suggests that both proteins have only one internal cation binding site. Second, EXAFS spectra of WT5Mn^{2+} show a strong change on going from pH 7 to 10, whereas 4Glu5Mn^{2+} is insensitive to this change. Therefore, the internal site of WT1Mn^{2+} or of 4Glu5Mn^{2+} is not sensitive to pH, whereas some of the more external sites of WT5Mn^{2+} are heavily affected by the pH change. Finally, the behavior of the 4Glu mutant is a strong evidence that some of the mutated Glu side chains are involved in the cation binding, in agreement with previous results,^{14–16} i.e. four of the 5 Mn^{2+} added to the 4Glu mutant are not fixed by the protein and remain in water solution. They are then eliminated in the centrifugation process used in the sample preparation.

Summarizing, these results delineate the presence of at least two binding sites for Mn^{2+} in the purple membrane: one internal high-affinity site located in the vicinity of Asp85[−] and Asp212[−], and an external site of lower affinity located near Glu194[−] and Glu204[−]. This hypothesis is in agreement with the results found in previous works,²⁶ where two different Mn—O distances (2.18 and 2.49 Å) for the $5\text{Mn}^{2+}/\text{BR}$ sample are observed, in contrast with the single distance of 2.17 Å found after the retinal extraction that induce tertiary structural changes in the protein. This implies the existence of at least two different geometries for cation binding sites, in agreement also with other authors.²⁵

Several works have shown the existence of water molecules in the extracellular region of the membrane forming a hydrogen-bonded network with key residues.^{33,57} This network permits to transmit protonation changes and to conduct the proton. More recently it was proposed that an H_5O_2^+ complex stabilized by Glu194[−] and Glu204[−] is responsible for the proton release.³⁴ In this sense, it is possible that the presence of cations in coordination with these two residues, as we propose, could have an important role in the stabilization and/or in the dynamics of this complex.

REFERENCES

- Lanyi JK. X-ray crystallography of bacteriorhodopsin and its photointermediates: insights into the mechanism of proton transport. *Biochemistry (Moscow)* 2001;66:1192–1196.
- Hirai T, Subramaniam S. Structural insights into the mechanism of proton pumping by bacteriorhodopsin. *FEBS Lett* 2003;545:2–8.
- Dracheva S, Bose S, Hendler RW. Chemical and functional studies on the importance of purple membrane lipids in BR photocycle behavior. *FEBS Lett* 1996;382:209–212.
- Kimura Y, Ikegami A, Stoekenius W. Salt and pH-dependent changes of the purple membrane absorption spectrum. *Photochem Photobiol* 1984;40:641–646.
- Chang CH, Chen JG, Govindjee R, Ebrey T. Cation binding by BR. *Proc Natl Acad Sci USA* 1985;82:396–400.
- Griffiths JA, King J, Yang DF, Browner R, El-Sayed MA. Calcium and magnesium binding in native and structurally perturbed purple membrane. *J Phys Chem* 1996;100:929–933.
- Duñach M, Seigneuret M, Rigaud JL, Padrós E. Characterization of the cation binding sites of the purple membrane. Electron spin resonance and flash photolysis studies. *Biochemistry* 1987;26:1179–1186.
- Ariki M, Lanyi JK. Characterization of metal ion-binding sites in bacteriorhodopsin. *J Biol Chem* 1986;261:8167–8174.
- Chang CH, Jonas R, Melchiorre S, Govindjee R, Ebrey TG. Mechanism and role of divalent cation binding of bacteriorhodopsin. *Biophys J* 1986;49:731–739.
- Szundi I, Stoekenius W. Surface pH controls purple-to-blue transition of bacteriorhodopsin. A theoretical model of purple membrane surface. *Biophys J* 1989;56:369–383.
- Szundi I, Stoekenius W. Effect of lipid surface charges on the purple-to-blue transition of bacteriorhodopsin. *Proc Natl Acad Sci USA* 1987;84:3681–3684.
- Szundi I, Stoekenius W. Purple-to-blue transition of bacteriorhodopsin in a neutral lipid environment. *Biophys J* 1988;54:227–232.
- Varo G, Brown LS, Needleman R, Lanyi JK. Binding of calcium ions to bacteriorhodopsin. *Biophys J* 1999;76:3219–3226.
- Tuzi S, Yamaguchi S, Tanio M, Konishi H, Inoue S, Naito A, Needleman R, Lanyi JK, Saito H. Location of cation binding site in the loop between helices F and G of BR, as studied by ¹³C-NMR. *Biophys J* 1999;1523–1531.
- Eliash T, Weiner L, Ottolenghi M, Sheves M. Specific binding sites for cations in bacteriorhodopsin. *Biophys J* 2001;81:1155–1162.
- Sanz C, Marquez M, Perálvarez A, Elouatik S, Sepulcre F, Querol E, Lazarova T, Padrós E. Contribution of extracellular Glu residues to the structure and function of BR. *J Biol Chem* 2001;276:40788–40794.
- Jonas R, Ebrey TG. Binding of a single divalent cation directly correlates with the blue-to-purple transition in BR. *Proc Natl Acad Sci USA* 1991;88:149–153.
- Zhang YN, Sweetman LL, Awad ES, El-Sayed A. Nature of the individual Ca^{2+} binding sites in Ca^{2+} -regenerated BR. *Biophys J* 1992;61:1201–1206.
- Tan EHL, Govender DSK, Birge RR. Large organic cations can replace Mg^{2+} and Ca^{2+} ions in BR and maintain proton pumping ability. *J Am Chem Soc* 1996;118:2752–2753.
- Pardo L, Sepulcre F, Cladera J, Duñach M, Labarta A, Tejada J, Padrós E. Experimental and theoretical characterization of the high-affinity cation-binding site of the purple membrane. *Biophys J* 1998;75:777–784.
- Sepulcre F, Cladera J, García J, Proietti MG, Torres J, Padrós E. An EXAFS study of the high-affinity cation-binding site in the purple membrane. *Biophys J* 1996;70:852–856.
- Sepulcre F, Proietti MG, Benfatto M, Della LS, García J, Padrós E. A quantitative XANES analysis of the calcium high-affinity binding site of the purple membrane. *Biophys J* 2004;87:513–520.
- Stuart JA, Vought BW, Zhang C, Birge RR. The active site of BR. Two-photon spectroscopic evidence for a positively charged chromophore binding site mediated by calcium. *Biospectroscopy* 1995;1:9–28.
- Zhang KE, Song L, Dong J, El-Sayed MA. Studies of cation binding in ZnCl_2 -regenerated bacteriorhodopsin by X-ray absorption fine structures: effects of removing water molecules and adding Cl^- ions. *Biophys J* 1997;73:2097–2105.
- Heyes CD, Wang J, Sani LS, El-Sayed MA. Fourier transform infrared study of the effect of different cations on bacteriorhodopsin protein thermal stability. *Biophys J* 2002;82:1598–1606.
- Sepulcre F, Proietti MG, Benfatto M, Della Longa S, García J, Padrós E. An XAS study of the cation binding sites in the purple membrane of *Halobacterium salinarum*. *Phys Scr T* 2005;115:855–858.
- Oesterheld T, Stoekenius W. Isolation of the cell membrane of *Halobacterium halobium* and its fractionation into red and purple membrane. *Methods Enzymol* 1974;31:667–678.

28. Juncosa M, Pons J, Planas A, Querol E. Improved efficiency in site-directed mutagenesis by PCR using *Pyrococcus sp.* GB-D polymerase. *BioTechniques* 1994;16:820–821.
29. Frahm R. New method for time dependent x-ray absorption studies. *Rev Sci Instrum* 1989;60:2515–2518.
30. Solé VA, Gauthier G, Goulon J, Natali F. Undulator QEXAFS at the ESRF beamline ID26. *J Synchrotron Radiat* 1999;6:174–175.
31. Bornebusch H, Clause BS, Steffensen G, Lützenkirchen-Hecht D, Frahm R. A new approach for QEXAFS data acquisition. *J Synchrotron Radiat* 1999;6:209–211.
32. Berman HM, Westbrook J, Feng Z, Gilliland G, Bha TN, Weissig H, Shindyalov IN, Bourne PE. The protein data bank. *Nucleic Acids Res* 2000;28:235–242.
33. Lueke H, Schobert B, Richter HT, Cartailier JP, Lanyi JK. Structure of bacteriorhodopsin at 1.55 Angstrom resolution. *J Mol Biol* 1999;291:899–911.
34. Garczarek, F, Brown LS, Lanyi JK Gerwet K. Proton binding within a membrane protein by a protonated water cluster. *Proc Natl Acad Sci USA* 2005;102:3633–3638.
35. GRIND Version 21.0. Molecular Discovery Ltd., Oxford. 2003.
36. Goodford PJ. A computational procedure for determining energetically favorable binding sites on biologically important macromolecules. *J Med Chem* 1985;28:849–857.
37. AMBER 5. University of California, San Francisco. 1997.
38. Pearlman DA, Case DA, Caldwell JW, Ross WR, Cheatham TE, DeBolt S, Ferguson D, Seibel G, Kollman P. AMBER, a computer program for applying molecular mechanics, normal mode analysis, molecular dynamics and free energy calculations to elucidate the structures and energies of molecules. *Comput Phys Commun* 1995;91:1–41.
39. Wang JM, Cieplak P, Kollman PA. How well does a restrained electrostatic potential (Resp) model perform in calculating conformational energies of organic and biological molecules. *J Comput Chem* 2000;21:1049–1074.
40. Bradbrook GM, Gleichmann T, Harrop SJ, Habash J, Raftery J, Kalb J, Yariv J, Hillier IH, Helliwell JR. X-ray and molecular-dynamics studies of Concanavalin-A glucoside and mannoside complexes: relating structure to thermodynamics of binding. *J Chem Soc Faraday Trans* 1998;94:1603–1611.
41. Aqvist J. Ion water interaction potentials derived from free-energy perturbation simulations. *J Phys Chem* 1990;94:8021–8024.
42. Babu CS, Lim C. Empirical force fields for biologically active divalent metal cations in water. *J Phys Chem A* 2006;110:691–699.
43. Jorgensen WL, Chandrasekhar J, Madura JD, Impey RW, Klein ML. Comparison of simple potential functions for simulating liquid water. *J Chem Phys* 1983;79:926–935.
44. Hayashi S, Tajkhorshid E, Schulten K. Structural changes during the formation of early intermediates in the BR photocycle. *Biophys J* 2002;83:1281–1297.
45. Berendsen HJC, Postma JPM, DiNola S, Haak JR. Molecular dynamics with coupling to an external bath. *J Chem Phys* 1984;81:3684–3690.
46. Helm L, Merbach AE. Water exchange on metal ions: experiments and simulations. *Coord Chem Rev* 1999;187:151–181.
47. Ankudinov A, Ravel B, Rehr JJ, Conradson SD. Real-space multiple-scattering calculation and interpretation of X-ray-absorption near edge structure. *Phys Rev B* 1998;58:7565–7576.
48. Newville M. IFEFFIT: interactive XAFS analysis and FEFF fitting. *J Synchrotron Radiat* 2001;8:322–324.
49. Ravel B, Newville M. ATHENA, ARTEMIS, HEPHAESTUS: data analysis for x-ray absorption spectroscopy using IFEFFIT. *J Synchrotron Radiat* 2005;12:537–541.
50. Sevilano E, Meuth H, Rehr JJ. Extended x-ray absorption fine structure Debye-Waller factors. I. Monoatomic crystals. *Phys Rev B* 1979;41:8139–8149.
51. Hsiu-An Chu, Gardner MT, O'Brien JP, Babcock GT. Low-frequency Fourier transform infrared spectroscopy of the oxygen-evolving and quinone acceptor complexes in photosystem II. *Biochemistry* 1999;38:4533–4541.
52. Subías G, García J, Proietti MG, Blasco J. X-ray-absorption near-edge spectroscopy and circular magnetic X-ray dichroism at the Mn K edge of magnetoresistive manganites. *Phys Rev B* 1997; 68:8183–8191.
53. Sreerama SG, Pal S, Pal S. A trigonal prismatic Mn(II) complex, [MnL(H₂O)](2⁺), with bis(picolinylidenehydrazyl)(2-pyridyl)methane (L). Synthesis, structure and properties. *Inorg Chem Commun* 2001;4:656–660.
54. Duñach M, Seigneuret M, Rigaud JL, Padrós E. Influence of cations on the blue to purple transition of bacteriorhodopsin. Comparison of Ca²⁺ and Hg²⁺ binding and their effect on the surface potential. *J Biol Chem* 1988;263:17378–17384.
55. Yang D, El-Sayed MA. The Ca²⁺ binding to deionized monomerized and to retinal removed bacteriorhodopsin. *Biophys J* 1995;69: 2056–2059.
56. Wang J, El-Sayed MA. The effect of metal cations binding on the protein, lipid and retinal isomeric ratio in regenerated bacteriorhodopsin of purple membrane. *Photochem Photobiol* 2001;73:564–571.
57. Dencher NA, Sass HJ, Buldt G. Water and bacteriorhodopsin: structure, dynamics, and function. *Biochim Biophys Acta* 2000; 1460:192–203.

Chapter 4 – Conclusions

Chapter 4 - Conclusions

1.- Both the statistical ensemble and the type of treatment for long-range electrostatics affect the quality of the results regarding membrane protein MD simulations. The use of a cutoff to treat electrostatic interactions affects the description of some properties of the system including lipid bilayer thickness (similarly to what has already been reported for pure bilayers) and the distribution of ions. The use of the PME method provides a better description of lipids and ions but at a higher computational cost. Additionally, present results suggest that the use of NPT is necessary for the bilayer equilibration and for the process involving the bilayer rearrangement around the protein.

2.- The protein infers an ordering effect over the lipid bilayer that depends on the difference between the equilibrium thickness of the former and the hydrophobic thickness of the latter. This is reflected in the variation of the bilayer thickness with the distance from the protein. Moreover, lipids with saturated acyl chains evidence a poorer adaptation to the protein than lipids with unsaturated chains. Similarly, short acyl chains also show an impaired matching because of the extended conformations that are forced to adopt to accommodate to the hydrophobic protein surface.

3.- Both the interaction with lipid molecules and other proteins can modulate the structure of Rho by affecting the protein tilt as a rigid body and the motions involving helix kinks and tilts. However, the secondary elements of the protein are less sensitive to the environment. Specifically, whereas TM helices remain relatively unaltered with only the least structured secondary elements showing sensitivity to the environment, the conformations of the cytoplasmic loops and of the C-terminus are modulated by the interacting lipids/proteins. The alterations

can extend to the cytoplasmic side of neighboring helices, including the electrostatic lock between TM3 and TM6.

4.- The use of MD permitted to study the specific lipid-protein contacts at an atomistic level. Specifically, almost a third of the Rho residues participate in interactions with the surrounding lipids, mostly those with non-polar bulky side chains. Regarding the electrostatic contribution, a set of residues in Rho have been revealed to form hydrogen bonds with lipid oxygens that can be important for the anchoring of the protein to the membrane. The localization of these interactions is asymmetric regarding the two halves of the protein, suggesting that the cytoplasmic side of the protein is much more sensitive to the lipidic environment.

5.- A MD simulation has been performed with the aim to obtain an optimized rearrangement of a Rho dimer based on a semi-empirical model published in the literature. The analysis of the structure points to a certain asymmetry in the quaternary structure of the dimer due to the different conformation of the loops C2, C3 and E2 in the two subunits, creating subtle differences in the side chain interactions between subunits and ultimately altering some tilt and kink angles. Additionally, the regions and residues that play the most important role for the stability of the dimer have been characterized. The most important subunit-subunit interactions involve loops C2 and E2, and following these TM4 and TM5 although less important.

6.- MD simulations of membranes with different types of cations indicate that they bind to DPPC bilayers increasing lipid order, i.e. giving thicker bilayers and consequently smaller areas per lipid. The ions are being distributed in the lipid-water interface generating a double layer, organized in such a way that the positive ions sit closer to the bilayer interface and the negative ones much further. Potassium chloride is one exception that exhibits a different behavior by not

showing any binding to the lipid head-groups. The effects can be rationalized in terms of the specific properties of the different ions including: charge, radius, coordination numbers and hydration energies. The presence of ions gives a larger electrostatic potential across the membrane/water interface, although the different contributions tend to compensate each other and result only in a small net potential drop.

7.- The combination of MD simulations and site-directed mutagenesis experiments permitted to identify the interactions R135-E247 and R135-T251, between TM3 and TM6, as crucial in order to keep Rho in the inactive state. Additionally, R135-E134 interaction is important so that R135 adopts the necessary conformation that favors the previous interaction. The results suggest that the mutation of these residues can affect the Rho activation process by: i) alleviating the network of interactions in the region around the ERY motif, favoring activation, and/or ii) altering the conformation of the third loop, disrupting the interaction with the G-protein.

8.- The study of the methylation of retinal at position C7 indicated that the modification not only introduced an additional steric volume in the cavity, but also modulated significantly the conformation of the β -ionone ring relative to the polyene chain, which changed from a more co-planar conformation in the case of Rho to an almost perpendicular conformation in the case of 7-methyl-Rho. This together with the induced alterations on the residues forming the binding site can result in a partially blocked transition to the active metaRholl.

9.- The putative Mn^{2+} binding sites of BR have been studied by combining theoretical calculations with experimental EXAFS data, under the assumption that Mn^{2+} and Ca^{2+} binding sites are the same for both metals. The local environment of all these clusters is formed by carboxyl side chains of aspartic acid and glutamic acid residues. The results delineate the presence of at least two binding

sites for Mn^{2+} in the purple membrane: one internal high-affinity site located in the vicinity of D85 and D212, and an external site of lower affinity located near E194 and E204.

10.- It is shown that MD is able to provide structural and dynamical information about membranes and membrane proteins not accessible from experimental methods. The use of an explicit lipidic environment is crucial for the study of the dynamics of protein as well as for the protein-protein and lipid-protein interactions. The combination of the OPLS-AA force field together with the lipid parameters developed by Berger et al. adopted in this study resulted to produce realistic results both for the protein and the lipids as well as for the remaining components of the system.

Bibliography

Bibliography

- Akutsu H, Seelig J. 1981. Interaction of Metal-Ions with Phosphatidylcholine Bilayer-Membranes. *Biochemistry* 20(26):7366-7373.
- Albeck A, Friedman N, Ottolenghi M, Sheves M, Einterz CM, Hug SJ, Lewis JW, Kliger DS. 1989. Photolysis intermediates of the artificial visual pigment cis-5,6-dihydro-isorhodopsin. *Biophys J* 55(2):233-41.
- Allen MP, Tildesley DJ. 1987. Computer simulations of liquids. Oxford University Press, Oxford, New York.
- Altenbach C, Seelig J. 1984. Ca²⁺ binding to phosphatidylcholine bilayers as studied by deuterium magnetic resonance. Evidence for the formation of a Ca²⁺ complex with two phospholipid molecules. *Biochemistry* 23(17):3913-20.
- Alvarez R, Dominguez M, Pazos Y, Sussman F, de Lera AR. 2003. (9Z)- and (11Z)-8-methylretinals for artificial visual pigment studies: stereoselective synthesis, structure, and binding models. *Chemistry* 9(23):5821-31.
- Anézo C, de Vries AH, Holtje HD, Tieleman DP, Marrink SJ. 2003. Methodological issues in lipid bilayer simulations. *J. Phys. Chem. B* 107(35):9424-9433.
- Angers S, Salahpour A, Bouvier M. 2002. Dimerization: an emerging concept for G protein-coupled receptor ontogeny and function. *Annu Rev Pharmacol Toxicol* 42:409-35.
- Åqvist J. 1990. Ion Water Interaction Potentials Derived from Free-Energy Perturbation Simulations. *Journal of Physical Chemistry* 94(21):8021-8024.
- Åqvist J. 1994. Comment on Transferability of Ion Models. *Journal of Physical Chemistry* 98(33):8253-8255.
- Åqvist J, Luzhkov V. 2000. Ion permeation mechanism of the potassium channel. *Nature* 404(6780):881-4.
- Archer E, Maigret B, Escrieut C, Pradayrol L, Fourmy D. 2003. Rhodopsin crystal: new template yielding realistic models of G-protein-coupled receptors? *Trends Pharmacol. Sci.* 24(1):36-40.
- Ariki M, Lanyi JK. 1986. Characterization of Metal Ion-Binding Sites in Bacteriorhodopsin. *Journal of Biological Chemistry* 261(18):8167-8174.
- Arnis S, Fahmy K, Hofmann KP, Sakmar TP. 1994. A conserved carboxylic acid group mediates light-dependent proton uptake and signaling by rhodopsin. *J Biol Chem* 269(39):23879-81.
- Ash WL, Zlomislic MR, Oloo EO, Tieleman DP. 2004. Computer simulations of membrane proteins. *Biochim. Biophys. Acta* 1666(1-2):158-189.
- Attwood TK, Findlay JB. 1994. Fingerprinting G-protein-coupled receptors. *Protein Eng* 7(2):195-203.
- Auffinger P, Beveridge DL. 1995. A Simple Test for Evaluating the Truncation Effects in Simulations of Systems Involving Charged Groups. *Chemical Physics Letters* 234(4-6):413-415.

- Babu CS, Lim C. 2006. Empirical force fields for biologically active divalent metal cations in water. *J Phys Chem A* 110(2):691-9.
- Bachar M, Brunelle P, Tieleman DP, Rauk A. 2004. Molecular dynamics simulation of a polyunsaturated lipid bilayer susceptible to lipid peroxidation. *J. Phys. Chem. B* 108(22):7170-7179.
- Ballesteros J, Kitanovic S, Guarnieri F, Davies P, Fromme BJ, Konvicka K, Chi L, Millar RP, Davidson JS, Weinstein H and others. 1998. Functional microdomains in G-protein-coupled receptors. The conserved arginine-cage motif in the gonadotropin-releasing hormone receptor. *J Biol Chem* 273(17):10445-53.
- Ballesteros JA, Jensen AD, Liapakis G, Rasmussen SG, Shi L, Gether U, Javitch JA. 2001. Activation of the beta 2-adrenergic receptor involves disruption of an ionic lock between the cytoplasmic ends of transmembrane segments 3 and 6. *J. Biol. Chem.* 276(31):29171-7.
- Ballesteros JA, Weinstein H. 1995. Integrated Methods for Modeling G-Protein Coupled Receptors. *Methods Neurosci.* 25:366-428.
- Baumketner A, Shea JE. 2005. The influence of different treatments of electrostatic interactions on the thermodynamics of folding of peptides. *J. Phys. Chem. B* 109(45):21322-21328.
- Beck DA, Armen RS, Daggett V. 2005. Cutoff size need not strongly influence molecular dynamics results for solvated polypeptides. *Biochemistry* 44(2):609-16.
- Berendsen HJC, Grigera JR, Straatsma TP. 1987. The Missing Term in Effective Pair Potentials. *Journal of Physical Chemistry* 91(24):6269-6271.
- Berendsen HJC, Postma JPM, DiNola A, Haak JR. 1984. Molecular dynamics with coupling to an external bath. *J. Chem. Phys.* 81:3684.
- Berendsen HJC, van der Spoel D, van Drunen R. 1995. Gromacs - a Message-Passing Parallel Molecular-Dynamics Implementation. *Comput. Phys. Commun.* 91(1-3):43-56.
- Berger O, Edholm O, Jähnig F. 1997. Molecular dynamics simulations of a fluid bilayer of dipalmitoylphosphatidylcholine at full hydration, constant pressure, and constant temperature. *Biophys. J.* 72(5):2002-2013.
- Berkowitz ML, Bostick DL, Pandit S. 2006. Aqueous solutions next to phospholipid membrane surfaces: Insights from simulations. *Chem. Rev.* 106(4):1527-1539.
- Berman HM, Westbrook J, Feng Z, Gilliland G, Bhat TN, Weissig H, Shindyalov IN, Bourne PE. 2000. The Protein Data Bank. *Nucleic Acids Res* 28(1):235-42.
- Binder H, Zschornig O. 2002. The effect of metal cations on the phase behavior and hydration characteristics of phospholipid membranes. *Chem. Phys. Lipids* 115(1-2):39-61.
- Böckmann RA, Grubmüller H. 2004. Multistep binding of divalent cations to phospholipid bilayers: a molecular dynamics study. *Angew. Chem. Int. Ed. Engl.* 43(8):1021-4.
- Böckmann RA, Hac A, Heimburg T, Grubmüller H. 2003. Effect of sodium chloride on a lipid bilayer. *Biophys. J.* 85(3):1647-1655.
- Bond PJ, Sansom MS. 2006. Insertion and assembly of membrane

- proteins via simulation. *J. Am. Chem. Soc.* 128(8):2697-704.
- Boyd D, Schierle C, Beckwith J. 1998. How many membrane proteins are there? *Protein Science* 7(1):201-205.
- Brooks BR, Bruccoleri RE, Olafson BD, States DJ, Swaminathan S, Karplus M. 1983. Charmm - a Program for Macromolecular Energy, Minimization, and Dynamics Calculations. *J. Comput. Chem.* 4(2):187-217.
- Brown MF, Seelig J. 1977. Ion-Induced Changes in Head Group Conformation of Lecithin Bilayers. *Nature* 269(5630):721-723.
- Bulenger S, Marullo S, Bouvier M. 2005. Emerging role of homo- and heterodimerization in G-protein-coupled receptor biosynthesis and maturation. *Trends Pharmacol Sci* 26(3):131-7.
- Carrillo-Tripp M, Feller SE. 2005. Evidence for a mechanism by which omega-3 polyunsaturated lipids may affect membrane protein function. *Biochemistry* 44(30):10164-9.
- Case DA, Cheatham TE, Darden T, Gohlke H, Luo R, Merz KM, Onufriev A, Simmerling C, Wang B, Woods RJ. 2005. The Amber biomolecular simulation programs. *Journal of Computational Chemistry* 26(16):1668-1688.
- Chang CH, Chen JG, Govindjee R, Ebrey T. 1985. Cation Binding by Bacteriorhodopsin. *Proceedings of the National Academy of Sciences of the United States of America* 82(2):396-400.
- Chang CH, Jonas R, Melchiorre S, Govindjee R, Ebrey TG. 1986. Mechanism and Role of Divalent-Cation Binding of Bacteriorhodopsin. *Biophysical Journal* 49(3):731-739.
- Cheatham TE, Miller JL, Fox T, Darden TA, Kollman PA. 1995. Molecular-Dynamics Simulations on Solvated Biomolecular Systems - the Particle Mesh Ewald Method Leads to Stable Trajectories of DNA, Rna, and Proteins. *J. Am. Chem. Soc.* 117(14):4193-4194.
- Cherezov V, Rosenbaum DM, Hanson MA, Rasmussen SG, Thian FS, Kobilka TS, Choi HJ, Kuhn P, Weis WI, Kobilka BK and others. 2007. High-Resolution Crystal Structure of an Engineered Human β 2-Adrenergic G Protein Coupled Receptor. *Science*.
- Clarke RJ, Lufert C. 1999. Influence of anions and cations on the dipole potential of phosphatidylcholine vesicles: A basis for the Hofmeister effect. *Biophys. J.* 76(5):2614-2624.
- Cohen GB, Yang T, Robinson PR, Oprian DD. 1993. Constitutive activation of opsin: influence of charge at position 134 and size at position 296. *Biochemistry* 32(23):6111-5.
- Cone RA. 1972. Rotational diffusion of rhodopsin in the visual receptor membrane. *Nat New Biol* 236(63):39-43.
- Cramer CJ. 2002. *Essentials of Computational Chemistry. Theories and Models.* Wiley, Chichester, England.
- Crozier PS, Stevens MJ, Forrest LR, Woolf TB. 2003. Molecular dynamics simulation of dark-adapted rhodopsin in an explicit membrane bilayer: Coupling between local retinal and larger scale conformational change. *J. Mol. Biol.* 333(3):493-514.
- Cunningham BA, Gelerinter E, Lis LJ. 1988. Mono-Valent Ion-Phosphatidylcholine Interactions - an Electron-Paramagnetic

- Resonance Study. *Chem. Phys. Lipids* 46(3):205-211.
- Darden T, York D, Pedersen L. 1993. Particle Mesh Ewald - an $N \cdot \log(N)$ Method for Ewald Sums in Large Systems. *J. Chem. Phys.* 98(12):10089-10092.
- Deol SS, Bond PJ, Domene C, Sansom MS. 2004. Lipid-protein interactions of integral membrane proteins: a comparative simulation study. *Biophys. J.* 87(6):3737-49.
- Deupi X, Olivella M, Govaerts C, Ballesteros JA, Campillo M, Pardo L. 2004. Ser and Thr residues modulate the conformation of pro-kinked transmembrane alpha-helices. *Biophys. J.* 86(1):105-115.
- Dracheva S, Bose S, Hendler RW. 1996. Chemical and functional studies on the importance of purple membrane lipids in bacteriorhodopsin photocycle behavior. *Febs Letters* 382(1-2):209-212.
- Dumas F, Lebrun MC, Tocanne JF. 1999. Is the protein/lipid hydrophobic matching principle relevant to membrane organization and functions? *Febs Letters* 458(3):271-277.
- Dunach M, Seigneuret M, Rigaud JL, Padros E. 1987. Characterization of the Cation Binding-Sites of the Purple Membrane - Electron-Spin-Resonance and Flash-Photolysis Studies. *Biochemistry* 26(4):1179-1186.
- Edholm O, Berger O, Jähnig F. 1995. Structure and Fluctuations of Bacteriorhodopsin in the Purple Membrane - a Molecular-Dynamics Study. *Journal of Molecular Biology* 250(1):94-111.
- Eliash T, Weiner L, Ottolenghi M, Sheves M. 2001. Specific binding sites for cations in bacteriorhodopsin. *Biophys. J.* 81(2):1155-62.
- Ellis C. 2004. The state of GPCR research in 2004. *Nat. Rev. Drug Discov.* 3(7):575, 577-626.
- Elmore DE. 2006. Molecular dynamics simulation of a phosphatidylglycerol membrane. *FEBS Lett.* 580(1):144-8.
- Engelman DM. 2005. Membranes are more mosaic than fluid. *Nature* 438(7068):578-580.
- Fanelli F, De Benedetti PG. 2005. Computational modeling approaches to structure-function analysis of G protein-coupled receptors. *Chem Rev* 105(9):3297-351.
- Farrens DL, Altenbach C, Yang K, Hubbell WL, Khorana HG. 1996. Requirement of rigid-body motion of transmembrane helices for light activation of rhodopsin. *Science* 274(5288):768-70.
- Feller SE. 2000. Molecular dynamics simulations of lipid bilayers. *Curr. Opin. Struct. Biol.* 5(3-4):217-223.
- Feller SE, Gawrisch K, MacKerell AD, Jr. 2002. Polyunsaturated fatty acids in lipid bilayers: intrinsic and environmental contributions to their unique physical properties. *J. Am. Chem. Soc.* 124(2):318-26.
- Feller SE, Gawrisch K, Woolf TB. 2003. Rhodopsin exhibits a preference for solvation by polyunsaturated docosahexaenoic acid. *J. Am. Chem. Soc.* 125(15):4434-5.
- Feller SE, Pastor RW, Rojnuckarin A, Bogusz S, Brooks BR. 1996. Effect of electrostatic force truncation on interfacial and transport properties of water. *Journal of Physical Chemistry* 100(42):17011-17020.
- Filipek S, Krzysko KA, Fotiadis D, Liang Y, Saperstein DA, Engel A, Palczewski K. 2004. A concept for

- G protein activation by G protein-coupled receptor dimers: the transducin/rhodopsin interface. *Photochem Photobiol Sci* 3(6):628-38.
- Filipek S, Stenkamp RE, Teller DC, Palczewski K. 2003. G protein-coupled receptor rhodopsin: a prospectus. *Annu Rev Physiol* 65:851-79.
- Filipek S, Teller DC, Palczewski K, Stenkamp R. 2003. The crystallographic model of rhodopsin and its use in studies of other G protein-coupled receptors. *Annu Rev Biophys Biomol Struct* 32:375-97.
- Filizola M, Wang SX, Weinstein H. 2006. Dynamic models of G-protein coupled receptor dimers: indications of asymmetry in the rhodopsin dimer from molecular dynamics simulations in a POPC bilayer. *J Comput Aided Mol Des* 20(7-8):405-16.
- Filizola M, Weinstein H. 2005. The structure and dynamics of GPCR oligomers: A new focus in models of cell-signaling mechanisms and drug design. *Current Opinion in Drug Discovery & Development* 8(5):577-584.
- Fishkin N, Berova N, Nakanishi K. 2004. Primary events in dim light vision: a chemical and spectroscopic approach toward understanding protein/chromophore interactions in rhodopsin. *Chem Rec* 4(2):120-35.
- Fotiadis D, Jastrzebska B, Philippsen A, Muller DJ, Palczewski K, Engel A. 2006. Structure of the rhodopsin dimer: a working model for G-protein-coupled receptors. *Curr Opin Struct Biol* 16(2):252-9.
- Fotiadis D, Liang Y, Filipek S, Saperstein DA, Engel A, Palczewski K. 2003. Atomic-force microscopy: Rhodopsin dimers in native disc membranes. *Nature* 421(6919):127-8.
- Fotiadis D, Liang Y, Filipek S, Saperstein DA, Engel A, Palczewski K. 2004. The G protein-coupled receptor rhodopsin in the native membrane. *FEBS Lett* 564(3):281-8.
- Franke RR, Konig B, Sakmar TP, Khorana HG, Hofmann KP. 1990. Rhodopsin mutants that bind but fail to activate transducin. *Science* 250(4977):123-5.
- Frenkel D, Smit B. 1996. *Understanding Molecular Simulation. From Algorithms to Applications*. Academic Press, San Diego, USA.
- Fujimoto Y, Fishkin N, Pescitelli G, Decatur J, Berova N, Nakanishi K. 2002. Solution and biologically relevant conformations of enantiomeric 11-cis-locked cyclopropyl retinals. *Journal of the American Chemical Society* 124(25):7294-7302.
- Fujimoto Y, Ishihara J, Maki S, Fujioka N, Wang T, Furuta T, Fishkin N, Borhan B, Berova N, Nakanishi K. 2001. On the bioactive conformation of the rhodopsin chromophore: Absolute sense of twist around the 6-s-cis bond. *Chemistry-a European Journal* 7(19):4198-4204.
- Ganchev DN, Rijkers DTS, Snel MME, Killian JA, de Kruijff B. 2004. Strength of integration of transmembrane alpha-helical peptides in lipid bilayers as determined by atomic force spectroscopy. *Biochemistry* 43(47):14987-14993.
- Garcia-Manyes S, Oncins G, Sanz F. 2005. Effect of ion-binding and chemical phospholipid structure on the nanomechanics of lipid bilayers studied by force

- spectroscopy. *Biophys. J.* 89(3):1812-1826.
- Gazi L, Lopez-Gimenez JF, Strange PG. 2002. Formation of oligomers by G protein-coupled receptors. *Curr Opin Drug Discov Devel* 5(5):756-63.
- George SR, O'Dowd BF, Lee SP. 2002. G-protein-coupled receptor oligomerization and its potential for drug discovery. *Nat Rev Drug Discov* 1(10):808-20.
- Gether U, Ballesteros JA, Seifert R, SandersBush E, Weinstein H, Kobilka BK. 1997. Structural instability of a constitutively active G protein-coupled receptor - Agonist-independent activation due to conformational flexibility. *Journal of Biological Chemistry* 272(5):2587-2590.
- Gilson MK. 1995. Theory of electrostatic interactions in macromolecules. *Curr. Opin. Struct. Biol.* 5(2):216-23.
- Gomes I, Jordan BA, Gupta A, Rios C, Trapaidze N, Devi LA. 2001. G protein coupled receptor dimerization: implications in modulating receptor function. *Journal of Molecular Medicine-Jmm* 79(5-6):226-242.
- Goodyear DJ, Sharpe S, Grant CW, Morrow MR. 2005. Molecular dynamics simulation of transmembrane polypeptide orientational fluctuations. *Biophys. J.* 88(1):105-17.
- Govaerts C, Lefort A, Costagliola S, Wodak SJ, Ballesteros JA, Van Sande J, Pardo L, Vassart G. 2001. A conserved Asn in transmembrane helix 7 is an on/off switch in the activation of the thyrotropin receptor. *J. Biol. Chem.* 276(25):22991-9.
- Greasley PJ, Fanelli F, Rossier O, Abuin L, Cotecchia S. 2002. Mutagenesis and modelling of the alpha(1b)-adrenergic receptor highlight the role of the helix 3/helix 6 interface in receptor activation. *Mol Pharmacol* 61(5):1025-32.
- Griffiths JA, King J, Yang DF, Browner R, ElSayed MA. 1996. Calcium and magnesium binding in native and structurally perturbed purple membrane. *Journal of Physical Chemistry* 100(3):929-933.
- Grossfield A, Feller SE, Pitman MC. 2006. A role for direct interactions in the modulation of rhodopsin by omega-3 polyunsaturated lipids. *Proc. Natl. Acad. Sci. U.S.A.* 103(13):4888-93.
- Grossfield A, Woolf TB. 2002. Interaction of tryptophan analogs with POPC lipid bilayers investigated by molecular dynamics calculations. *Langmuir* 18(1):198-210.
- Guidotti G. 1972. Membrane Proteins. *Annual Review of Biochemistry* 41:731-&.
- Guillot B. 2002. A reappraisal of what we have learnt during three decades of computer simulations on water. *Journal of Molecular Liquids* 101(1-3):219-260.
- Gurtovenko AA. 2005. Asymmetry of lipid bilayers induced by monovalent salt: Atomistic molecular-dynamics study. *J. Chem. Phys.* 122(24):-.
- Gurtovenko AA, Patra M, Karttunen M, Vattulainen I. 2004. Cationic DMPC/DMTAP lipid bilayers: Molecular dynamics study. *Biophys. J.* 86(6):3461-3472.
- Gurtovenko AA, Vattulainen I. 2007. Ion leakage through transient water pores in protein-free lipid membranes driven by transmembrane ionic charge imbalance. *Biophys J* 92(6):1878-90.
- Haile JM. 1992. *Molecular Dynamics Simulation: Elementary Methods.*

- John Willey & Sons, New York, USA.
- Hanson SM, Gurevich EV, Vishnivetskiy SA, Ahmed MR, Song X, Gurevich VV. 2007. Each rhodopsin molecule binds its own arrestin. *Proc Natl Acad Sci U S A* 104(9):3125-8.
- Harroun TA, Heller WT, Weiss TM, Yang L, Huang HW. 1999a. Experimental evidence for hydrophobic matching and membrane-mediated interactions in lipid bilayers containing gramicidin. *Biophys. J.* 76(2):937-945.
- Harroun TA, Heller WT, Weiss TM, Yang L, Huang HW. 1999b. Theoretical analysis of hydrophobic matching and membrane-mediated interactions in lipid bilayers containing gramicidin. *Biophys. J.* 76(6):3176-3185.
- Hauser H, Shipley GG. 1984. Interactions of divalent cations with phosphatidylserine bilayer membranes. *Biochemistry* 23(1):34-41.
- Heinz TN, Hunenberger PH. 2005. Combining the lattice-sum and reaction-field approaches for evaluating long-range electrostatic interactions in molecular simulations. *J. Chem. Phys.* 123(3):34107.
- Henderson R, Baldwin JM, Ceska TA, Zemlin F, Beckmann E, Downing KH. 1990. Model for the Structure of Bacteriorhodopsin Based on High-Resolution Electron Cryomicroscopy. *Journal of Molecular Biology* 213(4):899-929.
- Henderson R, Schertler GF. 1990. The structure of bacteriorhodopsin and its relevance to the visual opsins and other seven-helix G-protein coupled receptors. *Philos Trans R Soc Lond B Biol Sci* 326(1236):379-89.
- Herbette L, Napolitano CA, McDaniel RV. 1984. Direct determination of the calcium profile structure for dipalmitoyllecithin multilayers using neutron diffraction. *Biophys. J.* 46(6):677-85.
- Hess B. 2002. Determining the shear viscosity of model liquids from molecular dynamics simulations. *J. Chem. Phys.* 116(1):209-217.
- Hess B, Bekker H, Berendsen HJC, Fraaije JGEM. 1997. LINC: A linear constraint solver for molecular simulations. *J. Comput. Chem.* 18(12):1463-1472.
- Heyes CD, Wang JP, Sanii LS, El-Sayed MA. 2002. Fourier transform infrared study of the effect of different cations on bacteriorhodopsin protein thermal stability. *Biophysical Journal* 82(3):1598-1606.
- Hirai T, Subramaniam S. 2003. Structural insights into the mechanism of proton pumping by bacteriorhodopsin. *Febs Letters* 545(1):2-8.
- Hofsäß C, Lindahl E, Edholm O. 2003. Molecular dynamics simulations of phospholipid bilayers with cholesterol. *Biophys. J.* 84(4):2192-2206.
- Huang P, Visiers I, Weinstein H, Liu-Chen LY. 2002. The local environment at the cytoplasmic end of TM6 of the mu opioid receptor differs from those of rhodopsin and monoamine receptors: introduction of an ionic lock between the cytoplasmic ends of helices 3 and 6 by a L6.30(275)E mutation inactivates the mu opioid receptor and reduces the constitutive activity of its T6.34(279)K mutant. *Biochemistry* 41(40):11972-80.

- Huber T, Botelho AV, Beyer K, Brown MF. 2004. Membrane model for the G-protein-coupled receptor rhodopsin: Hydrophobic interface and dynamical structure. *Biophys. J.* 86(4):2078-2100.
- Im W, Feig M, Brooks CL, 3rd. 2003. An implicit membrane generalized born theory for the study of structure, stability, and interactions of membrane proteins. *Biophys. J.* 85(5):2900-18.
- Im W, Lee MS, Brooks CL, 3rd. 2003. Generalized born model with a simple smoothing function. *J Comput Chem* 24(14):1691-702.
- Im W, Roux B. 2002. Ion permeation and selectivity of OmpF porin: a theoretical study based on molecular dynamics, Brownian dynamics, and continuum electrodiffusion theory. *J Mol Biol* 322(4):851-69.
- Ishiguro M. 2000. A mechanism of primary photoactivation reactions of rhodopsin: Modeling of the intermediates in the rhodopsin photocycle. *Journal of the American Chemical Society* 122(3):444-451.
- Izvekov S, Voth GA. 2005. Multiscale coarse graining of liquid-state systems. *Journal of Chemical Physics* 123(13):-.
- Jang GF, Kuksa V, Filipek S, Bartl F, Ritter E, Gelb MH, Hofmann KP, Palczewski K. 2001. Mechanism of rhodopsin activation as examined with ring-constrained retinal analogs and the crystal structure of the ground state protein. *J Biol Chem* 276(28):26148-53.
- Jastrzebska B, Fotiadis D, Jang GF, Stenkamp RE, Engel A, Palczewski K. 2006. Functional and structural characterization of rhodopsin oligomers. *J Biol Chem* 281(17):11917-22.
- Jayasinghe S, Hristova K, White SH. 2001. MPtopo: A database of membrane protein topology. *Protein Science* 10(2):455-458.
- Jensen MO, Mouritsen OG. 2004. Lipids do influence protein function-the hydrophobic matching hypothesis revisited. *Biochim. Biophys. Acta* 1666(1-2):205-26.
- Jonas R, Ebrey TG. 1991. Binding of a Single Divalent-Cation Directly Correlates with the Blue-to-Purple Transition in Bacteriorhodopsin. *Proceedings of the National Academy of Sciences of the United States of America* 88(1):149-153.
- Jorgensen WL, Chandrasekhar J, Madura JD, Impey RW, Klein ML. 1983. Comparison of Simple Potential Functions for Simulating Liquid Water. *J. Chem. Phys.* 79(2):926-935.
- Jorgensen WL, Maxwell DS, TiradoRives J. 1996. Development and testing of the OPLS all-atom force field on conformational energetics and properties of organic liquids. *J. Am. Chem. Soc.* 118(45):11225-11236.
- Jorgensen WL, Tirado-Rives J. 2005. Potential energy functions for atomic-level simulations of water and organic and biomolecular systems. *Proceedings of the National Academy of Sciences of the United States of America* 102(19):6665-6670.
- Kandasamy SK, Larson RG. 2006. Molecular dynamics simulations of model trans-membrane peptides in lipid bilayers: A systematic investigation of hydrophobic mismatch. *Biophys. J.* 90(7):2326-2343.

- Karplus M. 2003. Molecular dynamics of biological macromolecules: A brief history and perspective. *Biopolymers* 68(3):350-358.
- Killian JA. 2003. Synthetic peptides as models for intrinsic membrane proteins. *Febs Letters* 555(1):134-138.
- Kim JM, Altenbach C, Thurmond RL, Khorana HG, Hubbell WL. 1997. Structure and function in rhodopsin: rhodopsin mutants with a neutral amino acid at E134 have a partially activated conformation in the dark state. *Proc Natl Acad Sci U S A* 94(26):14273-8.
- Kimura Y, Ikegami A, Stoeckenius W. 1984. Salt and Ph-Dependent Changes of the Purple Membrane Absorption-Spectrum. *Photochemistry and Photobiology* 40(5):641-646.
- Klauda JB, Wu X, Pastor RW, Brooks BR. 2007. Long-range Lennard-Jones and electrostatic interactions in interfaces: application of the isotropic periodic sum method. *J Phys Chem B* 111(17):4393-400.
- Kota P, Reeves PJ, Rajbhandary UL, Khorana HG. 2006. Opsin is present as dimers in COS1 cells: identification of amino acids at the dimeric interface. *Proc Natl Acad Sci U S A* 103(9):3054-9.
- Krebs MP, Isenbarger TA. 2000. Structural determinants of purple membrane assembly. *Biochim Biophys Acta* 1460(1):15-26.
- Kristiansen K. 2004. Molecular mechanisms of ligand binding, signaling, and regulation within the superfamily of G-protein-coupled receptors: molecular modeling and mutagenesis approaches to receptor structure and function. *Pharmacol Ther* 103(1):21-80.
- Lague P, Pastor RW, Brooks BR. 2004. Pressure-based long-range correction for Lennard-Jones interactions in molecular dynamics simulations: Application to alkanes and interfaces. *Journal of Physical Chemistry B* 108(1):363-368.
- Lanyi JK, Luecke H. 2001. Bacteriorhodopsin. *Current Opinion in Structural Biology* 11(4):415-419.
- Lau PW, Grossfield A, Feller SE, Pitman MC, Brown MF. 2007. Dynamic structure of retinylidene ligand of rhodopsin probed by molecular simulations. *J Mol Biol* 372(4):906-17.
- Leach AR. 2001. *Molecular Modelling: Principles and Applications*. Longman Group, United Kingdom.
- Lee AG. 2003. Lipid-protein interactions in biological membranes: a structural perspective. *Biochim. Biophys. Acta* 1612(1):1-40.
- Lee AG. 2004. How lipids affect the activities of integral membrane proteins. *Biochimica Et Biophysica Acta-Biomembranes* 1666(1-2):62-87.
- Lee SP, O'Dowd BF, George SR. 2003. Homo- and hetero-oligomerization of G protein-coupled receptors. *Life Sci* 74(2-3):173-80.
- Leekumjorn S, Sum AK. 2006. Molecular simulation study of structural and dynamic properties of mixed DPPC/DPPE bilayers. *Biophys. J.* 90(11):3951-65.
- Lemaitre V, Yeagle P, Watts A. 2005. Molecular dynamics simulations of retinal in rhodopsin: from the dark-adapted state towards lumirhodopsin. *Biochemistry* 44(38):12667-80.
- Lennard-Jones JE. 1931. Cohesion. *Proceedings of the Physical Society* 43:461-482.

- Leontiadou H, Mark AE, Marrink SJ. 2006. Antimicrobial peptides in action. *J. Am. Chem. Soc.* 128(37):12156-61.
- Li J, Edwards PC, Burghammer M, Villa C, Schertler GFX. 2004. Structure of bovine rhodopsin in a trigonal crystal form. *J Mol Biol* 343(5):1409-1438.
- Li J, Huang P, Chen C, de Riel JK, Weinstein H, Liu-Chen LY. 2001. Constitutive activation of the mu opioid receptor by mutation of D3.49(164), but not D3.32(147): D3.49(164) is critical for stabilization of the inactive form of the receptor and for its expression. *Biochemistry* 40(40):12039-50.
- Liang Y, Fotiadis D, Filipek S, Saperstein DA, Palczewski K, Engel A. 2003. Organization of the G protein-coupled receptors rhodopsin and opsin in native membranes. *J. Biol. Chem.* 278(24):21655-21662.
- Liebman PA, Entine G. 1974. Lateral diffusion of visual pigment in photoreceptor disk membranes. *Science* 185(149):457-9.
- Lindahl E, Edholm O. 2000. Mesoscopic undulations and thickness fluctuations in lipid bilayers from molecular dynamics simulations. *Biophys. J.* 79(1):426-433.
- Lindahl E, Hess B, van der Spoel D. 2001. GROMACS 3.0: a package for molecular simulation and trajectory analysis. *J. Mol. Model.* 7(8):306-317.
- Lis LJ, Lis WT, Parsegian VA, Rand RP. 1981. Adsorption of divalent cations to a variety of phosphatidylcholine bilayers. *Biochemistry* 20(7):1771-7.
- Lis LJ, Parsegian VA, Rand RP. 1981. Binding of divalent cations of dipalmitoylphosphatidylcholine bilayers and its effect on bilayer interaction. *Biochemistry* 20(7):1761-70.
- Loncharich RJ, Brooks BR. 1989. The effects of truncating long-range forces on protein dynamics. *Proteins* 6(1):32-45.
- Loosleymillman ME, Rand RP, Parsegian VA. 1982. Effects of Mono-Valent Ion Binding and Screening on Measured Electrostatic Forces between Charged Phospholipid-Bilayers. *Biophys. J.* 40(3):221-232.
- Louise-May S, Auffinger P, Westhof E. 1996. Calculations of nucleic acid conformations. *Curr. Opin. Struct. Biol.* 6(3):289-98.
- Luecke H, Richter HT, Lanyi JK. 1998. Proton transfer pathways in bacteriorhodopsin at 2.3 angstrom resolution. *Science* 280(5371):1934-7.
- Luecke H, Schobert B, Richter HT, Cartailler JP, Lanyi JK. 1999. Structure of Bacteriorhodopsin at 1.55 Angstrom Resolution. *JOURNAL OF MOLECULAR BIOLOGY* 291(4):899-911.
- MacKerell AD, Bashford D, Bellott M, Dunbrack RL, Evanseck JD, Field MJ, Fischer S, Gao J, Guo H, Ha S and others. 1998. All-atom empirical potential for molecular modeling and dynamics studies of proteins. *Journal of Physical Chemistry B* 102(18):3586-3616.
- Mackerell AD, Jr., Feig M, Brooks CL, 3rd. 2004. Extending the treatment of backbone energetics in protein force fields: limitations of gas-phase quantum mechanics in reproducing protein conformational distributions in molecular dynamics simulations. *J Comput Chem* 25(11):1400-15.
- Marrink SJ, Risselada HJ, Yefimov S, Tieleman DP, de Vries AH. 2007. The MARTINI force field: coarse grained model for biomolecular

- simulations. *J Phys Chem B* 111(27):7812-24.
- Marrink SJ, Risselada J, Mark AE. 2005. Simulation of gel phase formation and melting in lipid bilayers using a coarse grained model. *Chem Phys Lipids* 135(2):223-44.
- Martinez-Mayorga K, Pitman MC, Grossfield A, Feller SE, Brown MF. 2006. Retinal counterion switch mechanism in vision evaluated by molecular simulations. *J Am Chem Soc* 128(51):16502-3.
- McBee JK, Palczewski K, Baehr W, Pepperberg DR. 2001. Confronting complexity: the interlink of phototransduction and retinoid metabolism in the vertebrate retina. *Prog Retin Eye Res* 20(4):469-529.
- Milligan G. 2004. G protein-coupled receptor dimerization: function and ligand pharmacology. *Mol Pharmacol* 66(1):1-7.
- Milligan G. 2006. G-protein-coupled receptor heterodimers: pharmacology, function and relevance to drug discovery. *Drug Discov Today* 11(11-12):541-9.
- Milligan G. 2007. G protein-coupled receptor dimerisation: molecular basis and relevance to function. *Biochim Biophys Acta* 1768(4):825-35.
- Min KC, Zvyaga TA, Cypess AM, Sakmar TP. 1993. Characterization of mutant rhodopsins responsible for autosomal dominant retinitis pigmentosa. Mutations on the cytoplasmic surface affect transducin activation. *J Biol Chem* 268(13):9400-4.
- Mishra VK, Palgunachari MN, Segrest JP, Anantharamaiah GM. 1994. Interactions of Synthetic Peptide Analogs of the Class a Amphipathic Helix with Lipids - Evidence for the Snorkel Hypothesis. *J. Biol. Chem.* 269(10):7185-7191.
- Mitra K, Ubarretxena-Belandia I, Taguchi T, Warren G, Engelman DM. 2004. Modulation of the bilayer thickness of exocytic pathway membranes by membrane proteins rather than cholesterol. *Proc. Natl. Acad. Sci. U.S.A.* 101(12):4083-8.
- Modzelewska A, Filipek S, Palczewski K, Park PS. 2006. Arrestin interaction with rhodopsin: conceptual models. *Cell Biochem Biophys* 46(1):1-15.
- Monticelli L, Colombo G. 2004. The influence of simulation conditions in molecular dynamics investigations of model beta-sheet peptides. *Theoretical Chemistry Accounts* 112(3):145-157.
- Monticelli L, Simoes C, Belvisi L, Colombo G. 2006. Assessing the influence of electrostatic schemes on molecular dynamics simulations of secondary structure forming peptides. *Journal of Physics-Condensed Matter* 18(14):S329-S345.
- Mouritsen OG, Bloom M. 1984. Mattress Model of Lipid-Protein Interactions in Membranes. *Biophysical Journal* 46(2):141-153.
- Mukhopadhyay P, Monticelli L, Tieleman DP. 2004. Molecular dynamics simulation of a palmitoyl-oleoyl phosphatidylserine bilayer with Na⁺ counterions and NaCl. *Biophys. J.* 86(3):1601-9.
- Muller M, Katsov K, Schick M. 2006. Biological and synthetic membranes: What can be learned from a coarse-grained description? *Physics Reports-Review Section of Physics Letters* 434(5-6):113-176.

- Nagle JF, Tristram-Nagle S. 2000. Structure of lipid bilayers. *Biochim. Biophys. Acta* 1469(3):159-195.
- Nakamichi H, Okada T. 2006a. Crystallographic analysis of primary visual photochemistry. *Angew Chem Int Ed Engl* 45(26):4270-3.
- Nakamichi H, Okada T. 2006b. Local peptide movement in the photoreaction intermediate of rhodopsin. *Proc Natl Acad Sci U S A* 103(34):12729-34.
- Nakanishi K. 2000. Recent bioorganic studies on rhodopsin and visual transduction. *Chemical & Pharmaceutical Bulletin* 48(10):1399-1409.
- Nakanishi K, Crouch R. 1995. Application of artificial pigments to structure determination and study of photoinduced transformations of retinal proteins. *Israel Journal of Chemistry* 35(3-4):253-272.
- Nose S. 1984. A Molecular-Dynamics Method for Simulations in the Canonical Ensemble. *Molecular Physics* 52(2):255-268.
- Nose S, Klein ML. 1983. Constant Pressure Molecular-Dynamics for Molecular-Systems. *Molecular Physics* 50(5):1055-1076.
- Nymeyer H, Woolf TB, Garcia AE. 2005. Folding is not required for bilayer insertion: replica exchange simulations of an alpha-helical peptide with an explicit lipid bilayer. *Proteins* 59(4):783-90.
- Okada T, Fujiyoshi Y, Silow M, Navarro J, Landau EM, Shichida Y. 2002. Functional role of internal water molecules in rhodopsin revealed by x-ray crystallography. *Proc. Natl. Acad. Sci. U.S.A.* 99(9):5982-5987.
- Okada T, Sugihara M, Bondar AN, Elstner M, Entel P, Buss V. 2004. The retinal conformation and its environment in rhodopsin in light of a new 2.2 angstrom crystal structure. *J. Mol. Biol.* 342(2):571-583.
- Oliveira L, Hulsen T, Lutje Hulsik D, Paiva AC, Vriend G. 2004. Heavier-than-air flying machines are impossible. *FEBS Lett* 564(3):269-73.
- Ovchinnikov Yu A. 1982. Rhodopsin and bacteriorhodopsin: structure-function relationships. *FEBS Lett* 148(2):179-91.
- Palczewski K. 2006. G protein-coupled receptor rhodopsin. *Annual Review of Biochemistry* 75:743-767.
- Palczewski K, Kumasaka T, Hori T, Behnke CA, Motoshima H, Fox BA, Le Trong I, Teller DC, Okada T, Stenkamp RE and others. 2000. Crystal structure of rhodopsin: A G protein-coupled receptor. *Science* 289(5480):739-745.
- Pandit SA, Berkowitz ML. 2002. Molecular dynamics simulation of dipalmitoylphosphatidylserine bilayer with Na⁺ counterions. *Biophys. J.* 82(4):1818-1827.
- Pandit SA, Bostick D, Berkowitz ML. 2003a. Mixed bilayer containing dipalmitoylphosphatidylcholine and dipalmitoylphosphatidylserine: lipid complexation, ion binding, and electrostatics. *Biophys. J.* 85(5):3120-31.
- Pandit SA, Bostick D, Berkowitz ML. 2003b. Molecular dynamics simulation of a dipalmitoylphosphatidylcholine bilayer with NaCl. *Biophys. J.* 84(6):3743-3750.
- Pardo L, Sepulcre F, Cladera J, Dunach M, Labarta A, Tejada J, Padros E. 1998. Experimental and theoretical characterization of the high-affinity cation-binding site of

- the purple membrane. *Biophys. J.* 75(2):777-784.
- Park PS, Filipek S, Wells JW, Palczewski K. 2004. Oligomerization of G protein-coupled receptors: past, present, and future. *Biochemistry* 43(50):15643-56.
- Parrinello M, Rahman A. 1981. Polymorphic Transitions in Single-Crystals - a New Molecular-Dynamics Method. *Journal of Applied Physics* 52(12):7182-7190.
- Parsegian VA. 1975. Ion-Membrane Interactions as Structural Forces. *Ann. Ny. Acad. Sci.* 264(DEC30):161-174.
- Patra M, Karttunen M. 2004. Systematic comparison of force fields for microscopic simulations of NaCl in aqueous solutions: diffusion, free energy of hydration, and structural properties. *J Comput Chem* 25(5):678-89.
- Patra M, Karttunen M, Hyvönen MT, Falck E, Lindqvist P, Vattulainen I. 2003. Molecular dynamics simulations of lipid bilayers: major artifacts due to truncating electrostatic interactions. *Biophys. J.* 84(6):3636-45.
- Patra M, Karttunen M, Hyvonen MT, Falck E, Vattulainen I. 2004. Lipid bilayers driven to a wrong lane in molecular dynamics simulations by subtle changes in long-range electrostatic interactions. *J. Phys. Chem. B* 108(14):4485-4494.
- Pearlman DA, Case DA, Caldwell JW, Ross WS, Cheatham TE, Debolt S, Ferguson D, Seibel G, Kollman P. 1995. Amber, a Package of Computer-Programs for Applying Molecular Mechanics, Normal-Mode Analysis, Molecular-Dynamics and Free-Energy Calculations to Simulate the Structural and Energetic Properties of Molecules. *Comput. Phys. Commun.* 91(1-3):1-41.
- Pebay-Peyroula E, Rummel G, Rosenbusch JP, Landau EM. 1997. X-ray structure of bacteriorhodopsin at 2.5 angstroms from microcrystals grown in lipidic cubic phases. *Science* 277(5332):1676-81.
- Pedersen UR, Leidy C, Westh P, Peters GH. 2006. The effect of calcium on the properties of charged phospholipid bilayers. *Biochim. Biophys. Acta* 1758(5):573-82.
- Periole X, Ceruso MA, Mehler EL. 2004. Acid-base equilibria in rhodopsin: dependence of the protonation state of glu134 on its environment. *Biochemistry* 43(22):6858-64.
- Periole X, Huber T, Marrink SJ, Sakmar TP. 2007. G protein-coupled receptors self-assemble in dynamics simulations of model bilayers. *J Am Chem Soc* 129(33):10126-32.
- Petrache HI, Grossfield A, MacKenzie KR, Engelman DM, Woolf TB. 2000. Modulation of glycoporphin A transmembrane helix interactions by lipid bilayers: molecular dynamics calculations. *J Mol Biol* 302(3):727-46.
- Petrache HI, Tristram-Nagle S, Harries D, Kucerka N, Nagle JF, Parsegian VA. 2006. Swelling of phospholipids by monovalent salt. *J. Lipid Res.* 47(2):302-9.
- Pitman MC, Grossfield A, Suits F, Feller SE. 2005. Role of cholesterol and polyunsaturated chains in lipid-protein interactions: molecular dynamics simulation of rhodopsin in a realistic membrane environment. *J. Am. Chem. Soc.* 127(13):4576-7.
- Pitman MC, Suits F, Mackerell AD, Jr., Feller SE. 2004. Molecular-level organization of saturated and

- polyunsaturated fatty acids in a phosphatidylcholine bilayer containing cholesterol. *Biochemistry* 43(49):15318-28.
- Praprotnik M, Delle Site L, Kremer K. 2007. A macromolecule in a solvent: Adaptive resolution molecular dynamics simulation. *Journal of Chemical Physics* 126(13):-.
- Praprotnik M, Matysiak S, Delle Site L, Kremer K, Clementi C. 2007. Adaptive resolution simulation of liquid water. *Journal of Physics-Condensed Matter* 19(29):-.
- Raman P, Cherezov V, Caffrey M. 2006. The membrane protein data bank. *Cellular and Molecular Life Sciences* 63(1):36-51.
- Rando RR. 2001. The biochemistry of the visual cycle. *Chem Rev* 101(7):1881-96.
- Rapaport DC. 2004. *The Art of Molecular Dynamics Simulation*. University Press, Cambridge, United Kingdom.
- Rasmussen SG, Choi HJ, Rosenbaum DM, Kobilka TS, Thian FS, Edwards PC, Burghammer M, Ratnala VR, Sanishvili R, Fischetti RF and others. 2007. Crystal structure of the human beta(2) adrenergic G-protein-coupled receptor. *Nature*.
- Rasmussen SG, Jensen AD, Liapakis G, Ghanouni P, Javitch JA, Gether U. 1999. Mutation of a highly conserved aspartic acid in the beta2 adrenergic receptor: constitutive activation, structural instability, and conformational rearrangement of transmembrane segment 6. *Mol Pharmacol* 56(1):175-84.
- Rohrig UF, Guidoni L, Rothlisberger U. 2002. Early steps of the intramolecular signal transduction in rhodopsin explored by molecular dynamics simulations. *Biochemistry* 41(35):10799-809.
- Rosenbaum DM, Cherezov V, Hanson MA, Rasmussen SG, Thian FS, Kobilka TS, Choi HJ, Yao XJ, Weis WI, Stevens RC and others. 2007. GPCR Engineering Yields High-Resolution Structural Insights into β_2 Adrenergic Receptor Function. *Science*.
- Rosenthal W, Antaramian A, Gilbert S, Birnbaumer M. 1993. Nephrogenic diabetes insipidus. A V2 vasopressin receptor unable to stimulate adenylyl cyclase. *J Biol Chem* 268(18):13030-3.
- Roux B, Berneche S, Im W. 2000. Ion channels, permeation, and electrostatics: insight into the function of KcsA. *Biochemistry* 39(44):13295-306.
- Roux B, Karplus M. 1994. Molecular dynamics simulations of the gramicidin channel. *Annu Rev Biophys Biomol Struct* 23:731-61.
- Roux M, Bloom M. 1990. Ca²⁺, Mg²⁺, Li⁺, Na⁺, and K⁺ Distributions in the Headgroup Region of Binary Membranes of Phosphatidylcholine and Phosphatidylserine as Seen by Deuterium Nmr. *Biochemistry* 29(30):7077-7089.
- Rubenstein LA, Lanzara RG. 1998. Activation of G protein-coupled receptors entails cysteine modulation of agonist binding. *Journal of Molecular Structure-Theochem* 430:57-71.
- Saam J, Tajkhorshid E, Hayashi S, Schulten K. 2002. Molecular dynamics investigation of primary photoinduced events in the activation of rhodopsin. *Biophys. J.* 83(6):3097-3112.
- Sachs JN, Nanda H, Petrache HI, Woolf TB. 2004. Changes in phosphatidylcholine headgroup tilt and water order induced by

- monovalent salts: Molecular dynamics simulations. *Biophys. J.* 86(6):3772-3782.
- Saiz L, Bandyopadhyay S, Klein ML. 2004. Effect of the pore region of a transmembrane ion channel on the physical properties of a simple membrane. *J. Phys. Chem. B* 108(8):2608-2613.
- Saiz L, Klein ML. 2002. Computer simulation studies of model biological membranes. *Accounts of Chemical Research* 35(6):482-489.
- Sakmar TP. 2002. Structure of rhodopsin and the superfamily of seven-helical receptors: the same and not the same. *Curr Opin Cell Biol* 14(2):189-95.
- Sakmar TP, Franke RR, Khorana HG. 1991. The role of the retinylidene Schiff base counterion in rhodopsin in determining wavelength absorbance and Schiff base pKa. *Proc Natl Acad Sci U S A* 88(8):3079-83.
- Salahpour A, Angers S, Bouvier M. 2000. Functional significance of oligomerization of G-protein-coupled receptors. *Trends Endocrinol Metab* 11(5):163-8.
- Salom D, Lodowski DT, Stenkamp RE, Le Trong I, Golczak M, Jastrzebska B, Harris T, Ballesteros JA, Palczewski K. 2006. Crystal structure of a photoactivated deprotonated intermediate of rhodopsin. *Proc Natl Acad Sci U S A* 103(44):16123-8.
- Samama P, Cotecchia S, Costa T, Lefkowitz RJ. 1993. A Mutation-Induced Activated State of the Beta(2)-Adrenergic Receptor - Extending the Ternary Complex Model. *Journal of Biological Chemistry* 268(7):4625-4636.
- Sankaramakrishnan R, Weinstein H. 2004. Surface tension parameterization in molecular dynamics simulations of a phospholipid-bilayer membrane: Calibration and effects. *J. Phys. Chem. B* 108(31):11802-11811.
- Sanz C, Marquez M, Peralvarez A, Elouatik S, Sepulcre F, Querol E, Lazarova T, Padros E. 2001. Contribution of extracellular Glu residues to the structure and function of bacteriorhodopsin. Presence of specific cation-binding sites. *J. Biol. Chem.* 276(44):40788-94.
- Scheer A, Fanelli F, Costa T, De Benedetti PG, Cotecchia S. 1996. Constitutively active mutants of the alpha 1B-adrenergic receptor: role of highly conserved polar amino acids in receptor activation. *Embo J* 15(14):3566-78.
- Schlegel B, Sippl W, Holtje HD. 2005. Molecular dynamics simulations of bovine rhodopsin: influence of protonation states and different membrane-mimicking environments. *J. Mol. Model.* (Online) 12(1):49-64.
- Schlick T. 2002. *Molecular Modeling and Simulation*. Springer-Verlag, New York.
- Schreiber H, Steinhauser O. 1992a. Cutoff size does strongly influence molecular dynamics results on solvated polypeptides. *Biochemistry* 31(25):5856-60.
- Schreiber H, Steinhauser O. 1992b. Taming cut-off induced artifacts in molecular dynamics studies of solvated polypeptides. The reaction field method. *J Mol Biol* 228(3):909-23.
- Sepulcre F, Cladera J, Garcia J, Proietti MG, Torres J, Padros E. 1996. An extended X-ray absorption fine structure study of the high-affinity cation-binding site in the purple membrane. *Biophysical Journal* 70(2):852-856.

- Sepulcre F, Proietti MG, Benfatto M, Della Longa S, Garcia J, Padros E. 2004. A quantitative XANES analysis of the calcium high-affinity binding site of the purple membrane. *Biophysical Journal* 87(1):513-520.
- Sheikh SP, Zvyaga TA, Lichtarge O, Sakmar TP, Bourne HR. 1996. Rhodopsin activation blocked by metal-ion-binding sites linking transmembrane helices C and F. *Nature* 383(6598):347-50.
- Shih AY, Arkhipov A, Freddolino PL, Schulten K. 2006. Coarse grained protein-lipid model with application to lipoprotein particles. *Journal of Physical Chemistry B* 110(8):3674-3684.
- Simons K, Ikonen E. 1997. Functional rafts in cell membranes. *Nature* 387(6633):569-572.
- Singer SJ, Nicolson GL. 1972. Fluid Mosaic Model of Structure of Cell-Membranes. *Science* 175(4023):720-731.
- Smondryev AM, Berkowitz ML. 1999. United atom force field for phospholipid membranes: Constant pressure molecular dynamics simulation of dipalmitoylphosphatidicholine/water system. *J. Comput. Chem.* 20(5):531-545.
- Sperotto MM, May S, Baumgaertner A. 2006. Modelling of proteins in membranes. *Chem. Phys. Lipids.*
- Spooner PJ, Sharples JM, Goodall SC, Bovee-Geurts PH, Verhoeven MA, Lugtenburg J, Pistorius AM, Degrip WJ, Watts A. 2004. The ring of the rhodopsin chromophore in a hydrophobic activation switch within the binding pocket. *J Mol Biol* 343(3):719-30.
- Spooner PJ, Sharples JM, Goodall SC, Seedorf H, Verhoeven MA, Lugtenburg J, Bovee-Geurts PH, DeGrip WJ, Watts A. 2003. Conformational similarities in the beta-ionone ring region of the rhodopsin chromophore in its ground state and after photoactivation to the metarhodopsin-I intermediate. *Biochemistry* 42(46):13371-8.
- Spooner PJ, Sharples JM, Verhoeven MA, Lugtenburg J, Glaubitz C, Watts A. 2002. Relative orientation between the beta-ionone ring and the polyene chain for the chromophore of rhodopsin in native membranes. *Biochemistry* 41(24):7549-55.
- Stenkamp RE, Filipek S, Driessen CA, Teller DC, Palczewski K. 2002. Crystal structure of rhodopsin: a template for cone visual pigments and other G protein-coupled receptors. *Biochim Biophys Acta* 1565(2):168-82.
- Stenkamp RE, Teller DC, Palczewski K. 2002. Crystal structure of rhodopsin: a G-protein-coupled receptor. *ChemBiochem* 3(10):963-7.
- Strahs D, Weinstein H. 1997. Comparative modeling and molecular dynamics studies of the delta, kappa and mu opioid receptors. *Protein Eng* 10(9):1019-38.
- Strandberg E, Killian JA. 2003. Snorkeling of lysine side chains in transmembrane helices: how easy can it get? *Febs Letters* 544(1-3):69-73.
- Stryer L. 1991. Visual excitation and recovery. *J Biol Chem* 266(17):10711-4.
- Stuart JA, Vought BW, Zhang CF, Birge RR. 1995. The Active-Site of Bacteriorhodopsin - 2-Photon Spectroscopic Evidence for a Positively Charged Chromophore Binding-Site Mediated by

- Calcium. *Biospectroscopy* 1(1):9-28.
- Sugihara M, Buss V, Entel P, Elstner M, Frauenheim T. 2002. 11-cis-retinal protonated Schiff base: Influence of the protein environment on the geometry of the rhodopsin chromophore. *Biochemistry* 41(51):15259-15266.
- Szundi I, Steckenius W. 1987. Effect of Lipid Surface-Charges on the Purple-to-Blue Transition of Bacteriorhodopsin. *Proceedings of the National Academy of Sciences of the United States of America* 84(11):3681-3684.
- Szundi I, Stoeckenius W. 1988a. Purple-to-Blue Transition of Bacteriorhodopsin in a Neutral Lipid Environment. *Biophysical Journal* 54(2):227-232.
- Szundi I, Stoeckenius W. 1989. Surface Ph Controls Purple-to-Blue Transition of Bacteriorhodopsin - a Theoretical-Model of Purple Membrane-Surface. *Biophysical Journal* 56(2):369-383.
- Szundi T, Stoeckenius W. 1988b. Cations Affect the Purple-to-Blue Transition of Bacteriorhodopsin in Purple Membrane Via Changes in Surface Ph. *Biophysical Journal* 53(2):A383-A383.
- Takeda K, Sato H, Hino T, Kono M, Fukuda K, Sakurai I, Okada T, Kouyama T. 1998. A novel three-dimensional crystal of bacteriorhodopsin obtained by successive fusion of the vesicular assemblies. *J Mol Biol* 283(2):463-74.
- Tan EHL, Govender DSK, Birge RR. 1996. Large organic cations can replace Mg²⁺ and Ca²⁺ ions in bacteriorhodopsin and maintain proton pumping ability. *Journal of the American Chemical Society* 118(11):2752-2753.
- Tanford. 1973. *The Hydrophobic Effect*. Wiley (New York).
- Tatulian SA. 1987. Binding of Alkaline-Earth Metal-Cations and Some Anions to Phosphatidylcholine Liposomes. *Eur. J. Biochem.* 170(1-2):413-420.
- Teller DC, Okada T, Behnke CA, Palczewski K, Stenkamp RE. 2001. Advances in determination of a high-resolution three-dimensional structure of rhodopsin, a model of G-protein-coupled receptors (GPCRs). *Biochemistry* 40(26):7761-7772.
- Terrillon S, Bouvier M. 2004. Receptor activity-independent recruitment of betaarrestin2 reveals specific signalling modes. *Embo J* 23(20):3950-61.
- Tieleman DP, Berendsen HJ, Sansom MS. 1999. An alamethicin channel in a lipid bilayer: molecular dynamics simulations. *Biophys. J.* 76(4):1757-69.
- Tieleman DP, Berendsen HJC. 1996. Molecular dynamics simulations of a fully hydrated dipalmitoyl phosphatidylcholine bilayer with different macroscopic boundary conditions and parameters. *J. Chem. Phys.* 105(11):4871-4880.
- Tieleman DP, Forrest LR, Sansom MS, Berendsen HJ. 1998. Lipid properties and the orientation of aromatic residues in OmpF, influenza M2, and alamethicin systems: molecular dynamics simulations. *Biochemistry* 37(50):17554-61.
- Tieleman DP, MacCallum JL, Ash WL, Kandt C, Xu ZT, Monticelli L. 2006. Membrane protein simulations with a united-atom lipid and all-atom protein model: lipid-protein interactions, side chain transfer free energies and model proteins. *J. Phys-Condens. Mat.* 18(28):S1221-S1234.

- Tieleman DP, Marrink SJ, Berendsen HJC. 1997. A computer perspective of membranes: molecular dynamics studies of lipid bilayer systems. *Biochim. Biophys. Acta* 1331(3):235-270.
- Tieleman DP, Sansom MS, Berendsen HJ. 1999. Alamethicin helices in a bilayer and in solution: molecular dynamics simulations. *Biophys. J.* 76(1 Pt 1):40-9.
- Tobias DJ. 2001. Electrostatics calculations: recent methodological advances and applications to membranes. *Current Opinion in Structural Biology* 11(2):253-261.
- Tuzi S, Yamaguchi S, Tanio M, Konishi H, Inoue S, Naito A, Needleman R, Lanyi JK, Saito H. 1999. Location of a cation-binding site in the loop between helices F and G of bacteriorhodopsin as studied by C-13 NMR. *Biophysical Journal* 76(3):1523-1531.
- Urizar E, Claeysen S, Deupi X, Govaerts C, Costagliola S, Vassart G, Pardo L. 2005. An activation switch in the rhodopsin family of G protein-coupled receptors: the thyrotropin receptor. *J Biol Chem* 280(17):17135-41.
- van der Ploeg P, Berendsen HJC. 1982. Molecular-Dynamics Simulation of a Bilayer-Membrane. *J. Chem. Phys.* 76(6):3271-3276.
- Van Gunsteren WF. 1987. GROMOS. Groningen Molecular Simulation Program Package. (Groningen: University of Groningen).
- Van Gunsteren WF, Berendsen HJC. 1977. Algorithms for Macromolecular Dynamics and Constraint Dynamics. *Molecular Physics* 34(5):1311-1327.
- Van Gunsteren WF, Berendsen HJC. 1990. Computer-Simulation of Molecular-Dynamics - Methodology, Applications, and Perspectives in Chemistry. *Angewandte Chemie-International Edition in English* 29(9):992-1023.
- Varo G, Brown LS, Needleman R, Lanyi JK. 1999. Binding of calcium ions to bacteriorhodopsin. *Biophysical Journal* 76(6):3219-3226.
- Venable RM, Brooks BR, Pastor RW. 2000. Molecular dynamics simulations of gel (L-beta I) phase lipid bilayers in constant pressure and constant surface area ensembles. *J. Chem. Phys.* 112(10):4822-4832.
- Venturoli M, Smit B, Sperotto MM. 2005. Simulation studies of protein-induced bilayer deformations, and lipid-induced protein tilting, on a mesoscopic model for lipid bilayers with embedded proteins. *Biophys. J.* 88(3):1778-1798.
- Vigh L, Escriba PV, Sonnleitner A, Sonnleitner M, Piotto S, Maresca B, Horvath I, Harwood JL. 2005. The significance of lipid composition for membrane activity: New concepts and ways of assessing function. *Progress in Lipid Research* 44(5):303-344.
- Vogel R, Siebert F, Ludeke S, Hirshfeld A, Sheves M. 2005. Agonists and partial agonists of rhodopsin: retinals with ring modifications. *Biochemistry* 44(35):11684-99.
- Wallqvist A, Mountain RD. 1999. Molecular models of water: Derivation and description. *Reviews in Computational Chemistry* 13:183-247.
- Watts A, Harlos K, Marsh D. 1981. Charge-induced tilt in ordered-phase phosphatidylglycerol bilayers evidence from X-ray diffraction. *Biochim. Biophys. Acta* 645(1):91-6.
- Weiss JM, Morgan PH, Lutz MW, Kenakin TP. 1996a. The cubic ternary complex receptor-occupancy model .1. Model

- description. *Journal of Theoretical Biology* 178(2):151-167.
- Weiss JM, Morgan PH, Lutz MW, Kenakin TP. 1996b. The cubic ternary complex receptor-occupancy model .2. Understanding apparent affinity. *Journal of Theoretical Biology* 178(2):169-182.
- Weiss JM, Morgan PH, Lutz MW, Kenakin TP. 1996c. The cubic ternary complex receptor-occupancy model .3. Resurrecting efficacy. *Journal of Theoretical Biology* 181(4):381-397.
- Weiss TM, van der Wel PC, Killian JA, Koeppe RE, 2nd, Huang HW. 2003. Hydrophobic mismatch between helices and lipid bilayers. *Biophys. J.* 84(1):379-85.
- White SH. 2004. The progress of membrane protein structure determination. *Protein Sci* 13(7):1948-9.
- White SH, Wimley WC. 1999. Membrane protein folding and stability: Physical principles. *Annu. Rev. Bioph. Biom.* 28:319-365.
- Wiener MC, White SH. 1992. Structure of a fluid dioleoylphosphatidylcholine bilayer determined by joint refinement of x-ray and neutron diffraction data. III. Complete structure. *Biophys J* 61(2):434-47.
- Wohlert J, Edholm O. 2004. The range and shielding of dipole-dipole interactions in phospholipid bilayers. *Biophys. J.* 87(4):2433-2445.
- Yandek LE, Pokorny A, Floren A, Knoelke K, Langel U, Almeida PF. 2007. Mechanism of the Cell-Penetrating Peptide Tp10 Permeation of Lipid Bilayers. *Biophys. J.*
- Yeagle PL, Albert AD. 2006. G-protein coupled receptor structure. *Biochim. Biophys. Acta.*
- Yeagle PL, Bennett M, Lemaitre V, Watts A. 2006. Transmembrane helices of membrane proteins may flex to satisfy hydrophobic mismatch. *Biochim. Biophys. Acta.*
- Zhang K, Song L, Dong J, ElSayed MA. 1997. Studies of cation binding in ZnCl₂ regenerated bacteriorhodopsin by XAFS. *Biophysical Journal* 72(2):Tu411-Tu411.
- Zhang YN, Sweetman LL, Awad ES, Elsayed MA. 1992. Nature of the Individual Ca(2+) Binding-Sites in Ca(2+)-Regenerated Bacteriorhodopsin. *Biophysical Journal* 61(5):1201-1206.
- Zhao W, Rog T, Gurtovenko AA, Vattulainen I, Karttunen M. 2007. Atomic-scale structure and electrostatics of anionic palmitoyl-oleoyl-phosphatidylglycerol lipid bilayers with Na⁺ counterions. *Biophys. J.* 92(4):1114-24.
- Zhu Q, Vaughn MW. 2005. Surface tension effect on transmembrane channel stability in a model membrane. *J. Phys. Chem. B* 109(41):19474-19483.